Investigations of the role of spatial dimensionality and interparticle interactions in model glass-formers

A Thesis

Submitted For the Degree of

DOCTOR OF PHILOSOPHY

in the Faculty of Science

by

Shiladitya Sengupta

THEORETICAL SCIENCES UNIT
JAWAHARLAL NEHRU CENTRE FOR
ADVANCED SCIENTIFIC RESEARCH
Bangalore – 560 064

MARCH 2013

To my mother Arundhati and my aunt Anuradha

DECLARATION

I hereby declare that the matter embodied in the thesis entitled "**Investigations of the role of spatial dimensionality and interparticle interactions in model glass-formers**" is the result of investigations carried out by me at the Theoretical Sciences Unit, Jawaharlal Nehru Centre for Advanced Scientific Research, Bangalore, India under the supervision of Prof. Srikanth Sastry and that it has not been submitted elsewhere for the award of any degree or diploma.

In keeping with the general practice in reporting scientific observations, due acknowledgement has been made whenever the work described is based on the findings of other investigators.

Shiladitya Sengupta

CERTIFICATE

I hereby certify that the matter embodied in this thesis entitled "**Investigations of the role of spatial dimensionality and interparticle interactions in model glass-formers**" has been carried out by Mr. Shiladitya Sengupta at the Theoretical Sciences Unit, Jawaharlal Nehru Centre for Advanced Scientific Research, Bangalore, India under my supervision and that it has not been submitted elsewhere for the award of any degree or diploma.

Prof. Srikanth Sastry
(Research Supervisor)

Acknowledgments

David Mermin in his Knight lecture in 1999 remarked that the "*dominant tradition in late 20th century scientific prose has been to produce something suitable for direct transmission from one computer to another, from which any trace of human origin has been purged, and in which any suggestion of the humanity of the author or the reader would be in bad taste.*" [http://www.lassp.cornell.edu/mermin/KnightLecture.html] So in the present thesis, this is the "only" section where some traces of human origin will be found in the sincere hope of reminding the student reader, if any, that scientific research is after all a very much humane enterprise. I take this opportunity to thank people who have helped me in various ways to complete Ph. D.

I thank my Guru, Prof. Srikanth Sastry for his guidance and advices on diverse subjects - both scientific and outside science. He is a born teacher who has taught by example how to do good science. I was fortunate to have him as my adviser.

I would like to thank Prof. Chandan Dasgupta, Dr. Smarajit Karmakar, Dr. Vishwas Vasisht and Dr. Moumita Maiti for fruitful and lively scientific discussions. I have tried to learn from their diverse working styles and scientific approaches, in particular from Vishwas and Moumita.

I was fortunate to come across many talented friends and seniors right from the school days. In particular, I would like to acknowledge the help of - Arnab Sen, Sayantan Sharma, Hridis Pal, Anindya Roy, Anindya Dey, Sabyasachi Mukhopadhyay, Nihal Arju, Sumilan Banerjee - to learn mathematics, physics and science in general. I also thank the many excellent and unconventional teachers who has taught great physics courses - the excellent teachers of the Physics department of Jadavpur University including the "gang of four" (Prof. Dhiranjan Roy, Prof. Ranjan Banerjee, Prof. S. K.

Roy, Prof. Narayan Banerjee) and Prof. Soumitra Sengupta from IACS; from the Physics department of IIT Kharagpur in particular Prof. Sayan Kar and Dr. Pratik Khastagir; faculties of the Theoretical Sciences Unit in particular Dr. Kavita Jain and faculties of the Physics Department of Indian Institute of Science in particular Prof. Chandan Dasgupta. I also acknowledge Dr. Taraknath Tarafdar for teaching everything from Bengali to Biology and offering guidance during school days.

I thank past and present labmates - Ashwin, Niels, Bhaswati, Anil, Shibu, Moumita, Vishwas, Aparna, Anshul, Vinutha, summer students and visitors and friends from JNCASR for making the lab and the campus a lively place.

I thank all the TSU faculties for generous help when required.

I thank the JNCASR administration, the Doctors in particular Dr. Subba Rao and the system administrators of the sampige and the booruga clusters

I acknowledge CCMS, JNCASR for the computational facility and CSIR, India and JNCASR for financial support.

And last but not the least I thank my mother Arundhati and my aunt Anuradha for their love and unconditional support that enabled me to complete the Ph. D.

Synopsis

This is the synopsis of the thesis titled "**Investigations of the role of spatial dimensionality and interparticle interactions in model glass-formers**", delivered by Shiladitya Sengupta of the Theoretical Sciences Unit, Jawaharlal Nehru Centre for Advanced Research, Bangalore, India.

The aim of the present thesis is twofold:

1. To examine the relationship between dynamics, spatial correlations, and thermodynamics by *explicitly computing* characteristic time scales, length scales and the configurational entropy in several model liquids.

2. To explore the dependence of the characteristic time scales on various control parameters. In addition to the more familiar parameters like temperature and density we study the effect of spatial dimensionality and the interaction potential.

The thesis is divided into seven chapters. The outline of the thesis is presented below:

- Chapter 1 introduces to the general area of research described in the thesis. A brief summary to the phenomenology of the dynamic and thermodynamic signatures of slow dynamics and the relevant theoretical approaches are discussed. Also the recent analyses of liquid state properties in terms of density temperature scaling are briefly introduced.

- Chapter 2 details the definitions of the different quantities computed, the computational methods used to perform simulations and the description of the model glass-forming liquids studied.

- Chapter 3 describes an analysis of the dependence on the spatial dimension of the Adam Gibbs (AG) relation. The AG relation describes the

dependence of relaxation times (dynamics) on the configurational entropy (thermodynamics) and is of central importance in the understanding of glass forming liquids. Although the AG relation is successful in describing a wide range of experimental and simulation data, its physical origins are unclear and a universally accepted satisfactory derivation of the relation is lacking. Specifically, according to the original formulation , the AG relation has no dependence on spatial dimensionality D while latter formulations suggest *explicit* dimensional dependence. Analysis of extensive numerical simulations of a variety of models in 2, 3 and 4 dimensions indicates that while AG relation works in 3 and 4 dimensions, it breaks down in 2 dimensions. Further, the deviation from the AG relation in 2 dimensions depends on the nature of the interaction potential.

- Chapter 4 describes the dependence on spatial dimension (D) of the breakdown of Stokes Einstein (SE) relation between diffusion coefficient and viscosity (relaxation time , an often used substitution). In 3D, the SE relation is studied in a well-studied model glass-former (Kob-Andersen or KA model) using both viscosity and structural relaxation time and is found to breakdown at low temperature while at high temperature the SE relation between diffusivity and viscosity is recovered. Using several model glass-formers the SE relation between diffusivity and structural relaxation time is found to break down at low T in 2D and 4D as well. The fractional breakdown exponent is found to be closer to 1 at higher dimension suggesting the SE breakdown is weaker at higher dimension. The SE breakdown is usually considered to be a consequence of the dynamic heterogeneity (DH) which develops at low temperatures in a supercooled liquid. DH is characterized in this work by (i) the dynamical susceptibility (ii) the KWW exponent and (iii) the fragility. Systems at higher dimension is found to be more heterogeneous as well as more fragile. While this trend is consistent with positive correlation between heterogeneity and fragility claimed previously in 3D, it is opposite to the expectation based on the dimension dependence of the SE breakdown.

- Chapter 5 analyzes the dependence of fragility on the softness of the interparticle interaction. Fragility is a material parameter which measures the rapidity of change of the viscosity (or relaxation time) with temperature and is a useful organizing principle to understand data for a wide range of glass forming liquids. Fragility can be defined purely from kinetics

(kinetic fragility) as well as purely from thermodynamics (thermodynamic fragility). By studying three model fragile glass-formers of varying softness (by tuning the inter-particle interactions) kinetic fragility is found to increase with softness while the thermodynamic fragility is found to decrease with softness. This apparently contradictory trend is reconciled by taking into account the softness dependence of the activation energy at high temperature and the corresponding modification of the thermodynamic fragility *via.* the AG relation. Finally, the softness dependence of the high T activation energy is partially rationalized from the density-temperature scaling of relaxation times.

- Chapter 6 explores the density-temperature (DT) scaling of relaxation times and the strong pressure-energy correlation in KA model in 3D and studies its implication on the density dependence of fragility. Both the above-mentioned properties are verified in 3D KA model. The strong pressure-energy correlation is found to rationalize *approximately* the density-temperature scaling. The density dependence of kinetic fragility is found to be consistent but stronger than predicted by DT scaling.

- Chapter 7 analyzes the anomalous behaviour of isothermal diffusion coefficient in modified Stillinger-Weber (mSW) model. The standard Stillinger Weber model is a model for silicon and has a 2-body and a 3-body interaction s. By changing the strength of the 3-body interaction (measured by the parameter λ), it is verified that the isothermal diffusivity as a function of λ goes through a maximum as observed in a previous work. It is shown that the isothermal pair correlation entropy (S_2) as a function of λ also undergoes a maximum. Thus the anomalous behaviour in diffusivity can be rationalized from the anomalous behaviour in thermodynamics.

Contents

List of Figures

Chapter 1

Introduction

1.1 Glass forming liquids

1.1.1 Supercooled liquids

Liquids and solids are low temperature phases of matter and are ubiquitous in nature. When a liquid is cooled to temperature below the freezing temperature, under equilibrium condition, it undergoes a first order phase transition to a crystalline solid. However a finite amount of time is required for the development ("nucleation") of crystalline order ("nucleation time" $\tau_{nucleation}$). Similarly, a finite amount of time ("relaxation time" $\tau_{relaxation}$) is required for the liquid to reach equilibrium at a given temperature T. The typical temperature dependence of $\tau_{nucleation}$ and $\tau_{relaxation}$ are schematically shown in Fig. 1.1(a) (the red and the blue lines respectively). Typically, as a liquid is cooled, $\tau_{nucleation}$ goes through a minimum (because it is determined by the competition between (i) a free energy barrier-crossing probability which increases monotonically and (ii) the mobility which decreases monotonically as T decreases) and $\tau_{relaxation}$ increases monotonically. Further $\tau_{nucleation} > \tau_{relaxation}$ at any given T so that the two curves do not intersect each other. Thus there is the following interesting possibility : if a liquid is cooled with a cooling rate such that the amount of time spent at a given temperature is more than $\tau_{relaxation}$ but less than $\tau_{nucleation}$ then it can avoid crystallization and can remain in the liquid phase even below its freezing point. This is the window between the red (non-monotonic) line and the blue (monotonic) line at any given temperature in Fig. 1.1(a). A

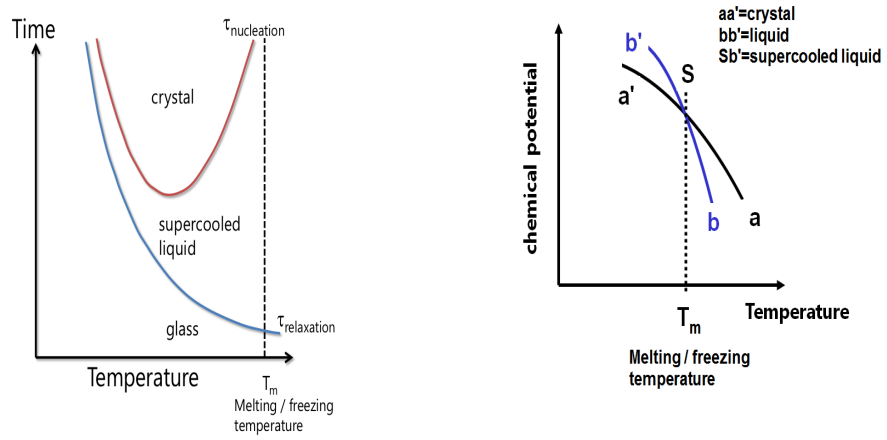

Figure 1.1: Left: The schematic temperature dependence of nucleation time and relaxation time below equilibrium freezing point (T_m). At any given temperature, the supercooled liquid exists in the time window between red (above) and blue (below) curves. Right: The schematic temperature dependence of the chemical potential of crystal ($aa^{'}$) and liquid ($bb^{'}$) phases. At the point of coexistence S the free energy of liquid and crystal phases are equal, thus it corresponds to the equilibrium melting / freezing point. The branch $Sb^{'}$ represent the supercooled liquid.

liquid below its normal freezing point is called a supercooled liquid. (Certain materials have no known crystal phases. In those cases the liquid is considered to be "supercooled" below some characteristic temperature other than the freezing point, *e.g.* the temperature where the dynamics show cross-over from high temperature behaviour to low temperature behaviour).

1.1.2 Metastability

The free energy of a supercooled liquid is higher than the crystal phase. In Fig. 1.1(b), aa' is the chemical potential $\mu(P,T)$ of the crystal phase and bb' is that of the liquid phase. They intersect at the point of coexistence S corresponding to the equilibrium melting / freezing temperature T_m. The liquid branch sb' represents the supercooled liquid. A supercooled liquid is said to be *metastable* with respect to the crystal phase. A metastable phase has a *finite lifetime* (τ_{life}) so that given infinite observation time one would see the transition to the stable phase. One then needs to specify under what condition the properties of a metastable system are measurable and reproducible. This can be specified by comparing three time scales: (i) the

characteristic time scale of observation (τ_{obs}) in an experiment (ii) the longest relaxation time τ of the system and (iii) the life-time (τ_{life}) of the system.

Consider the case in which $\tau \ll \tau_{obs}$. In this case the system can be considered to be in thermodynamic equilibrium in the sense that the system properties are expected to be invariant under time translation. Further one requires the lifetime to be longer than the observation time, $\tau_{life} > \tau_{obs}$, to measure the system properties. Hence the situation when a metastable state can be treated as a reproducible equilibrium state is given by :

$$\tau_{life} >> \tau_{obs} >> \tau \tag{1.1}$$

The relaxation time τ of a liquid increases monotonically on cooling and it is feasible that τ may *cross-over* from being less than τ_{obs} to being comparable and eventually greater than τ_{obs}. In this case, the relaxation process corresponding to τ is too slow to measure in the experiment and the system is not in thermodynamic equilibrium. Further, if τ corresponds to the time scale of structural relaxation, then the structure of the system will appear to be *frozen* in the experiment but observations made at intervals comparable to the relaxation time τ will yield different results, i.e. the system will "age". In other words, the liquid may cross-over from a regime where properties are invariant under time translation to a regime where properties depend on the choice of time origin. Such a cross-over takes place near the glass transition.

Supercooled liquids, whose relaxation times are a subject of interest in the present thesis, obey the condition 1.1 above and are treated as systems with reproducible properties. However, even if the properties of a supercooled liquid is measurable reproducibly, rigorously speaking, one should justify the application of *equilibrium* statistical mechanics and thermodynamics to describe a metastable phase. This is because, *in the thermodynamic limit*, the relative weight of metastable states to the partition function is insignificant compared to the most stable state (having the minimum free energy). Thus, strictly speaking, one should apply appropriate *constraints* to sum over only restricted regions of the phase space (see [15, 16] and Chapter 2 of [38]). These caveats should be kept in mind in studying supercooled liquids or other metastable states.

1.1.3 The laboratory glass transition

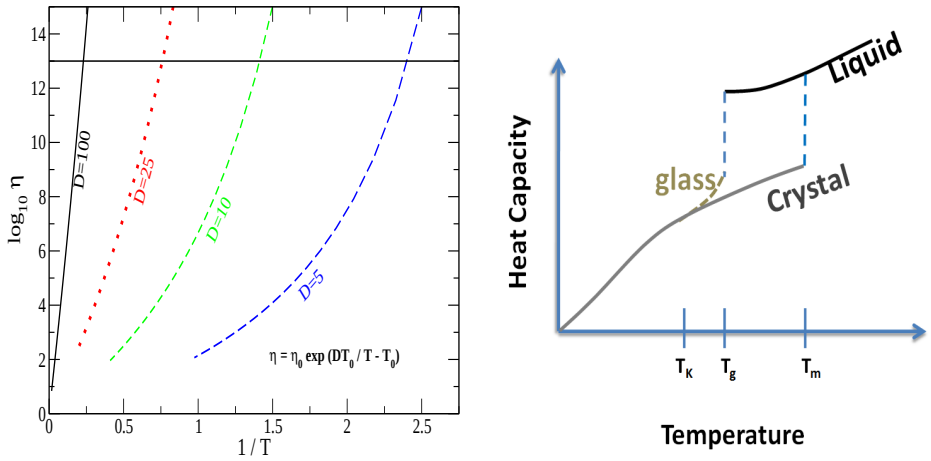

Figure 1.2: Definitions of the laboratory glass transition temperature T_g. Left: The temperature at which the logarithm of viscosity is 13 is the dynamic measure of T_g. D is a material parameter that determines how non-linear the rise of logarithm of viscosity with decreasing temperature is. D is defined by the equation $\eta = \eta_0 \exp(DT_0/(T - T_0))$. Right: The temperature at which the specific heat of the liquid shows a sharp but continuous drop is the calorimetric measure of T_g.

What happens when a liquid is cooled further and further below its freezing point? One expects that eventually it will crystallize, which is indeed true for many liquids. However there are many other liquids which does not crystallize. Instead their ability to flow reduces to such an extent that on the timescale of observation in laboratory they stop flowing. This is quantified by viscosity (discussed in detail later) which can *increase by 14 orders of magnitude* by only a modest decrease of temperature (Fig. 1.2(a)). Thus such a state mechanically behave as an "solid" despite having *no obvious structural difference* with the corresponding liquid phase. Such a solid is called an "amorphous solid" because unlike a crystalline solid, it *does not have any obvious long range structural order*. This state is known as the *structural glass* and this phenomenon of a liquid transforming into an amorphous solid upon supercooling is known as the *glass transition*. It is said to take place at a material-specific glass transition temperature (T_g) which is usually defined in the following ways:

1. *From the temperature dependence of viscosity:* T_g is taken, *by convention*, to be the temperature at which the viscosity is 10^{13} Poise (Fig. 1.2(a))

(alternatively, the relaxation time is $100s$). This is a convenient demarcation line in temperature below which the supercooled liquid is no longer considered to be in equilibrium. T_g thus defined depends on the cooling rate to some extent.

2. *From the drop of specific heat (C_P):* The falling out of equilibrium is also manifested in the changes in the temperature dependence of thermodynamic quantities like volume, specific heat and thermal expansion coefficient. As the supercooled liquid falls out of equilibrium the number of degrees of freedom accessed on the experimental time scale is reduced and consequently the specific heat shows a sharp but continuous drop at a temperature which is the calorimetric measure of T_g (Fig. 1.2(b)).

1.1.4 Slow dynamics

The glass transition identified from the above criteria depends somewhat on convention and is known as the laboratory glass transition. It is a *kinetic effect* as the phenomenology depends on the cooling rate (discussed in more detail later). The more interesting question is whether the *laboratory* glass transition is a signature of a *thermodynamic* transition to a new phase of matter. Even after many years of extensive theoretical and experimental research, the answer to this question is still inconclusive. Although glasses can be prepared by many different routes [1], the formation by the cooling of the supercooled liquid from above the glass transition temperature (in a way that crystallization is avoided) has been studied most extensively. Supercooled liquids which avoid crystallization and form glasses may be called *glass forming liquids*. Glass forming liquids in the temperature range between the laboratory glass transition temperature T_g and the equilibrium freezing/melting point T_m can be studied by equilibrium statistical mechanics and thermodynamics. The *dynamics* of glass forming liquids become *dramatically slow* as T_g is approached from above. This is signaled by a number of *signature properties* which will be discussed in the next section. A remarkable aspect of this phenomenology is that they are sufficiently generic so that *materials with very different chemical properties show similar signatures of slow dynamics*. Different kinds of materials may be colloidal suspensions, network forming liquids (*e.g.* silica - one of the main components of the earth's crust and the window glasses), polymers (*e.g.* industrial plastics) and even metals

(See *e.g.* Table 4.2 in [38]). This generality implies that it may be possible to describe some aspects of the phenomenology in a unified and universal theoretical framework. To *predict* the phenomenology of slow dynamics for glass forming liquids starting from microscopic theories may be considered the central theoretical aim to study glass forming liquids.

1.1.5 Phenomenology of the slow dynamics

One may ask five fundamental, inter-related and "grand" questions to comprehend the complex behaviour of glass-forming liquids as they are cooled.

1. How to predict the conditions under which a liquid avoids crystallization upon supercooling and forms glass i.e. how to *predict* whether a given liquid is a poor or good glass-former?
2. How to understand the dramatic increase in viscosity (slowdown of dynamics) as the liquid is supercooled?
3. What is the nature of the glass transition? Is it a thermodynamic transition?
4. How to characterize structural order in supercooled liquids and glasses which help rationalize their dynamical and thermodynamic behaviour?
5. What is a satisfactory theoretical framework within which the phenomenology of the aging behaviour can be described?

The present thesis deals mainly with the second question. The slowdown of dynamics in glass forming liquids show diverse phenomenology and excellent review articles (see *e.g.* [1–8, 10–12, 71, 72] and the book [38]) are available discussing various aspects of this phenomenology. Here we briefly discuss some of the signature properties.

1.2 Thermodynamic signatures of the slow dynamics

As a liquid is supercooled, the structure and the thermodynamics of a liquid show characteristic changes which are briefly discussed here. The importance

of such structural and thermodynamic signatures of the slowdown of dynamics is that one is naturally led to seek an understanding of the rapid rise of viscosity in terms of structure and thermodynamics.

1.2.1 Structural arrest

Figure 1.3(a) shows the schematic temperature dependence of the volume of a supercooled liquid [7]. As the liquid is cooled at constant pressure at a constant cooling rate, there is a *sharp but continuous change in the slope* as the glass transition temperature T_g is approached. In other words, the thermal expansion coefficient $\alpha_P = \frac{1}{V}\left(\frac{\partial V}{\partial T}\right)_P$ shows a sharp but continuous drop as the T_g is approached. The sharp drop in α_P is a thermodynamic signature of the structural arrest. Figure 1.3(b) illustrates that the final volume at a temperature below T_g is less for a slower cooling rate. Not only that, the glass transition temperature (identified by the temperature where the slope changes) itself is lower for a slower cooling rate. Thus the glass obtained depends on the history of preparation. Figure 1.3(b) also illustrates that if the glass obtained from a given cooling rate is heated up, for T near T_g, the heating curve is different from the cooling curve if the heating rate is different. Thus the properties of the system near T_g are also path dependent. The dependence on cooling rate and path demonstrates that the *laboratory* glass transition occurs when the liquid falls out of equilibrium and is *kinetic* in nature.

1.2.2 Kauzmann's paradox

The entropy of any system at a temperature T may be obtained from integrating the specific heat $C_P(T)$ from a reference temperature T_{ref} (Eqn. 1.2).

$$S(T) = S(T_{ref}) + \int_{T_{ref}}^{T} \frac{C_p}{T'} dT' \tag{1.2}$$

Taking the melting point T_m as the reference temperature and defining $\Delta S(T) = S_{Liquid}(T) - S_{Crystal}(T)$ as the *excess entropy* of the liquid over the crystal and $\Delta C_p = C_{P,Liquid} - C_{P,crystal}(T)$, one obtains for $T \leq T_m$:

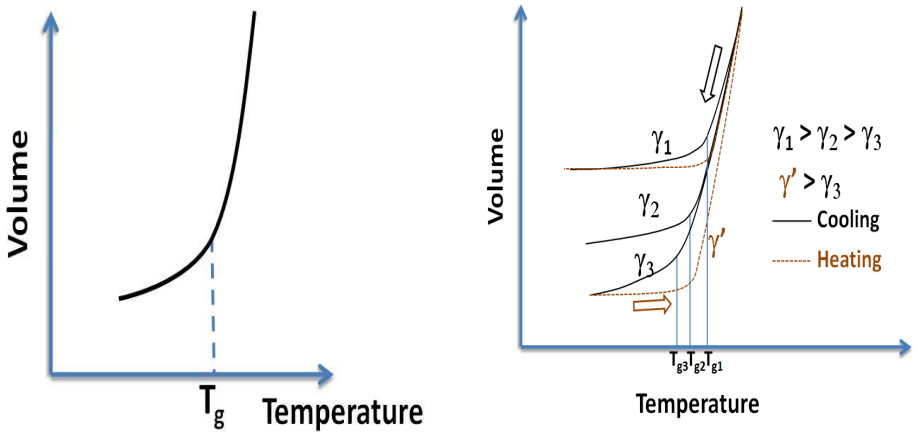

Figure 1.3: Schematic temperature dependence of the volume of a supercooled liquid as it approaches T_g. In the right drawing, $\gamma_1, \gamma_2, \gamma_3$ are cooling rates and $\gamma^{'}$ is the heating rate. See also text.

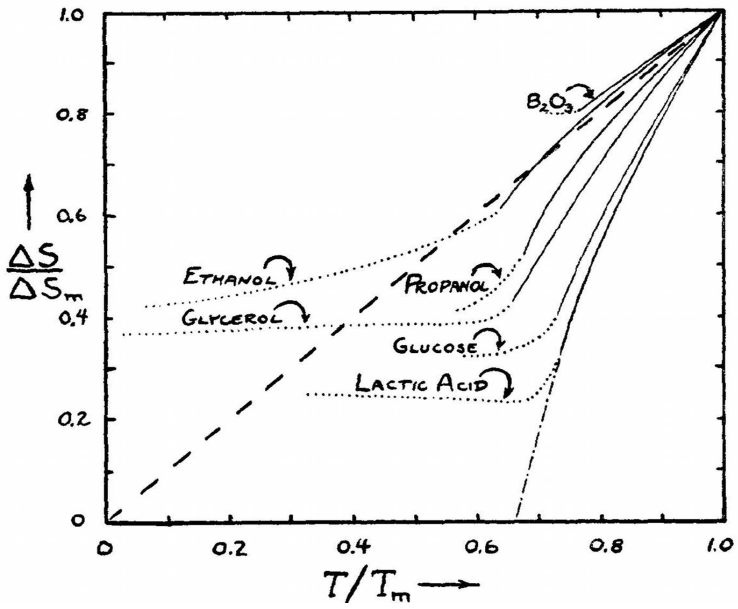

Figure 1.4: The temperature dependence of the excess entropy illustrating the Kauzmann's paradox. Figure reproduced with permission from [17].

$$\begin{aligned} \Delta S(T) &= S_{Liquid}(T) - S_{Crystal}(T) \\ &= \Delta S(T_m) - \int_T^{T_m} \frac{\Delta C_p}{T'} dT' \qquad (T \leq T_m) \end{aligned} \tag{1.3}$$

Since the specific heat for a liquid is higher than that of a crystal, the excess entropy of a supercooled liquid *decreases* with temperature. Further, from Eqn. 1.3, there may exist a *non-zero, finite* temperature T_K where the difference vanishes: $\Delta S(T_K) = 0$. Thus in the temperature range $0 \leq T \leq T_K$, the entropy of the liquid will be lower than that of the crystal. Although this is very counter-intuitive, it does not violate any known laws of physics. However, since the crystal entropy tends to zero as temperature approaches absolute zero, the *extrapolated* liquid entropy will be *negative* at zero temperature which violates both the Boltzmann's definition of entropy and the third law of thermodynamics. This possibility was pointed out by Kauzmann [17] and is known as the Kauzmann's paradox.

The Kauzmann temperature T_K may be considered to be the absolute lower limit at which a material can exist as a liquid. It can be estimated from the *extrapolated* temperature dependence of the excess entropy (Fig. 1.4). For all known liquids, $T_K < T_g$ so that the temperature T_K is not experimentally accessible by a *liquid* ([18, 38]). However, one may always hypothesize that in the limit of infinitely long observation time and infinitesimally small cooling rate, one may reach arbitrarily low temperature *in equilibrium*. Thus there have been various proposals to resolve the paradox. Gibbs and Dimarzio [36] showed that for a lattice model of polymer, the liquid undergoes a true *thermodynamic* phase transition at a finite non zero temperature to an *amorphous* phase called the "the ideal glass" (as opposed to the laboratory glasses). The phase transition is characterized by the vanishing of the entropy associated with the number of possible polymer configurations. This entropy is (approximately) equal to the excess entropy defined in Eqn. 1.3. This work leads to a possible resolution of the Kauzmann paradox which is based on the *thermodynamic* behaviour of the system. Although this scenario of a thermodynamic phase transition to an ideal glass is neither the only resolution of the Kauzmann paradox nor rigorously demonstrated for real glass forming liquids, it clearly shows that thermodynamic behaviour, specifically entropy, plays a central role in determining the phenomenology of the slow dynamics in glass forming liquids.

1.2.3 No *obvious* change in static structure

To emphasize the differences, we compare the glass transition phenomena with the case of the critical phenomena near the critical point of a second order phase transition (*e.g.* liquid-gas) which is well understood. In the case of the critical phenomena, there is a dramatic increase in the density fluctuations and a divergence of the compressibility as T approaches the critical temperature T_c. Consequently there are dramatic changes in structural correlations ([19]). The simplest descriptions of static structural correlations are given by the the pair correlation function $g(r)$ and the static structure factor $S(q)$. They contain equivalent information as they are related to each other by a Fourier transform. As $T \to T_c$, $S(q)$ for $q \to 0$ shows dramatic increase in magnitude. Similarly the static correlation length obtained from $g(r)$ becomes comparable to the wavelength of the visible light and leads to strong scattering of the visible light known as the "critical opalescence".

In glass forming liquids, unlike the case of critical phenomena, $S(q)$ and $g(r)$ does not show any dramatic change as $T \to T_g$ that can be used to locate T_g [5]. The $g(r)$ and the $S(q)$ of a glass forming liquid is only weakly T-dependent and are qualitatively similar below and above T_g. This has lead to the currently open question of whether and what structural change and corresponding lengths may be relevant for the glass transition and if higher order correlation functions capturing more subtle signatures of static structural correlations are required to describe the glass transition.

1.3 Dynamic signatures of the slow dynamics

The rapid increase in the viscosity and the structural relaxation time is the most dramatic signature of the slow dynamics. Here we first define viscosity and various relaxation times. Then we discuss the characteristic dynamic signatures of the slow dynamics.

1.3.1 Viscosity

Viscosity is a material property that measures the strength of the internal frictional forces in a liquid and characterizes the ability of a liquid to flow.

Consider a cube of volume V *fixed in space* inside a flowing liquid. The contact forces *on* the faces of the cube *by* the surrounding fluid can be described phenomenologically by a *stress tensor*. In liquids with viscous dissipation, the stress is proportional to the strain rate (as opposed to an elastic solid where stress is proportional to strain) and the proportionality constant is the viscosity (bulk and shear). A phenomenological expression for the viscous forces can be written down considering the following properties [119]:

1. Viscous forces occur only if different parts of the fluid move with different velocities *i.e.*, if there are non-zero velocity gradients. Consequently, if the fluid moves with a uniform, constant velocity then the viscous forces are zero everywhere.

2. For a fluid rotating with constant angular velocity, viscous forces are zero everywhere.

Under the above conditions, the most general second rank tensor is given by,

$$\sigma_{ik}^{visc} = \eta \left(\frac{\partial v_i}{\partial x_k} + \frac{\partial v_k}{\partial x_i} - \frac{2}{3}\delta_{ik}\frac{\partial v_l}{\partial x_l} \right) + \zeta \delta_{ik}\frac{\partial v_l}{\partial x_l} \tag{1.4}$$

Where $\vec{v}$ is the velocity field of the fluid, i, k represents Cartesian components and the coefficients η and ζ are the coefficients of shear and bulk viscosities respectively. If the liquid is assumed to be incompressible, then from the local continuity equation for mass density, $\frac{\partial v_l}{\partial x_l} = 0$ and the viscous forces are described only by the shear viscosity η. Hence we discuss only the shear viscosity here. Since the fluid is isotropic, η is scalar. The S.I. unit of viscosity is Poise.

The methods used to compute the shear viscosity η in the present thesis are described later in Chapter 2.

1.3.2 Relaxation time

The *relaxation time (τ)* is the characteristic time that a system takes to go spontaneously (owing to incessant atomic motions) from a given microscopic configuration at an arbitrary initial time $t = 0$ to another completely uncorrelated microscopic configuration. In other words, it is the time taken by the system to "forget" its initial conditions. One may also define the relaxation

time as the time taken by a system to return to equilibrium after it was suddenly taken out of equilibrium condition at $t = 0$. It is typically measured from the decay of appropriate correlation functions.

1.3.3 Shear relaxation time

One may define a relaxation time that is *derived from* the viscosity. Consider a situation [20] where Eqn. 1.4 is particularly simple: a liquid is placed between two parallel solid plates of area A and separation d. One plate is held fixed and the other is pulled with a velocity v. The shear force required to sustain that motion in the liquid is given by $F = \eta\frac{vA}{d}$. In terms of shear stress $\sigma = F/A$ and shear displacement $\gamma = x/d$ where x is the relative displacement of plates in time t, Eqn. 1.4 reduces to (incompressible fluid)

$$\sigma = \eta\dot{\gamma} \tag{1.5}$$

Maxwell argued [4] that on sufficiently short timescales a liquid behaves like an elastic solid characterized by an shear modulus $G = \sigma/\gamma$ and on longer timescales a liquid behaves like a viscous fluid. He proposed a generalized relation to describe all time scales:

$$\dot{\gamma} = \frac{\dot{\sigma}}{G} + \frac{\sigma}{\eta} \tag{1.6}$$

If the liquid is given a *sudden* instantaneous shear displacement from equilibrium, $\dot{\gamma}(t) = \gamma_0\delta(t)$, then the solution of Eqn. 1.6 gives the relaxation of stress: $\sigma(t) = \sigma(0)\exp(-t/\tau_{shear})$ where $\tau_{shear} = \eta/G$. By integrating upto an infinitesimal time immediately after $t = 0$, one gets $\sigma(0) = G\gamma_0$. This suggests that G represents the instantaneous value of shear modulus or equivalently the infinite frequency limit of shear modulus and hence is denoted by G_∞. The relaxation time describing the relaxation of shear strain is called the shear relaxation time:

$$\tau_{shear} = \frac{\eta}{G_\infty} \tag{1.7}$$

1.3.4 Relaxation of density fluctuations

At a given temperature and density, a liquid can have different processes of relaxation and hence *many* different relaxation times. In the present thesis, we are interested in the *structural relaxation* which corresponds to *long time* dynamics at low temperatures describing the space-time evolution of the *slow* degrees of freedom. Ideally, one considers the slowest degrees of freedom to measure the *longest* relaxation time of the system (to ensure metastable equilibrium). However, one does not know *a priori* all the slow degrees of freedom. Hence it is usually not possible to determine *a priori* the longest relaxation time. Instead one expects that structural relaxation takes place by spontaneous density fluctuations and hence studies the space-time evolution of the local density $\rho(\vec{r}, t)$ as the relevant *microscopic dynamical variable*.

1.3.5 Time correlation functions

The relaxation of fluctuations (*e.g.* density fluctuations) is given by time correlation functions (*e.g.* the self intermediate scattering function and the overlap function) of $\rho(\vec{r}, t)$. The usefulness of time correlation functions may be judged from the following points:

1. It is relatively easy to define and *directly compute* the real space real time correlation functions in simulation studies in which positions and momenta of particles of the system are directly measured. More importantly, information on the *Fourier transforms* of real space-time correlation functions can be *directly obtained in experiments* (for example, neutron scattering and various spectroscopic methods). For this connection with experiments, correlation functions are described both in real space-time and in wave-vector ($\vec{k}$), frequency (ω) spaces. Using both simulations and experiments, *microscopic* dynamics of liquids can be *directly* measured in quantitative detail.

2. Various transport coefficients like diffusivity and viscosity can be formally computed as the time integral of certain correlation functions using what are generically known as Green-Kubo relations.

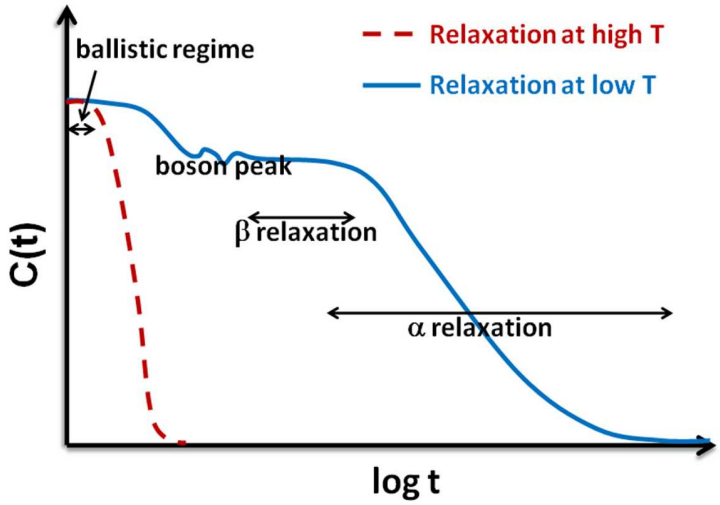

Figure 1.5: Schematic representation of the decay of density correlation function at high and low temperatures.

Here we are interested in the instantaneous local density $\rho(\vec{r}, t)$ as the fluctuating variable and discuss the *universal* features of a typical density correlation function of structural relaxation $C(t)$ expected for a dense, cold liquid. Here $C(t)$ may be the self intermediate scattering function or the overlap function. The definitions of different correlation functions used in the present thesis will be discussed in more detail in Chapter 2.

1.3.6 Signature 1: Non exponential decay of correlation functions at low T

Fig. 1.5 shows that there are qualitative differences between high T and low T density correlation functions [11]. At *high T*, the relaxation function is relatively featureless. At short times (so short that the effect of acceleration on the velocity can be neglected) the particles move with approximately constant velocity and $C(t) \propto t^2$ (*ballistic regime*) and at longer times $C(t)$ decays *exponentially in one step.*

As the temperature is lowered, new features appear in the correlation function at longer timescales [1,4,7,8,11]. At *low T*, a plateau appears at intermediate time scales. The width of the plateau increases as T decreases. Thus the correlation function shows *two step decay.* The time window around the plateau is known as the *β relaxation regime* and the decay at the longer time

scale is known as the α *relaxation regime*. The two step decay implies the presence of a short time process (β) and a long time process (α) which are well separated in time at low T. The short time decay is thought to be related to the vibrational dynamics and the long time decay to the hopping motion of particles ([74], [77] and references therein).

In the α regime, the density correlation function decays *slower than exponentially*. It is *empirically* described by a *stretched exponential* function (also known as Kohlrausch-Williams-Watts function):

$$C(t,T) = f_c(T) \exp\left[-\left(\frac{t}{\tau(T)}\right)^{\beta(T)}\right] \tag{1.8}$$

Here $0 \leq \beta(T) \leq 1$ is a measure of the deviation from the exponential behaviour and is called the stretching exponent (also the KWW exponent).

How does one explain the non-exponential relaxation? There are two distinct interpretations about the origin of the KWW function [21]:

1. In the homogeneous point of view, KWW function represents a *single* relaxation process which is *intrinsically non-exponential.*

2. In the heterogeneous point of view, there is a *distribution* of relaxation processes, each of them on its own is exponentially decaying but with different relaxation times. Consequently, the average effect is a stretched exponential function:

$$\exp\left(-(t/\tau_{KWW})^{\beta_{KWW}}\right) = \int_0^\infty d\tau \rho(\tau) \exp(-t/\tau) \tag{1.9}$$

   where $\rho(\tau)$ represents the unknown distribution function of the relaxation times. Formally Eqn. 1.9 is a Laplace transform of $\rho(\tau)$. There is no closed form expression known for the inverse Laplace transform except for such special values of β_{KWW} as 0.5 [21].

The debate over which of the above interpretations is correct is not fully resolved yet (see also section 1.3.9).

1.3.7 Signature 2: Non Arrhenius temperature dependence of relaxation times and transport coefficients at low T

The most prominent signature of the slow dynamics of many glass forming liquids is the dramatic change by as many as $14-17$ orders of magnitude in experiment and $5-6$ orders of magnitude in simulations (with present-day computing power) in the viscosity (η), self diffusion coefficients (D)and α relaxation times τ_α with only a modest decrease in temperature T. *Empirically,* at relatively high temperatures, the T dependence of α relaxation times (*also* of viscosity and self diffusion coefficients) are *exponential* in $1/T$ which is known as the *Arrhenius law*:

$$\begin{aligned} \eta(T) &= \eta_0 \exp(E_0/k_BT) \\ \tau_\alpha(T) &= \tau_0 \exp(E_0^{'}/k_BT) \\ D(T) &= D_0 \exp(-E_0^{"}/k_BT) \end{aligned} \tag{1.10}$$

where $(E_0, E_0^{'}, E_0^{"})$ represent energy barriers which are *independent* of temperature. They are different for different quantities and also different for different materials. The prefactors (η_0, τ_0, D_0) formally represent the infinite temperature values of the respective quantities. As the temperature is lowered, many glass forming liquids show *faster than exponential* change in viscosity, self diffusion coefficients and α relaxation times. This is not a sharp change but a gradual *cross-over* occurring over a limited T range which is characteristic of the system (Fig. 1.2(a)). Liquids which show this Arrhenius to non-Arrhenius cross-over are called *fragile* liquids. Ortho-terphenyl (OTP) is a typical example. Liquids that obey Arrhenius law down to the glass transition temperature are called *strong* liquids. Silica is a prototype example. From Eqn. 3.1, the energy barrier $E(T)$ at a given T can be written in terms of viscosity, self diffusion coefficients or α relaxation times. Non Arrhenius behaviour formally implies that $E(T)$ becomes T dependent which is written for τ_α below:

$$\frac{E(T)}{E_0} = \frac{T}{E_0} \ln \frac{\tau_\alpha(T)}{A'} \quad = \quad \text{Constant} \quad = 1 \quad \text{if Arrhenius}$$
$$\text{not constant if non-Arrhenius} \qquad (1.11)$$

How does one understand the rapid rise in dynamical quantities described above ? This has proved to be a very difficult question to answer in a satisfactory fashion in terms of microscopic properties of glass forming liquids. Here we briefly discuss some of the issues which are relevant for the present thesis. For a fuller discussion see [3, 4, 6–8].

Many different timescales: The dynamics of a glass forming liquid is characterized by more than one time scales : *e.g.* hydrodynamic transport coefficients (translational and rotational diffusion coefficient, shear viscosity) and α and β relaxation times. Besides, the different experimental techniques (*e.g.* for relaxation time measurements - dielectric relaxation, mechanical shear relaxation, electron spin correlation and nuclear spin lattice correlation methods) and simulation studies probe different processes and ranges of time and frequency [7]. It is a remarkable fact that despite wide variations in time (and frequency) scale and physical processes, the T dependence of the time scales show similar patterns.

Empirical fitting functions: What is the best possible description of the T dependence of different time scales *measured* for a large number of glass forming liquids ? To answer this question, owing to the absence of a generally accepted universal microscopic theory, one has to resort to fitting functions with adjustable fit parameters. There are many such fits with varying degree of applicability and theoretical basis (see [7] and references therein). Since the Arrhenius law has two adjustable parameters, the simplest fitting function to describe non-Arrhenius T dependence requires three such parameters. However there also exist fitting functions with four or more adjustable parameters. A simple way to classify the different fitting functions is according to whether they predict a divergence of relaxation time / viscosity at a finite temperature. Two of the widely used three-parameter fit functions for supercooled liquids are the Vogel-Fulcher-Tammann-Hesse (VFTH or VFT)

law (which is equivalent to the Williams-Landel-Ferry equation [26]):

$$\tau = \tau_0 \exp(\frac{B}{T - T_0}) \tag{1.12}$$

and the mode coupling theory (MCT) prediction of power law divergence:

$$\tau = \tau_0 (T - T_c)^{-\gamma} \tag{1.13}$$

An example of a fitting function that does not imply finite T divergence is the Zwanzig-Bessler law : $\tau = A \exp(E/RT^2)$. There have been critical comparisons of different fitting functions in literature [7, 22–25]. An important issue is whether a single fitting function can describe the full range of data.

Characteristic temperatures: As a glass forming liquid is cooled from high T, a number of characteristic temperatures can be identified which mark *qualitative* changes in the dynamics of the system. The melting temperature T_m (when exists) separates the normal liquid from the supercooled liquid. Below T_m, the change from Arrhenius to non-Arrhenius T dependence of dynamics occur at a *cross-over* temperature T_{onset}. At this temperature, a qualitative change occur in the way the system samples its configuration space [47] which is reflected in many properties of the system [68]. Thus T_{onset} marks the onset of the slow dynamics. Further down in temperature, one encounters the temperatures T_c predicted by MCT and T_0 predicted by VFT law where the structural relaxation time (and viscosity) is *predicted* to diverge. The divergence at T_c predicted by MCT is not seen in practice presumably because the mode coupling theory of structural relaxation is incomplete. The temperature T_0 is physically unattainable in liquid state as the laboratory glass transition temperature T_g is higher than T_0 for all known systems. However, T_0 is empirically found to be tantalizingly close in many glass forming liquids [7] to the Kauzmann temperature T_K where the thermodynamic glass transition is predicted due to the vanishing of configurational entropy.

$$T_K \approx T_0 < T_g < T_c < T_{onset} < T_m \tag{1.14}$$

1.3.8 Signature 3: Decoupling

The dynamics of a glass-forming liquid is commonly described by at least 5 characteristic time scales: the transport coefficients - shear viscosity (η), translational (D) diffusion coefficient and rotational (τ_c) correlation time; and the relaxation times - β and α (long time decay). At high T one finds various pairs of these quantities are *coupled* - by coupling we mean that if one knows the T dependence of one quantity in terms of, say, an empirical fitting function involving a set of fit parameters, then one can *predict* the value of the other quantity *using the same set of fit parameters*. As the temperature of the supercooled liquid decreases, those pairs get *decoupled*. The various couplings and decouplings are briefly discussed below:

The relation between D and η: The translational diffusion coefficient (D) of a particle in a liquid can be connected to the shear viscosity (η) of the liquid by the phenomenological Stokes-Einstein relation (SER). Consider a spherical particle of radius R and mass m undergoing Brownian motion in a viscous liquid of friction coefficient ξ at a constant temperature T. The motion of the particle can be described by the Langevin equation [120]:

$$m\ddot{\vec{r}} + \xi\dot{\vec{r}} + \vec{F}_{random}(t) \;=\; 0 \tag{1.15}$$

where $-\xi\dot{\vec{r}}$ is the drag force due to viscosity and $\vec{F}_{random}(t)$ is the time-dependent, fluctuating force by the particles of liquid colliding with the Brownian sphere. The equation of motion can be solved exactly if one assumes the fluctuating force has zero average: $< \vec{F}_{random}(t) >= 0$ and forces at different times have δ function correlation: $< \vec{F}_{random}(t_1)\vec{F}_{random}(t_2) >= g\delta(t_1 - t_2)$. Einstein derived [122] the relation between the diffusion coefficient (D) of the Brownian particle and the friction coefficient (ξ) of the liquid at a given temperature T:

$$D = \frac{k_B T}{\xi} \tag{1.16}$$

This relation is known as the "Einstein relation". Further, the friction coefficient ξ can be connected to the viscosity η of the liquid through Stokes' formula ([119], §20):

$$\xi = \frac{6\pi\eta R}{m} \tag{1.17}$$

(the factor 6 depends on the boundary condition [83]). Combining the two, we get the "Stokes - Einstein relation" (or the "Stokes - Einstein - Sutherland relation" as it was independently obtained by Sutherland [121]):

$$D = \frac{mk_B}{6\pi R}\frac{T}{\eta} \tag{1.18}$$

This relation is well-established for a wide range of liquids at high T (above their melting points) [108]. Another remarkable point is that the Stokes formula was derived for *macroscopic* spheres - hence Eqn. 4.1 is expected to hold for diffusing particles whose radius (R) are much larger than the size of the liquid particles. However, the relation is known to be applicable for the diffusion of small tracer particles and even for the self diffusion of liquid particles [108].

The relation between D and τ: In the literature, in the context of SER one often studies the relation between the diffusion coefficient and the relaxation time. In such cases, it is implicitly assumed that the viscosity is proportional to an appropriate relaxation time - usually the α relaxation time (τ). We note that the diffusion coefficient D is a single particle property while the structural relaxation time τ is a collective property of all particles of the system. Hence a relation between D and τ is far from a trivial one. One can deduce the relation between D and τ assuming the self van Hove function is Gaussian which is expected to be true in the diffusive regime (at all T in the limit of long time):

$$\begin{aligned} G_s(r,t) &\equiv \langle \frac{1}{N}\sum_{i=1}^{N}\delta(\vec{r}-\vec{r}_i(t)+\vec{r}_i(0))\rangle \\ &= \frac{1}{\sqrt{2\pi\sigma^2}}\exp(-\frac{r^2}{2\sigma^2(t)}) \text{ in 3D} \end{aligned}$$

Hence its Fourier transform $F_s(k,t)$ is Gaussian in the wave vector k:

$$\begin{aligned} F_s(\vec{k},t) &\equiv \int d\vec{r} G_s(\vec{r},t)\exp\left(-\imath\vec{k}\cdot\vec{r}\right) \\ &= \exp(-\frac{3k^2\sigma^2(t)}{2}) \end{aligned} \tag{1.19}$$

In the diffusive regime $\sigma^2(t) = 2Dt$, hence the $F_s(k,t)$ is also exponential in t:

$$F_s(\vec{k},t) = \exp(-3k^2Dt) \tag{1.20}$$

If the definition of the relaxation time is such that $F_s(k,\tau) = 1/e$ then Eqn. 1.20 implies that

$$D\tau_k k^2 = \text{ constant} \tag{1.21}$$

The Debye Stokes Einstein relation: We also mention that an analogous relation exists for the rotational diffusion. The rotational correlation time τ_c is given by,

$$\tau_c = \frac{4\pi R^3}{3}\frac{\eta}{k_B T} \tag{1.22}$$

This is known as the "Debye-Stokes-Einstein" (DSE) relation.

Decoupling of D and η, τ: Several experiments and simulation studies in the last three decades [84–106, 175] have discovered that in supercooled liquids, the Stokes - Einstein relation (Eqn. 4.1) and the relation between D and τ (Eqn. 4.2) break down at low temperature. For simplicity, we do not distinguish here between the different types of relaxation time, nor do we distinguish between relaxation times measured by different experimental methods. The diffusion coefficient can be of probe particles in a liquid solvent or of the solvent itself. The different ways of representing the SE breakdown may be summarized as follows:

1. Measured D has weaker T dependence than predicted D from the SER [86, 88, 89].

2. The radius parameter R (inversely proportional to $D\eta/T$ in the SER) becomes T dependent and decreases with lowering T [86, 92, 94, 106, 175]. We note that sometimes the T dependence of $D\tau/T$ are reported [86, 101, 102] instead of $D\eta/T$.

3. The fractional SE relation, reported variously as $D \propto (\eta/T)^{-\xi}$ or $D \propto \eta^{-\xi}$

or $(D/T) \propto \eta^{-\xi}$ or $D \propto (\tau/T)^{-\xi}$ or $D \propto \tau^{-\xi}$, with a fractional exponent ξ describes data well [84, 91–93, 101–103, 105].

4. The derivative $\frac{\partial(1/D\eta)}{\partial(1/T)}$ from $1/D\eta$ *vs.* $1/T$ plot changes sign from positive to negative [93]. If the SER is valid then from Eqn. 4.1, $\frac{\partial(1/D\eta)}{\partial(1/T)} = \frac{6\pi R}{mk_B}$ which should always be positive.

We also note in passing that the relation between the rotational diffusion coefficient and the viscosity (the DSE relation) is less clear [102]. The DSE relation is found to be both valid ([88, 89]) and violated [93, 102, 103] at low temperatures.

Decoupling of D and τ_c: If the DSE relation between τ_c and η is valid down to T_g [88, 89] then one expects a decoupling between the translational and the rotational diffusion. This decoupling is represented by showing that the product $D\tau_c$ of translational and rotational diffusion coefficients becomes T dependent.

Decoupling of α and β relaxation times: At high T the β and α processes are not separated. However, as the temperature decreases the two time scales get separated. This is manifested in the dielectric relaxation measurements where the single peak frequency at high T *bifurcates* into slow (α) and fast (β) peaks at low T with the slow peak showing non-Arrhenius T dependence and disappearing at T_g while the fast peak obeying Arrhenius law down to T_g [8]. The decoupling of β and α processes is also evident from the decay of time correlation changing from being single-step at high T to two-step at low T.

1.3.9 Signature 4: Dynamical heterogeneity

The existence of spatially heterogeneous dynamics in glass forming liquids (also in granular media) is a comparatively recent observation and has gained much attention in the last two decades [6, 13]. Dynamical heterogeneity (DH) refers to the coexistence of *mobile* and *immobile* particles in the system leading to a *spatial* distribution of mobility (or equivalently, relaxation time). The possibility of the spatial heterogeneity of dynamics arises owing to the *non-exponential decay* of the correlation function. As discussed in section

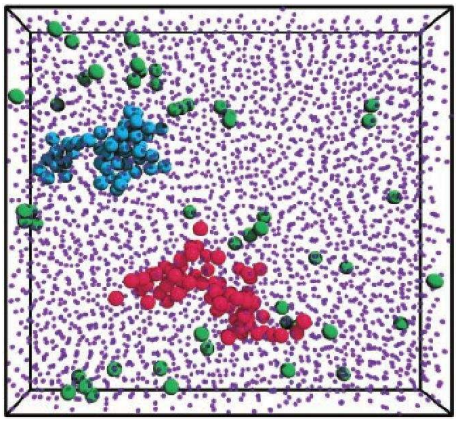

Figure 1.6: Dynamic heterogeneity seen in a three dimensional supercooled colloid using confocal microscopy. Particles are observed for a time window of 1000 seconds. For clarity, the fast particles are represented as large spheres (red and blue) and slow particles as small spheres (violet) although all particles in the system have the same size. Figure reproduced with permission from [34].

1.3.6 the non-exponential decay of a correlation function can have either a homogeneous (single non-exponential decay having a single relaxation time) or a heterogeneous (a distribution of exponential decays with different relaxation times) interpretation. Such a distribution of relaxation times can naturally occur in the system if the dynamics in different regions of space are different. To illustrate the difference between homogeneous and spatially heterogeneous dynamics, consider a *movie* showing the time evolution of the system where in addition to the position and velocity, every particle is given a third label representing its *mobility* with respect to the initial configuration at $t = 0$ (for clarity, mobility which is a single particle property is chosen over relaxation time). This label is represented by a *color* defined by an appropriate color code. At the start of the movie all particles have the same color (zero displacement by definition). As the movie progresses, in a dynamically *homogeneous* system, characterized by a Gaussian $G_s(r, t)$, the particles continue to have the *same* color at any given time t. However, if the system is dynamically *heterogeneous*, then different particles will have different color (*mobile* and *immobile*) at any given time t. One may still imagine that at any given t, the mobile and the immobile particles (with different colors) form a homogeneous mixture. However, many different types of experiments and simulation have provided evidences that particles with same color tend

to cluster together (see Fig. 1.6) - indicative of cooperative motion. Finally, any given particle at different points of time has different colors *i.e.* mobility is not an intrinsic property - the same particle becomes mobile and immobile at different points of time. Thus DH implies the presence of a characteristic *dynamical* length scale and an associated characteristic time scale in the system. The interest in DH lies in the fact that such dynamical length scales (and also the time scales) *increases* as the temperature *decreases* which is reminiscent of the critical phenomena of the more familiar second order phase transitions (*e.g.* liquid - gas) and hence a successful theory of glass transition should be able to explain it.

One of the earliest evidences of DH was found in multi-dimensional NMR experiments [28]. Later, other experimental methods like photo bleaching probe rotation experiments [29] and atomic force microscopy probed polarization noise experiments [30] also detected DH. Simulation studies are particularly suitable to track single particle motions much analysis of DH has been done by simulation [31,32]. Finally, DH has also been *directly observed* from single particle motions *e.g.* in the experiments on colloids [33,34] and in simulations *e.g.* [35].

In order to analyze DH, an important issue is how to define the mobile and immobile particles in an *unambiguous* way *i.e.* not involving externally imposed cutoffs which are somewhat arbitrary. Using four point correlation function [63] is a successful approach to overcome this problem [13]. We will discuss the definitions of four point functions and the relaxation times and correlation lengths extracted from them later in Chapter 2.

1.3.10 Signature 5: Aging

We mention briefly a signature of out of equilibrium dynamics in glass-formers. Aging occurs when the system breaks the time translational invariance and the properties of the system depends on its "age" . *i.e.* the time elapsed (denoted by t_w) since the start of the experiment at $t = 0$. This is a hallmark of the system being in out of equilibrium and hence is expected below T_g when the time window of observation τ_{obs} is *less* than the longest relaxation time (τ) of the system. The effect of aging is more dramatic in two time quantities *e.g.* two point time correlation function $F_s(k, t, t_w)$ compared to one time quantities *e.g.* energy. In an aging system the properties depend

on the experimental protocol and new effects like *memory* and *rejuvenation* are observed [12].

1.4 Principles to organize data

1.4.1 Fragility

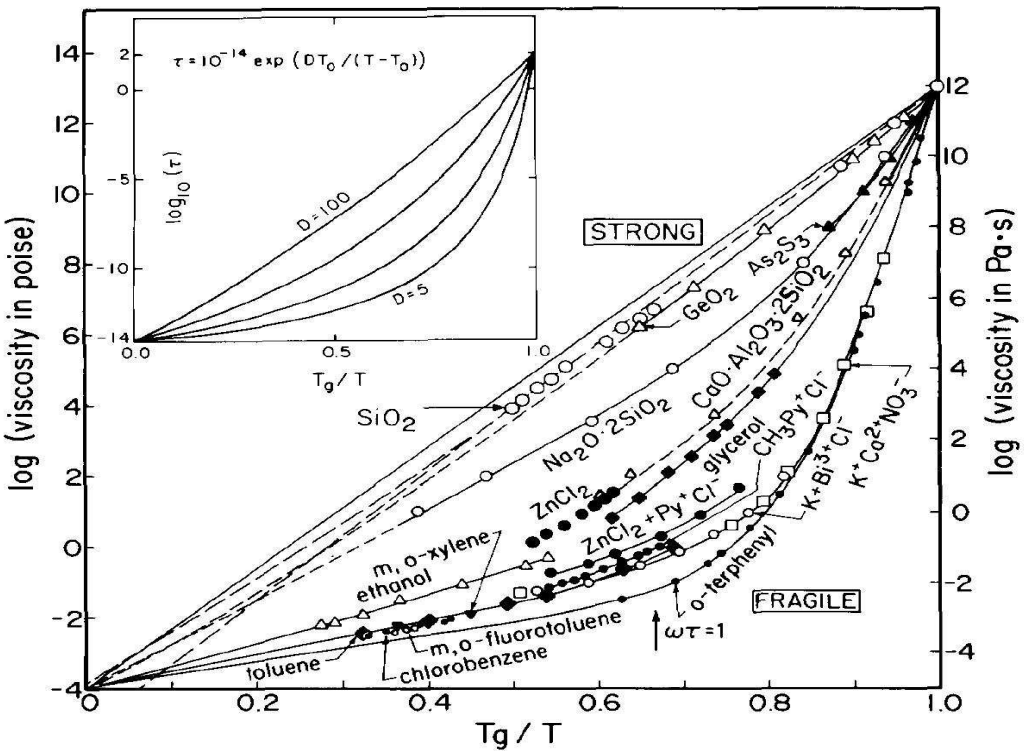

Figure 1.7: Angell plot of the logarithm of viscosity *vs.* the *scaled* inverse temperature $\frac{T_g}{T}$. Inset shows that the Angell plot can be generated using the VFT fit in Eqn. 6.3. Figure reproduced with permission from [126].

The Angell plot: As emphasized above, the rapid rise of relaxation times in glass-forming liquids shows a complex and diverse phenomenology. The so-called Angell plot [1, 27, 126] of *logarithm of viscosity (relaxation time) vs.* the *scaled inverse temperature* $\frac{T_g}{T}$ provides a useful way to organize and understand the diverse behaviour (Fig. 1.7). In this representation, *strong* liquids, *i.e.* Arrhenius behaviour, follow a linear curve and *fragile* liquids, *i.e.* non-Arrhenius behaviour, follow a non-linear curve. This can be understood

by considering a slightly shifted Angell plot of $\log(\eta(T)/\eta(\infty))$ *vs.* $\frac{T_g}{T}$ which, from Eqns. 3.1 and 1.11, is a plot of $y = \frac{E(T)}{T}$ *vs.* $x = \frac{T_g}{T}$. Then $T = \frac{T_g}{x}$ and $E(T) = \frac{y(x)}{x}$. Considering the sign of $\frac{dE}{dT} = \frac{y}{T_g}\left(1 - \frac{d\ln y}{d\ln x}\right)$, we see that (i) $E(T) = constant$ corresponds to the straight line $y = Ax$, (ii) the bent curves correspond to energy barriers $E(T)$ *increasing* with *decreasing* T.

The usefulness of Angell plot is that, without knowing the energy barriers $E(T)$, the experimental viscosity (or relaxation time) data of liquids show two extreme patterns (strong and fragile) which help to rank liquids continuously from strong to fragile based on simple geometrical properties of the curves. Thus the rapidity of rise of viscosity / relaxation times can be *quantified* and hence *different materials* can be *quantitatively compared*. This is done by introducing a material specific parameter known as *fragility*.

The kinetic fragility: The fragility defined from transport quantities and relaxation times is called the *kinetic fragility*. There are multiple definitions of kinetic fragility in the literature which can be classified as based on properties (i) at a *single* temperature and (ii) over a broad temperature range [131]. We mention the original definition by Angell as the steepness index in the Angell plot defined as the slope (m) of logarithm of viscosity or relaxation time at $T = T_g$ with respect to the scaled inverse temperature $x = \frac{T_g}{T}$ (T_g is the laboratory glass transition temperature).

$$m = \left(\frac{d\log\tau}{d(\frac{T_g}{T})}\right)_{T=T_g} \tag{1.23}$$

A kinetic fragility (K_{VFT}) may also be defined from a VFT fit of the relaxation times (or the diffusion coefficients),

$$\tau(T) = \tau_0 \exp\left[\frac{1}{K_{VFT}(\frac{T}{T_{VFT}} - 1)}\right] \tag{1.24}$$

which is used in the present thesis.

Thermodynamic fragility: The concept of fragility re-frames the question about understanding the rapid rise of viscosity (and relaxation times) into the question about the origin of fragility, a fully satisfactory understanding about which has not been reached yet. However, a combination of

thermodynamic approaches *e.g.* the Adam Gibbs relation (AG) and the potential energy landscape (PEL) has been quite successful (The AG relation and the PEL formalism are discussed later). The AG relation explains the rapid rise of relaxation times in terms of the decrease of the configurational entropy (S_c). If TS_c is linear in T, a thermodynamic index of fragility (K_T) may be defined :

$$TS_c = K_T \left(\frac{T}{T_K} - 1 \right), \tag{1.25}$$

The origin of K_T may be understood from the properties of the PEL [128]. Since the kinetic fragility K_{VFT} may be related to the thermodynamic fragility K_T via the AG relation (if it is obeyed by the system), such analysis also yields insight about the kinetic fragility.

1.4.2 Density-temperature scaling

The previous discussions show that the phenomenology of the slow dynamics in glass forming liquids is complex. However, recent analyses of many liquids over a wide range of temperatures and densities (pressures) have shown two interesting properties which considerably simplifies the description of dynamics.

Hidden scaling: It has been found empirically that relaxation times of many liquids, *when expressed in appropriate units*, depend on density (ρ) and temperature (T) only through a specific combination implying a "hidden" density -temperature scaling law in liquids. Roland and co-workers [147–149] found this combination to be $\frac{\rho^\gamma}{T}$, *i.e.* $\tau = f(\frac{\rho^\gamma}{T})$ where the function f is in general unknown and depends on the material. The exponent γ can be found empirically by demanding collapse of relaxation times (or diffusion coefficients) at different densities (pressures) and temperatures on a single master curve. For certain class of liquids, it may also be computed from thermodynamic quantities as will be explained later. Alba-Simionesco and co-workers [130] also found similar empirical data collapse for relaxation times with the above mentioned functional form. However, they show that data collapse can also be obtained with a different form $\tau = f(\frac{\rho - \rho^*}{T})$ as well. In a separate line of reasoning, Alba-Simionesco and co-workers [130] propose that the density

dependence of relaxation times for many liquids can be described by a *single* density-dependent parameter, say the activation energy $E_0(\rho)$ obtained from the Arrhenius behaviour at high T. According to their hypothesis, when the scaled T dependent activation energy at different densities - $E(\rho, T)/E_0(\rho)$ is plotted against $T/E_0(\rho)$, one should get a data collapse.

Strong pressure-energy correlation: In model liquids with purely repulsive inverse power law (IPL) potential $v(r) \sim r^{-n}$, the instantaneous potential energy (PE) is proportional to the instantaneous virial (W). This is a consequence of the scale invariance of the power law nature of the potential [159, 160]. Since $U = \sum_i \sum_{j>i} v(r)$ and $v(r) \sim r^{-n}$ hence $W = \frac{1}{d}\left(\sum_i \vec{r}_i \cdot \frac{\partial}{\partial \vec{r}_i}\right) U = \frac{n}{d} U$ where d is the spatial dimension. Hence in IPL liquids, the PE and the virial are exactly correlated.

Schrøder and co-workers have recently shown [146] that many *non-IPL* liquids show *strong correlation* (defined as correlation coefficient > 0.9) between instantaneous potential energy (U) and virial (W). Such strong correlation in non-IPL liquids has been rationalized by approximating the interaction potential by an *effective* IPL potential where the power is *different* from the repulsive part of the original potential. This is further generalized by introducing the concept of *isomorphs* [146].

Connection between the two properties: There is an interesting possibility that the above mentioned properties are inter-related. Schrøder and co-workers have shown that the exponent γ in density-temperature scaling of relaxation time can be *predicted* from the virial-potential energy correlation. However, the value of γ computed from virial-potential energy correlation depend on state points. It is also not clear if such strong correlation is obeyed over the entire liquid phase. Despite these limitations strong pressure-energy correlation is conceptually interesting as it considerably simplifies the analysis of liquid state properties. In the present thesis, we explore this possibility of simplification of dynamics by using a scaling relation.

1.5 The configurational entropy

The configurational entropy is a measure of the number of "independent" (or uncorrelated) configurations that a system can sample in the configuration space at a given density and temperature. Intuitively, the configurational entropy should be inversely related to the structural relaxation time. Entropy based theories like the Adam Gibbs (AG) relation and the RFOT aim to establish such connections *quantitatively*. However, in order to *measure* the configurational entropy one needs to define the idea of "independent configurations" clearly. The potential energy landscape (PEL) offers a natural conceptual framework and computational tools to define and measure configurational entropy of a system. The details of the method is discussed below.

1.5.1 The potential energy landscape (PEL) formalism

Dynamics in the configuration space: Goldstein [74] emphasized that the dynamics of viscous liquids at low temperatures can be more easily described in terms of the topology of the abstract, high dimensional configuration space than in real space. Although in real space we can directly *see* the time evolution of the system, the structural changes with cooling are not easy to identify. This is manifested in negligible changes in the pair correlation function with cooling. On the contrary, the configuration space is impossible to visualize for realistic liquids, but Goldstein pointed out that the qualitative difference between high and low T behaviour of a liquid is clearer from the potential energy landscape (PEL) perspective rather than from a real space picture. The PEL is a hypersurface representing the interaction potential as a function of coordinates of all particles in a $ND + 1$ dimensional space for a N-particle liquid in D dimensions. A configuration *as a whole* is represented by a *single* point on this hypersurface. The movement of the point along this hypersurface represents the microscopic dynamics of the system. The PEL typically have enormous number of *local potential energy minima, known as the inherent structures*. Inherent structures are then, by definition, the configurations with mechanically stable packing of particles. The crystal phase(s) and crystalline defect configurations also correspond to local PEL minima and expected to be of lower potential energy than liquid

local minima. Usually, when discussing inherent structures of liquid phase, crystalline (both perfect and defects) configurations are excluded.

Owing to the presence of many potential energy minima, the system is required to overcome the energy barriers to go from one to another minimum. At high temperatures, the thermal energy k_BT is much larger than typical energy barriers and the system should sample all possible configurations without needing to overcome barriers. On the contrary, at low temperatures, when energy barriers are expected to be larger than the thermal energy k_BT, the system is expected to sample configurations inside one basin most of the time with occasional jump between basins (a *rare event*). This picture is true if the time scales of local sampling and of hopping between basins are well separated. The two step decay of time-correlation functions supports this expectation, where the short-time β relaxation time is associated with time scale of local sampling inside a basin or vibration about the inherent structure and the long time α relaxation time is associated with the hopping between basins. The latter is tested in [77] for a model liquid and is shown in Fig. 1.8 where $F_s(q,t)$ *vs.* t are plotted for a range of temperatures. The top panel shows the $F_{sA}(q,t)$ (for only A type particles) computed from the time evolution trajectories of the liquid obtained from molecular dynamics (MD) (in which Newton's laws of motion are numerically solved to obtain the time evolution trajectories of particles) simulation and a two step decay process is seen in the temperature range studied. The bottom panel shows the $F_s^I(q,t)$ computed from the "inherent structure trajectories" which are nothing but a sequence of inherent structures obtained from the MD trajectories in the top panel by potential energy minimization. In the "inherent structure trajectories" the vibrational dynamics is removed by construction. The $F_s^I(q,t)$ shows a single step decay which is consistent with the expectation that the time scale of vibrations within a basin and that of hopping between basins are well separated. Comparing the time scales in the top and the bottom panel of Fig. 1.8 also shows that the long time α relaxation time is associated with the process of hopping between basins.

1.5.2 The basin decomposition

It is easy to see that the configuration space can be completely divided into *basins* such that each basin have *exactly one* inherent structure and each

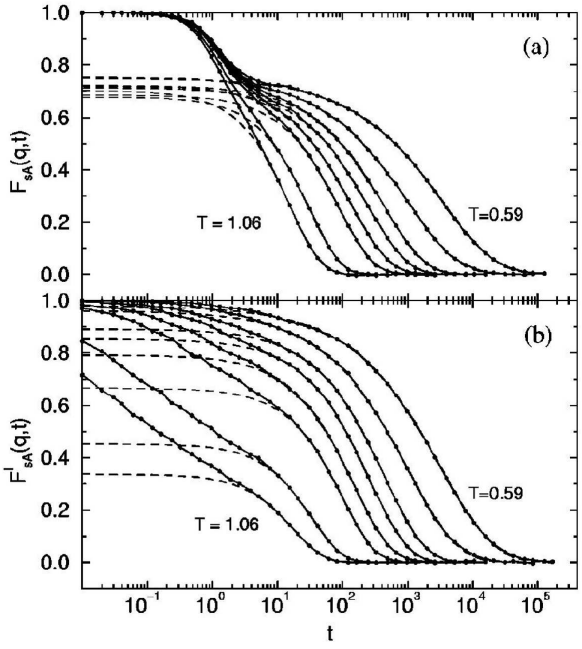

Figure 1.8: Top: $F_{sA}(q,t)$ *vs.* t plotted for a model binary mixture (for only A type particles) at a range of temperatures where $F_s(q,t)$ computed from MD trajectories. Bottom: $F_s^I(q,t)$ *vs.* t plotted for same temperatures where $F_s^I(q,t)$ computed from inherent structure trajectories obtained from potential energy minimization of the MD trajectories used in the top panel. Lines are fits to the stretched exponential form: $f(t) = f_c \exp(-t/\tau)^\beta$. This plot shows that at low temperature, relaxation occurs in two steps and the true (MD) dynamics can be separated into short time vibrational and long time basin-hopping motion. Figure reproduced with permission from [77].

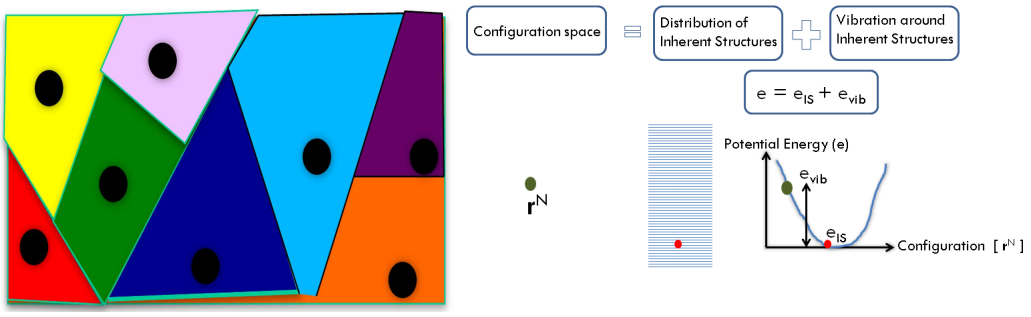

Figure 1.9: Cartoon of basin decomposition in configuration space and separation of configurations into local potential energy minima (inherent structures) and vibration about minima. The black circles represent the inherent structures in the left drawing. The inherent structures are labeled by energy in the right drawing.

configuration in a basin can be *uniquely mapped* to that inherent structure (excluding saddle points on the boundary between adjacent basins. But the total volume of saddle points is vanishingly small compared to the total volume of configurations). Further, the inherent structures can be labeled by their energies. The problem of computing the partition function (configuration part) of the whole system is then reduced to computing the partition function of a single basin plus a *one* dimensional integral over inherent structure energies (denoted by e_{IS}). This reduction is known as the *basin decomposition* and is illustrated in Fig. 1.9. The canonical partition function of the system $Z(N,V,T)$ can be re-written in terms of basin partition function $z_{basin}(e_{IS},N,V,T)$:

$$\begin{aligned} Z &= exp\left[-\beta A\right] \\ &= \int_{e_{IS}} de_{IS}\Omega(e_{IS},N) z_{basin}(e_{IS},N) \\ &\equiv \int_{e_{IS}} de_{IS} \exp\left[S_c(e_{IS},N)/k_B\right] \exp\left[-\beta(e_{IS}+f_{basin})\right] \end{aligned} \tag{1.26}$$

Where $A(N,V,T)$ is the total Helmholtz free energy of the system, $S_c(e_{IS},N) = k_B \ln \Omega(e_{IS},N)$ and $\Omega(e_{IS},N)de_{IS}$ denotes the number of inherent structures in the energy range e_{IS} to $e_{IS}+de_{IS}$. Thus $S_c(e_{IS},N)$ is the *configurational entropy density*. From the above expression, the probability density of sampling inherent structures with energy between e_{IS} and $e_{IS}+de_{IS}$ at a temperature T can be written as

$$P(e_{IS},T,N) = \frac{exp\left[-\beta\left(e_{IS}+f_{basin}-TS_c\right)\right]}{\exp\left(-\beta A\right)} \tag{1.27}$$

$P(e_{IS},T,N)$ may be obtained numerically from the histogram of inherent structures sampled at a given temperature T. Thus configurational entropy density $S_c(e_{IS},N)$ can be numerically computed by inverting Eqn. 1.27

$$S_c(e_{IS},N) = \ln P + \beta\left[e_{IS}+f_{basin}-A\right] \tag{1.28}$$

Although terms on the right hand side of Eqn. 1.28 has temperature dependence, $S_c(e_{IS},N)$ does not depend on temperature as it represents geometrical features of the underlying potential energy surface which is temperature independent (but density dependent).

1.5.3 The basin free energy and the basin entropy

The harmonic approximation: The partition function of a *single* basin can be computed *analytically* by making the harmonic approximation to the potential energy expanded about the minimum (inherent structure) of a given basin :

$$\begin{aligned} U(\vec{q}^N) &\simeq e_{IS} + \sum H_{i\alpha j\beta}\delta q_i^\alpha \delta q_j^\beta \qquad\qquad e_{IS}\text{=inherent structure energy} \\ H_{i\alpha j\beta} &= \text{Hessian matrix of the potential energy } U(\vec{q}^N) \\ &= \left[\frac{\partial^2 U}{\partial q_i^\alpha \partial q_j^\beta}\right]_{IS} \end{aligned} \tag{1.29}$$

The basin partition function: Using the harmonic approximation, the canonical partition function of a single basin ($z_{basin}(e_{IS}, N, V, T)$) can be written as the product of the partition functions ($z_{harmonic}$) of $3N$ one dimensional harmonic oscillators (ND in D dimensions) with frequencies (ω_i) equal to the eigenvalues (ω_i^2) of the above Hessian matrix of potential energy at the inherent structure. The eigenvalues are computed by diagonalizing the Hessian matrix. This gives $3N$ (in $3D$) independent eigenvalues (ω_i^2) out of which $3N-3$ are non zero. The canonical partition functions of a one dimensional harmonic oscillator with a non-zero frequency ω and zero frequency are respectively (mass = 1 for simplicity) :

$$\begin{aligned} z_{harmonic}(\omega, T, V) &= \int \frac{dpdq}{h} \exp\left[-\frac{\beta p^2}{2} - \frac{\beta\omega^2 q^2}{2}\right] \\ &= \frac{1}{\beta\hbar\omega} \\ z_{harmonic}(0, T, V) &= \int \frac{dpdq}{h} \exp\left[-\frac{\beta p^2}{2}\right] \\ &= \left[\frac{1}{h}\left(\sqrt{\frac{2\pi}{\beta}}\right) V^{1/3}\right] \\ &\equiv z_0 \end{aligned} \tag{1.30}$$

So, under harmonic approximation the basin partition function can be written as:

$$\begin{aligned} z_{basin}(e_{IS}, N, V, T) &= \exp\left(-\beta e_{IS}\right) \left[\prod_{i=1}^{3N-3} \frac{1}{\beta\hbar\omega_i}\right] z_0^3 \\ &\equiv \exp\left(-\beta e_{IS}\right) \exp\left(-\beta f_{basin}\right) \end{aligned} \tag{1.31}$$

The basin free energy and the basin entropy: Finally, the basin free energy f_{basin} and basin entropy S_{basin} in the harmonic approximation are given by (note that the energy of the inherent structure is *excluded* in our definition of f_{basin}, *i.e.* f_{basin} *is the vibrational component of the basin free energy*):

$$\begin{aligned} \beta e_{IS} + \beta f_{basin} &= -\ln z_{basin} \\ \beta f_{basin} &= \sum_{i=1}^{3N-3} \ln\left(\beta\hbar\omega_i\right) - \ln\left(z_0^3\right) \\ S_{basin} &= -\frac{\partial f_{basin}}{\partial T} \end{aligned} \tag{1.32}$$

1.5.4 The average configurational entropy

The average configurational entropy ($S_c(N, V, T)$) is the average of configurational entropy density sampled at a given temperature and related to $S_c(e_{IS})$ as $S_c = \int de_{IS} S_c(e_{IS}, N) P(e_{IS}, N, T)$. Thus the average configurational entropy explicitly depends on temperature. In the present thesis, it is directly obtained by subtracting the basin entropy from the total entropy (S_{total}, also called the "bulk entropy") of the system:

$$S_c(N, V, T) = S_{total}(N, V, T) - S_{basin}(N, V, T) \tag{1.33}$$

which can be obtained from Eqn. 1.26 in saddle point approximation ($\tilde{e}_{IS}$ and similarly for the other quantities denote the values which maximize the

argument in Eqn. 1.26 and for simplicity $k_B = 1$) :

$$\begin{aligned} Z &\simeq \exp(\tilde{S}_c) \exp\left[-\beta(\tilde{e}_{IS} + \tilde{f}_{basin})\right] \\ A &= -T \ln Z \\ S_{total} &= -\frac{\partial A}{\partial T} \\ &\simeq \tilde{S}_c - \frac{\partial \tilde{f}_{basin}}{\partial T} \\ &= \tilde{S}_c + \tilde{S}_{basin} \end{aligned} \tag{1.34}$$

1.6 Entropy based theories of glass transition

There are many theories of glass transition attempting to explain the dramatic slow down of dynamics as T approaches T_g from above with varying degrees of success. Excellent review articles (*e.g.* [3–5,10]) are available which gives an overview of different theories. Here we briefly discusses the Adam Gibbs relation (AG) and the random first order transition theory (RFOT) which are relevant for the present thesis.

1.6.1 The Adam Gibbs relation

The Adam-Gibbs (AG) relation [36–38, 40] explains the behaviour of the relaxation time *i.e.* dynamics in terms of the configurational entropy *i.e.* thermodynamics. The AG relation is based on the picture that as the temperature is lowered, the motion of particles in liquids become correlated, hence relaxation in glass forming liquids occurs through the collective rearrangement of "cooperatively rearranging regions" (CRR). The CRRs define a minimum size of groups of rearranging particles (atoms, molecules *etc.* depending on the nature of the glass former) such that smaller groups of particles are incapable of rearrangement independently of their surroundings. Adam and Gibbs argued that the configurational entropy - the entropy associated with the multiplicity of distinct arrangements of particles, obtained by subtracting a "vibrational" component from the total entropy - per particle $S_c(T)$ of a liquid varies inversely as the size of the CRR, $z(T)$, since the configurational entropy per CRR, S^*, is roughly independent of temperature:

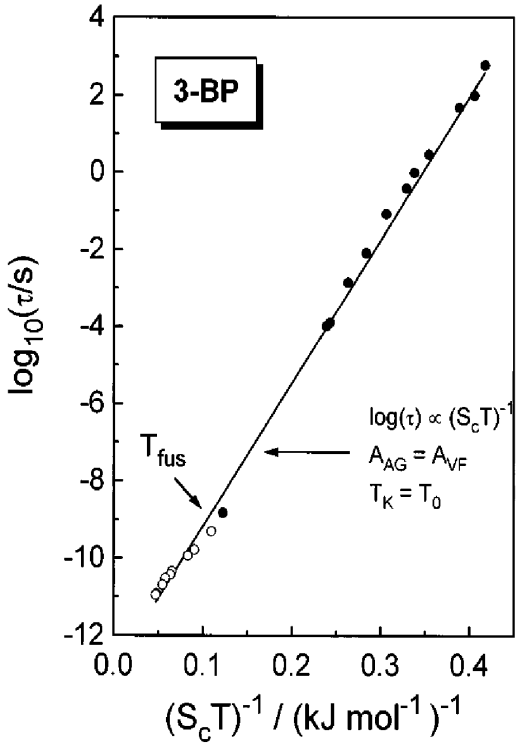

Figure 1.10: Experimental verification of the Adam Gibbs relation 6.4. Fig. reproduced with permission from [42].

$$S_c(T) = \frac{S^*}{z(T)} \tag{1.35}$$

The further assumption that the free energy barrier for a rearrangement is proportional to the size of the CRR ($\Delta G = z\delta\mu, \delta\mu$ = chemical potential barrier per particle) results in the Adam-Gibbs relation:

$$\begin{aligned} \tau(T) &= \tau(\infty) \exp\left(\frac{S^* k_B^{-1} \delta\mu}{T S_c(T)}\right) \\ &= \tau(\infty) \exp\left(\frac{C}{T S_c}\right) \end{aligned} \tag{1.36}$$

The Adam Gibbs relation (Eqn. 6.4) has been tested extensively (See Figs. 1.10 and 1.11). In Fig. 1.11 different curves correspond to different densities. Note that the slope for different densities are different. This point will be relevant for later chapters of the present thesis) and is quite successful to account for experimental and simulation data [41–45, 48, 128]. Besides, combining with the linear T dependence of the quantity TS_c (Eqn. 5.3:

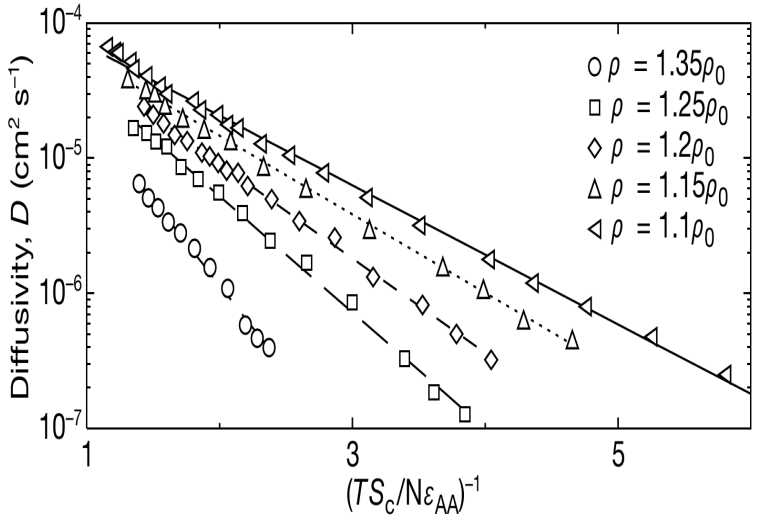

Figure 1.11: Validation of the Adam Gibbs relation in simulation in Kob Andersen model. Fig. reproduced with permission from [128]. Different curves correspond to different densities. Note that the slope for different densities are different. This point will be relevant for later chapters of the present thesis.

$TS_c = \frac{K}{T_k}(T - T_K)$) the AG relation Eqn. 6.4 predicts the empirical VFT law Eqn. 1.12,

$$\tau(T) = \tau_0 \exp\left(\frac{A}{T - T_0}\right) \tag{1.37}$$

provided the VFT divergence temperature T_0 is same as the Kauzmann temperature T_K. Experimentally, for many liquids it is found that indeed $T_0 \approx T_K$ ([42] and Table 4.6, ref [38]), although significant disagreements are also known.

However, because of the many assumptions, the AG relation is not rigorously derived and thus not a fully satisfactory theory. Some of the weaknesses [40] are mentioned below:

1. Although the concept of cooperatively rearranging region (CRR) is a key ingredient of the theory, it is not clearly defined [5] in the sense that the theory does not provide any method to estimate the size and shape of CRR's.

2. Similarly, the theory does not precisely define the meaning of (metastable) configurations of a CRR.

3. AG assumes that configurational entropy of a CRR S^* is a constant. It is not obvious why the number of metastable configurations of a region of size z^* should be independent of z^*. One may expect that instead it should be exponential in z^*.

In spite of these deficiencies, the AG relation is of central importance to understand the behaviour of relaxation times in glass forming liquids.

1.6.2 The random first order transition theory

The random first order transition theory (RFOT) originated in the study of mean-field models of Ising and Potts spin glasses. Spin glasses are also disordered systems, like supercooled liquids and structural glasses. However, there are two important differences: (i) unlike the structural glasses in which the disorder is *self-generated* (disorder in the real space positions but not in the Hamiltonian), in spin glasses the disorder is *quenched* (disorder in the Hamiltonian) [2]. (ii) the relevant spin glass models are mean-field like *i.e.* the range of interaction is *infinite* whereas in supercooled liquids and structural glasses the range of interaction is *finite*.

In the spin glass models mentioned above, below a *finite* temperature $T = T_d$, the free energy develops an *exponentially large* number of metastable minima. This is called a transition from the ergodic to the non-ergodic behaviour. The canonical free energy $F(T)$ below T_d is given by

$$F(T) = -k_B T \ln \sum_k \exp(-F_k/k_B T) = \langle F_k \rangle - T S_c(T) \tag{1.38}$$

where F_k is the free energy of the kth minimum and $S_c(T)$ which is a measure of the number of the minima and an *extensive* quantity, is called the configurational entropy or *complexity* of the free energy minima. As the temperature is lowered further below T_d, the configurational entropy per spin goes to zero at a temperature $T_s < T_d$ and a *thermodynamic* transition is said to take place at this temperature. Note that the above minima refer to the free energy landscape and not to the potential energy landscape. The potential energy landscape is independent of temperature but the free energy landscape can be different at different tempeatures. Hence there is no conceptual problem for new minima being "developed" at low temperatures.

Kirkpatrick, Thirumalai and Wolynes pointed out [39,56–58] the analogy between this phenomenology of spin glass models to those of supercooled liquids and structural glasses. The ergodicity breaking temperature T_d was associated with the ideal glass transition temperature (T_c) predicted by mode coupling theory (see Eqn. 1.13) and the thermodynamic transition temperature T_s with the Kauzmann temperature T_K where the configurational entropy of liquid vanishes [10].

Based on the above analogy if one postulates that the free energy of supercooled liquids also develops exponentially large number of minima below T_C then dynamics for $T < T_C$ in *supercooled liquids* can be governed by transitions between such free energy minima. Wolynes and co-workers have proposed a mechanism of entropy driven nucleation of one free energy minima inside another [39]. This theory of *structural* glasses and supercooled liquids is known as the random first order transition theory (RFOT).

In the RFOT scenario, one considers under what condition a liquid is trapped in a single metastable state or is able to sample exponentially large number of such metastable states. Let us assume that initially the liquid is in a single metastable state. Consider a region of characteristic size $\xi(T)$. It is argued in the RFOT (as detailed below) that there is a characteristic length scale $\xi^*(T)$ above which such a cluster will be unstable and the liquid will sample other (exponentially large number of) metastable states. Thus at any instant of time different regions of the liquid will be in different metastable states. In other words the liquid is a "mosaic" of exponentially large number of metastable regions of characteristic size $\xi^*(T)$.

The transition from one metastable state to others is hindered by formation of surface at the cost of surface free energy (ΔG_s) which explicitly depends on spatial dimensions (D):

$$\frac{\Delta G_s}{k_B T} \propto \frac{Y \xi^\theta}{k_B T} \tag{1.39}$$

where $\theta \leq D$ is an unknown exponent and Y = surface tension. The driving force for the transition is the free energy gain (ΔG_b) corresponding to the possibility of sampling exponentially large number of other metastable minima :

$$\frac{\Delta G_b}{k_B T} \propto -\frac{T S_c \xi^D}{k_B T} \tag{1.40}$$

where S_c is the configurational entropy measuring the number of metastable

states. Thus in the RFOT scenario the total free energy (ΔG) depends on a characteristic length scale :

$$\Delta G(\xi) = \Delta G_s + \Delta G_b \tag{1.41}$$

If one uses the argument of the classical nucleation theory, then the free energy barrier corresponds to the *maximum* of ΔG in Eqn. 1.41 occurring at a characteristic length scale ξ^* :

$$\begin{aligned}
\left[\frac{\partial \Delta G}{\partial \xi}\right]_{\xi^*} &= 0 \\
\xi^* &= \frac{\theta}{D}\left(\frac{Y}{TS_c}\right)^{1/D-\theta} \sim \left(\frac{Y}{TS_c}\right)^{1/D-\theta} \\
\Delta G(\xi^*) &= Y(1-\frac{\theta}{D})(\xi^*)^{\theta} \\
\Delta G(\xi^*) &= (1-\frac{\theta}{D})\frac{\theta}{D} Y \left(\frac{Y}{TS_c}\right)^{\theta/D-\theta}
\end{aligned} \tag{1.42}$$

Note that (i) the characteristic lengthscale $\xi^*(T)$ diverges as $S_C(T) \to 0$. (ii) According to the above scenario, θ is an *unknown* exponent. Wolynes *et al.* argued that [39, 60] that $\theta = D/2$ in D dimensions.

Later, Bouchaud and Biroli [40] proposed a re-interpretation of the entropy driven nucleation picture of Wolynes *et al.* while keeping the underlying picture of exponentially large number of free energy minima intact. They considered a thought experiment in which the liquid is trapped into one (denoted by α) of the exponentially large number of metastable minima. The motion of all particles outside a sphere of radius ξ were frozen in the state α. This provided a boundary condition which acted like an external field for the thermodynamics of the particles inside the sphere. Configurations in which the inside particles are also in the state α matched the boundary condition provided by the outside particles frozen in the state α. Thus they were energetically more favored than others. The canonical partition function of the particles inside the sphere was given by :

$$\begin{aligned}
Z(\xi, T) &\approx \sum_{\beta \neq \alpha} \exp\left[-\frac{\xi^D f_\beta}{k_B T}\right] + \exp\left[-\frac{\xi^D f_\alpha}{k_B T} + \frac{Y\xi^\theta}{k_B T}\right] \\
&\approx \int_0^\infty df \exp\left[\frac{\xi^D\,(TS_c - f)}{k_B T}\right] + \exp\left[-\frac{\xi^D f_\alpha}{k_B T} + \frac{Y\xi^\theta}{k_B T}\right]
\end{aligned} \tag{1.43}$$

where f_β was the excess free energy per unit volume in a state β with a typical and random boundary field. $Y\xi^\theta$ was the relative gain in free energy in the state α owing to the favourable boundary condition. $S_c(f,T)$ is the configurational entropy per unit volume corresponding to the exponentially large number of the metastable states at the free energy density f. In the saddle point approximation, the integral in Eqn. 1.43 was approximately given by the value of the free energy f^* which maximizes the argument :

$$Z(\xi,T) \approx \exp\left[-\frac{\xi^D f^*_\beta}{k_B T}\right]\left[\exp\left(\frac{TS^*_c\xi^D}{k_B T}\right)+\exp\left(\frac{Y\xi^\theta}{k_B T}\right)\right]$$

From Eqn. 1.44 Bouchaud and Biroli argued that for small ξ (*i..e* small cluster of particles) and for $\theta < D$, the second term dominated the partition function. This implied that the state with the lower free energy is the one in which the system would lose the configurational entropy to gain the surface free energy. As ξ increases (larger and larger cluster of particles), eventually the first term in Eqn. 1.44 would dominate the partition function which then corresponded to the bulk free energy of the liquid in the mean-field approximation. This implied that for very large ξ, the state with the lower free energy is the one in which the system would sample all metastable states β to gain the configurational entropy at the cost of the surface free energy. The cross-over would occur at a temperature dependent characteristic lengthscale

$$\xi^*(T) = \left(\frac{Y}{TS_c}\right)^{\frac{1}{D-\theta}} \tag{1.44}$$

We note that the two definitions of ξ^* (Eqns. 1.42 and 1.44) are mutually proportional hence the scaling relation between the free energy barrier and the lengthscale is the same using either definitions.

Finally, the relation among the relaxation time τ, the characteristic length

scale ξ and the configurational entropy S_c according to the RFOT becomes,

$$\begin{aligned} \tau &= \tau_0 \exp\left(\Delta G/k_B T\right) \\ \Delta G &\propto \xi^{\psi} \\ &= \left(Y/TS_c\right)^{\psi/D-\theta} \\ \tau &= \tau_0 \exp\left(A\xi^{\psi}\right) \\ &= \tau_0 \exp\left[\frac{A}{k_B T}\left(\frac{Y}{TS_c}\right)^{\psi/D-\theta}\right] \end{aligned} \tag{1.45}$$

Note that in the Bouchaud-Biroli picture there is a second unknown exponent ψ and $\psi \neq \theta$ in general. (in the literature there are some non-uniformity about the notations. we follow the notations used in [40]). Eqn. 1.45 is a generalization of the Adam Gibbs relation - Eqn. 1.36. The spatial dimension D explicitly appears in 1.45. However, in addition, there are two *a priori unknown* exponents θ and ψ in Eqn. 1.45. Hence it is not immediately clear if Eqn. 1.45 reduces to the Adam Gibbs relation (Eqn. 1.36) or gets generalized in a D dependent way. This question will be addressed in more detail in Chapter 3.

1.7 Outline of the thesis

The aim of the present thesis is twofold:

1. To examine the relationship between dynamics and thermodynamics by *explicitly computing* the time scales, the length scales and the configurational entropy in several model liquids.

2. To explore the dependence of the characteristic time scales on various control parameters. In addition to the more familiar parameters like temperature and density we study the effect of spatial dimensionality and the interaction potential.

The outline of the thesis is presented below:

- In Chapter 2, we detail the definitions of the different quantities computed, the computational methods used to perform simulations and the description of the model glass-forming liquids studied.

- In chapter 3, we study the dependence on the spatial dimension of the Adam Gibbs (AG) relation between the relaxation time *i.e.* dynamics and the configurational entropy *i.e.* thermodynamics by analyzing a variety of model glass-forming liquids in 2,3 and 4 dimensions.

- In chapter 4, we explore the the dependence on spatial dimension (D) of the relation among the breakdown of the Stokes Einstein (SE) relation, the dynamical heterogeneity (by considering *direct* indicators *e.g.* χ_4^{peak} and β_{KWW} and the fragility by analyzing several model glass-formers in 2,3 and 4 dimensions.

- In chapter 5, we analyze the dependence of fragility on the softness of the interaction by studying three model fragile glass-formers of varying softness.

- In chapter 6, we study the density-temperature (DT) scaling of relaxation times and the strong pressure-energy correlation in the Kob-Andersen model in three dimensions and their implication for the density dependence of isochoric fragility.

- In chapter 7, we study the unusual behaviour of the diffusion coefficient in the modified Stillinger-Weber (mSW) model.

Chapter 2

Definitions, methods and models

After introducing the phenomenology of the glass-forming liquids and the relevant theories of glass transition, in the present chapter we summarize the details of the computer simulation in the present study. First, we describe the relevant definitions and working formulas used to compute the different quantities of interest. Then we describe the NVT MD algorithm used in the present study to simulate various glass-formers. Finally, we depict the details of the model glass-forming liquids studied in the present thesis.

2.1 Definitions

2.1.1 Two point time correlation functions

Consider a system made up of N *structureless* particles. The instantaneous local density $\rho(\vec{r}, t)$ is given by

$$\rho(\vec{r}, t) = \sum_{i=1}^{N} \delta(\vec{r} - \vec{r}_i(t)) \tag{2.1}$$

Owing to the local conservation of mass (or number of particles, if we consider number density instead of mass density), it obeys the continuity equation

$$\frac{\partial \rho(\vec{r}, t)}{\partial t} + \nabla \cdot \vec{j}(\vec{r}, t) = 0$$

with the associated current

$$j(\vec{r},t) = \sum_{i=1}^{N} \vec{v}_i \delta(\vec{r} - \vec{r}_i(t))$$

where $\vec{v}_i$ is the instantaneous velocity of the ith particle. In general any other microscopic dynamical variable for N structureless particles can be defined as

$$A(\vec{r},t) = \sum_{i=1}^{N} a_i(t) \delta(\vec{r} - \vec{r}_i(t))$$

where $a_i(t)$ represents the relevant single particle property under study.

Most widely studied correlation functions are *two point correlation functions* which are the simplest possible correlation functions. In real space-time one defines the *van Hove function* as

$$\begin{aligned} G(\vec{r},t) &= \frac{1}{\rho}\langle \rho(\vec{r},t)\rho(\vec{0},0)\rangle \\ &= \langle \frac{1}{N}\int d\vec{r'}\rho(\vec{r'}+\vec{r},t)\rho(\vec{r'},0)\rangle \\ &= \langle \frac{1}{N}\int d\vec{r'}\sum_{i=1}^{N}\sum_{j=1}^{N}\delta(\vec{r'}+\vec{r}-\vec{r}_j(t),t)\delta(\vec{r'}-\vec{r}_i(0),0)\rangle \\ &= \langle \frac{1}{N}\sum_{i=1}^{N}\sum_{j=1}^{N}\delta(\vec{r}-\vec{r}_j(t)+\vec{r}_i(0))\rangle \end{aligned} \tag{2.2}$$

where ρ is the average density - the angled bracket representing the "averaging" which can be either over time intervals or over statistical ensembles. In (supercooled) liquid state, one assumes they equal each other (ergodic hypothesis).

The Fourier transform of $G(\vec{r},t)$ from the real to the k space is called the *intermediate scattering function* $F(\vec{k},t)$:

$$\begin{aligned} F(\vec{k},t) &= \int d\vec{r} G(\vec{r},t)\exp\left(-\imath\vec{k}\cdot\vec{r}\right) \\ &= \frac{1}{N}\langle \rho(\vec{k},t)\rho(-\vec{k},0)\rangle \end{aligned} \tag{2.3}$$

where

$$\begin{aligned}\rho(\vec{k},t) &= \int d\vec{r}\rho(\vec{r},t)\exp\left(-\imath\vec{k}\cdot\vec{r}\right)\\ &= \sum_{i=1}^{N}\exp\left(-\imath\vec{k}\cdot\vec{r}_i(t)\right)\end{aligned}$$

is the Fourier transform of the local density. Taking further Fourier transform to frequency, one gets

$$S(\vec{k},\omega)=\frac{1}{2\pi}\int_{-\infty}^{\infty}dtF(\vec{k},t)\exp\left(\imath\omega t\right) \tag{2.4}$$

which is called the *dynamic structure factor*.

$G(\vec{r},t)$ and $F(\vec{k},t)$ can be naturally separated into two terms based on particle indices. These are called the *self (s)* and the *distinct (d)* parts:

$$\begin{aligned}G(\vec{r},t) &= G_s(\vec{r},t)+G_d(\vec{r},t)\\ G_s(\vec{r},t) &= \langle\frac{1}{N}\sum_{i=1}^{N}\delta(\vec{r}-\vec{r}_i(t)+\vec{r}_i(0))\rangle\\ G_d(\vec{r},t) &= \langle\frac{1}{N}\sum_{i=1}^{N}\sum_{j\neq i}^{N}\delta(\vec{r}-\vec{r}_j(t)+\vec{r}_i(0))\rangle\end{aligned} \tag{2.5}$$

$$\begin{aligned}F(\vec{k},t) &= F_s(\vec{k},t)+F_d(\vec{k},t)\\ F_s(\vec{k},t) &= \int d\vec{r}G_s(\vec{r},t)\exp\left(-\imath\vec{k}\cdot\vec{r}\right)\\ F_d(\vec{k},t) &= \int d\vec{r}G_d(\vec{r},t)\exp\left(-\imath\vec{k}\cdot\vec{r}\right)\end{aligned} \tag{2.6}$$

In the present thesis, the dynamics is also studied by another two-point time correlation function of local density, the *overlap function* ($q(t)$) [63–65] which is defined below.

$$\begin{aligned}q(t) &\equiv \int d\vec{r}\rho(\vec{r},t_0)\rho(\vec{r},t+t_0)\\ &= \sum_{i=1}^{N}\sum_{j=1}^{N}\delta(\vec{r}_j(t_0)-\vec{r}_i(t+t_0))\end{aligned} \tag{2.7}$$

Here the averaging over time origins t_0 is implied. Like $F(\vec{k},t)$, overlap

function also naturally separates into "self" and "distinct" terms:

$$q(t) = \sum_{i=1}^{N} \delta(\vec{r}_i(t_0) - \vec{r}_i(t+t_0)) + \sum_i \sum_{j \neq i} \delta(\vec{r}_i(t_0) - \vec{r}_j(t+t_0))$$

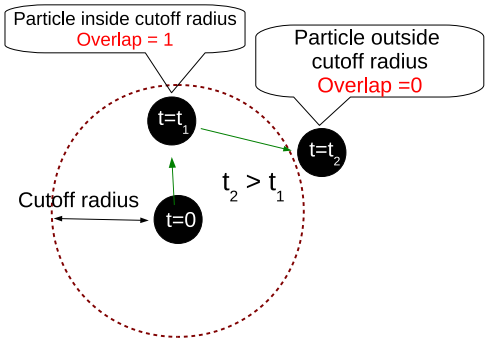

Figure 2.1: Illustrating the definition of the "overlap" function $q(t)$.

In the present thesis, we study only the self part of the total overlap function (that is neglecting $i \neq j$ terms in the double summation) is used, based on the observation [66] that the results obtained from the self part are not signicantly different from those obtained by considering the collective overlap function.

$$q(t) \approx \sum_{i=1}^{N} \delta(\vec{r}_i(t_0) - \vec{r}_i(t+t_0))$$

Further, for numerical computation, δ function is approximated by a window function $w(x)$ which defines the condition of "overlap" between two particle positions separated by a time interval t [Fig. 2.1]:

$$\begin{aligned} q(t) &\approx \sum_{i=1}^{N} w(|\vec{r}_i(t_0) - \vec{r}_i(t_0+t)|) \\ w(x) &= 1, x \leq a \text{ implying "overlap"} \\ &= 0 \text{ otherwise} \end{aligned} \tag{2.8}$$

Choice of the cutoff a for the overlap function: Eqn. 2.8 implies that in simulation, the value of the overlap function depends on the choice of the cutoff parameter a. This parameter is chosen such that particle positions

separated due to small amplitude vibrational motion are treated as the same - a is such that a^2 lies in the plateau region on the MSD curve. Further, the choice of a is fine-tuned to maximize the peak height of the dynamical susceptiblity χ_4^{peak} (at a representative intermediate temperature). Here we show the choice of the cutoff parameter a for the 4D KA and the 2D R10 models in Figs. 2.2 and 2.3 respectively.

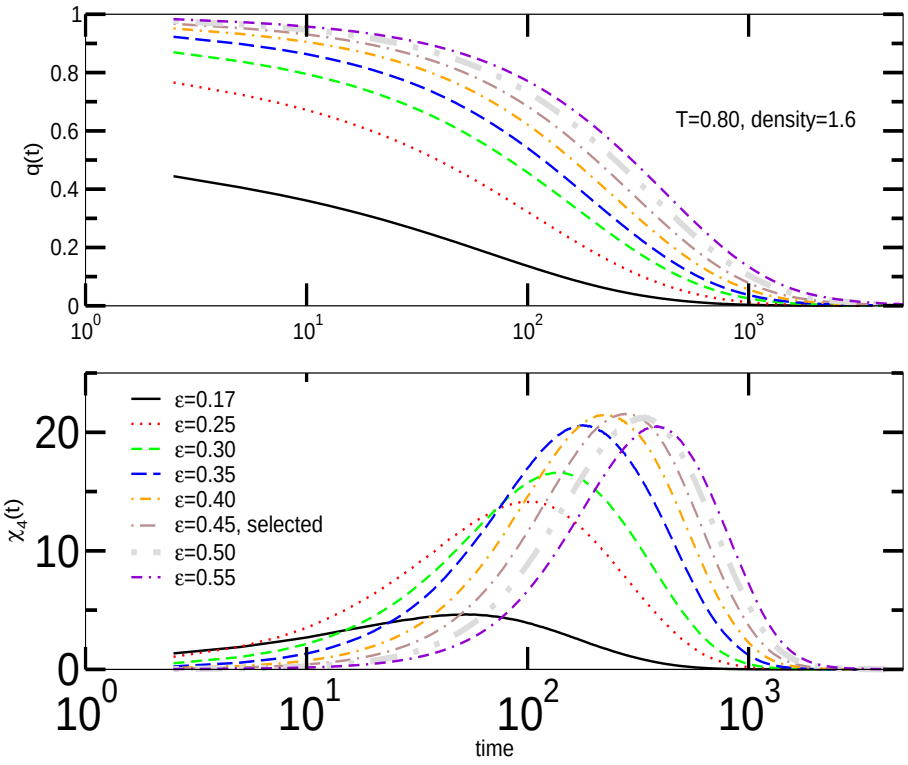

Figure 2.2: Choice of the cutoff parameter a for the overlap function for the 4D KA model taking $T = 0.80$ as the representative temperature. $a = 0.45$.

2.1.2 Four point correlation functions

We have also studied the variance $\chi_4(t)$ of the fluctuation of the overlap function ($\chi_4(t)$ - also called the *dynamic susceptibility*) - defined as,

$$\chi_4(t) = \frac{1}{N}\left(\langle q(t)^2\rangle - \langle q(t)\rangle^2\right) \tag{2.9}$$

The quantity $\chi_4(t)$ can be written as an integral to a higher order, *four point correlation function* $g_4(\vec{r}, t)$ [63–65] commonly used in the context of

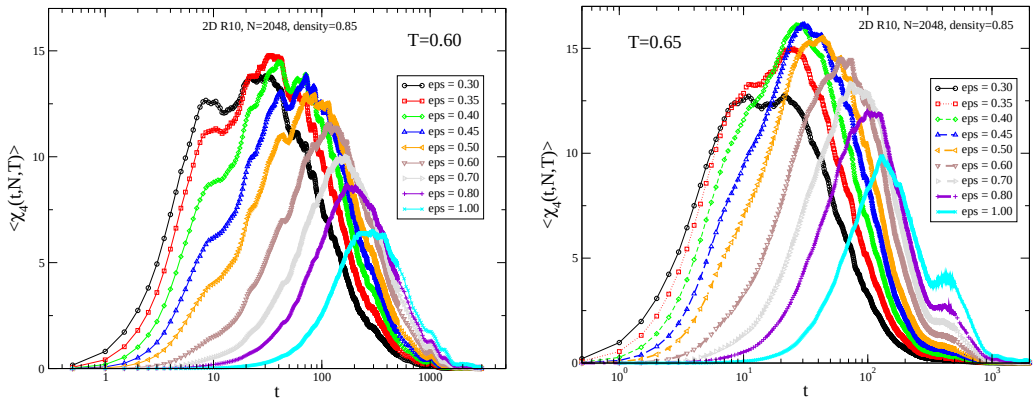

Figure 2.3: Choice of the cutoff parameter for the overlap function for the 2D $R10$ model taking $T = 0.60$ (top) and $T = 0.65$ (bottom) as representative intermediate temperatures. $a = 0.40$.

dynamical heterogeneity:

$$\begin{aligned} g_4(\vec{r},t) &= \langle\rho(0,0)\rho(0,t)\rho(\vec{r},0)\rho(\vec{r},t)\rangle - \langle\rho(0,0)\rho(0,t)\rangle\langle\rho(\vec{r},0)\rho(\vec{r},t)\rangle \\ \chi_4(t) &= \int d\vec{r} g_4(\vec{r},t) \end{aligned} \tag{2.10}$$

In k space, the *four point dynamic structure factor* $S_4(k,t)$ is defined as

$$S_4(k,t) = \frac{1}{N}\left(\langle\tilde{Q}(k,t)\tilde{Q}(-k,t)\rangle\right) \tag{2.11}$$

where $\tilde{Q}(k,t)$ is the Fourier transform of the overlap function:

$$\tilde{Q}(k,t) = \sum_{i=1}^{N} \exp(\imath\vec{k}\cdot\vec{r}_i(0))w(|\vec{r}_i(0) - \vec{r}_i(t)|) \tag{2.12}$$

The four point dynamic structure factor $S_4(k,t)$ is related to the dynamic susceptibility $\chi_4(t)$:

$$\lim_{k\to 0} S_4(k,t) = \chi_4(t) \tag{2.13}$$

2.1.3 Estimate of the dynamical correlation length

Assuming that the $S_4(k,t)$ is described by the Ornstein-Zernicke relation as it approaches the limit of $k \to 0$, one may extract a *dynamical correlation*

length ξ from $S_4(k,t)$:

$$S_4(k,\tau,T) = \frac{S_4(0,\tau,T)}{1+(k\xi)^2} \tag{2.14}$$

2.1.4 Estimates of the α relaxation time

The structural relaxation time can be extracted from the overlap and the other two-point correlation functions and $\chi_4(t)$ in several different ways:

1. At high T, the two-point time correlation functions decay exponentially $C(t,T) = C(0,T)\exp(-t/\tau(T))$. As the temperature decreases, the correlation function develops a plateau that is the relaxation process becomes a multi step process. Then structural relaxation time τ of α regime can be estimated by fitting the overlap function in the α regime to the stretched exponential form:

   $$C(t,T) = C(0,T)\exp(-(t/\tau(T))^{\beta(T)})$$

   Here $C(t,T)$ may be the overlap function $(q(t,T)/N)$, the self intermediate scattering function $F_s(\vec{k},t)$ or the full intermediate scattering function $F(\vec{k},t)$.

2. Alternatively, the relaxation time may be estimated from the decay of two-point correlation functions to a arbitrarily fixed value, usually $1/e$:

   $$C(\tau,T) = 1/e \tag{2.15}$$

3. The main interesting feature in $\chi_4(t)$ *vs.* time is that it goes through a maximum at some characteristic time $\tau_4(T)$ and both the peak time $\tau_4(T)$ and the peak height $\chi_4(\tau_4)$ increases as the temperature decreases [64,67]. This is because by definition 2.9, $\chi_4(t) \to 0$ when the fluctuation in the overlap function is low which is the case both in the limit $t \to 0$ when almost all the particles are inside the cutoff distance a $(q(t)/N \sim 1)$ and in the limit $t \to \infty$ when all the particles have moved beyond the cutoff distance a $(q(t)/N \sim 0)$. The characteristic time $\tau_4(T)$ is called the characteristic *timescale of dynamic heterogeneity*. From the present study as well as previous work [66], it is found that this timescale is

proportional to α relaxation time obtained from the decay of two point correlation functions. Hence $\tau_4(T)$ may be considered another measure of the α relaxation time.

$$\chi_4(t = \tau_4) = \chi_4^{\max}(T) \tag{2.16}$$

2.1.5 The mean squared displacement and the diffusion coefficient

The mean squared displacement (MSD) characterizes the particle-averaged translational motion in the system. The translational diffusion coefficient (D) is a transport coefficient which can be computed from the MSD. The MSD is also a useful quantity to check if the runs are sufficiently long - for a sufficiently long run the MSD is well into the diffusive (linear t dependence) regime. D is computed from asymptotic fit of the following form to MSD :

$$\begin{aligned} \text{MSD} &= \frac{1}{N}\sum_{i=1}^{N} < (\vec{r}_i(t) - \vec{r}_i(0))^2 > \\ \lim_{t\to\infty} MSD(t) &= 2dDt \quad \text{where} \quad d = \text{spatial dimension} \end{aligned} \tag{2.17}$$

2.1.6 The non-Gaussian parameter $\alpha_2(t)$

The non-Gaussian parameter $\alpha_2(t)$ is defined as [124]:

$$\begin{aligned} \alpha_2(t) &= C_D \frac{\langle r^4 \rangle}{\langle r^2 \rangle^2} - 1 \\ \langle r^{2n} \rangle &= \frac{1}{N}\sum_{i=1}^{N} \langle (\vec{r}_i(t) - \vec{r}_i(0))^{2n} \rangle, n = 1, 2 \end{aligned} \tag{2.18}$$

C_D is a spatial dimension (D) dependent coefficient to ensure that $\alpha_2(t) = 0$ when the distribution of displacements is a Gaussian. $C_D = \frac{1}{2}, \frac{3}{5}, \frac{2}{3}$ in $D = 2, 3, 4$ respectively. The time t^* at which the non-Gaussian parameter $\alpha_2(t)$ is maximum is a measure of the time scale of heterogeneity in the system.

2.1.7 The shear viscosity η

The shear viscosity η is computed from equilibrium simulation using both the Green Kubo and the Einstein relation which we briefly discuss below.

Green Kubo and Einstein relations: Let us consider a system of N particles in volume V and interacting with each other via pair-wise interaction potential $U(r_{ij})$. At equilibrium, the system is described by the Hamiltonian

$$H = \sum_{i=1}^{N} \frac{p_i^2}{2m} + \sum_{i=1}^{N} \sum_{j>i}^{N} U(r_{ij})$$

For such a system, the pressure (stress) tensor is given by

$$P_{\alpha\beta}(t) = \frac{1}{V} \left(\sum_{i=1}^{N} p_{i\alpha} p_{i\beta}/m + \sum_{i=1}^{N} \sum_{j>i}^{N} r_{ij\alpha} f_{ij\beta} \right)$$

where $\alpha, \beta \in (x, y, z)$ denotes Cartesian components. $r_{ij} = |\vec{r}_i - \vec{r}_j|$ and $f_{ij} = -\frac{\partial U(r_{ij})}{\partial r_{ij}}$.

The shear viscosity η can be computed from the following Green-Kubo relation involving the auto-correlation function of the pressure tensor:

$$\eta = \frac{V}{k_B T} \int_0^\infty dt < P_{\alpha\beta}(t) P_{\alpha\beta}(0) > \tag{2.19}$$

The integral of the stress-correlation function can be related the integral of the stress tensor as a generalized Einstein relation. Let us define the Helfand moment $A_{\alpha\beta}(t)$ (following ref. [125]) such that

$$\frac{dA_{\alpha\beta}(t)}{dt} = P_{\alpha\beta}(t) V$$

Then

$$
\begin{aligned}
A_{\alpha\beta}(t) - A_{\alpha\beta}(0) &= V \int_0^t dt^{'} P_{\alpha\beta}(t^{'}) \\
\frac{1}{V^2} < (A_{\alpha\beta}(t) - A_{\alpha\beta}(0))^2 > &= \int_0^t \int_0^t dt^{'} dt^{''} < P_{\alpha\beta}(t^{'}) P_{\alpha\beta}(t^{''}) > \\
&= 2 \int_0^t dt^{''} \int_0^{t^{''}} d\tau < P_{\alpha\beta}(\tau) P_{\alpha\beta}(0) >, (\tau = t'' - t') \\
&= 2 \left(\int_0^t d\tau < P_{\alpha\beta}(\tau) P_{\alpha\beta}(0) > \right) \int_\tau^t dt^{''} \\
&= \left(\int_0^t d\tau < P_{\alpha\beta}(\tau) P_{\alpha\beta}(0) > \right) 2t(1 - \frac{\tau}{t})
\end{aligned}
$$

So that

$$
\int_0^t d\tau < P_{\alpha\beta}(\tau) P_{\alpha\beta}(0) > = \lim_{t \to \infty} \frac{< (A_{\alpha\beta}(t) - A_{\alpha\beta}(0))^2 >}{2t} \frac{1}{V^2}
$$

Hence the shear viscosity η can be computed from $A_{\alpha\beta}$ as

$$
\eta = \frac{1}{V k_B T} \lim_{t \to \infty} \frac{< (A_{\alpha\beta}(t) - A_{\alpha\beta}(0))^2 >}{2t} \tag{2.20}
$$

Averaging over different components: Since shear viscosity is a collective property of N particles, numerical accuracy is a big issue when computing shear viscosity using either Eqn. 2.19 or Eqn. 2.20. To improve numerical accuracy we use the component averaged stress-correlation function and Helfand moments:

$$
\begin{aligned}
\eta &= \frac{V}{k_B T} \int_0^\infty dt < P_{\alpha\beta}(t) P_{\alpha\beta}(0) >_{avg} \\
< P_{\alpha\beta}(t) P_{\alpha\beta}(0) >_{avg} &= \frac{< P_{xy}(t) P_{xy}(0) > + < P_{yz}(t) P_{yz}(0) > + < P_{zx}(t) P_{zx}(0) >}{3}
\end{aligned} \tag{2.21}
$$

$$\begin{aligned}
\eta &= \frac{1}{Vk_BT}\lim_{t\to\infty}\frac{<(A_{\alpha\beta}(t)-A_{\alpha\beta}(0))^2>_{avg}}{2t} \\
<(A_{\alpha\beta}(t)-A_{\alpha\beta}(0))^2>_{avg} &= \frac{1}{3}[<(A_{xy}(t)-A_{xy}(0))^2> + \\
&\quad <(A_{yz}(t)-A_{yz}(0))^2> + \\
&\quad <(A_{zx}(t)-A_{zx}(0))^2>] \qquad (2.22)
\end{aligned}$$

Estimates of the shear viscosity η: The cumulative sum of the component averaged stress auto correlation function is taken as the measure of the integral in Eqn. 2.21. As the stress auto correlation function decays to zero, the cumulative sum should approach a constant value. An approximate plateau in the cumulative sum is observed typically around the region when the correlation function first goes to zero. This value is taken to be the measure of the shear viscosity η from the Green Kubo relation. The component averaged Helfand moment is $\propto t^2$ at short time and crosses over to linear t dependence at long time. The slope of the component averaged Helfand moment at long time and in linear regime is taken to be the measure of the shear viscosity from the Einstein relation.

2.1.8 The Hessian of a two body potential

We derive the general expression for the double derivative $H(j,k)$ of a two-body potential $u(r_{jk})$ with respect to the coordinates of the particles j and k.

$$\begin{aligned}
H(j,k) &= \frac{\partial}{\partial\vec{r}_j}\frac{\partial}{\partial\vec{r}_k}u(r_{jk}) \\
\frac{\partial}{\partial\vec{r}_j} &\equiv \hat{i}\frac{\partial}{\partial x_j}+\hat{j}\frac{\partial}{\partial y_j}+\hat{k}\frac{\partial}{\partial z_j}
\end{aligned}$$

where (x_j, y_j, z_j) are the Cartesian coordinates of the particle j in three dimensions. For a system of N particles in 3 dimensions, the Hessian is a $3N\times 3N$ matrix. However, we first compute the double derivative with respect to one pair of particles. Next we write down the explicit formula for all the elements of the Hessian matrix. Finally we generalize for D dimensions. The

following identities will be repeatedly used:

$$\begin{aligned} r_{jk} &= [(x_j - x_k)^2 + (y_j - y_k)^2 + (z_j - z_k)^2]^{1/2} \\ \frac{\partial r_{jk}}{\partial x_j} &= \frac{x_j - x_k}{r_{jk}} \equiv \frac{x_{jk}}{r_{jk}} \\ \frac{\partial r_{jk}}{\partial x_k} &= -\frac{x_j - x_k}{r_{jk}} \equiv -\frac{x_{jk}}{r_{jk}} \end{aligned}$$

The first derivative is

$$\begin{aligned} \frac{\partial u(r_{jk})}{\partial \vec{r}_k} &= \hat{i}\frac{\partial u}{\partial x_k} + \hat{j}\frac{\partial u}{\partial y_k} + \hat{k}\frac{\partial u}{\partial z_k} \\ \hat{i}\frac{\partial u(r_{jk})}{\partial x_k} &= \hat{i}\frac{\partial r_{jk}}{\partial x_k}\frac{\partial u(r_{jk})}{\partial r_{jk}} \text{ (chain rule)} \\ &= \frac{-\hat{i}(x_j - x_k)}{r_{jk}}\frac{\partial u(r_{jk})}{\partial r_{jk}} \end{aligned}$$

Similarly for y and z components. Combining them and expressing in vector notation,

$$\frac{\partial}{\partial \vec{r}_k} u(r_{jk}) = -\frac{\partial u(r_{jk})}{\partial r_{jk}} \hat{r}_{jk} \tag{2.23}$$

Now, the second derivative is

$$\frac{\partial}{\partial \vec{r}_j}\left(-\frac{\partial u(r_{jk})}{\partial r_{jk}}\hat{r}_{jk}\right) = \left(\hat{i}\frac{\partial}{\partial x_j} + \hat{j}\frac{\partial}{\partial y_j} + \hat{k}\frac{\partial}{\partial z_j}\right)\left(-\frac{\partial u(r_{jk})}{\partial r_{jk}}\hat{r}_{jk}\right)$$

We will show details of algebra for the x component only.

$$\hat{i}\frac{\partial}{\partial x_j}\left(-\frac{\partial u(r_{jk})}{\partial r_{jk}}\hat{r}_{jk}\right) = \left(\hat{i}\frac{\partial}{\partial x_j}\frac{-\partial u}{\partial r_{jk}}\right) \otimes \hat{r}_{jk} + \frac{-\partial u}{\partial r_{jk}}\left(\hat{i}\frac{\partial}{\partial x_j} \otimes \hat{r}_{jk}\right)$$

where $\otimes$ denotes tensor product between two vectors. The first term is

$$\begin{aligned} \left(\hat{i}\frac{\partial}{\partial x_j}\frac{-\partial u}{\partial r_{jk}}\right) \otimes \hat{r}_{jk} &= \left(\hat{i}\frac{\partial r_{jk}}{\partial x_j}\frac{\partial}{\partial r_{jk}}\frac{-\partial u(r_{jk})}{\partial r_{jk}}\right) \otimes \hat{r}_{jk} \\ &= \left(\frac{\hat{i}x_{jk}}{r_{jk}}\frac{-\partial^2 u}{\partial^2 r_{jk}}\right) \otimes \hat{r}_{jk} \\ &= -\frac{\partial^2 u}{\partial r_{jk}^2}(\frac{\vec{r}_{jk}}{r_{jk}})_{x-component} \otimes \frac{\vec{r}_{jk}}{r_{jk}} \\ &= -\frac{1}{r_{jk}^2}\frac{\partial^2 u}{\partial r_{jk}^2}(\vec{r}_{jk} \otimes \vec{r}_{jk})_{x-component} \end{aligned}$$

The second term is

$$\begin{aligned}
\frac{-\partial u}{\partial r_{jk}}\left(\hat{i}\frac{\partial}{\partial x_j}\otimes\hat{r}_{jk}\right) &= \frac{-\partial u}{\partial r_{jk}}\left(\hat{i}\frac{\partial}{\partial x_j}\otimes\frac{x_{jk}\hat{i}+y_{jk}\hat{j}+z_{jk}\hat{k}}{r_{jk}}\right)\\
&= \frac{-\partial u}{\partial r_{jk}}\left(\frac{1}{r_{jk}}\hat{i}\otimes\hat{i}+\hat{i}\frac{\partial}{\partial x_j}(\frac{1}{r_{jk}})\otimes\vec{r}_{jk}\right)\\
&= \frac{-\partial u}{\partial r_{jk}}\left(\frac{1}{r_{jk}}\hat{i}\otimes\hat{i}+\hat{i}\frac{\partial r_{jk}}{\partial x_j}\frac{\partial}{\partial r_{jk}}(\frac{1}{r_{jk}})\otimes\vec{r}_{jk}\right)\\
&= \frac{-\partial u}{\partial r_{jk}}\left(\frac{1}{r_{jk}}\hat{i}\otimes\hat{i}+\frac{\hat{i}x_{jk}}{r_{jk}}\frac{-1}{r_{jk}^2}\otimes\vec{r}_{jk}\right)\\
&= -\frac{1}{r_{jk}}\frac{\partial u}{\partial r_{jk}}(\mathbb{I})_{x-component}+\frac{1}{r_{jk}^3}\frac{\partial u}{\partial r_{jk}}(\vec{r}_{jk}\otimes\vec{r}_{jk})_{x-component}
\end{aligned}$$

where $\mathbb{I}=\hat{i}\otimes\hat{i}+\hat{j}\otimes\hat{j}+\hat{k}\otimes\hat{k}$ is the 3×3 identity matrix in three dimensions. So combining the first and the second term, the second derivative becomes,

$$\begin{aligned}
H(j,k) &= \frac{\partial}{\partial\vec{r}_j}\frac{\partial}{\partial\vec{r}_k}u(r_{jk})\\
&= \left(-\frac{1}{r_{jk}^2}\frac{\partial^2 u}{\partial r_{jk}^2}+\frac{1}{r_{jk}^3}\frac{\partial u}{\partial r_{jk}}\right)\vec{r}_{jk}\otimes\vec{r}_{jk}-\frac{1}{r_{jk}}\frac{\partial u}{\partial r_{jk}}\mathbb{I} \qquad (2.24)
\end{aligned}$$

2.2 Computational methods

2.2.1 The Brown and Clarke algorithm for NVTMD

We have used the Brown and Clarke algorithm for performing the molecular dynamics (MD) simulation at the condition of constant T, V and N. Here we describe the details of the algorithm and the checks done to validate the implementation.

Hoover's equations of motion: In MD, one solves the Newton's equations of motion for each particle. For keeping the temperature constant in MD simulation, Hoover([178]) added a velocity dependant damping force to the interaction forces. The equations of motion for the particle i in the so-called Hoover dynamics becomes

$$\begin{aligned} \frac{d\vec{r_i}(t)}{dt} &= \vec{v_i}(t) \equiv \frac{\vec{p_i}(t)}{m} \\ \frac{d\vec{v_i}(t)}{dt} &= \frac{\vec{F_i}(t) - \alpha\vec{v_i}(t)}{m} \end{aligned} \tag{2.25}$$

The constant α is chosen to make the kinetic temperature (T) a constant of motion. The kinetic temperature (T) is given by

$$\frac{fT}{2} = \frac{m}{2}\sum_{i=1}^{N}\vec{v_i}^2 \tag{2.26}$$

where f is the no. of degrees of freedom of the N-particle system. At equilibrium total force is zero and the centre of mass can be set at rest. So in D spatial dimensions there are $D+1$ constraints (D coordinates of the centre of mass and the kinetic temperature).Hence $f = N \times D - (D+1)$.

Setting

$$\frac{dT}{dt} = 0 \Rightarrow \alpha = \frac{\sum \vec{F_i}\cdot\vec{v_i}}{\sum \vec{v_i}\cdot\vec{v_i}} = -\frac{\dot{U}}{2K} \tag{2.27}$$

where U is the total potential energy and K is the total kinetic energy of the N-particle system.

The Hoover dynamics is not the same as the Newtonian dynamics. So the

simulated trajectory should not be same as the physical (Newtonian) trajectory of the system. However, there is a principle of least constraint ([178]) which says that out of all possible constrained equations of motion, Hoover's equation of motion is the one for which the deviation between the simulated trajectory and the physical trajectory is minimum.

The Brown and Clarke algorithm - derivation: In our implementation, the equations of motion were integrated using the algorithm given by Brown and Clarke ([177]) implementation of the Hoover dynamics. In this metod, the equations of motion are integrated *via* the leap-frog scheme [179]:

$$\begin{aligned} \vec{v}_i(t+\frac{\Delta t}{2}) &= \vec{v}_i(t-\frac{\Delta t}{2}) + \frac{\vec{F}_i(t)}{m}\Delta t + \mathcal{O}(\Delta t^2) \\ \vec{r}_i(t+\Delta t) &= \vec{r}_i(t) + \vec{v}_i(t+\frac{\Delta t}{2})\Delta t + \mathcal{O}(\Delta t^2) \end{aligned} \tag{2.28}$$

Notice that in this algorithm, the initial conditions (positions and velocities) are *not* at the same instant. They are offset by $\frac{\Delta t}{2}$,e.g. $\vec{r}_i(0)$ and $\vec{v}_i(\frac{\Delta t}{2})$. The velocity at the same time step can be written as

$$\vec{v}_i(t) \approx \frac{1}{2}\left[\vec{v}_i(t-\frac{\Delta t}{2}) + \vec{v}_i(t+\frac{\Delta t}{2})\right] \tag{2.29}$$

The leap frog algorithm will reduce to the Verlet algorithm ([179]) if we *define*

$$\vec{v}_i(t-\frac{\Delta t}{2}) = \frac{\vec{r}_i(t) - \vec{r}_i(t-\Delta t)}{\Delta t}$$

Brown and Clarke showed ([177]) that if one uses the leap frog algorithm to integrate Hoover's equation of motion (2.25), then one need not use Eqn. (2.27) to calculate the constant α. Instead one can use a simple velocity scaling (presumably cheaper for computation) as described below.

The leap frog scheme for Hoover's equation of motion (2.25) will be ($\vec{a}_i(t) =$ acceleration of particle i at time t)

$$\begin{aligned} \vec{v}_i(t+\frac{\Delta t}{2}) &= \vec{v}_i(t-\frac{\Delta t}{2}) + \vec{a}_i(t)\Delta t - \frac{\alpha \vec{v}_i(t)}{m}\Delta t \\ \vec{r}_i(t+\Delta t) &= \vec{r}_i(t) + \vec{v}_i(t+\frac{\Delta t}{2})\Delta t \end{aligned} \tag{2.30}$$

Let us define an intermediate velocity update by

$$\vec{v}_i^{'}(t) = \vec{v}_i(t-\frac{\Delta t}{2}) + \vec{a}_i(t)\frac{\Delta t}{2} \tag{2.31}$$

Now, from (2.29) and (2.30) we get,

$$\begin{aligned} \vec{v}_i(t) &= \frac{1}{2}\left[2\vec{v}_i(t-\frac{\Delta t}{2}) + \vec{a}_i(t)\Delta t - \frac{\alpha \vec{v}_i(t)}{m}\Delta t\right] \\ &= \vec{v}_i(t-\frac{\Delta t}{2}) + \vec{a}_i(t)\frac{\Delta t}{2} - \frac{\alpha \Delta t}{2m}\vec{v}_i(t) \end{aligned}$$

or,

$$\begin{aligned} \vec{v}_i(t)\left[1+\frac{\alpha \Delta t}{2m}\right] &= \vec{v}_i(t-\frac{\Delta t}{2}) + \vec{a}_i(t)\frac{\Delta t}{2} \\ &= \vec{v}_i^{'}(t) \end{aligned}$$

or,

$$\vec{v}_i(t) = \beta \vec{v}_i^{'}(t)$$

where

$$\beta \equiv \frac{1}{1+\frac{\alpha \Delta t}{2m}} \tag{2.32}$$

Using (2.32) in (2.30) we get,

$$\begin{aligned}
\vec{v}_i(t+\frac{\Delta t}{2}) &= \vec{v}_i(t-\frac{\Delta t}{2}) + \vec{a}_i(t)\Delta t - \frac{\alpha \vec{v}_i(t)}{m}\Delta t \\
&= \vec{v}_i(t-\frac{\Delta t}{2}) + \vec{a}_i(t)\Delta t - \frac{\alpha \Delta t}{m}\beta \vec{v}_i'(t) \\
&= \vec{v}_i(t-\frac{\Delta t}{2}) + \vec{a}_i(t)\Delta t - \frac{\alpha\beta\Delta t}{m}\left[\vec{v}_i(t-\frac{\Delta t}{2}) + \vec{a}_i(t)\frac{\Delta t}{2}\right] \\
&= \vec{v}_i(t-\frac{\Delta t}{2})\left[1-\frac{\alpha\beta\Delta t}{m}\right] + \vec{a}_i(t)\left[1-\frac{\alpha\beta\Delta t}{2m}\right]\Delta t \\
&= (2\beta-1)\,\vec{v}_i(t-\frac{\Delta t}{2}) + \beta\vec{a}_i(t)\Delta t \qquad (2.33)
\end{aligned}$$

So, α has been replaced by β in the equation of motion. The quantity β is calculated from (2.26):

$$\begin{aligned}
T(t) &= \frac{m}{f}\sum_{i=1}^{N}\vec{v}_i^2(t) \\
&= \frac{m}{f}\left(\sum_{i=1}^{N}\vec{v'}_i^2(t)\right)\beta^2
\end{aligned}$$

Demanding instantaneous kinetic temperature $T(t)$ to be equal to runtemp T_r we get

$$\beta^2 = \frac{fT_r}{m\sum_{i=1}^{N}\vec{v'}_i^2(t)} \qquad (2.34)$$

So finally, the Brown and Clarke scheme of integrating Hoover's equation of motion becomes:

$$\begin{aligned}
\vec{v}_i(t+\frac{\Delta t}{2}) &= (2\beta-1)\,\vec{v}_i(t-\frac{\Delta t}{2}) + \beta\vec{a}_i(t)\Delta t \\
\vec{r}_i(t+\Delta t) &= \vec{r}_i(t) + \vec{v}_i(t+\frac{\Delta t}{2})\Delta t \qquad (2.35)
\end{aligned}$$

Implementing in the code: In the code the implementation is done in the following order:

```
CALL xupdate(N)              ==> r(t)=r(t-dt)+v(t-dt/2)dt
CALL engforce1(u,vir,N)      ==> calc a(t)
CALL betacalc(beta,N)        ==> calc beta from v(t-dt/2)
```

```
CALL vupdate(beta,temp,ke,N) ==> v(t+dt/2)=(2 beta-1)v(t-dt/2)+beta a(t)
```

Generating the initial condition: The initial condition for each run is either random or from square lattice or from a configuration equilibrated at a higher temperature. At high temperatures, relaxation time is small and the system quickly equilibrates. For low temperatures, the runs are started by choosing arbitrary configuration (equilibrated) at a higher temperature.

Checking the reliability of the code:

- The NVT code is tested by reproducing the energy, pressure data of reference [172]. The data tabulated in tables 2.1 - 2.3 show excellent matching (difference $< 1\%$).
- The centre of mass velocity is constrained to be zero, which is shown in Fig 2.4.

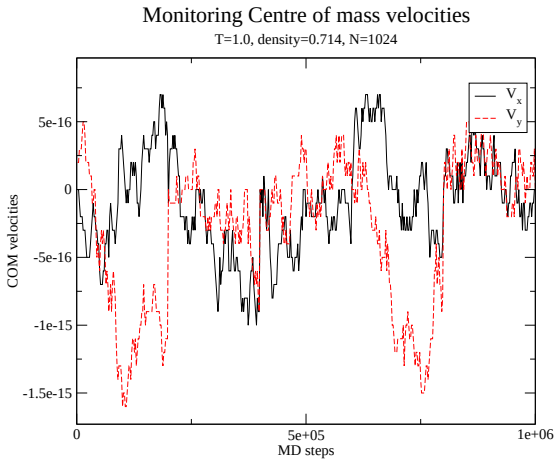

Figure 2.4: The COM velocity is constrained to be zero during initialization. Here the COM velocities are monitord during MD simulation to check that the COM is not drifting.

Table 2.1: Pressure comparison

T	density	ref [172] Pressure (exact)	my Pressure	%difference
5.0	0.57567	13.5	13.498	0.01
3.0	0.63375	13.5	13.477	0.17
1.0	0.71435	13.5	13.490	0.07
0.9	0.71943	13.5	13.498	0.01
0.8	0.72466	13.5	13.509	0.07
0.7	0.72991	13.5	13.492	0.06
0.6	0.73532	13.5	13.499	0.01

Table 2.2: Potential energy comparison

T	density	ref [172] PE	my PE	%difference
5.0	0.57567	3.0753	3.0742	0.04
3.0	0.63375	3.0503	3.0439	0.21
1.0	0.71435	2.9830	2.9805	0.08
0.9	0.71943	2.9775	2.9767	0.03
0.8	0.72466	2.9716	2.9734	0.06
0.7	0.72991	2.9659	2.9639	0.07
0.6	0.73532	2.9599	2.9594	0.02

Table 2.3: Total energy comparison

T	density	ref [172] E	my E	%difference
5.0	0.57567	8.0753	8.0697	0.07
3.0	0.63375	6.0503	6.0411	0.15
1.0	0.71435	3.9830	3.9796	0.09
0.9	0.71943	3.9775	3.8771	2.56
0.8	0.72466	3.7716	3.7738	0.06
0.7	0.72991	3.6659	3.6642	0.05
0.6	0.73532	3.5599	3.5597	0.01

2.2.2 Computation of the total free energy and the total entropy

A consequence of the second law of thermodynamics is that for a system in contact with a thermal reservoir so that the temperature (T), the volume (V) and the number of particles (N) of the system are held fixed, the Helmholtz free energy $A = U - TS$ is at minimum when the system is at thermodynamic

equilibrium and all the information about the equilibrium thermodynamic properties of the system are contained in the Helmholtz free energy. In the present thesis, computation of the total entropy $S = -\frac{\partial A}{\partial T}$ is required to compute the *absolute* value of the configurational entropy. Hence one needs to compute the total free energy. However, the *absolute* value of Helmholtz free energy is not *directly* measurable in simulation (or in experiments).

$$\begin{aligned} Z &= \frac{1}{N!}\int \frac{d\vec{p}^N d\vec{r}^N}{h^{DN}} \exp\left(-\beta H(\vec{p}^N, \vec{r}^N)\right) \\ A &= -k_B T \ln Z \end{aligned} \tag{2.36}$$

From Eqn. 2.36 it is clear that free energy is related to the total *volume* of the phase space and hence the free energy can not be written as an canonical *average* over phase space. Hence, to compute the absolute free energy one uses indirect methods such as thermodynamic intergration which is discussed below.

The thermodynamic integration method: We have computed numerically the *absolute* value of the total (or bulk) Helmholz free energy and the total entropy by the *thermodynamic integration method* [79]. In this method a *derivative* of the total free energy with respect to either a thermodynamic variable like density, temperature or other parameters like strength of perturbation of a perturbed Hamiltonian, is computed directly in simulation along a *specified, reversible* path. This derivative is then integrated along the specified path to obtain the *difference* in free energy of the target state point from a reference state point. The reference state point is a state point where the free energy is *exactly known* either from exact formulas or computed from other methods. To obtain the *absolute value* of the free energy at the target state point the free energy at the reference state point are added to the difference obtained by the thermodynamic integration. The implementation is discussed in more detail below.

The path of integration and computational details: Let us consider that the thermodynamic integration is done along the path shown in Fig. 2.5:

1. A high temperature (T_{ref}) and the zero density limit of the liquid, where the system obeys the ideal gas equation of state, is chosen as the reference

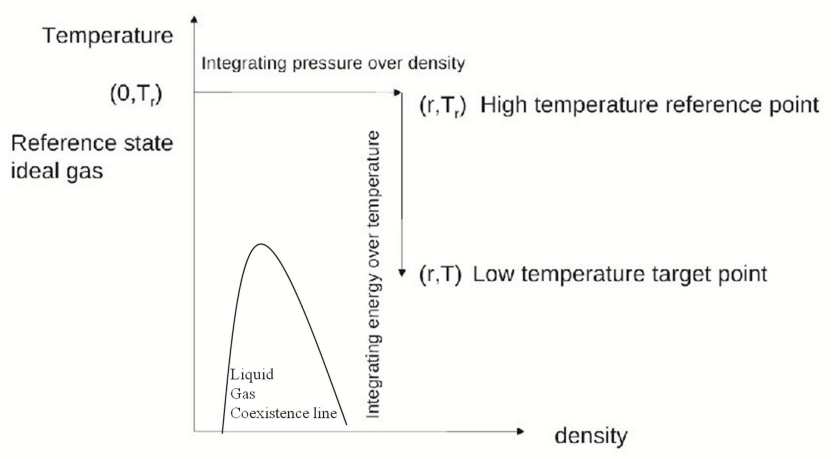

Figure 2.5: The path used for thermodynamic integration is illustrated in the $T-\rho$ plane.

state point of known free energy of a *single component* ideal gas. Since the Hamiltonian of a system can be written as a sum of a kinetic (K) and a potential part (U) : $H(\vec{p}^N, \vec{r}^N) = K(\vec{p}^N) + U(\vec{r}^N)$, hence the Helmholtz free energy $A(\rho, T)$ can be written as a sum of an ideal gas term $A_{id}(\rho, T)$ (contribution from the kinetic part of the Hamiltonian) and an excess part $A_{ex}(\rho, T)$ (contribution from the potential part of the Hamiltonian). Further, if the system is a binary mixture (multi-component) then one takes into account the mixing entropy. Hence for a binary mixture, even at the reference state $(0, T_r)$ the excess free energy is non-zero:

$$\begin{aligned} Z_{bi}(0,T_r) &= \frac{N!}{N_A!N_B!} Z_{id}(0,T_r) \\ A(0,T_r) &= A_{id}(0,T_r) + A_{ex}(0,T_r) \\ A_{ex}(0,T_r) &= -T_r \ln\left(\frac{N!}{N_A!N_B!}\right) \end{aligned} \tag{2.37}$$

2. The *excess* free energy $A_{ex}(\rho, T_r)$ at the target density (ρ) and the high reference temperature (T_r) is obtained by integrating the excess pressure P_{ex} along the isotherm at T_r. The integration is done in the present thesis

numerically by $n-$point Gaussian quadrature [80] (with n usually 10).

$$\begin{aligned} P_{ex} &= \rho^2 \left(\frac{\partial (A_{ex}/N)}{\partial \rho} \right)_{N,T} \\ &= P - P_{id} \\ A_{ex}(\rho, T_r) - A_{ex}(0, T_r) &= N T_r \int_0^{\rho} d\rho \left(\frac{\beta_r P}{\rho^2} - \frac{1}{\rho} \right) \end{aligned} \tag{2.38}$$

3. Then the *excess* free energy $A_{ex}(\rho, T)$ at the target temperature (T) is obtained by integrating the potential energy from T_r to T along the isochore at ρ.

$$\begin{aligned} U(N) &= \left(\frac{\partial (\beta A_{ex})}{\partial \beta} \right)_{N,\rho} \\ A_{ex}(\rho, T) &= T \left(\beta_{ref} A_{ex}(\rho, T_{ref}) + \int_{\beta_{ref}}^{\beta} d\beta' U(\rho, \beta') \right) \end{aligned}$$

The temperature dependence of potential energy is empirically obtained by fitting to the Rosenfeld-Tarazona scaling form [78] $U(\rho, T) = a + bT^c$:

4. Finally, the total free energy $A(\rho, T)$ is obtained by adding the ideal gas free energy at the target density and temperature (ρ, T) :

$$\begin{aligned} A(\rho, T) &= A_{ex}(\rho, T) + A_{id}(\rho, T) \\ A_{id}(\rho, T) &= NT \left(D \ln \Lambda + \ln \rho - 1 \right) \\ \Lambda &= \frac{h}{\sqrt{2\pi T}} \end{aligned}$$

Here Λ is the thermal de Broglie wavelength, D is the space dimension and h is Planck's constant. In the reduced Argon unit for energy, length and time $h = 0.1856$ (shown below).

5. The total (or bulk) entropy S_{total} at the target density and temperature (ρ, T) is obtained by taking derivative of the free energy or equivalently

using the relation $S_{total} = \frac{U-A}{T}$

$$\begin{aligned}
S_{total} &= -\frac{\partial A(\rho,T)}{\partial T} \\
\frac{\partial A(\rho,T)}{\partial T} &= N(d\,\ln\Lambda + \ln\rho - 1) + \beta_r A_{ex}(\rho,T_r) \\
&\quad +N\left(a(\beta-\beta_r) + \frac{b}{1-c}\left(\beta^{1-c} - \beta_r^{1-c}\right)\right) \\
&\quad -\frac{Nd}{2} - \frac{N}{T}\left(a + b\beta^{-c}\right) \\
\frac{\partial A(\rho,T)}{\partial T} &= \frac{A(\rho,T)}{T} - \frac{E(\rho,T)}{T} - \frac{Nd}{2}
\end{aligned}$$

6. If one is interested to compute the free energy of the stable phase, then one must be careful to choose the path of integration such that there should be no *first order phase transition* at any points along the path. This is because at a first order transition point the derivative of the Helmholtz free energy $S = -\frac{\partial A(\rho,T)}{\partial T}$ is discontinuous due to the latent heat of transformation.

Value of the Planck's constant in Argon unit Let h and h^* be the magnitude of Planck's constant in SI and in Argon units respectively. Let $m^*, \epsilon^*, \sigma^*, \tau^*$ be the Argon units for mass, energy, length and time respectively. $\tau^* = \sqrt{\frac{m^*}{\epsilon^*}}\sigma^*$. Conversion factors are taken from [79], page 42.

$$\begin{aligned}
h \times Js &= h^* \times \epsilon^*\tau^* \\
&= h^* \times \epsilon^* \sqrt{\frac{m^*}{\epsilon^*}}\sigma^* \\
&= h^* \times \sigma^* \sqrt{m^*\epsilon^*} \\
&= h^* \times 0.3405 \times 10^{-9} m \times \sqrt{0.03994 \frac{kg}{mol} \times (k_B \times 119.8K)} \\
6.626 \times 10^{-34} Js &= h^* \times 35.6519 \times 10^{-34} \times Js \\
h^* &= \frac{6.626}{35.6519} \simeq 0.186
\end{aligned}$$

2.3 Model definitions and simulation details

2.3.1 Kob Andersen model (two, three and four dimensions)

The binary mixture ($A_{80}B_{20}$) of Lennard Jones particles introduced by Kob and Andersen [173] is a model glass forming liquid in three dimensions. The interaction potential of Kob-Andersen model (with correction terms that make both potential and force to go to zero smoothly at the cutoff) is given by

$$\begin{aligned} V_{\alpha\beta}(r) &= 4\epsilon_{\alpha\beta}\left[\left(\frac{\sigma_{\alpha\beta}}{r}\right)^{12} - \left(\frac{\sigma_{\alpha\beta}}{r}\right)^{6}\right] + 4\epsilon_{\alpha\beta}\left[c_0 + c_2\left(\frac{r}{\sigma_{\alpha\beta}}\right)^{2}\right], r_{\alpha\beta} < \text{cutoff} \\ &= 0, r_{\alpha\beta} > \text{cutoff} \end{aligned} \tag{2.39}$$

where $\alpha, \beta \in \{A, B\}$ and $\epsilon_{AA} = 1.0$, $\epsilon_{AB} = 1.5$, $\epsilon_{BB} = 0.5$, $\sigma_{AB} = 0.80$, $\sigma_{BB} = 0.88$. Units of length, energy and time scales are $\sigma_{AA}, \epsilon_{AA}$ and $\sqrt{\frac{\sigma_{AA}^2}{\epsilon_{AA}}}$ respectively. $c_0 = -7\left(\frac{\sigma_{\alpha\beta}}{r_{cutoff\alpha\beta}}\right)^{12} + 4\left(\frac{\sigma_{\alpha\beta}}{r_{cutoff\alpha\beta}}\right)^{6} = 0.016266559$ and $c_2 = 6\left(\frac{\sigma_{\alpha\beta}}{r_{cutoff\alpha\beta}}\right)^{14} - 3\left(\frac{\sigma_{\alpha\beta}}{r_{cutoff\alpha\beta}}\right)^{8} = -0.001949974$ are correction terms to make the potential and force continuously go to zero at cutoff. The interaction potential was cutoff at $2.5\sigma_{\alpha\beta}$. NVT MD simulations were done in square (2D), cubic (3D) and hypercubic (4D) box with periodic boundary conditions in canonical (NVT) ensemble for a range of densities and temperatures and for different system sizes.

2.3.2 Modified Kob Andersen model ($A_{65}B_{35}$) (two dimensions)

In the original Kob-Andersen (KA) model in three dimensions, the composition taken was $A = 80\%; B = 20\%$. In the modified KA model in two dimensions, the composition is set to $A = 65\%; B = 35\%$ (ref: [174]). The interaction potential of Kob-Andersen model (with correction terms that make both potential and force to go to zero smoothly at the cutoff) remains the same:

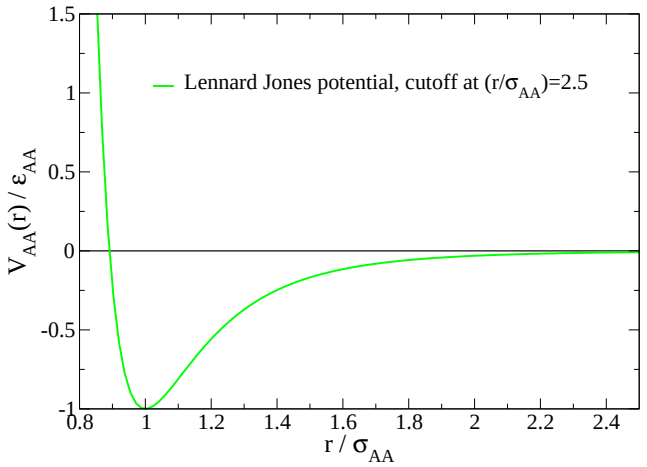

Figure 2.6: The interaction potential of the KA model($A-A$ pairs)

$$V_{\alpha\beta}(r) = 4\epsilon_{\alpha\beta}\left[\left(\frac{\sigma_{\alpha\beta}}{r}\right)^{12} - \left(\frac{\sigma_{\alpha\beta}}{r}\right)^{6}\right] + 4\epsilon_{\alpha\beta}\left[c_0 + c_2\left(\frac{r}{\sigma_{\alpha\beta}}\right)^2\right], r_{\alpha\beta} < \text{cutoff}$$
$$= 0, r_{\alpha\beta} > \text{cutoff} \quad (2.40)$$

where $\alpha, \beta \in \{A, B\}$ and $\epsilon_{AA} = 1.0$, $\epsilon_{AB} = 1.5$, $\epsilon_{BB} = 0.5$, $\sigma_{AB} = 0.80$, $\sigma_{BB} = 0.88$. Units of length, energy and time scales are $\sigma_{AA}, \epsilon_{AA}$ and $\sqrt{\frac{\sigma_{AA}^2}{\epsilon_{AA}}}$ respectively. The interaction potential was cutoff at $2.5\sigma_{\alpha\beta}$. MD simulations were done in a 2D square box with periodic boundary conditions in canonical (NVT) ensemble. The integration time step was in the range $dt = 0.001 - 0.006$. Temperatures were kept constant using Brown and Clarke algorithm [177]. Simulations were done at a fixed number density $\rho = 1.20$ for a range of temperatures and different system sizes.

2.3.3 $R10$ model (two dimensions)

It is a model of 50 : 50 binary mixture of repulsive soft disks in two dimensions. This model was used to study mechanical properties of amorphous solids [171]. The interaction potential is

$$\begin{aligned} V_{\alpha\beta}(r) &= \epsilon\left[\left(\frac{\sigma_{\alpha\beta}}{r}\right)^{10}\right] + \epsilon\left[\sum_{l=0}^{2} c_{2l}\left(\frac{r}{\sigma_{\alpha\beta}}\right)^{2l}\right], r < \text{cutoff} \\ &= 0, r > \text{cutoff} \end{aligned} \tag{2.41}$$

where $\alpha, \beta \in \{A, B\}$ and $\epsilon = 1.0$; $\sigma_{AA} = 1.0$, $\sigma_{BB} = 1.40$, $\sigma_{BB} = 1.18 \neq \frac{\sigma_{AA}+\sigma_{BB}}{2}$; $c_0 = -0.806140903539923$, $c_2 = 0.7$, $c_4 = -0.156300219287607$. c_0, c_2, c_4 represent the correction to make the potential vanish at cutoff continuously upto the second derivative. Units of length, energy and time scales are σ_{AA}, ϵ and $\sqrt{\frac{\sigma_{AA}^2}{\epsilon_{AA}}}$ respectively. The interaction potential was cutoff at $1.385418025\sigma_{\alpha\beta}$. The cutoff is smaller than the other two dimensional models (Kob-Andersen and $R12$ model) used in the present thesis. Hence this model is faster to simulate.

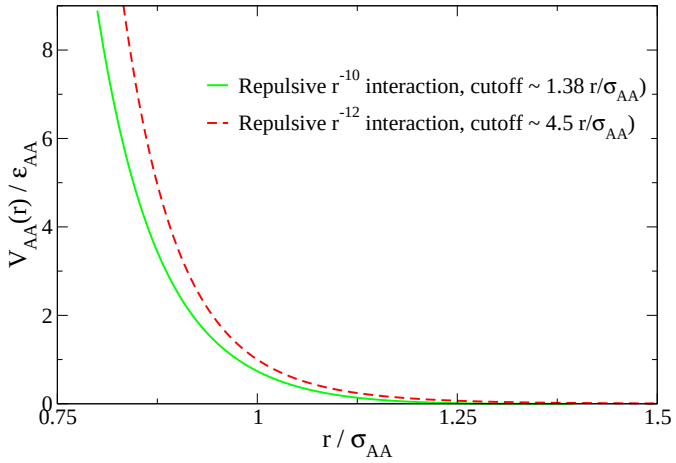

Figure 2.7: The interaction potential ($A - A$ pairs) of the $R10$ and $R12$ models including cutoff corrections.

2.3.4 $LJ(p, q)$ models (three dimensions)

This family of models are binary mixtures of modified Lennard Jones particles in three dimensions. The interaction potential is

$$
\begin{aligned}
V_{\alpha\beta}(r) &= \frac{\epsilon_{\alpha\beta}}{q-p}\left[p\left(\frac{r_{\alpha\beta}^{min}}{r}\right)^q - q\left(\frac{r_{\alpha\beta}^{min}}{r}\right)^p\right] + c_1 r^2 + c_2 \qquad r < r_c = 2.5\sigma_{\alpha\beta} \\
&= 0, \qquad \text{otherwise} \\
c_1 &= \epsilon_{\alpha\beta}\frac{pq}{2(q-p)}\frac{1}{r_c^2}\left[\left(\frac{r_{\alpha\beta}^{min}}{r_c}\right)^q - \left(\frac{r_{\alpha\beta}^{min}}{r_c}\right)^p\right] \\
c_2 &= \frac{\epsilon_{\alpha\beta}}{q-p}\left[-\left(p+\frac{pq}{2}\right)\left(\frac{r_{\alpha\beta}^{min}}{r_c}\right)^q + \left(q+\frac{pq}{2}\right)\left(\frac{r_{\alpha\beta}^{min}}{r_c}\right)^p\right]
\end{aligned} \tag{2.42}
$$

where c_1, c_2 are used to make potential and force to smoothly go to zero at cutoff and are determined from the conditions :

$$
\begin{aligned}
V_{\alpha\beta}(r_c) &= 0 \\
\left(\frac{dV_{\alpha\beta}}{dr}\right)_{r_c} &= 0
\end{aligned} \tag{2.43}
$$

$\alpha, \beta \in \{A, B\}$ and $r_{\alpha\beta}^{min} = 2^{\frac{1}{6}}\sigma_{\alpha\beta}$ and $\epsilon_{\alpha\beta}$ are respectively the position and the value of the minimum of the pair potential. Units of length, energy and time scales are $\sigma_{AA}, \epsilon_{AA}$ and $\sqrt{\frac{\sigma_{AA}^2}{\epsilon_{AA}}}$ respectively ([133]). In this unit, $\epsilon_{AB} = 1.5$, $\epsilon_{BB} = 0.5$, $\sigma_{AB} = 0.80$, $\sigma_{BB} = 0.88$. The interaction potential was cutoff at $2.5\sigma_{\alpha\beta}$ ([133]). The potential is designed so that for the choice $(q = 12, p = 6)$, it reduces to Kob-Andersen model.

MD simulations were done in a 3D cubic box with periodic boundary conditions using canonical (NVT) ensemble. The integration time step was in the range $dt = 0.001 - 0.005$. Temperatures were kept constant using the Brown and Clarke algorithm [177]. Simulations were done in the temperature range $T \in [0.85, 5]$ for the $LJ(12, 11)$ model; $T \in [0.45, 5]$ for the $LJ(12, 6)$ model and $T \in [0.23, 5]$ for the $LJ(8, 5)$ model respectively. System size were $N = 1500, N_A = 1200$ (N = total no. of particle, N_A = no. of particles of species A) and the number density was $\rho = 1.2$ ([133]). For all models, one sample per state point above the onset temperature (described below) and three to five samples per state points below the onset temperature were used with runlengths $> 100\tau_\alpha$ (τ_α is the relaxation time).

Chapter 3

The Adam-Gibbs relation for glass-forming liquids in 2,3 and 4 dimensions

3.1 Introduction

One of the central questions about glass-forming liquids is to satisfactorily explain the behaviour of relaxation times *over the entire range of temperature* where they are observed. At high temperatures (typically above the melting point), relaxation times obey the Arrhenius law:

$$\ln \tau(T) = \ln \tau(\infty) + \frac{E_0}{k_B T} \tag{3.1}$$

which may be understood in terms of a transition probability between two states separated by an energy barrier ('activation energy') E_0 which is independent of temperature. However, as the temperature is lowered, many glass-forming liquids show faster than exponential rise in relaxation times [6–8]. Various theories of relaxation times have been put forward to explain the super-exponential behaviour. The present study focusses on the predictions of the Adam Gibbs theory (AG) and the random first order transition theory (RFOT). According to the AG picture (see Chapter 1), the increase in the relaxation time with temperature is due to the corresponding decrease in the

configurational entropy $S_c(T)$ of the liquid :

$$\begin{aligned} \ln \tau(T) &= \ln \tau(\infty) + \frac{S^* \delta\mu}{k_B T S_c(T)} \\ &= \ln \tau(\infty) + \frac{C}{T S_c} \end{aligned} \tag{3.2}$$

where S^* is the configurational entropy of a cooperatively rearranging region (CRR) and assumed to be a material constant; $\delta\mu$ is the chemical potential difference between the two states involved in rearrangement and $S_c(T)$ is the configurational entropy per particle of the system.

The AG relation has been extensively tested in the past [41–45, 48, 49, 128]. One of the prototype glass-forming liquids in which AG relation is shown to be valid [67, 128] is the Kob-Andersen model (KA) [173]. In Fig. 3.1 the AG relation is shown for this model in three dimensions over several orders of magnitude in relaxation times with many system sizes.

Although the AG theory is well-known and well-tested but it is not well-understood. There are several ad-hoc assumptions which make the theory less rigorous. One of the attempts to improve upon the ideas of Adam and Gibbs is the random first order transition theory (RFOT) of glass transition [39, 40]. Although both are entropy-based theories, the details of the underlying physical picture differ. Here we focus on one particular aspect: whether the relation between configurational entropy and relaxation time is same or different in different spatial dimensions.

As a consequence of the AG assumption that the configurational entropy of a CRR S^* is a constant independent of the size of a CRR, the free energy barrier of rearrangement $\Delta G = z^* \delta\mu = \frac{S^* \delta\mu}{S_c}$ (z^* = the smallest possible size (number of particles) of a CRR) becomes independent of the size of the rearranging region. Hence, the Adam Gibbs relation is expected to be same in all spatial dimensions. In order to test this, simulations were done in the KA model in two dimensions and it was found that there is a systematic deviation (Fig 3.2) from the prediction of AG relation as the relaxation time increases. The α relaxation time in KA model in both two and three dimensions increases as system size decreases [67]; so this deviation occurs as the temperature is lowered and the system size is decreased.

In the RFOT scenario, there is a *possibility* of explicit dimension dependence

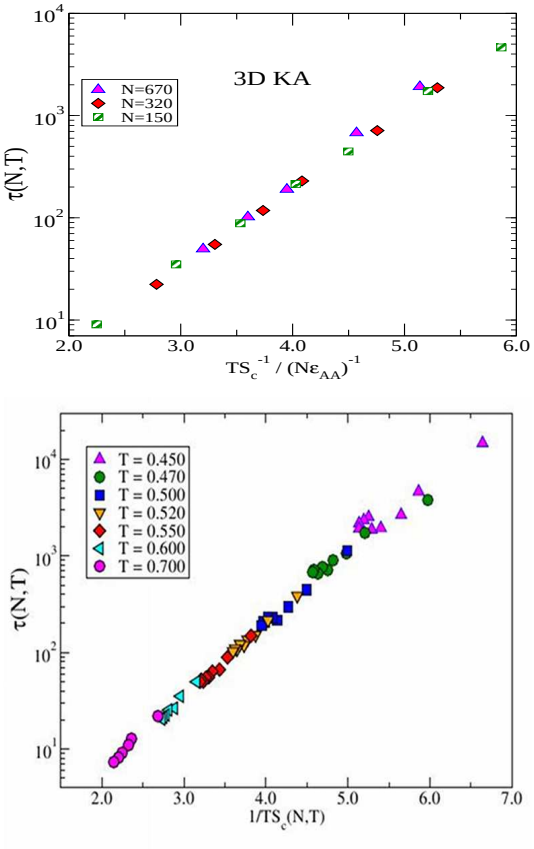

Figure 3.1: Adam Gibbs relation is valid in the KA model in three dimensions. Color code : Top fig : State points at same system size but different temperatures have same colour. Bottom fig: State points at same temperature for different system sizes have same color. [Data taken with permission from Dr. S. Karmakar.

(see Chapter 1) :

$$\begin{aligned} \ln \tau(T) &= \ln \tau(\infty) + \frac{A\xi^{\psi}}{k_B T} \\ &= \ln \tau(\infty) + \frac{A}{k_B T} \left(\frac{Y}{T S_c} \right)^{\frac{\psi}{D-\theta}} \end{aligned} \tag{3.3}$$

Even though the spatial dimension D explicitly appears in Eqn. 3.3, it does not necessarily mean that the RFOT prediction is inconsistent with the AG relation owing to the presence of the two unknown exponents θ and ψ. If one ignores the temperature dependent prefactor $\frac{A}{k_B T}$, then Eqns. 6.4 and 3.3 will be mutually consistent if $\frac{\psi}{D-\theta} = 1$. In the original formulation of the

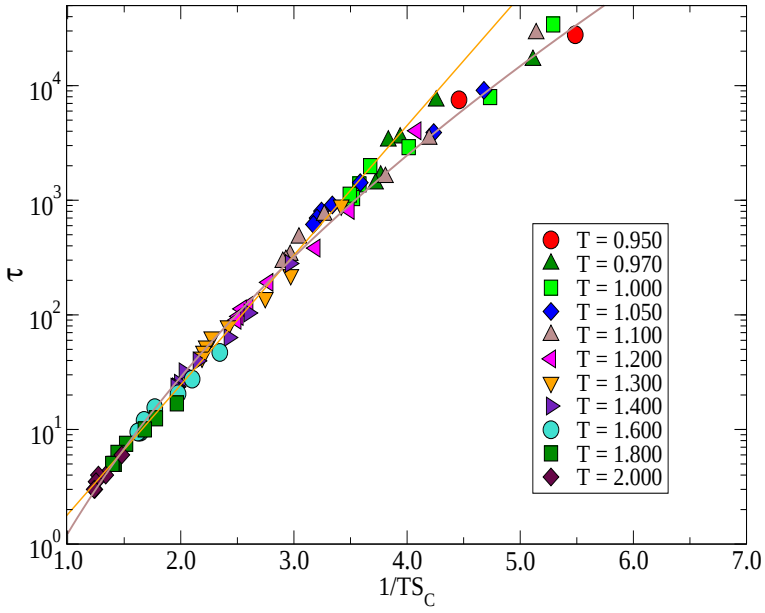

Figure 3.2: Systematic deviation from Adam Gibbs relation in KA model in two dimensions. [Data taken with permission from Dr. S. Karmakar]

AG theory, no exponent is introduced. However, according to the AG theory, $\Delta G(T) \propto z^*$. If one replaces z^* by the characteristic linear dimension (ξ^*) of a CRR by assuming $z^* \propto (\xi^*)^D$ then one gets $\psi_{AG} = D$ and consequently from the condition $\frac{\psi}{D-\theta} = 1$, $\theta_{AG} = 0$. In the formulation of the RFOT as entropy-driven nucleation by Wolynes *et al.*, $\psi = \theta$. However, in the Bouchaud and Biroli picture [40] θ and ψ are independent exponents and $\psi \neq \theta$ in general. Wolynes *et al.* further argued [39, 60] that $\psi = D/2$ in D dimensions. Thus the original RFOT prediction, although differs from the Adam Gibbs theory about the values of the exponents, is consistent with the Adam Gibbs relation. However, attempts to calculate the exponents either in real systems or models does not present a conclusive picture. By direct simulation in a model, Cammarota *et al.* obtained $\theta = 2, \psi = 1$ [60] which although consistent with AG relation, differs from both the AG and the RFOT predictions. Independent simulation study in a different model by Karmakar [51] obtained $\theta \sim 2.3$ and hence $\psi \sim 0.7$ using the condition $\frac{\psi}{D-\theta} = 1$. A more extensive study by Capaccioli *et al.* [59] of 45 glass-forming liquids show a lot of variation in both θ and ψ [$\theta \sim 1.8 - 2.6$, $\psi \sim 0.3 - 1.5$] owing to considerable numerical uncertainties and hence is not conclusive about the exponent $\frac{\psi}{D-\theta}$. The available exponent values are summarized in the Table 3.1.

In view of all the difficulties associated with determining the RFOT exponents directly, the possibility of an explicit dimension dependence of the AG relation can not be ruled out. Here we address the question of the dimension dependence of the Adam Gibbs relation by a different route, namely, by study of models in different (two to four) spatial dimensions. The strategy of exploring different dimensions is particularly suitable to simulation and at the same time offers a stringent check on both the Adam Gibbs relation (Eqn. 6.4) and the range of allowed values of the RFOT exponents.

Source	**AG exponent** $\frac{\psi}{D-\theta}$	θ	ψ	$\frac{\psi}{\theta}$
AG prediction	1	0	D=3	
RFOT prediction	1	$\frac{D}{2} = 1.5$	$\frac{D}{2}$	
Capaccioli *et al.* [59]	0.6-3.25	1.8-2.6		0.4-0.5
Cammarota *et al.* [60]	1	2	1	
Cavagna *et al.* [61]			1.41	
Franz [62]		2		
Karmakar [51]	1	2.3	0.7	

Table 3.1: The RFOT Exponents θ and ψ from the literature. All values are for three dimensional systems. Note that the definition of ψ used in [59] is different from [40], [60] and [61]. Ref. [59] called the exponent $\theta\psi$ what Refs. [40], [60] and [61] called ψ. Here the definition of Ref. [40] is followed. The scaling relations are $\xi \propto \frac{1}{TS_c}^{\frac{1}{D-\theta}}$; $\tau \propto \exp\left(\frac{\xi}{T}\right)^{\psi}$; $\tau \propto \exp\left(\left(\frac{1}{TS_c}\right)^{\frac{\psi}{D-\theta}}\right)$. Using these definitions, the exponent ψ reported in Ref. [59] becomes $\frac{\psi}{\theta}$. Owing to numerical uncertainties in the values of exponents we have not converted the exponent $\frac{\psi}{\theta}$ to our ψ. Ref. [61] calculated only ψ. The value for θ quoted for Ref. [62] is taken from Ref. [59]. We call the ratio $\frac{\psi}{D-\theta}$ the "AG exponent". The values of the AG exponent for Ref. [59] is calculated using $\frac{\left(\frac{\theta}{\psi}\right)\theta}{D-\theta}$, using the extreme values of the exponents reported: $0.6 = \frac{0.4\times1.8}{3-1.8}, 3.25 = \frac{0.5\times2.6}{3-2.6}$. If the Adam Gibbs relation is valid then $\theta + \psi = D$, where D is the spatial dimension.

3.2 Simulation details

We have studied the well-known Kob-Andersen model in 4 dimensions (4D KA), the modifed (different composition) KA model (2D MKA) and the repulsive soft sphere ($V(r) \sim r^{-10}$) model (2D R10) in two dimensions. The

definitions of each model are given in Chapter 2. Molecular dynamics simulations were done with periodic boundary condition in the canonical (NVT) ensemble. Temperatures werekept constant using the Brown and Clarke algorithm [177] (See Chapter 2). The integration time step dt was varied depending on the temperature. Smaller dt was used at higher temperatures. For good statistics, typically 3 (1-3 in 4D, 3-5 in 2D) independent runs of run-length $\geq 100\tau_\alpha$ were performed at each state point. The simulation details are summarized in Table 3.2.

Table 3.2: Simulation details in the Kob-Andersen model in 4 dimensions (4D KA), the modifed (different composition) KA model (2D MKA) and the repulsive soft sphere ($V(r) \sim r^{-10}$) model (2D R10) in two dimensions. See also Chapter 2.

Model	**System size** N	Density	Temperature range	time step (dt) range	Relaxation time range
4D KA	1500	1.60	0.685 - 3.00	0.001 - 0.006	upto $\mathcal{O}(10^4)$
2D MKA	400-10000	1.20	0.40 -6.0	0.001 - 0.005	upto $\mathcal{O}(10^5)$
2D R10	200-10000	0.85	0.46 - 5.0	0.001 - 0.006	upto $\mathcal{O}(10^5)$

3.3 Methods

3.3.1 Choice of density

In supercooled liquids, at low temperatures, a pressure *vs.* density isotherm go through a minimum. This minimum density is called the spinodal density. A spinodal is defined by the condition $\frac{\partial P}{\partial V}|_T = 0$. At a given temperature, the liquid state is unstable (system has negative compressibility) below the spinodal density. The value of the spinodal density increases as the temperature decreases [69]. The pressure calculated from inherent structure trajectories as a function of density also show this minimum which may be thought to correspond to the low temperature limit of the spinodal density. These properties are shown for KA model in 3D in Fig. 3.3. Any simulation of a system in (metastable) liquid state must be performed above the spinodal density.

The densities where simulations are done for different models are given in the Table 3.3.

Table 3.3: Choice of densities for different models (in units of σ_{AA}^3). The density value of the 3D KA model is considered a standard in the literature. The density value of the 2D KA model is taken with permission from [55].

Model	Composition	Simulation Density
4D KA	80:20	1.60
3D KA	80:20	1.20
2D KA	80:20	1.20
2D MKA	65:35	1.20
2D R10	50:50	0.85

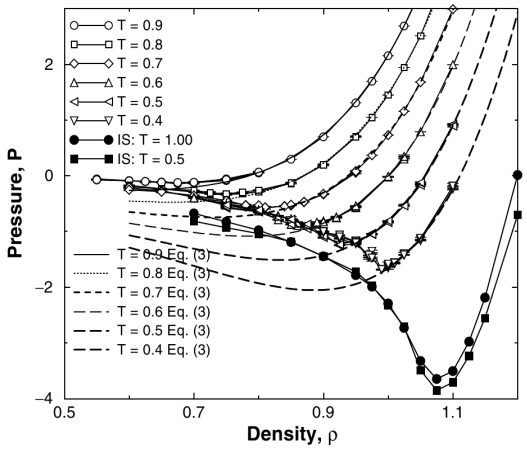

Figure 3.3: The pressure vs. density isotherms go through minima at low temperatures in the 3D KA model. "IS" means inherent structure pressure. Fig. taken with permission from [69].

3.3.2 Characteristic temperature scales

Here we list how the different characteristic temperatures (see Chapter 1) are determined in the present study.

1. T_{onset} : The onset temperatures have been obtained from the Arrhenius plots of the relaxation time ($\ln \tau$ *vs.* $1/T$) as well as from the inverse temperature dependence of the average inherent structure energy.

2. T_{MCT} : We have determined the apparent divergence temperature of the mode coupling theory from the fit $\ln \tau = a_0 - \delta \ln(T - T_{MCT})$.

3. T_{VFT} : The divergence temperature of the Vogel-Fulcher-Tamman (VFT) law is obtained from the fit $\ln \tau = a_0 + \dfrac{A}{T - T_{VFT}}$.

Table 3.4: Characteristic temperatures (in units of $\frac{\epsilon_{AA}}{k_B}$) of different models in 2,3,4 dimensions. The temperature values for the 2D KA model [50] and T_{VFT} for the 3D KA [51] model were obtained with permission from Dr. S. Karmakar. T_K and T_{MCT} for the 3D KA model were taken from [70] and [52] respectively.

Model	Density	T_K	T_{VFT}	T_{MCT}	$\sim T_{onset}$
4D KA	1.60	0.53	0.53	0.65	1.0
3D KA	1.20	0.2976	0.283	0.435	1.0
2D KA	1.20	0.488	0.50	0.94	2.0
2D MKA	1.20	0.251	0.21	0.33	0.8
2D R10	0.85	0.181	0.33	0.43	0.8

4. T_K : The Kauzmann temperature at which the configurational entropy *extrapolates* to zero is determined from the temperature dependence of the average configurational entropy using the condition $S_c(T_K) = 0$.

These characteristic temperatures help to chose the temperature range to simulate, *e.g.* T_{onset} serves as the reference temperature to differentiate the low and the high-T regimes on the temperature axis. The values of different characteristic temperatures for different models are shown in the Table 3.4).

3.3.3 Characteristic time scales

We have computed the following characteristic time scales (see Chapter 2) : (i) the self diffusion coefficient. As the systems studied are binary mixtures, two self diffusion coefficients are possible. The diffusion coefficient of A and B type particles are found to be proportional to each other. Here we always report the diffusion coefficients of the A species. (ii) the α relaxation time is obtained from the decay of the overlap function $q(t)$ using the definition $q(t = \tau_\alpha, T)/N = 1/e$ and the peak time of the dynamical susceptibility $\chi_4(t)$. These two estimates are mutually proportional. In the present study, we have avoided the stretched exponential fit $q(t)/N = A\exp(-(t/\tau(T))^{\beta(T)})$ to determine τ as the fit involves simultaneously determining three unknown parameters, hence expected to be less reliable than the $1/e$ definition.

The characteristic time scales are used to check that the runs are done in equilibrium and long-enough for good statistics by checking at all state points studied that (i) the overlap function has decayed to zero and (ii) the MSD

has entered a diffusive regime ($MDS \propto t$).

3.3.4 Configurational entropy

We have computed the configurational entropy using the potential energy landscape formalism (See Chapter 1). The configurational entropy (S_c) per particle is calculated [69] by subtracting from the total entropy of the system the vibrational component:

$$S_c(T) = S_{total}(T) - S_{basin}(T) \tag{3.4}$$

As a self-consistency check for the implemented method, we have verified that the configurational entropy density $S_c(e_{IS})$ computed at different temperatures fall on the same master curve (for a given system size).

3.4 Characterizations: the Kob - Andersen model in 4D

3.4.1 Choice of density for the 4D KA model

For KA model in 4D, the pressure and inherent structure pressure isotherms at a very low temperature $T = 0.5$ are shown in Fig. 3.4. The spinodal density is $\rho \sim 1.4$. The simulation density is chosen to be $\rho = 1.6$ which is safely above this value.

3.4.2 Characteristic time scales of the 4D KA model

The temperature dependence of the MSD of A type particles (majority component) and the overlap function have been shown in Figs. 3.5 and 3.6 respectively. They show that as the temperature decreases, the relaxation process gradually slows down and the relaxation time increases. However, the MSD is well into diffusive regime and overlap function decays to zero from which it may be concluded that runs are long enough for measurement. In Fig. 3.7 temperature dependence of $\chi_4(t)$ is plotted which show that $\chi_4(t) \to 0$ at

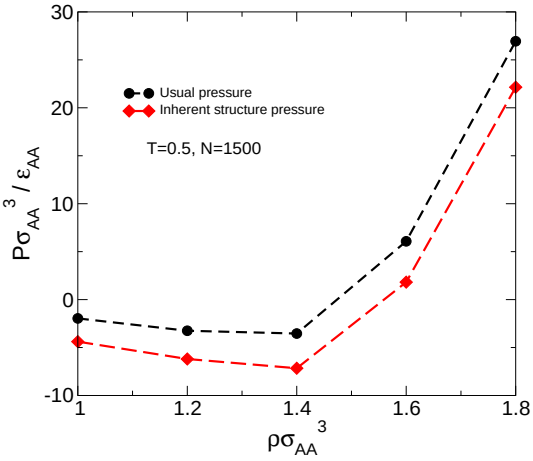

Figure 3.4: The inherent structure pressure as a function of density goes through a minimum in the 4D KA model. The simulation density (= 1.6) is chosen in the region where the inherent structure pressure is greater than the minimum.

both small and large time limit and goes through a maximum at an intermediate time. Also the peak height increases with temperature. The relaxation times extracted from $q(t)$ using the definition $q(t = \tau_\alpha, T)/N = 1/e$ is found to be always higher than the dynamical heterogeneity time scale obtained from $\chi_4(t)$ peak time. However, these two time scales are proportional to each other as shown in Fig. 3.8.

3.4.3 Characteristic temperature scales of the 4D KA model

For the KA model in 4D, the crossover from the Arrhenius to the non-Arrhenius behaviour occurs at $T_{onset} \sim 1.0$ as shown in Fig. 3.9. The inverse T dependence of the inherent structure energy in Fig. 3.9 shows that the change of system dynamics from landscape-independent to landscape-influenced regime also occur at around the same $T_{onset} \sim 1.0$. The VFT and the MCT fits to relaxation times are shown in Fig. 3.10. We find that the quality of VFT fit is marginally better than that of MCT fit. The Kauzmann temperature is determined from the *extrapolated* T-dependence of configurational entropy as shown in Fig. 3.11. The values of different characteristic temperatures are tabulated in Table 3.4.

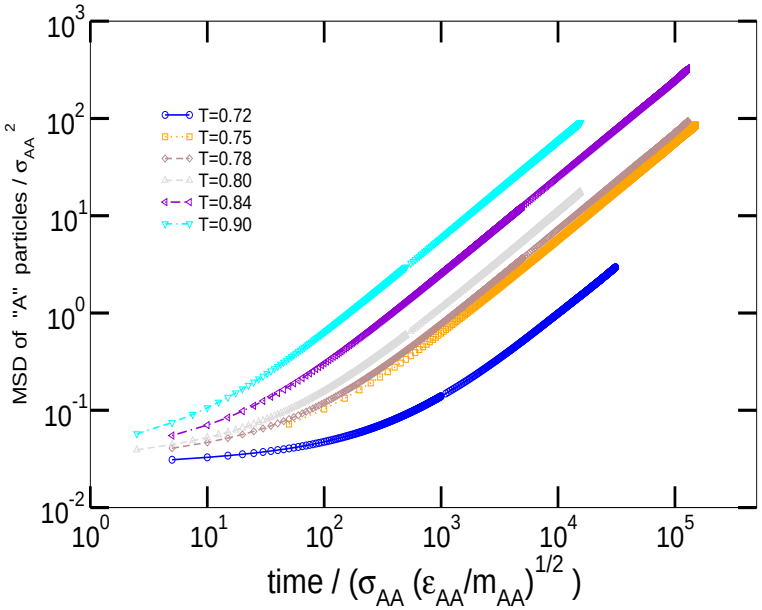

Figure 3.5: Temperature dependence of the mean squared displacement for the A species of the Kob-Andersen model in four dimensions

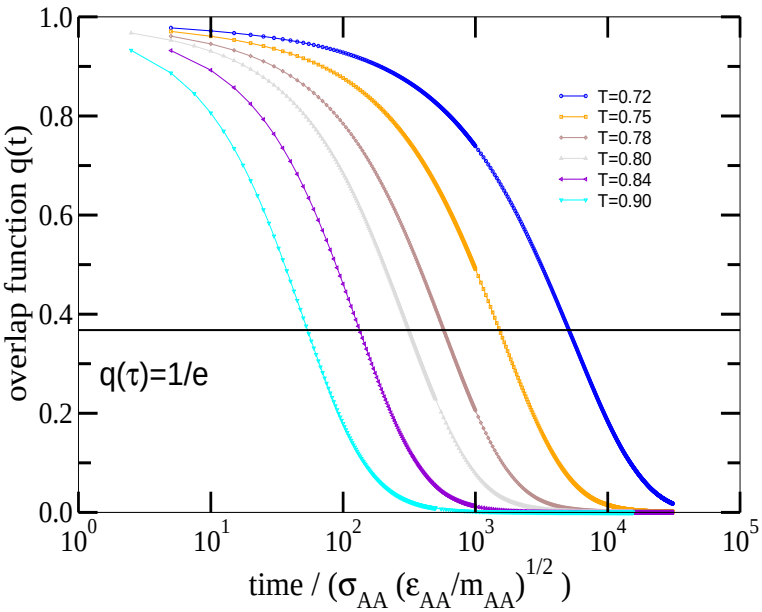

Figure 3.6: Temperature dependence of the overlap function of the Kob-Andersen model in four dimensions.

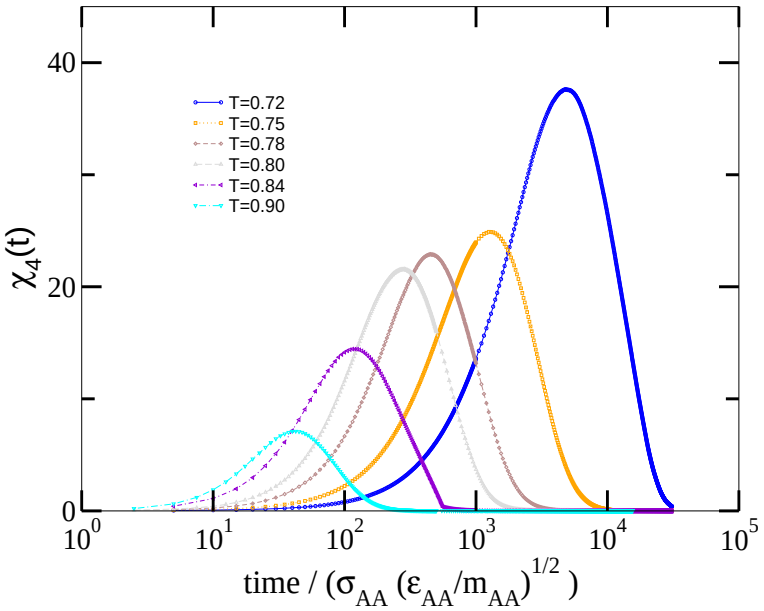

Figure 3.7: Temperature dependence of the dynamical susceptibility $\chi_4(t)$ of the Kob-Andersen model in four dimensions.

3.4.4 The configurational entropy of the 4D KA model

The total entropy: To calculate the configurational entropy from Eqn. 6.1, one needs to know the total (or bulk) entropy ($S_{total}(\rho, T)$) of the system which is computed from the total (or bulk) free energy *via* the thermodynamic integration (See Chapter 2). The pressure *vs.* density isotherms at the reference high T_{ref} and temperature dependence of potential energy (isochore) are shown in Fig. 3.12. To validate the calculation, we check in Figs. 3.13 and 3.14 that the values of the free energies and the entropies are independent of the choice of the T_{ref} by using two different reference high temperatures.

The basin and the configurational entropy: The basin entropy is computed in the harmonic approximation (see Chapter 2). The configurational entropy $S_c(T)$ is computed as the difference [Eqn. 6.1] of the total and the basin entropy. The temperature dependences are shown in Figs. 3.15, 3.16 and 3.11.

The configurational entropy density: By definition, the configurational entropy density $S_c(e_{IS})$ is independent of temperature (see Chapter 2). Hence

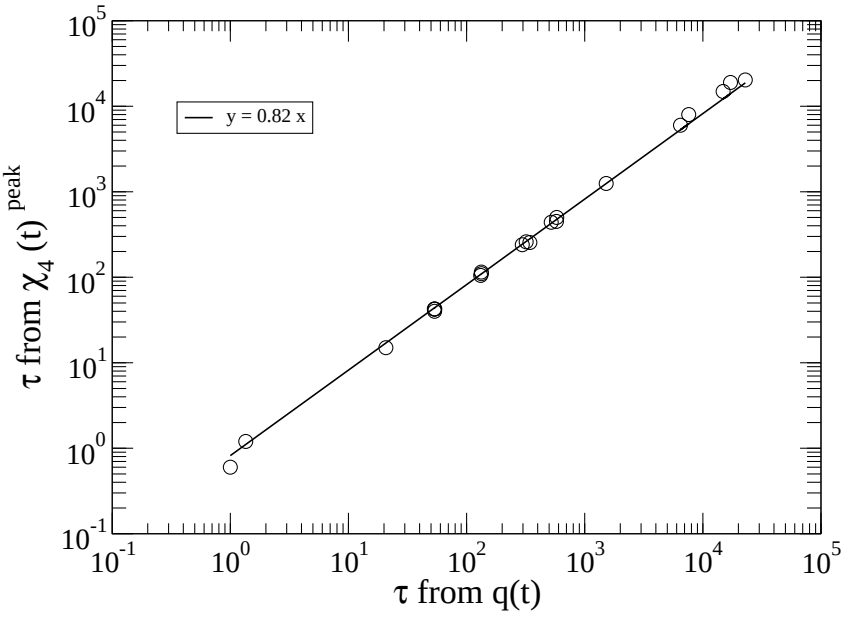

Figure 3.8: The relaxation times obtained from the $q(t)$ and the χ_4^{peak} are proportional to each other.

$S_c(e_{IS})$ calculated at different temperatures should fall on the same master curve. This is verified in Fig. 3.17 as a self-consistency check on the calculation.

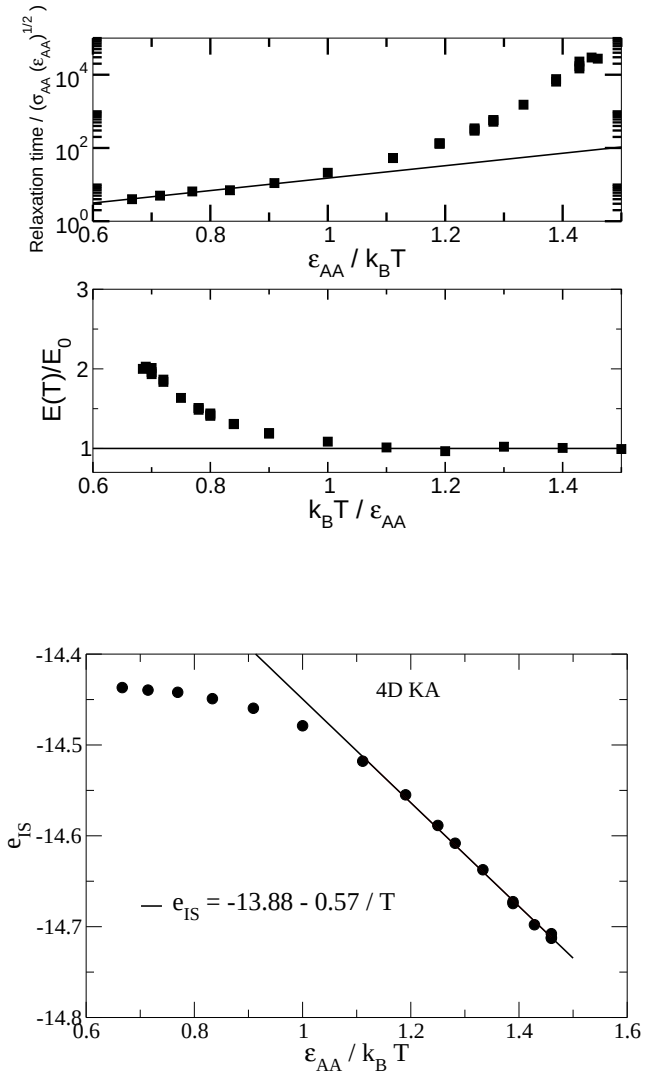

Figure 3.9: Top Fig: The temperature dependence of the α relaxation time shows crossover from the Arrhenius to the super-Arrhenius behaviour at a temperature $T_{onset} \sim 1.0$ in the Kob-Andersen model in 4D. The Adam Gibbs relation is tested below this temperature. The solid straight line in the upper panel is the Arrhenius fit above T_{onset}. $E(T) = T \ln \frac{\tau}{\tau_\infty}$ is the temperature dependent activation energy. E_0 is the high temperature activation energy where Arrhenius law is valid. Bottom Fig: The temperature dependence of average inherent structure energy $e_{IS}(T)$ sampled by the system also shows cross-over at around $T \sim 1.0$.

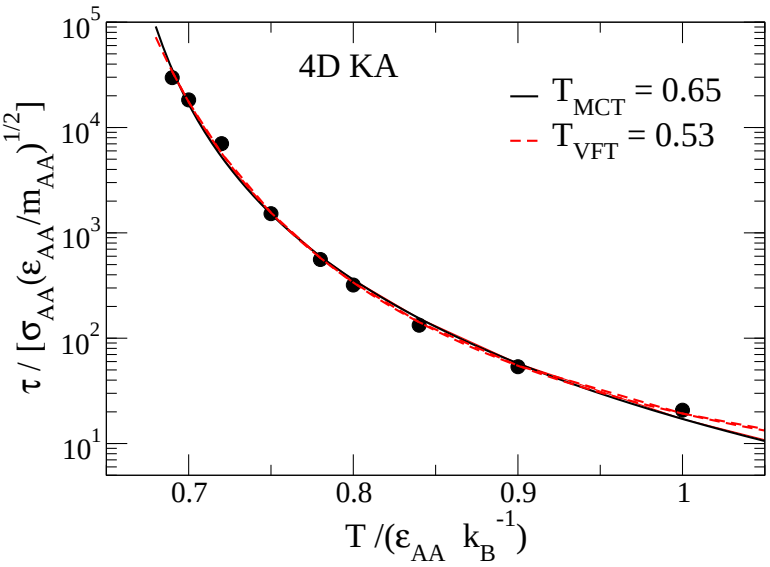

Figure 3.10: α relaxation times for the 4D KA model fitted to the mode coupling theory prediction and the VFT formula taking temperature range upto T_{onset}.

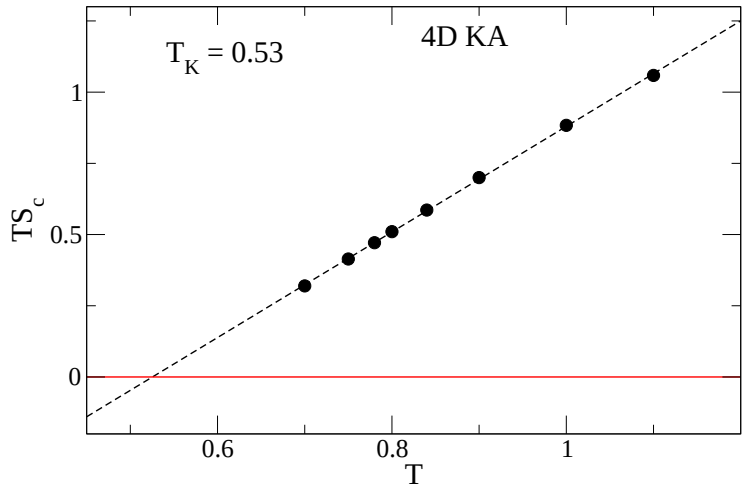

Figure 3.11: Kauzmann temperature for the 4D KA model is $T_K = 0.53$. It is calculated from the condition $TS_c(T_k) = 0$.

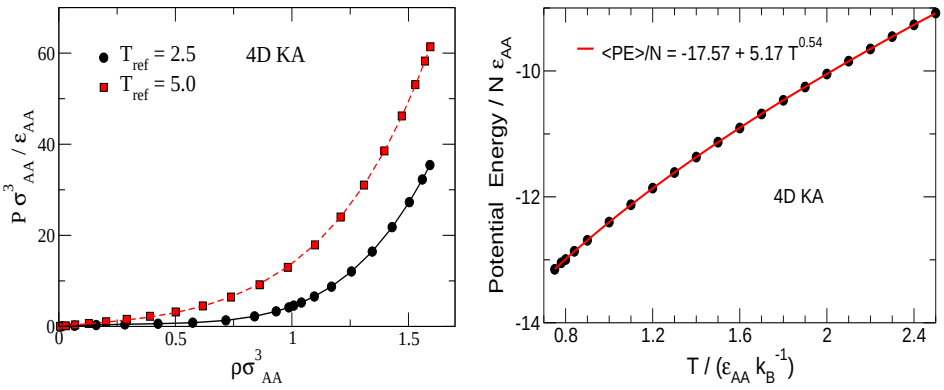

Figure 3.12: Left fig: The pressure *vs.* density isotherm at reference high temperatures ($T = 2.5, 5.0$). Right Fig: The average potential energy *vs.* temperature at the density = 1.6. The line is a fit of the form $PE = a + bT^c$.

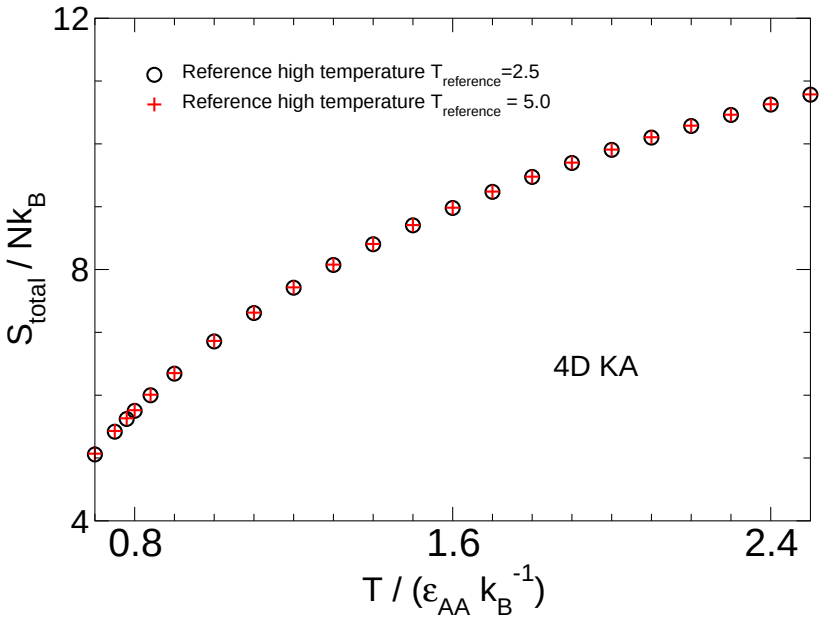

Figure 3.13: The temperature dependence of the total (or bulk) entropy for the 4D KA model. We check that the total entropy values are independent of the choice of the reference high temperature by using two different reference high temperatures.

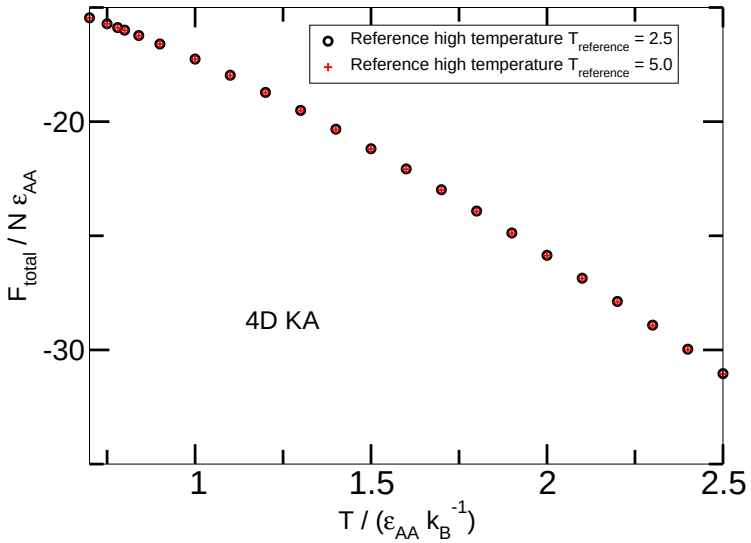

Figure 3.14: The temperature dependence of the total (or bulk) free energy for the 4D KA model. We check that the total entropy values are independent of the choice of the reference high temperature by using two different reference high temperatures.

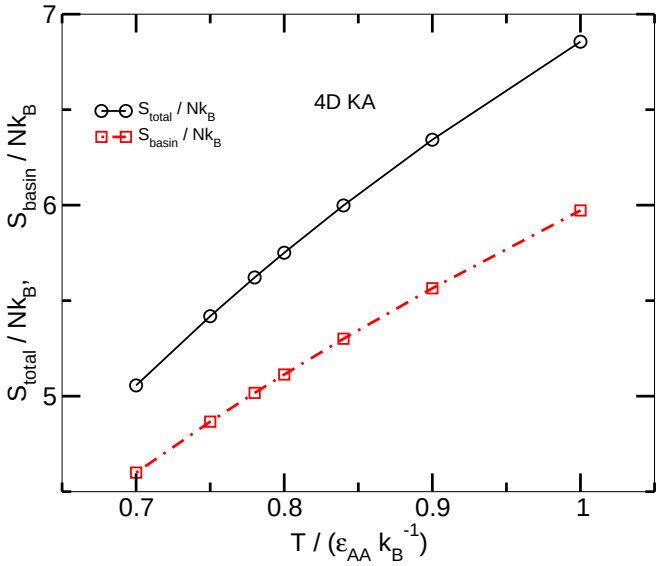

Figure 3.15: T dependences of the total and the basin entropy at low T (at and below the onset Temperature) for the 4D KA model. At any given temperature, the difference is an estimate of the configurational entropy at that temperature.

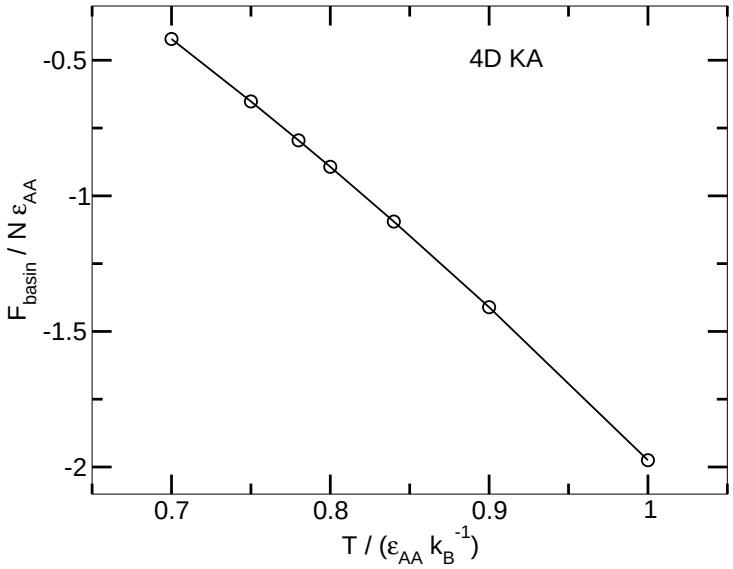

Figure 3.16: T dependence of the basin free energy at low T (at and below the onset Temperature) for the 4D KA model.

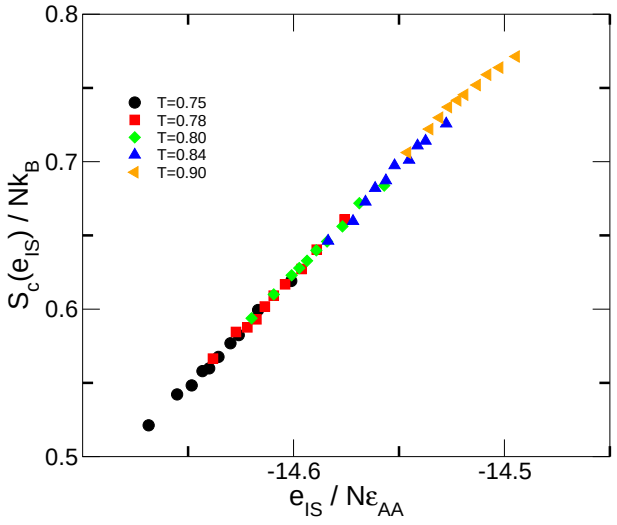

Figure 3.17: The configurational entropy densities $S_c(e_{IS})$ of inherent structure calculated at different temperature for the 4D KA model show good overlap with each other.

3.5 Characterizations: the modified Kob-Andersen model in 2D

3.5.1 Choice of density for the 2D MKA model

The modified KA model at 65 : 35 composition was introduced by Brüning *et al.* [173] as a way to avoid crystallization in two dimensions. They chose the number density ≈ 1.16 such that pressure tends to become zero at zero temperature when cooling at a constant rate. In order to change as few parameters as possible, we have kept the density to be same as in the canonical composition 80 : 20 of KA model in three dimensions. Consequently, we have simulated the MKA model at the number density = 1.20.

3.5.2 Characteristic time scales of the 2D MKA model

The overlap function and the mean squared displacement: The temperature dependences of the overlap function and the MSD of A particles for the 2D MKA 65 : 35 model are shown for system size $N = 2000$ in Fig. 3.18. We check for good statistics that each run is long enough so that (i) the overlap function decays to zero and (ii) the MSD is well into the diffusive regime.

System size dependence of the relaxation time: We show in Fig. 3.19 the system size dependence of α relaxation time in 2D MKA 65 : 35 model, for later use to compute static length scales. In the case of the KA model in 3D, it has been found [67] that α relaxation time *increases* as system size *decreases*. The same behaviour is observed in the 2D MKA 65 : 35 model implying this system size dependence to be a characteristic of the α relaxation. We also show for future reference the τ *vs.* $1/N$ plot to extract the relaxation time in the limit of infinite system size.

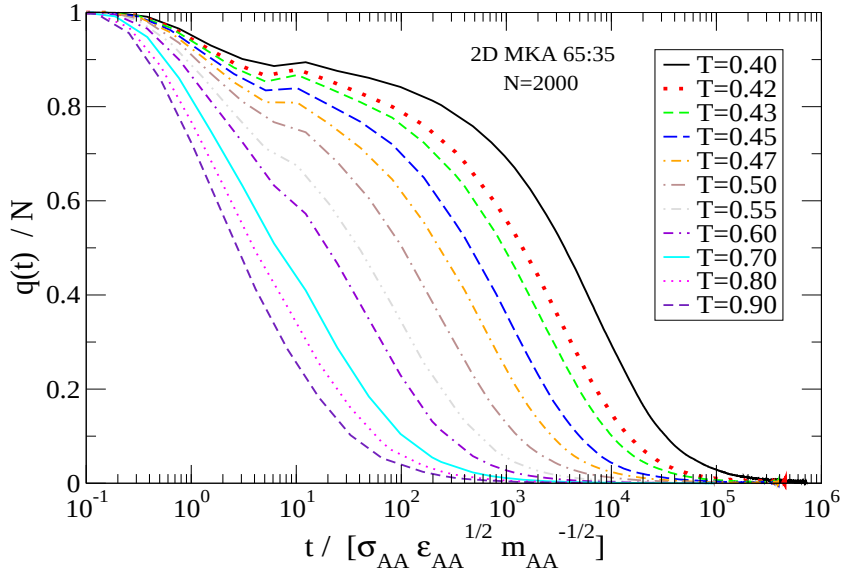

(a)

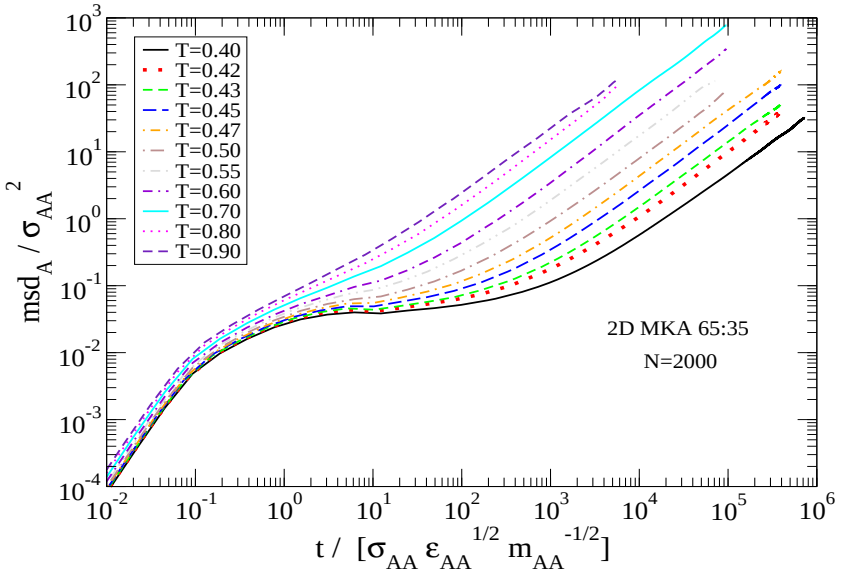

(b)

Figure 3.18: The overlap function and the MSD of A particles for the 2D MKA $65:35$ model.

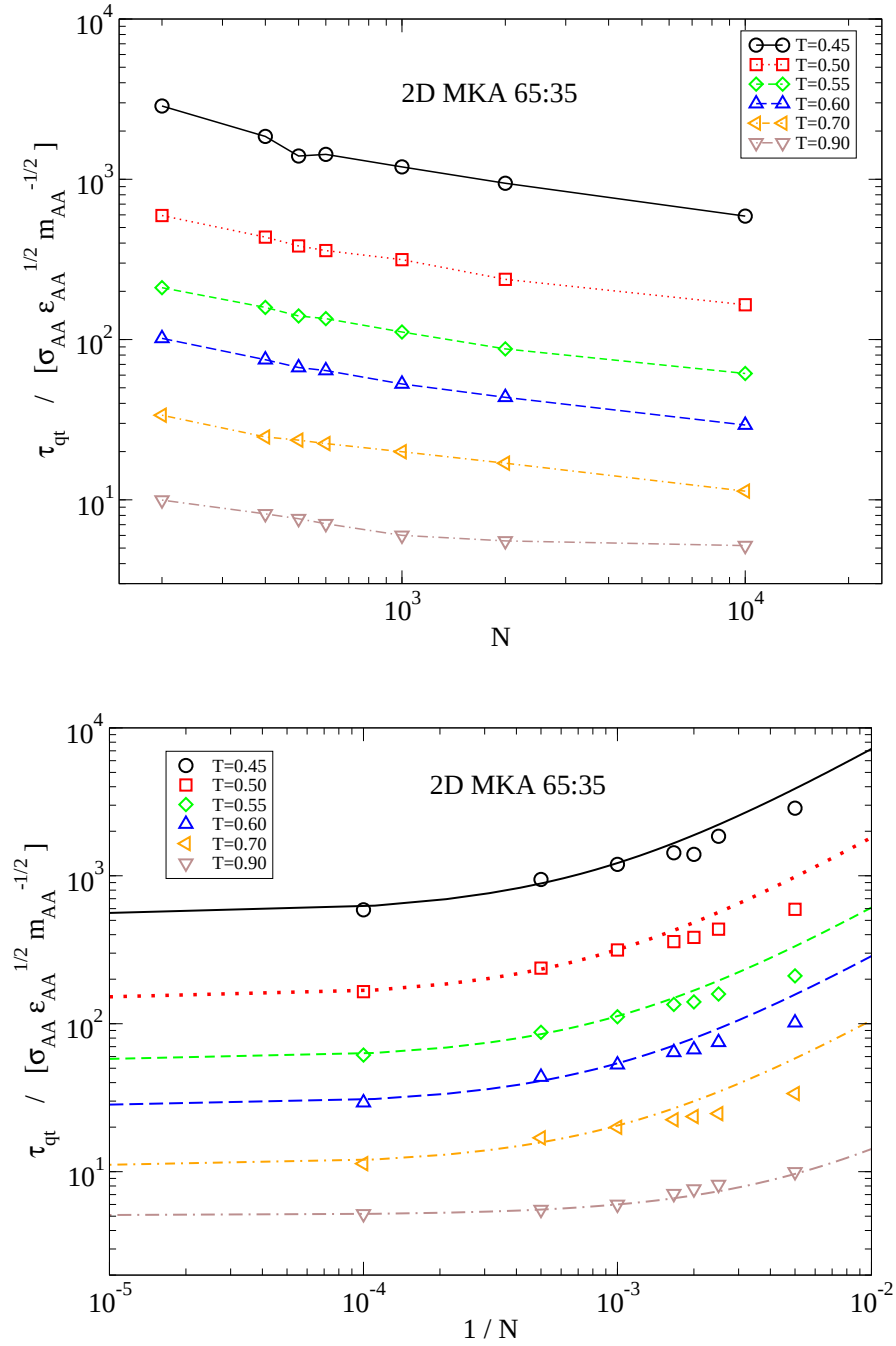

Figure 3.19: Top: System size dependence of the α relaxation time from the overlap function in the 2D MKA 65 : 35 model. Bottom: Extraction of the $\tau(\infty, T)$ from linear fits to the high system size data from the $\tau(N, T)$ *vs.* $1/N$ plot.

3.5.3 Characteristic temperature scales of the 2D MKA model

For the 2D MKA 65 : 35 model, the cross-over from the Arrhenius to the super-Arrhenius T-dependence of the relaxation time occurs at $T_{onset} \approx 0.8$ [Fig. 3.21]. The cross-over from the landscape independent high T to the landscape dependent low T behaviour also occurs at this temperature [Fig. 3.22(a)].

Although the inherent structure energy is linear with $\beta = 1/T$ at low T, the high T behaviour is different from other models, *e.g.* the KA model at 80:20 composition in two, three and four dimensions and the $R10$ model in two dimensions. Hence we briefly study the temperature dependence of the inherent structure (IS) energy of the 2D KA model for different compositions. We show in Fig. 3.22(b) that the high temperature behaviour *gradually* changes from the more familiar temperature dependence at the 80 : 20 composition to the less familiar temperature dependence at the 65 : 35 composition.

The divergence temperatures T_{MCT} predicted by mode coupling theory and T_{VFT} in VFT fit are estimated from Fig. 3.20 and the Kauzmann temperature T_K is estimated from Fig. 3.25. The values of different characteristic temperatures are tabulated in Table 3.4.

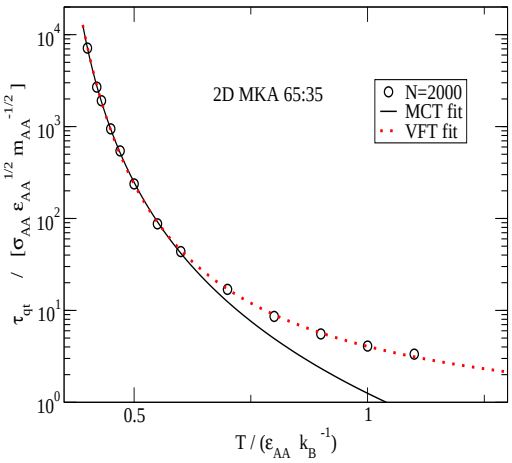

Figure 3.20: The VFT and the MCT fits to the relaxation times at $N = 2000$ for the 2D MKA model. The values of different characteristic temperatures are tabulated in Table 3.4.

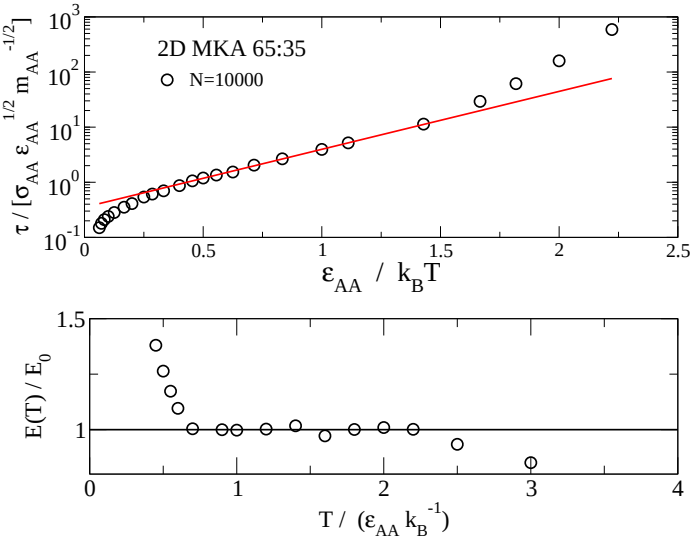

Figure 3.21: The Arrhenius fit to the high T relaxation time data at N=10000 for the 2D MKA 65 : 35 model. The temperature range is 0.45-16.00, the onset temperature being at ~ 0.80. There is a considerable deviation from the Arrhenius behaviour at very high T (more than three times onset T). Hence the Arrhenius fit is done in an intermediate temperature range where it is a good fit. The value of the infinite T relaxation time is 0.352 for the 2D MKA 65 : 35 model.

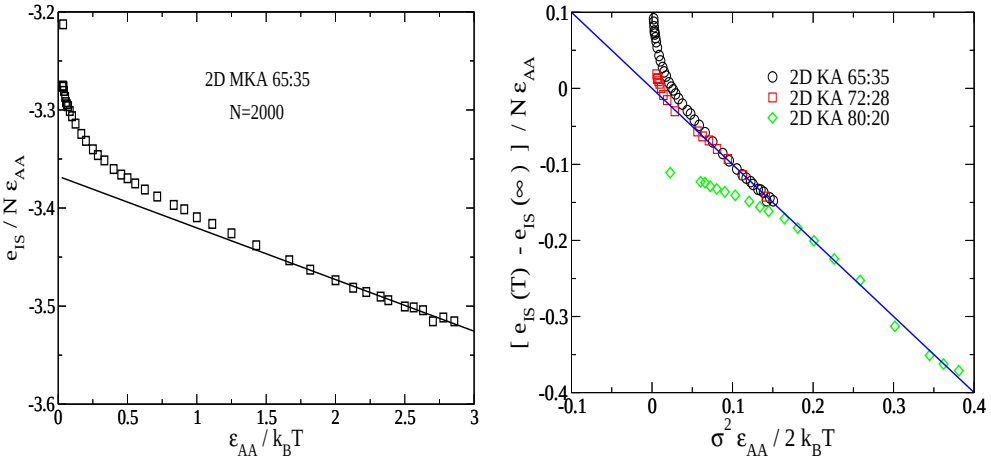

(a) (b)

Figure 3.22: Fig 3.22(a): The temperature dependence of the average inherent structure energy (per particle) e_{IS}/N for the 2D MKA 65 : 35 model. The solid line is a fit of the form $e_{IS}(T)/N = e_{IS}(\infty)/N + \frac{\sigma^2}{2T}$. The bending at high T is opposite to the KA model at the composition 80 : 20 (two to four dimensions). Fig 3.22(b): Comparison of the T dep. of the inherent structure energies at the compositions 80 : 20, 72 : 28 and 65 : 35 for the 2D Kob-Andersen model show that the change in high T behaviour is *gradual*.

3.5.4 The configurational entropy of the 2D MKA model

The total entropy: The total entropy is calculated from the total free energy using thermodynamic integration (see Chapter 2). Figs. 3.23 show the pressure *vs.* density isotherm at the reference high temperature (T_{ref}) and the temperature dependence of the average potential energy. The temperature dependence of the total (bulk) entropy and the total free energy are shown in Figs. 3.24 for the system size $N = 2000$.

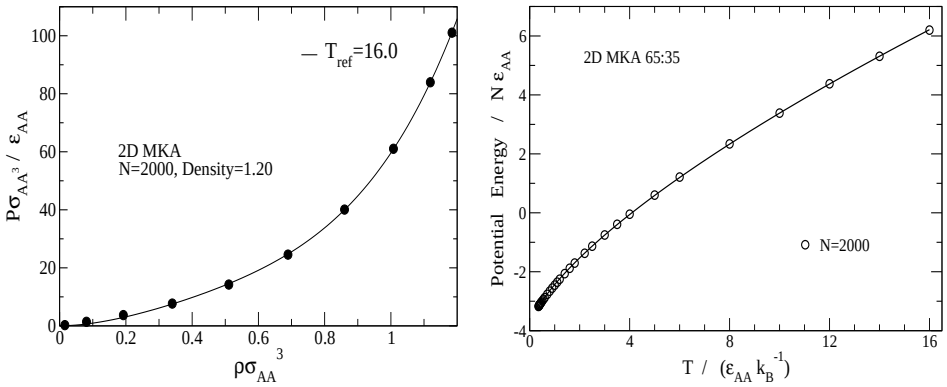

Figure 3.23: Left: The average pressure *vs.* density isotherm at a reference high temperature $T = 16.0$. Right: The average potential energy *vs.* temperature at density = 1.20. The line is a fit of the form $PE = a + bT^c$.

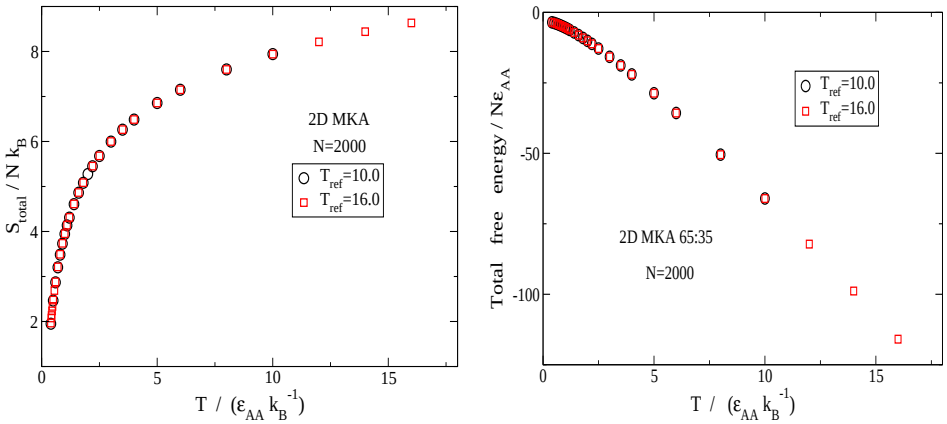

Figure 3.24: The temperature dependence of the total (bulk) entropy and the total free energy for the 2D MKA 65 : 35 model at $N = 2000$.

The basin and the configurational entropy: The basin entropy is calculated in harmonic approximation using inherent structure formalism (see

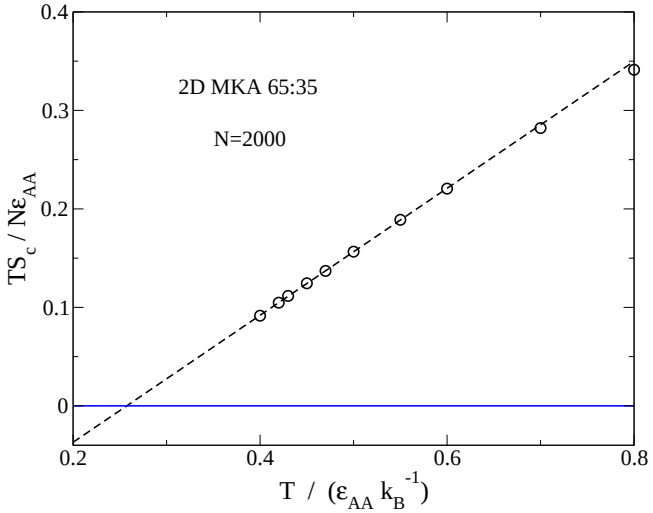

Figure 3.25: The temperature dependence of TS_c for the 2D MKA 65 : 35 model at $N = 2000$. The dashed line is a linear fit of the form $TS_c(T) = K_T(T/T_K - 1)$. The Kauzmann temperature T_K is estimated from this plot from the condition $TS_c(T_K) = 0$ *(by extrapolation)* and tabulated in Table 3.4.

Chapter 2). The configurational entropy $S_c(T)$ is computed as the difference [Eqn. 6.1] of the total and the basin entropy. The temperature dependences are shown in Figs. 3.26 and 3.25.

The configurational entropy density: The normalized probabilities of sampling different inherent structures at different low temperatures are shown in Fig. 3.27. This shows that the distribution can be well approximated by a Gaussian. This configurational entropy densities $S_c(e_{IS})$ at different temperatures are shown in Fig. 3.28 to check that the $S_c(e_{IS})$ computed at different temperatures fall on the same master curve.

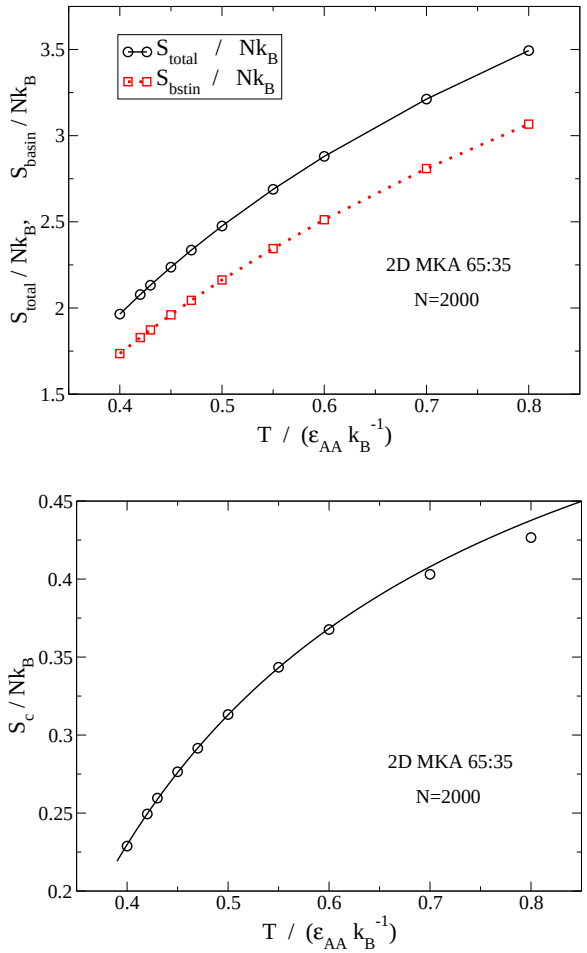

Figure 3.26: Top: The temperature dependence of the basin and the total entropy at low temperatures for the 2D MKA 65 : 35 model at $N = 2000$. Lines are guide to eyes. Bottom: the temperature dependence of the configurational entropy. The line is a fit of the form $S_c(T) = a + b/T$.

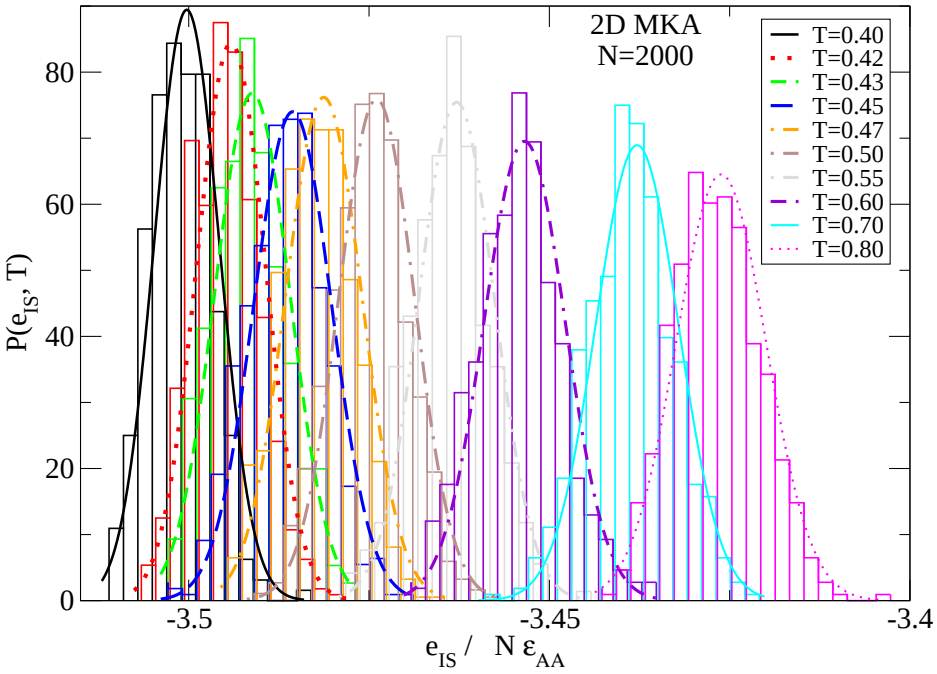

Figure 3.27: The normalized probability distribution ($P(eIS, T)$) of sampling inherent structures at low temperatures for the 2D MKA model at $N = 2000$.

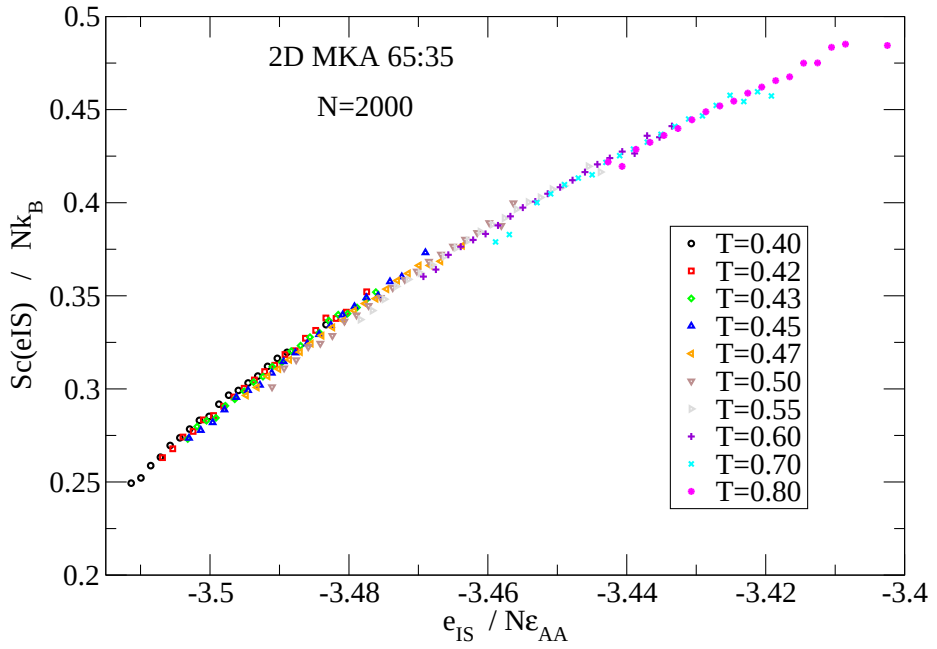

Figure 3.28: The configurational entropy densities ($S_c(e_{IS})$) at different low temperatures for the 2D MKA model at $N = 2000$ show that the $S_c(e_{IS})$ fall on the same master curve validating the computation method.

3.6 Characterizations: the repulsive soft sphere (R10) model in 2D

3.6.1 Choice of density for the 2D $R10$ model

For the $R10$ model in 2D, we have followed Ref. [171] and have done simulations at a fixed number density = 0.85.

3.6.2 Characteristic time scales of the 2D $R10$ model

The overlap function and the mean squared displacement: The temperature dependences of the overlap function and the MSD of A particles for the 2D $R10$ model are shown for the system size $N = 2048$ in Fig. 3.29. We check for good statistics that each run is long enough so that (i) the overlap function decays to zero and (ii) the MSD is well into the diffusive regime.

System size dependence of relaxation time We show in Fig. 3.30 the system size dependence of the α relaxation time in the 2D $R10$ model, for later use to compute static length scales. In the case of the Kob-Andersen model in 3D, it has been found [67] that the α relaxation time *increases* as the system size *decreases*. The same behaviour is observed in the 2D $R10$ model indicating that the observed system size dependence is a characteristic of the α relaxation. We also show for future reference the τ *vs.* $1/N$ plot to extract the relaxation time in the limit of infinite system size.

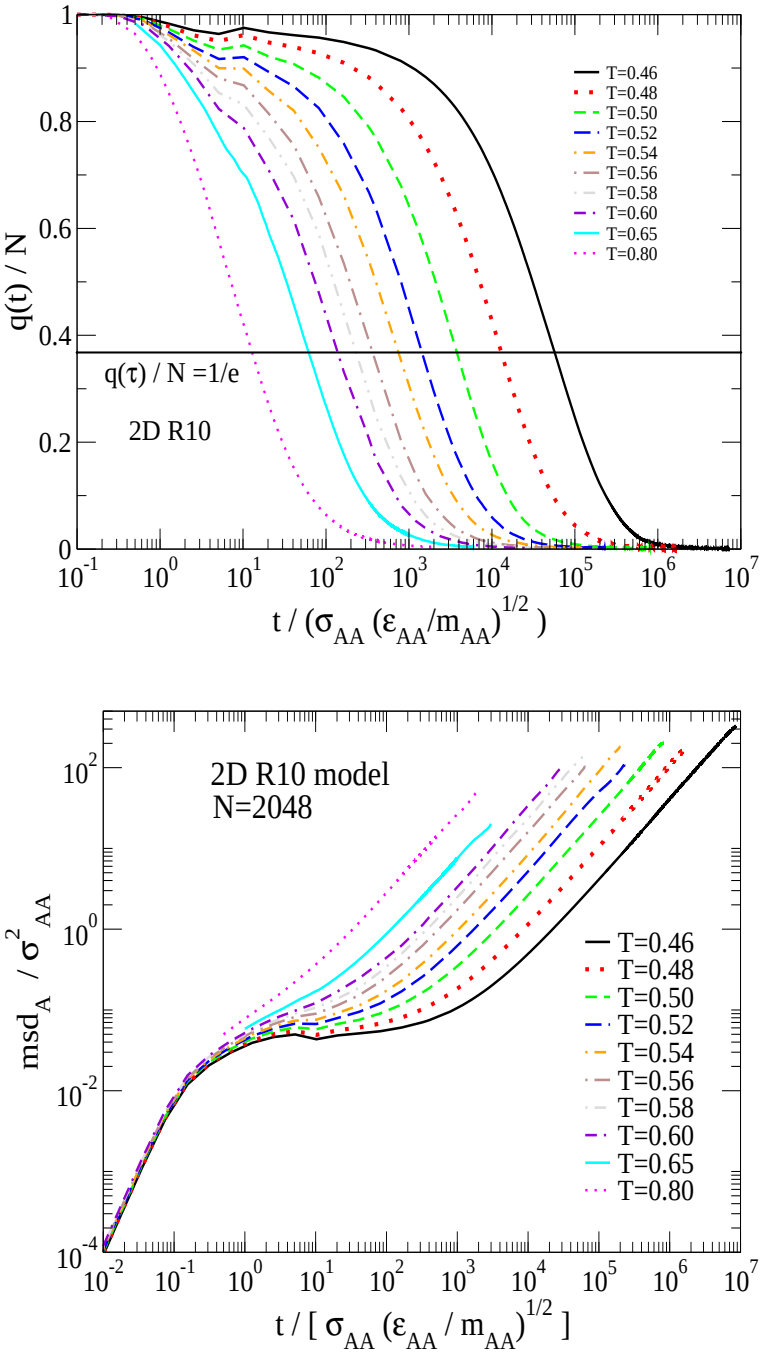

Figure 3.29: Top: The temperature dependence of the overlap function $q(t)$ of the 2D $R10$ model at the system size $N = 2048$. Relaxation times (τ) are extracted from the condition $q(t = \tau)/N = \frac{1}{e}$. Bottom: the temperature dependence of the MSD of A particles for the 2D $R10$ model at the system size $N = 2048$.

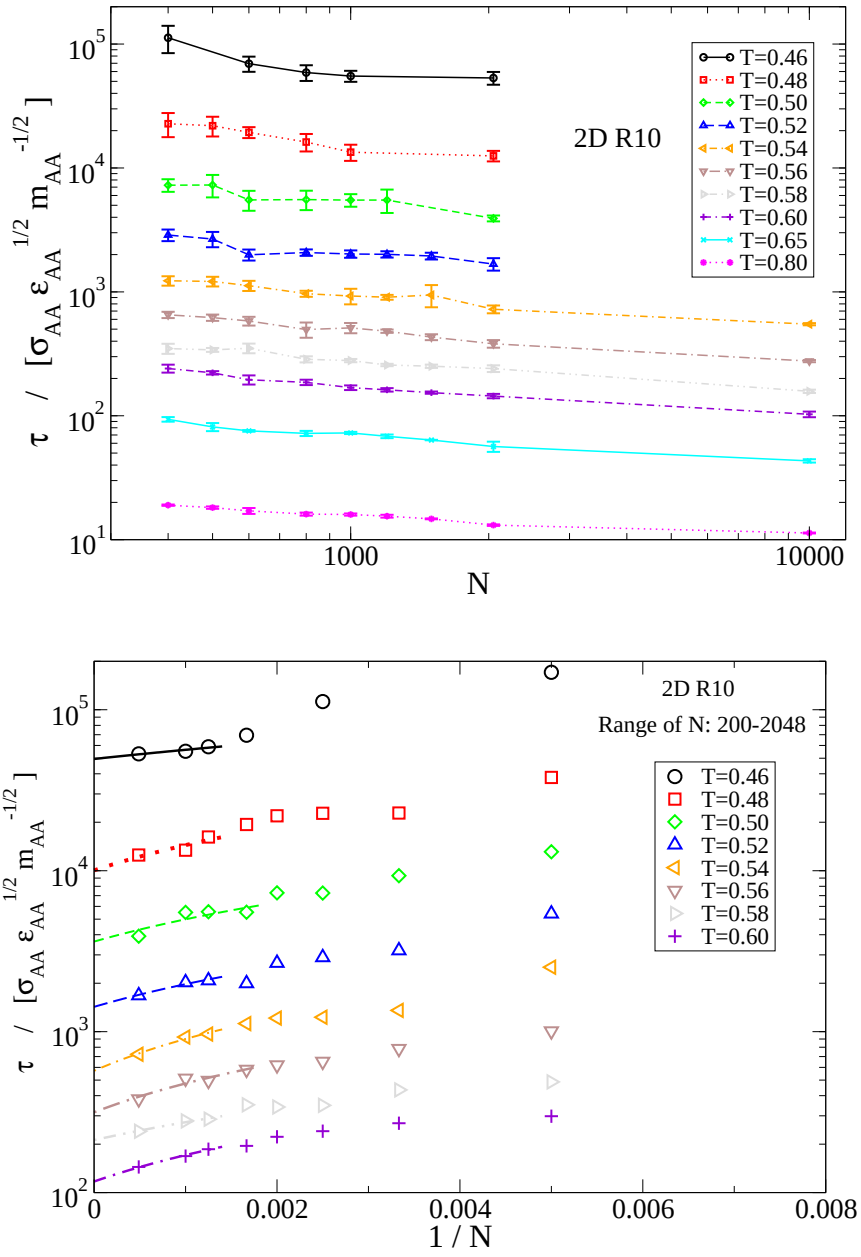

Figure 3.30: Top: System size dependence of the relaxation time from the overlap function below the onset temperature in the 2D $R10$ model. Bottom: estimates of the $\tau(N \to \infty, T)$ for the 2D R10 model by fitting lowest three or four data points to straight lines in the τ *vs.* $1/N$ plot.

3.6.3 Characteristic temperature scales of 2D R10 model

For the $R10$ model in 2D, the cross-over from the Arrhenius to the super-Arrhenius T-dependence occurs at the $T_{onset} \sim 0.8$ and is shown in Fig. 3.31. The cross-over from the landscape independent high T to the landscape dependent low T behaviour also occurs at the onset temperature which is shown in Fig. 3.32. The divergence temperatures (i) T_{MCT} predicted by the mode coupling theory and (ii) T_{VFT} in the VFT fit are estimated from Fig. 3.31. The Kauzmann temperature T_K is estimated from Fig. 3.36. The values of different characteristic temperatures are tabulated in Table 3.4.

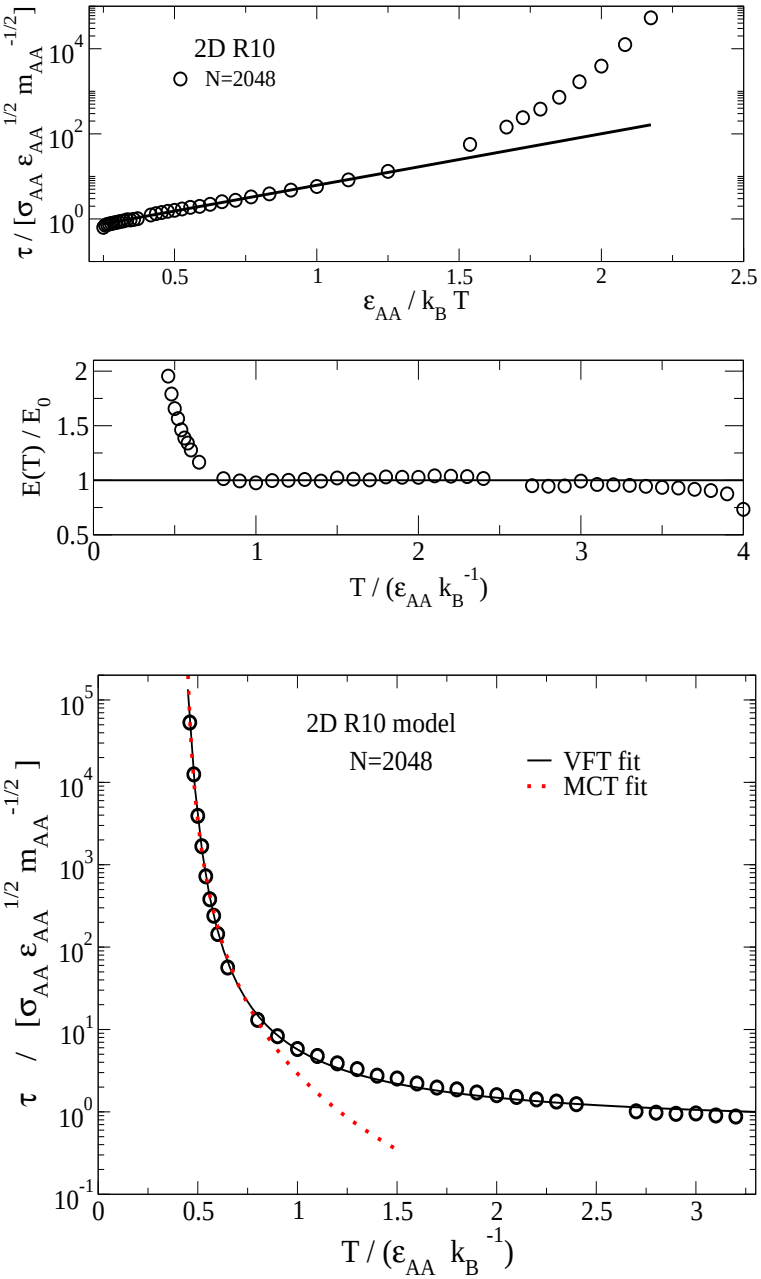

Figure 3.31: Top: Arrhenius fit to high T relaxation time data at $N = 2048$ for 2D $R10$ model. The temperature range is $0.46 - 4.00$, onset temperature being at ~ 0.80. Considerable deviation from Arrhenius behaviour at very high T is seen. Hence Arrhenius fit is done in an intermediate temperature range where it is a good fit. The value of infinite T relaxation time is 0.381 for 2D R10 model. Bottom: VFT and MCT fits to relaxation time for $N = 2048$. The values of different characteristic temperatures are tabulated in Table 3.4.

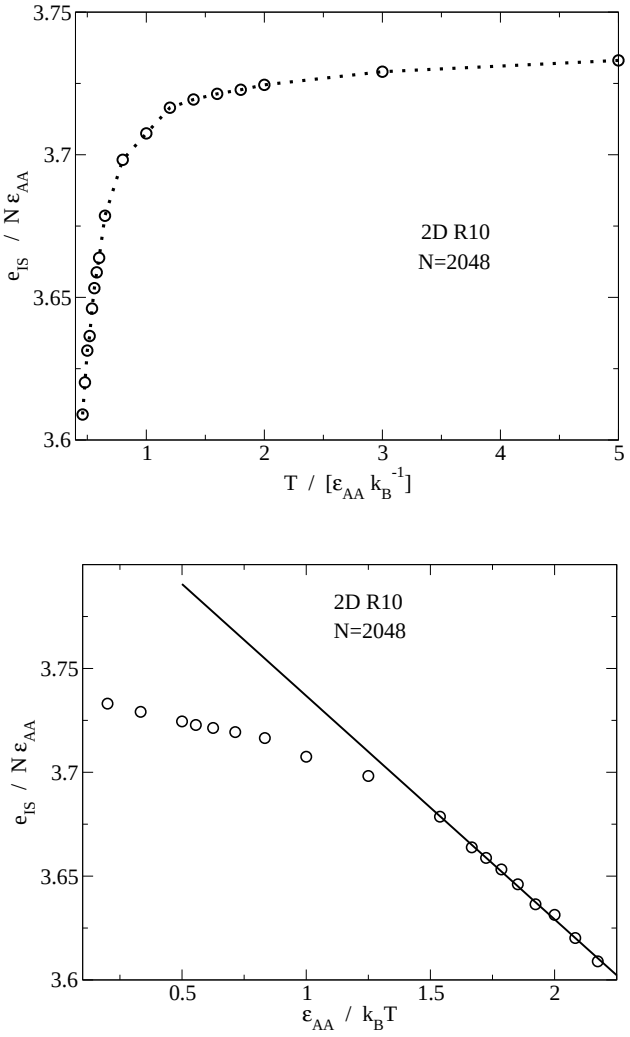

Figure 3.32: Top: Temperature dependence of the average inherent structure energy shows a crossover from a landscape independent high T regime to a landscape dependent low T regime at $\sim T_{onset} = 0.8$. Bottom: At low T, the average IS energy depends linearly on $1/T$.

3.6.4 The configurational entropy of the 2D $R10$ model

The total entropy: The total entropy is calculated from the total free energy using the thermodynamic integration (see Chapter 2). Fig. 3.33 show the pressure *vs.* density isotherm at the reference high temperature (T_{ref}) and the temperature dependence of the potential energy. The temperature dependences of the total (bulk) entropy and the total free energy are shown in Fig. 3.34 for a given system size.

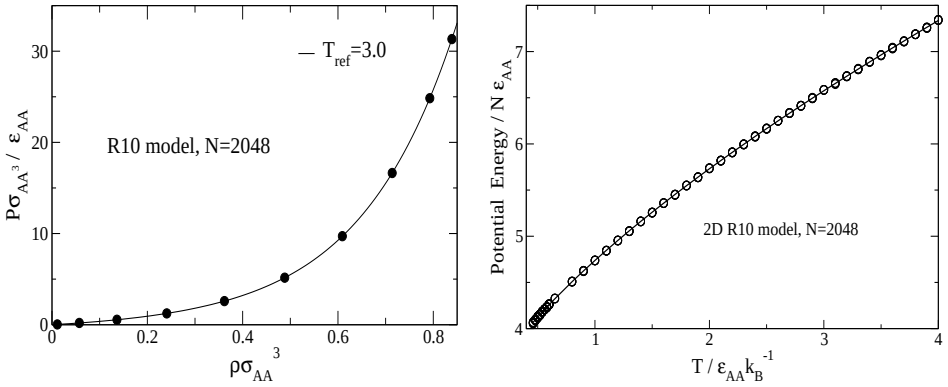

Figure 3.33: Left: The average pressure *vs.* density isotherm at the reference high temperatures ($T = 3.0$). Right: the average potential energy *vs.* temperature at the density = 0.85. The line is a fit of the form $PE = a + bT^c$.

The basin and the configurational entropy: The basin entropy is calculated in harmonic approximation using inherent structure formalism (see Chapter 2). The configurational entropy $S_c(T)$ is computed as the difference [Eqn. 6.1] of the total and the basin entropy. The temperature dependences are shown in Figs. 3.35 and 3.36.

The configurational entropy density: The normalized probability distributions of sampling different inherent structures at different low temperatures are shown in Fig. 3.37 which shows that the distribution can be well approximated by a Gaussian. The configurational entropy densities $S_c(e_{IS})$ at different temperatures are shown in Fig. 3.38 to show that the $S_c(e_{IS})$ computed at different temperatures fall on the same master curve.

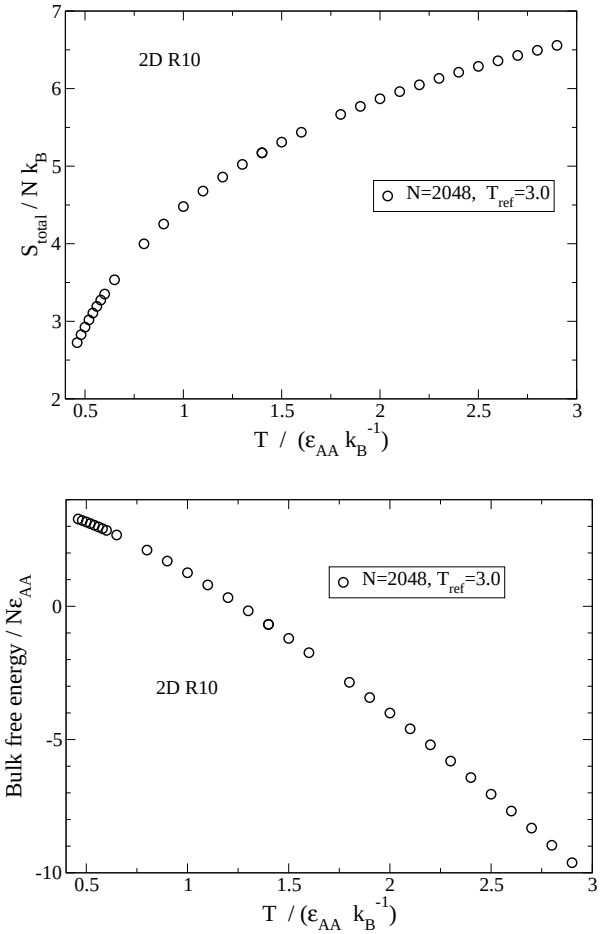

Figure 3.34: The temperature dependences of the total (bulk) entropy and the total free energy for the 2D $R10$ model at $N = 2048$.

The system size dependence of the configurational entropy: Since the α relaxation time increases as system size decreases, it is expected *via* the Adam Gibbs relation that the configurational entropy per particle should *decrease* as system size *decreases*. This is indeed found for the 2D $R10$ model as shown in Fig. 3.39. However, the variation with N is not smooth. To understand this, the relative contribution of the total and the basin entropy are shown in Figs. 3.40. It is seen that, with *decrease* in the system size, the basin entropy *increases* smoothly and the total entropy *slightly decreases*. The variation in total entropy is not smooth probably because the variation is comparable to the numerical uncertainty of the computed values.

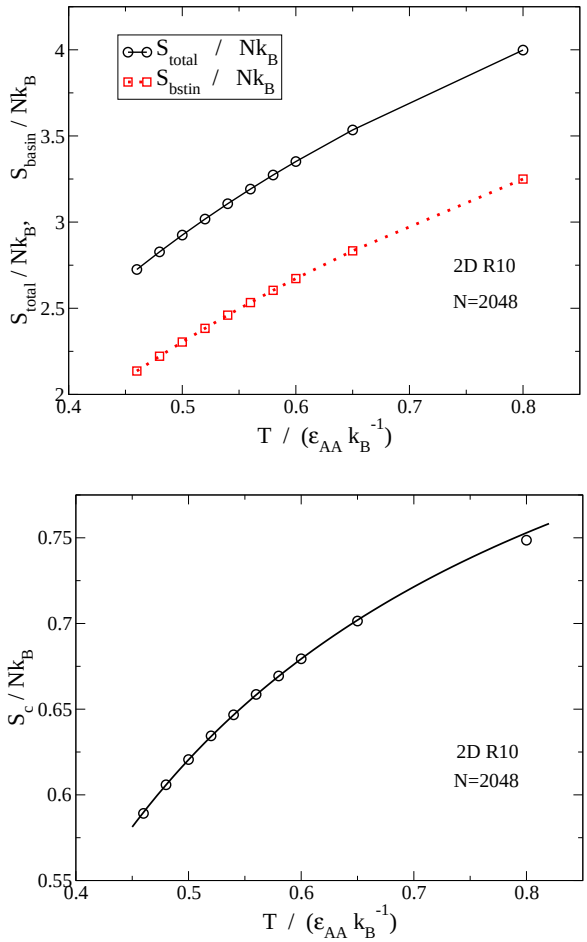

Figure 3.35: Top: the temperature dependence of the basin and the total entropy at low temperature for the 2D $R10$ model at $N = 2048$. Lines are guide to eyes. Bottom: temperature dependence of configurational entropy. The line is a fit of the form $S_c(T) = a + b/T$.

3.7 Dimension dependence in the AG relation

In the present section, we present evidences that the Adam Gibbs prediction (Eqn. 6.4) does not work in all spatial dimensions. We also discuss what are the possible factors responsible for the observed deviation from the AG relation and whether the RFOT predictions are consistent with our data.

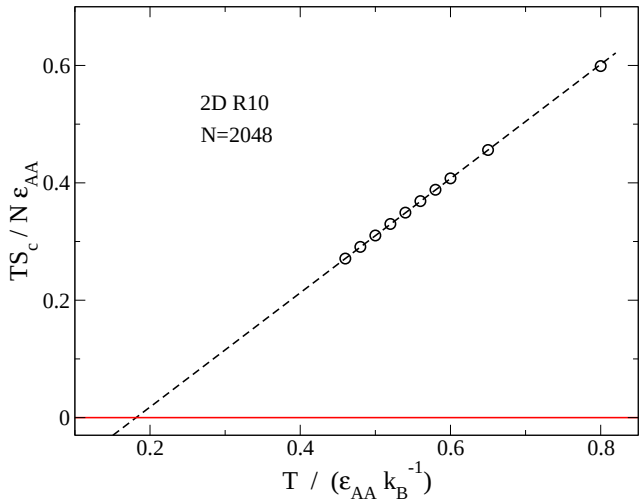

Figure 3.36: The Temperature dependence of the TS_c for the 2D $R10$ model at $N = 2048$. The dashed line is a linear fit of the form $TS_c(T) = K_T(T/T_K - 1)$. The Kauzmann temperature T_K is estimated from this plot and tabulated in Table 3.4.

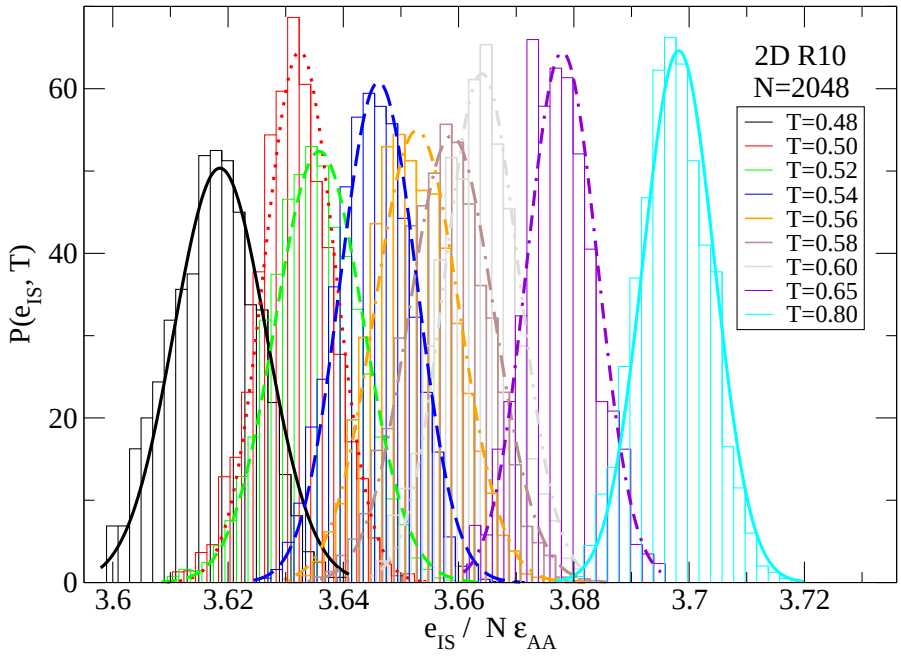

Figure 3.37: The normalized probability distribution ($P(eIS, T)$) of sampling inherent structures at different temperatures for the 2D $R10$ model at the system size $N = 2048$.

3.7.1 Effect of changing the spatial dimension

Three and four dimensions: In Fig. 3.41 we show the Adam Gibbs plots for the Kob-Andersen model in two and four dimensions at the same

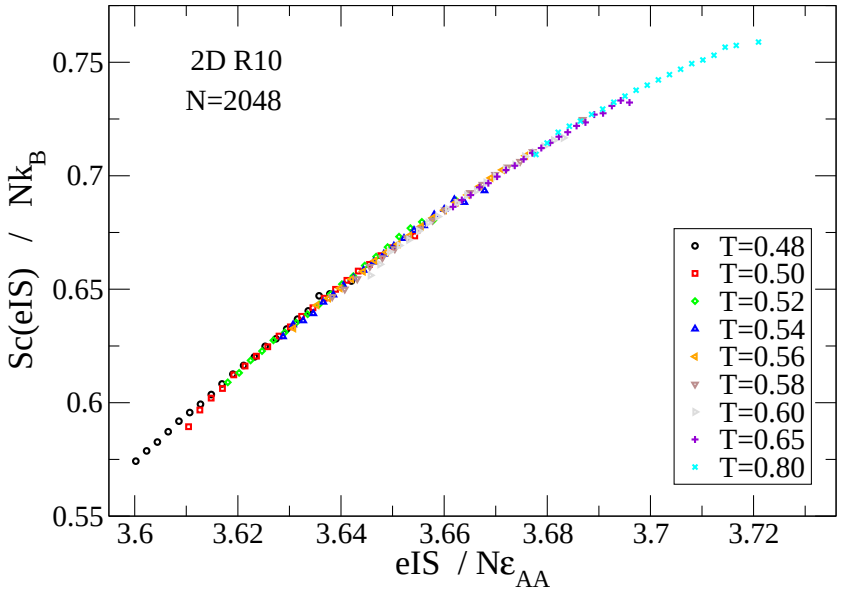

Figure 3.38: The configurational entropy density ($S_c(e_{IS})$) at different low temperatures for $N = 2048$ shows that the $S_c(e_{IS})$ falls on the same master curve validating the computation method.

composition 80:20 (note, however, that the densities are different - in 4D $\rho = 1.6$ and in 2D $\rho = 1.2$). We see that in 4D, the AG relation (solid black line in Fig. 3.41(a)) is validated over several orders of magnitude. In Fig. 3.41(a), we also show by dashed red line a fit to a *generalized* AG relation $\ln \tau(T) = \ln \tau(\infty) + A/(TS_c)^\alpha$ which is very close to Eqn. 3.3 (differs by a factor of T). In this fit, α is a free parameter and we get $\alpha \approx 1$. The evidence of the KA model in four dimensions along with the more familiar 3D KA model (Fig. 3.1) seems to suggest that AG relation does not change with spatial dimension.

Two dimensions: However, in the 2D KA 80 : 20 model, (Fig: 3.41(b)), we see a *systematic and smooth deviation* from the prediction of the Adam Gibbs relation as the relaxation time increases (see also Fig. 3.2). In Fig. 3.42 we show that (i) *systematic and smooth* deviations from the AG prediction are observed in two dimensions in MKA 65 : 35 and $R10$ models as well. (ii) the deviations in KA and$R10$ models are in *opposite* directions. We discuss the AG relation in 2D in more detail below.

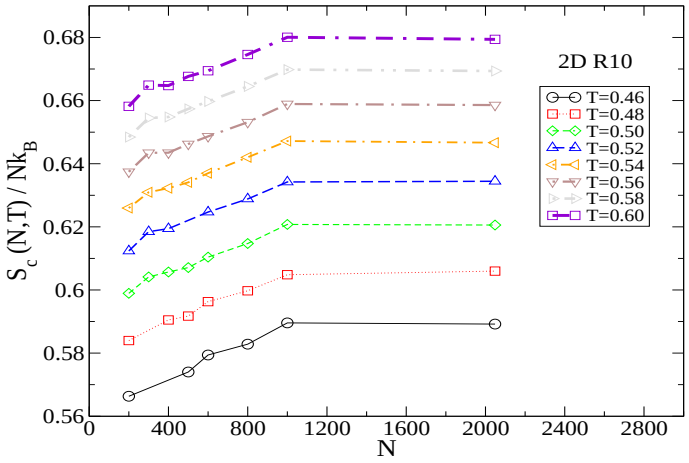

Figure 3.39: The system size dependence of the configurational entropy per particle $S_c(T) = S_{total}(T) - S_{basin}(T)$ in the 2D $R10$ model.

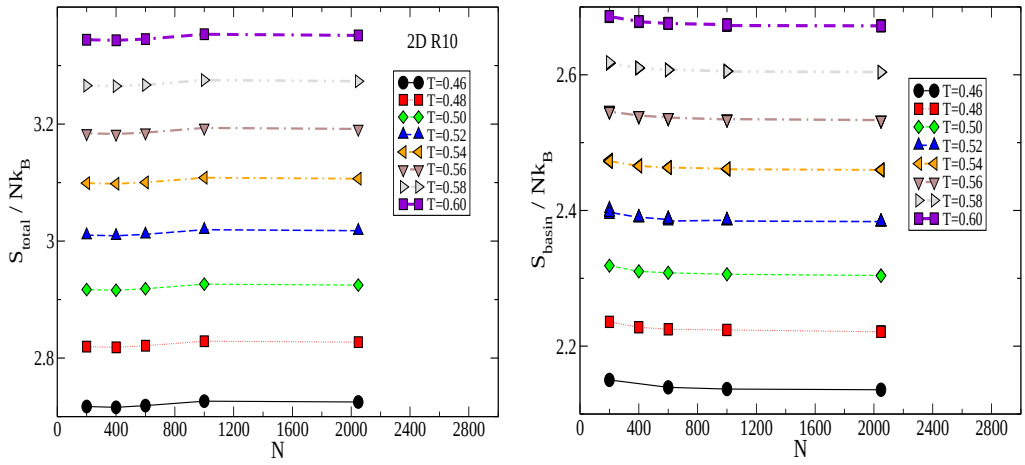

Figure 3.40: Left: The system size dependence of the total entropy $S_{total}(T)$ per particle below onset temperature in the 2D $R10$ model. Right: The system size dependence of the basin entropy $S_{basin}(T)$ per particle below the onset temperature.

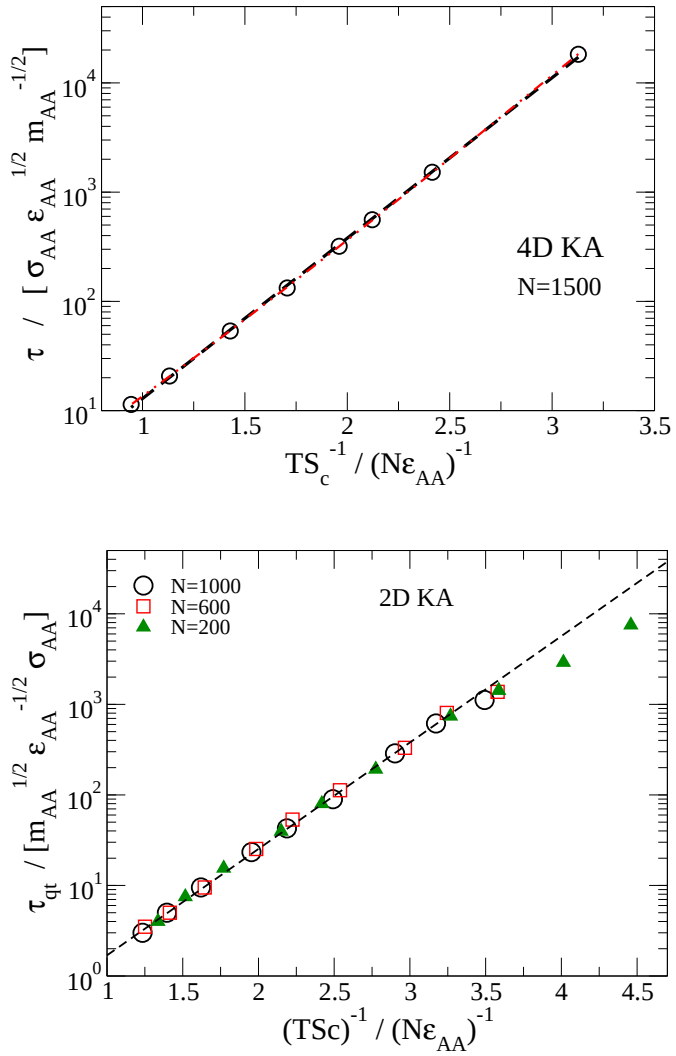

(b)

Figure 3.41: The Adam Gibbs relation for the Kob-Andersen model holds in four dimensions but there is a systematic and smooth deviation in two dimensions. Fig. 3.41(a): The 4D KA 80 : 20 model at the density = 1.60. The solid line is a fit to the AG relation (Eqn. 6.4) and the dashed line is a fit to a *generalized* AG relation : $\ln \tau(T) = \ln \tau(\infty) + A/(TS_c)^{\alpha}$ treating α as a free parameter. Fig. 3.41(b): The 2D KA 80 : 20 model at the density = 1.20. The dashed line is a fit to the AG relation for the largest system size.

3.7.2 Is the observed deviation an finite system size effect?

The α relaxation time in all models studied here in two and three dimensions *increases* as system size *decreases*. This fact has been used here to access

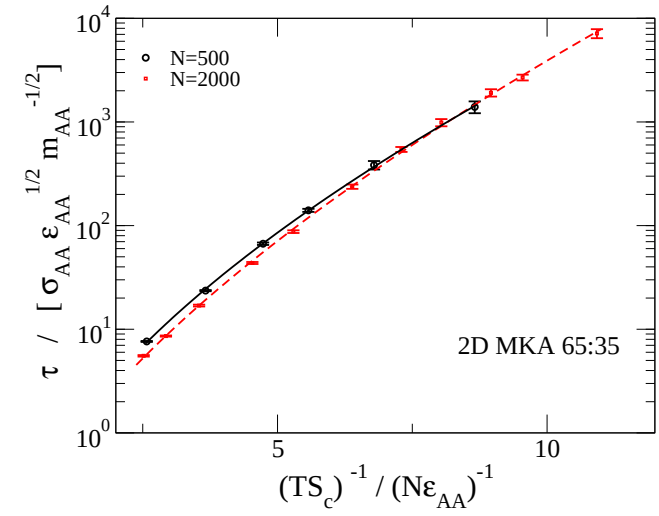

(a)

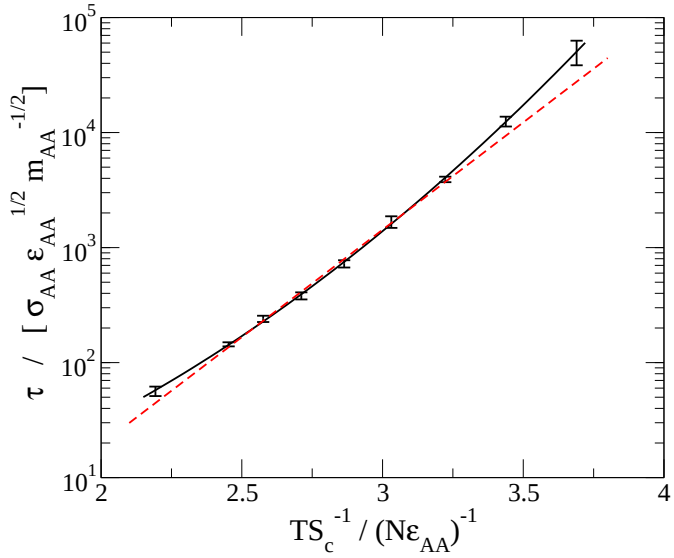

(b)

Figure 3.42: Systematic deviation from the Adam Gibbs relation is seen in 2D for both the repulsive $R10$ model and the attractive MKA model. Solid lines are fits to a generalized AG relation of the form $\ln \tau = \ln \tau_0 + A(\frac{1}{TS_c})^\alpha$ (see also Eqn. 3.3). For the $R10$ model, the dashed line is a fit according to the Adam Gibbs relation. The deviation in the attractive and the repulsive models are in opposite directions. For the 2D MKA model, $\alpha = 0.55$ for $N = 500$ (solid line) and $\alpha = 0.62$ for $N = 2000$ (dashed line). For the $R10$ model, the system size is $N = 2048$ and $\alpha = 2.1$ (dashed line).

high relaxation time range by simulating smaller system sizes. But are our system sizes large enough to study the Adam Gibbs relation? In the 3D KA model, the α relaxation time is more or less independent of system size for

$N > 600$ [67]. Although, the AG relation in the 3D KA model is shown to be valid using system sizes both below and above 600 (Fig. 3.1). In two dimensions in the MKA 65 : 35 and the $R10$ models, the α relaxation time does not become independent of system size till $N = 10^4$ (Figs. 3.19 and 3.30). Hence in two dimensions in all models, the AG relation has been tested using multiple system sizes. We note that Fig. 3.41(b) for the 2D KA 80 : 20 model seems to suggest that the deviation from the AG relation in 2D occurs as the temperature is *lowered* and the system size is *decreased*. However, no such systematic variation is observed for the 2D MKA 65 : 35 and the 2D $R10$ models. Further, in Fig. 3.43 we show for the 2D MKA model the system size dependence of the exponent α in the generalized Adam Gibbs relation : $\ln \tau = \ln \tau_0 + A(\frac{1}{TS_c})^\alpha$ (see also Eqn. 3.3). We see that the *extrapolated* value of α (≈ 0.7) in the limit of infinite system size is still very different from the value (=1) predicted by the Adam Gibbs relation.

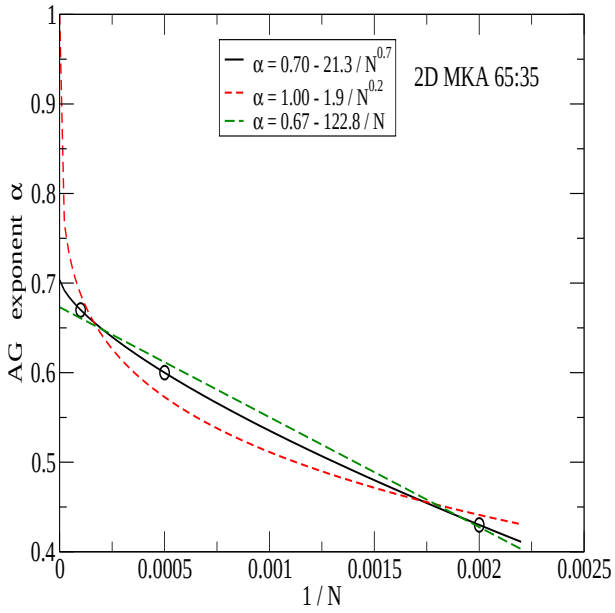

Figure 3.43: The system size dependence of the exponent α in the generalized Adam Gibbs relation : $\ln \tau = \ln \tau_0 + A(\frac{1}{TS_c})^\alpha$ (see also Eqn. 3.3) for the 2D MKA model shows that the *extrapolated* value of α (≈ 0.7) in the limit of infinite system size is still very different from the value (=1) predicted by the Adam Gibbs relation. The solid line is the best power law fit through the data points. For comparison, we also show (i) a fit where the infinite N value of α is set to 1 and (ii) a linear fit through the data points.

3.7.3 What causes the deviation in 2D?

In two dimensions, all models that we have studied show deviation from the AG relation. However, the nature of deviation is in the opposite direction for the Kob-Andersen (80:20 and 65:35) and the repulsive soft sphere (R10) models. This raises the question if the observed deviation is due to the spatial dimensionality or due to other factors. Here we discuss whether (1) the presence or the absence of the *local orientational order* and (2) the *nature of the interaction potential* has any role in causing the observed deviation.

Does local orientational order cause the deviation in 2D? It has been reported recently that the 2D KA 80 : 20 model is prone to form transient clusters of hexagonally arranged particles having high degree of local orientational order [174]. Such clusters appear in many supercooled liquids and have been used to build a scenario of glass transition phenomena analogous to the conventional critical phenomena [82]. There is a possibility that the deviation seen in 2D KA 80 : 20 model is due to the underestimation of the configurational entropy or the overestimation of the relaxation time due to this ordering. This orientational ordering can be suppressed by changing the composition of the 2D KA model from the standard value 80:20 to 65:35 [174]. In fact, this was the motivation to chose the modified KA model (2D MKA). However, as Fig. 3.42(a) shows, this does *not* suppress the deviation from the AG prediction. Further, we have tested that the local orientational order is not significant in the $R10$ model which also show deviation the from AG prediction. We also note that another repulsive soft sphere model popular in the literature as a *good* glass-former in 2D [172] shows considerable local orientational order. Hence, by comparing models, we conclude that the presence or the absence of local orientational order is *not* a factor controlling the observed deviation from the AG prediction in 2D.

Does the nature of the inter-particle interaction cause the deviation in 2D? According to the conventional wisdom, the *structure* of liquids is mainly determined by the short ranged repulsive interaction and the longer-ranged attractive part can be considered a a perturbation [161].

However, whether attractive interaction plays a *qualitatively and quantitatively* different role in determining *dynamics* of liquids is recently being debated [162, 163]. As the observed deviation in the 2D $R10$ (purely repulsive interaction) and the KA (both attractive and repulsive interactions present) models show deviation in opposite directions, it seems natural that the attractive *vs.* repulsive nature of the inter-particle interaction plays a role in causing the deviation. However, we note that in *three dimensions*, the AG relation have been verified in *both* the attractive models (*e.g.*: the Kob-Andersen [128] model, the Lewis-Wahnström model for ortho-Terphenyl [48] and the Dzugutov liquid [53]) *and* the repulsive models (*e.g.*: the repulsive soft spheres [54]). Hence, even if the attractive *vs.* repulsive nature of the inter-particle interaction has a role, it is not the only factor causing the deviation.

3.8 Discussion: is the deviation from the AG relation consistent with the RFOT?

To determine if the RFOT predictions are consistent with the observed deviations from the AG relation in 2D, we need to compute the RFOT exponents. To compute the RFOT exponents, in addition to the relaxation time and the configurational entropy, one needs to compute the characteristic length scales. Indeed, finding in a glass-forming liquid a characteristic lengthscale which increases as the temperature decreases, is an important open question related to the glass transition. There are many proposals in the literature to extract such a lengthscale. In this section we describe the analyses to extract two such length scales which are static in nature. (i) We extract a length scale (denoted here as ξ_{Sc}) from the finite size scaling of the configurational entropy. However, the computation of ξ_{Sc} is computationally demanding. (ii) Recently, a static length-scale (denoted here as ξ_λ) has been extracted from the vibrational properties of the interaction potential, namely, from the first non zero eigenvalue of the Hessian at the inherent structures [81]. The motivations behind computing ξ_λ are : (i) it was shown in that ξ_λ is proportional to ξ_{Sc} for the 3D KA model (ii) the scaling relation between ξ_λ and τ_α was claimed to be different for models in 3D with purely repulsive interactions and models having both attractive and repulsive interactions - which may

rationalize why the observed deviations from the AG relation are different for the 2D MKA and the 2D R10 models. (iii) Computing ξ_λ is cheaper than computing ξ_{Sc}.

3.8.1 The static lengthscale ξ_{Sc} from the configurational entropy

Definitions: To extract a static length scale by performing the finite size scaling analysis of the configurational entropy, we assume the configurational entropy to be a scaling function of N/ξ_{Sc}^2: $S_c(N,T) = S_c(\infty,T)f(N/\xi_{Sc}^2)$. Here $S_c(\infty,T)$ is the configurational entropy at any temperature T in the limit of infinite system size and $f(x)$ is the unknown scaling function. The length scale ξ_{Sc} is obtained by demanding collapse of $S_c(N,T)$ data at different system sizes and temperatures, on a master curve in the $S_c(N,T)/S_c(\infty,T)$ *vs.* N/ξ_{Sc}^2 plot.

Results: ξ_{Sc} for the 2D R10 model: The scaling plot of the configurational entropy for 2D $R10$ model from which ξ_{Sc} is computed, is shown in Fig. 3.44. The temperature dependence of ξ_{Sc} for the 2D R10 model is shown in Fig. 3.51.

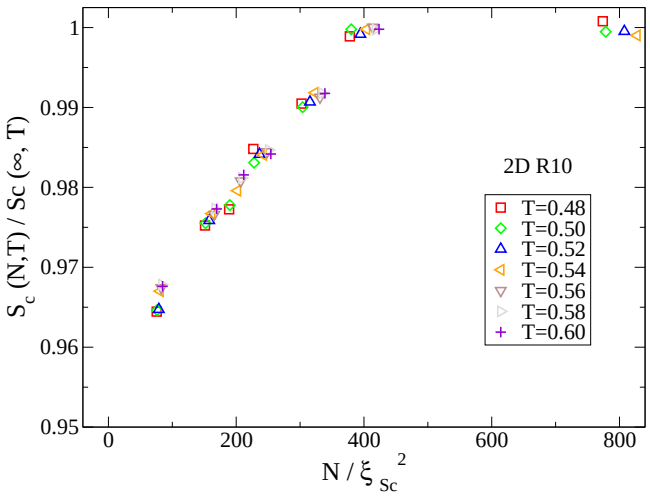

Figure 3.44: Finite size scaling of the configurational entropy S_c in the 2D R10 model where the lengthscale ξ_{sc} and the parameter $S_c(\infty,T)$ are obtained by collapsing configurational entropy the data in Fig. 3.39 on a master curve.

3.8.2 The static lengthscale ξ_λ from the minimal eigen values

Definitions: We describe the procedure used in the present study to extract the lengthscale ξ_λ. For more details we refer to [81].

1. The density of states $P(\lambda)$ of the eigen values of the Hessian of the interaction potential at an inherent structure is considered to be composed of approximately two parts: an elastic or Debye part and an additional plastic part:

$$P(\lambda) \approx A\left(\frac{\lambda}{\lambda_D}\right)^{\frac{d-2}{2}} + B(T) f_{pl}\left(\frac{\lambda}{\lambda_D}\right) \tag{3.5}$$

   The prefactors A and $B(T)$ gives the relative contribution of each type of modes. In the computation here, we consider A to be a universal constant independent of models. We take $A = 1/37$. The prefactor $B(T)$ is unknown.

2. Integrating the above equation from zero upto the first non-zero eigenvalue λ_{min},

$$\begin{aligned} N\int_0^{<\frac{\lambda_{min}}{\lambda_D}>} d(\frac{\lambda}{\lambda_D})P(\frac{\lambda}{\lambda_D}) &= 1 \\ \lambda_D \approx \mu\rho^{2/d-1} &\approx \mu \text{ in 2D} \end{aligned} \tag{3.6}$$

   where λ_D is called Debye frequency and μ is the shear modulus.

3. Inserting the form for $P(\lambda)$ the plastic contribution can be written as

$$G(<\frac{\lambda_{min}}{\lambda_D}>) = \left[\frac{1}{B(T)}\left(\frac{1}{N} - \frac{Ad}{2} <\frac{\lambda_{min}}{\lambda_D}>^{d/2}\right)\right] \tag{3.7}$$

   and inverting,

$$<\frac{\lambda_{min}}{\lambda_D}> = G^{-1}\left[\frac{1}{B(T)}\left(\frac{1}{N} - \frac{Ad}{2} <\frac{\lambda_{min}}{\lambda_D}>^{d/2}\right)\right] \tag{3.8}$$

4. We define $\xi^d \equiv 1/B(T)$. This quantity defines a static lengthscale that can be extracted by demanding data collapse in the plot of $<\frac{\lambda_{min}}{\lambda_D}>$ vs. $\left(\frac{1}{N} - \frac{Ad}{2} <\frac{\lambda_{min}}{\lambda_D}>^{d/2}\right)$.

5. In 2D, the above equation simplifies to

$$< \frac{\lambda_{min}}{\lambda_D} >= G^{-1}\left[\frac{1}{B(T)}\left(\frac{1}{N} - A < \frac{\lambda_{min}}{\lambda_D} >\right)\right] \tag{3.9}$$

So, in order to compute the lengthscale, one needs to compute the ensemble averaged $< \lambda_{min} >$ and the shear modulus μ (to compute λ_D).

Results: ξ_λ for the 2D MKA $65:35$ and the 2D R10 models: We show the raw data and the scaling plots to extract ξ_λ in Figs. 3.45 - 3.46 for the 2D MKA $65:35$ model and in Figs. 3.47 - 3.48 for the 2D $R10$ model. The temperature dependence of ξ_λ is shown in Fig. 3.49.

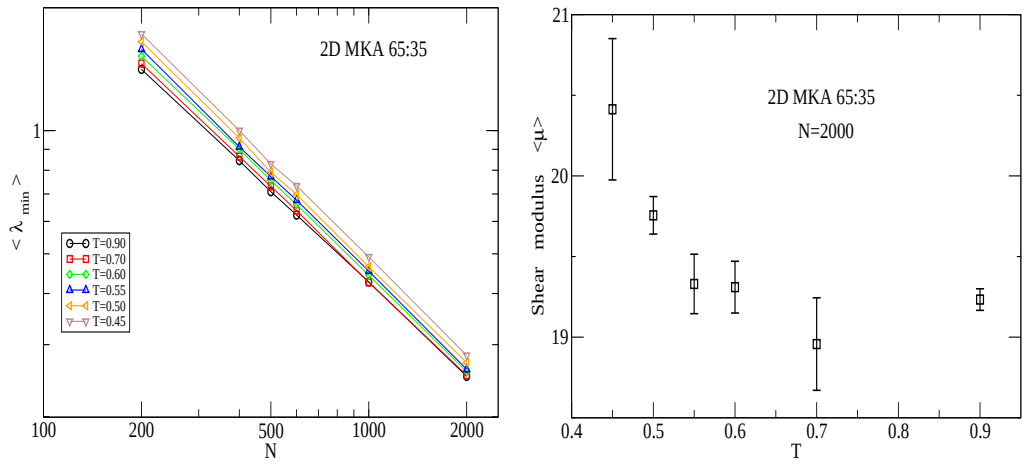

Figure 3.45: Fig. 3.45(a): The system size dependence of the ensemble averaged minimal eigenvalue of the Hessian at the inherent structures - $\langle \lambda_{min} \rangle$ for the 2D MKA $65:35$ model. Fig. 3.45(b): the temperature dependence of the ensemble averaged shear modulus μ at $N = 2000$. In two dimensions, the Debye frequency $\lambda_{min} \approx \mu$.

3.8.3 Are ξ_{Sc} and ξ_λ independent ?

In [81], it is shown by performing the finite size scaling of S_c using ξ_λ that the two lengthscales are ξ_{Sc} and ξ_λ mutually proportional in three dimensions. We test in Fig. 3.50 if the same is true in two dimensions. We find that the data collapse is poor. The two length scales ξ_λ and ξ_{Sc} in the 2D R10 model are also compared in Fig. 3.51 which shows that they are not proportional.

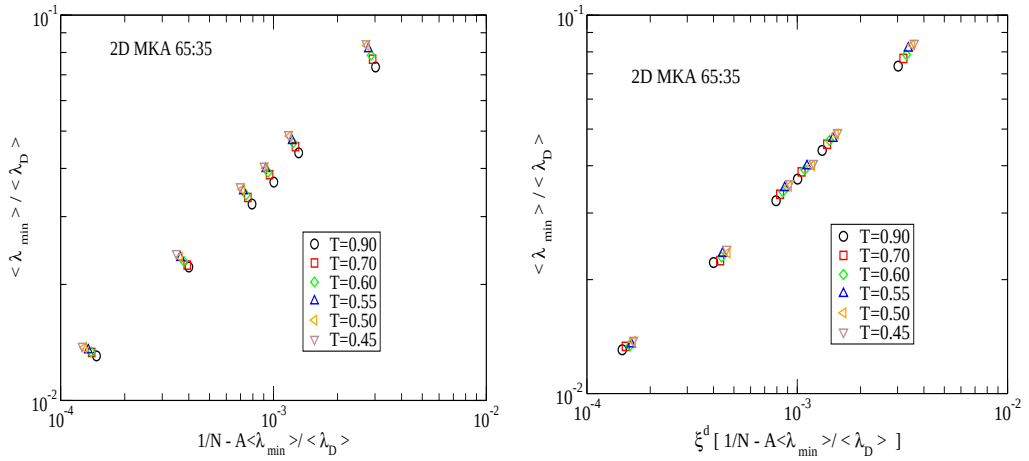

Figure 3.46: Scaling of the minimal eigenvalue $< \lambda_{min} >$ for the 2D MKA $65:35$ model. The static length scale ξ_λ is extracted by demanding collapse of the data in Fig. 3.46(a) onto the same master curve.

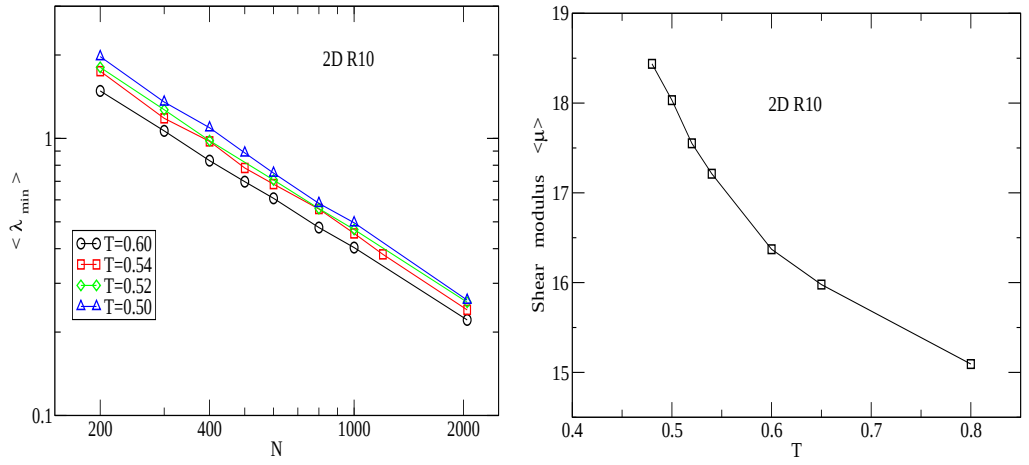

Figure 3.47: Fig. 3.47(a): The system size dependence of the ensemble averaged minimal eigenvalue of the Hessian at inherent structures $< \lambda_{min} >$ for the 2D $R10$ model. Fig. 3.47(b): The temperature dependence of the ensemble averaged shear modulus μ (values taken with permission from [81]. In two dimensions, the Debye frequency $\lambda_{min} \approx \mu$.

However we emphasize that improved data are required before concluding anything from these data.

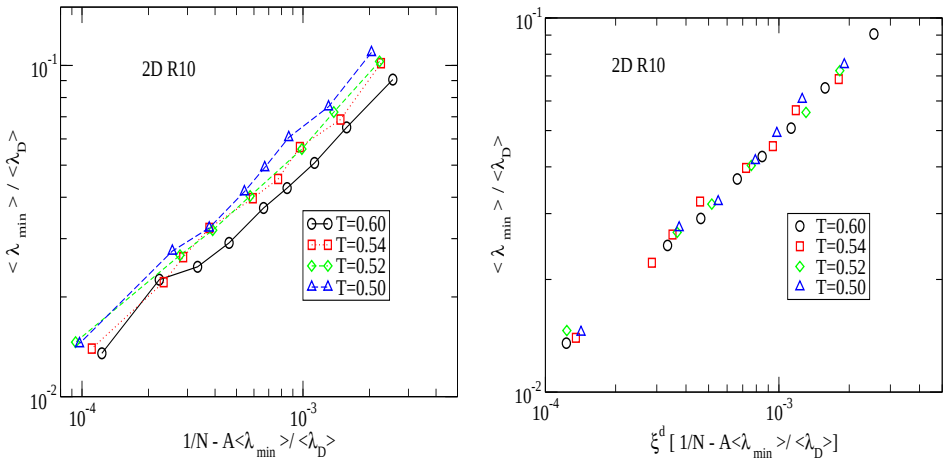

Figure 3.48: Scaling of the minimal eigenvalue $< \lambda_{min} >$ for the 2D $R10$ model. The static length scale ξ_λ is extracted by demanding collapse of the data in Fig. 3.48(a) onto the same master curve.

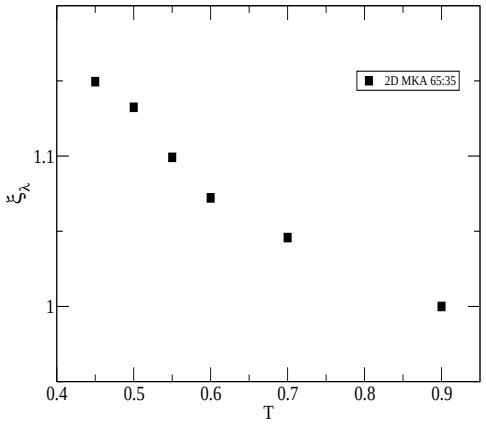

Figure 3.49: The T dependence of ξ_λ for the 2D MKA 65:35 model. The value of ξ_λ at the highest temperature, T=0.90 is taken to be 1.

3.8.4 The RFOT exponents

In the following analysis we use the static length scale ξ_λ as defined in section 3.8.2 and equate the characteristic lengthscale ξ of the RFOT to ξ_λ. In the RFOT, the free energy barrier for relaxation ΔG depends on the static correlation length ξ_λ as $\Delta G(T) \propto \xi(T)^\psi$ which defines the exponent ψ. Hence the RFOT relation between relaxation time $\tau(T)$ and static correlation length $\xi_\lambda(T)$ is

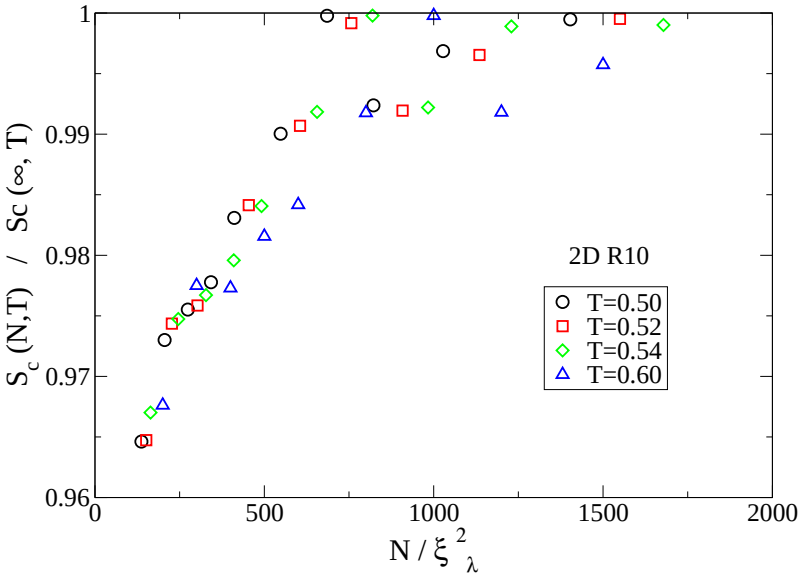

Figure 3.50: The finite size scaling of S_c in the 2D R10 model with the static lengthscale ξ_λ obtained from the vibrational properties of the interaction potential. Although considerable numerical uncertainty is present in extracting the parameter $(S_c(\infty, T)$, the poor data collapse compared to Fig. 3.44 suggests that perhaps ξ_{Sc} and ξ_λ are not same in 2D.

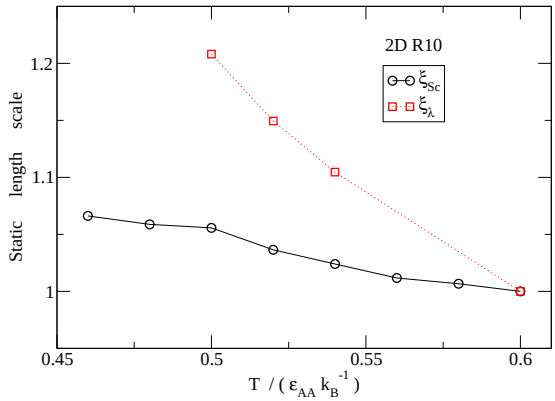

Figure 3.51: Comparison of the static lengthscales ξ_{Sc} and ξ_λ for the 2D R10 model. ξ_{sc} is multiplied by a constant to match ξ_λ at the highest available temperature.

$$\tau(T) \propto \exp\left[\frac{A\xi(T)^\psi}{k_B T}\right] \tag{3.10}$$

We also recall the RFOT relation between the relaxation time $\tau(T)$ and the configurational entropy $S_c(T)$:

$$\tau(T) \propto \frac{1}{k_B T} \left(\frac{Y}{T S_c} \right)^{\frac{\psi}{D-\theta}} \tag{3.11}$$

which defines another exponent $\frac{\psi}{D-\theta}$ which we denote by α. Both the RFOT exponents ψ and θ represents the dependence of energy barrier on lengths, hence they must be non-negative. From Eqns. 3.10 and 3.11 we get the upper bounds on ψ as :

$$\begin{aligned} \frac{\psi}{D-\theta} &\equiv \alpha \\ \psi + \alpha\theta &= \alpha D \\ \psi, \theta, \alpha &> 0 \\ 0 \leq \psi &\leq \alpha D \end{aligned} \tag{3.12}$$

We extract α from a fit of the form $\ln \tau(T) = \ln \tau(\infty) + A/(TS_c)^\alpha$ (Fig. 3.42. We extract ψ using two different fit forms as explained below:

Procedure 1: Rewriting Eqn. 3.10 we get,

$$\begin{aligned} \frac{\tau(T)}{\tau(\infty)} &= \exp\left[\frac{A\xi(T)^\psi}{k_B T} \right] \\ k_B T \left(\ln \frac{\tau(T)}{\tau(\infty)} \right) &= A\xi(T)^\psi \end{aligned} \tag{3.13}$$

Here we use as the estimate of the relaxation time at any temperature T $\tau(T)$, relaxation time value in the limit of infinite system size by extrapolating the finite size data (Figs. 3.30 and 3.19). $\tau(\infty)$ is the relaxation time in the limit of infinite temperature and obtained from the Arrhenius fit to the high T relaxation time data at the highest available system size. Whence ψ is estimated from a linear fit to $\ln \left[k_B T \left(\ln \frac{\tau(T)}{\tau(\infty)} \right) \right]$ *vs.* $\ln \xi_\lambda$.

Procedure 2: We start with the relation between the relaxation time $\tau(T)$ and the static correlation length $\xi_\lambda(T)$ in a form slightly different from Eqn. 3.10 (by a factor of T):

$$\tau(T) \propto \exp\left[\left(\frac{A\xi(T)}{k_B T} \right)^\psi \right] \tag{3.14}$$

Now at some reference temperature $T = T_0$ we choose the value of the correlation length $\xi_0 = 1.0$, that is we define the correlation length in units of this length ξ_0. So the relaxation time at that temperature will be given by

$$\tau(T_0) \propto \exp\left[\left(\frac{A\xi(T_0)}{k_B T_0}\right)^{\psi}\right] \tag{3.15}$$

So we have,

$$\begin{aligned}
\ln\left(\frac{\tau(T)}{\tau(T_0)}\right) &= \left(\frac{A\xi(T)}{k_B T}\right)^{\psi} - \left(\frac{A\xi(T_0)}{k_B T_0}\right)^{\psi} \\
&= \left(\frac{A\xi_0}{k_B T_0}\right)^{\psi}\left[\left(\frac{\xi}{\xi_0}/\frac{T}{T_0}\right)^{\psi} - 1\right] \\
&= B\left[\left(\frac{\xi}{\xi_0}/\frac{T}{T_0}\right)^{\psi} - 1\right]
\end{aligned} \tag{3.16}$$

Here the prefactor B is an unknown. Now ψ can be extracted from fit of $\ln\frac{\tau}{\tau_0}$ *vs.* $x = \frac{\xi}{\xi_0}/\frac{T}{T_0}$

Conclusions: We find that the fitting procedure 2 results in better quality fit. From Fig. 3.42 $\alpha = 0.62$ for the 2D MKA $65:35$ model and $\alpha = 2.1$ for the 2D $R10$ model. So, from the relation 3.12, RFOT predicts that $\psi \leq 0.31$ for the 2D MKA $65:35$ model and $\psi \leq 1.05$ for the 2D $R10$ model. From Figs. 3.52 - 3.55, however, we find that the computed ψ values does not satisfy the relation 3.12, which is inconsistent with the RFOT prediction. In addition, $\psi_{MKA} > \psi_{R10}$ contrary to the above expectation.

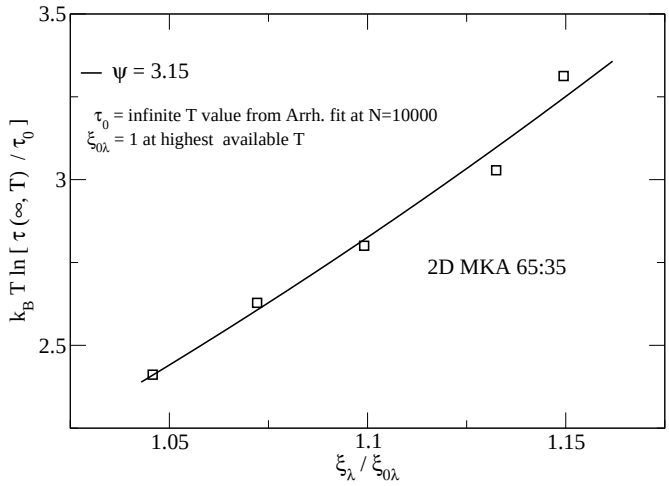

Figure 3.52: The RFOT exponent $\psi = 3.15$ in the 2D MKA 65:35 model obtained using the fitting procedure 1. $\xi_{0\lambda} = 1$ is the value of the correlation length at an arbitrary temperature to make the X-axis dimensionless.

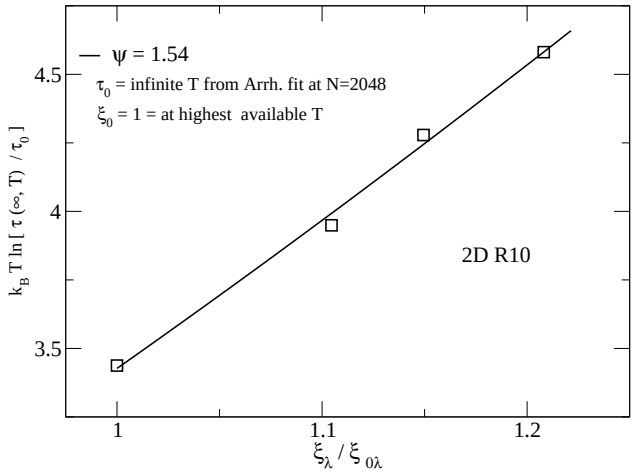

Figure 3.53: The RFOT exponent $\psi = 1.54$ in the 2D R10 model obtained using the fitting procedure 1. $\xi_{0\lambda} = 1$ is the value of correlation length at an arbitrary temperature to make the X-axis dimensionless.

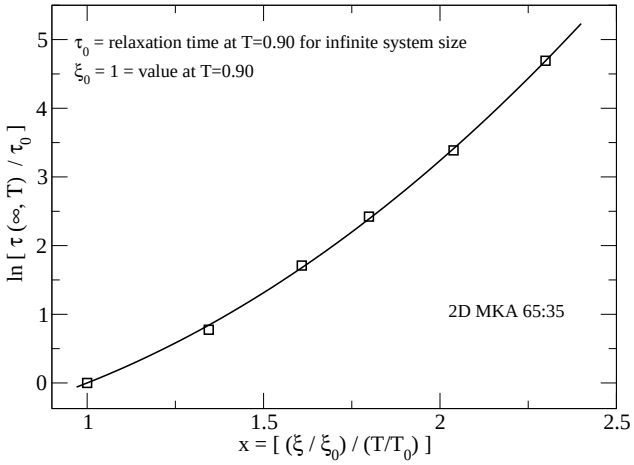

Figure 3.54: The RFOT exponent $\psi = 2.14$ in the 2D MKA 65:35 model obtained using the fitting procedure 2.

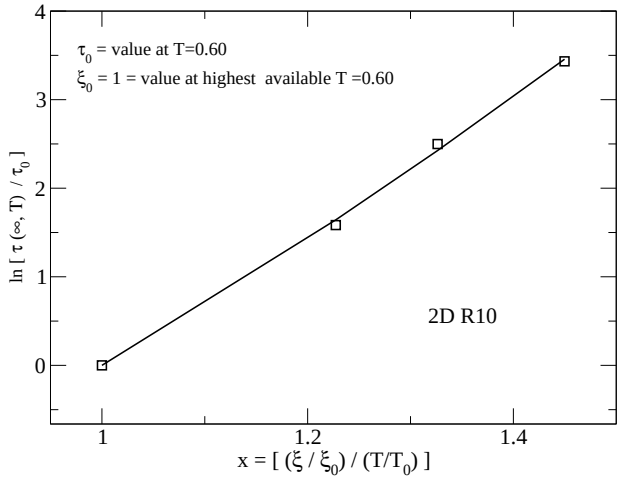

Figure 3.55: The RFOT exponent $\psi = 1.66$ in the 2D R10 model obtained using the fitting procedure 2.

3.9 Summary and conclusions

In summary, we examine the validity of the AG relation in different spatial dimensions by studying model liquids *via* computer simulations, for the first time in 2 and 4 dimensions. The Adam-Gibbs relation is valid in 4 and 3 dimensions, but is not obeyed in 2 dimensions and the nature of the deviation from the AG relation depends on the details of the interaction between particles. The known thermodynamic phase transitions *e.g.* the description of the standard critical phenomena is largely independent of the details of the interparticle interactions. Hence such a lack of universality in the present case is unexpected and surprising since both the Adam-Gibbs and the RFOT theories describe the glass transition as a thermodynamic phase transition. Although an understanding of this observation is lacking at present, they present constraints that a successful theoretical explanation of slow relaxation must meet. Attempts to compute the RFOT exponents from our data remained inconclusive.

Chapter 4

Breakdown of the Stokes Einstein relation in 2,3,4 dimensions

4.1 Introduction

The Stokes-Einstein relation (SER) [83,119,120,122] (independently obtained by Sutherland [121]) is a hydrodynamic relation between the translational diffusion coefficient (D) of a macroscopic Brownian particle of mass m and radius R in a viscous liquid and the shear viscosity (η) of the liquid.

$$D = \frac{mk_B}{6\pi R}\frac{T}{\eta} \tag{4.1}$$

(the factor 6 depends on the boundary condition [83]). In the literature on the SER, Eqn. 4.1, especially in simulations, often the shear viscosity, which involves costly computations, is replaced by the α relaxation time τ, which is computationally cheaper than the shear viscosity. This replacement is subject to the justification that η and τ are mutually proportional. In addition, if the self van Hove function $G_s(r,t)$ is Gaussian and the relaxation time is defined from its Fourier transform $F_s(k,t)$ as $F_s(k,\tau) = 1/e$, then one may deduce that

$$\exp(-Dk^2\tau) = -1/e$$
$$Dk^2\tau = \text{ constant} \tag{4.2}$$

The importance of the SE relation is that (i) the SE relation connects a single particle property to a collective property and (ii) if one knows the T dependence of one quantity, *e.g.* viscosity, in terms of, say, an empirical fitting function involving a set of fit parameters, then one can *predict* the value of the other quantity *using the same set of fit parameters.*

At high temperatures (above melting points), the SE relation is known to be valid for a wide range of liquids and is also known to be applicable for the diffusion of small tracer particles and even for the self diffusion of liquid particles [108]. However, several experiments and simulation studies in the last three decades [84–106, 175] have discovered that in supercooled liquids at low temperatures, the relations between D and η, τ (Eqns. 4.1 and 4.2) break down. In fact this breakdown is so ubiquitous that it is considered to be a signature of slowdown of dynamics [8] of supercooled liquids as the laboratory glass transition temperature (T_g) is approached (see Chapter 1).

One wonders if the temperature at which the breakdown occurs (denoted by T_{SEB}), coincides with already known temperatures characterizing the slow dynamics. Of course, the SE breakdown is a cross-over phenomena and thus T_{SEB} is not sharply defined. Besides, the definition of T_{SEB} depends somewhat on the choice of the way the SE breakdown is represented.

$\mathbf{T_{SEB} \sim T_c}$? Extensive experiments using different methods and both self and tracer diffusion in low molecular weight glass formers like OTP, Silescu and co-workers [6, 85–87], Ediger and co-workers [88, 90, 91] and Rössler [93] have shown that the SE breakdown occurs close to T_g : $T_{SEB} \approx 1.2T_g$. Here the definitions of T_{SEB} are: (i) the temperature of cross-over from the SE relation to the FSE relation [87]; (ii) the temperature at which the measured D decouples from η/T [86, 88, 90, 91]; (iii) the temperature at which $D\tau_c$ starts deviating from constancy [88, 90, 91]; (iv) the temperature at which the derivative $\frac{\partial(1/D\eta)}{\partial(1/T)}$ from $1/D\eta$ *vs.* $1/T$ plot changes sign from positive to negative [93]. In these systems, the apparent divergence temperature T_c predicted by the mode coupling theory is close to $1.2T_g$. For example, for

OTP, which is a prototype fragile glass former, $T_g = 243K$ [86], $T_c \approx 290K$ [123] and the melting point $T_m = 329K$ [123]. Hence these experiments provide compelling evidences that $T_{SEB} \sim T_c$.

$\mathbf{T_{SEB} \sim T_{onset}}$? However, other studies indicate that the SE breakdown can happen at a much higher temperature. In simulations of Kob-Andersen liquid and other binary LJ mixtures [94, 106, 175], the breakdown temperature was found to be close to the onset temperature (T_{onset}) where system dynamics crosses over from Arrhenius to non-Arrhenius behaviour. The onset temperature in the KA liquid in 3D is ~ 1.0 and is much higher than $T_c \sim 0.43$. A simulation of the metallic glass $Cu_{33.3}Zr_{66.7}$ [107] also finds $T_{SEB} \gg T_c$. In these studies, T_{SEB} is the temperature where the radius parameter R in the SER starts deviating from constancy.

Values of the breakdown exponent: Another interesting question is the observed values of the breakdown exponent ξ in the fractional SE relations, which quantifies how strong is the deviation from the SE behaviour. Besides, a complete theory of the SE breakdown should be able to *predict* the breakdown exponent. Table 4.1 below is a representative list (arranged chronologically) of the values of ξ found in the literature. In most cases the value of the exponent lies between $0.7 - 0.8$. For further compilation, see also Table I of Ref. [109].

Table 4.1: Breakdown exponents for the fractional Stokes Einstein relations.

Reference	System	Relations defining exponent	Exponent value
G. L. Pollack, (1981), [84]	Diffusion of Xe atoms through aqueous solution of sucrose	$D \propto \eta^{-\xi}$	$\xi = 0.63$
G. Heuberger and H. Silescu, (1996) [87]	Various combination from a set of 5 tracer molecules and 10 Solvent glass formers	$D \propto T/\eta^{\xi}$	ξ in the range $0.7 - 1.1$. Cross-over to normal ($\xi = 1$) SER as T increases.

Reference	System	Relations defining exponent	Exponent value
M. Ediger, (2000) [6]	OTP	$D_t \propto \eta^{-\alpha_t}$ (t=translation) $D_r \propto \eta^{-\alpha_r}$ (r=rotation)	$\alpha_t = 0.75$ $\alpha_r = 1$
S. R. Becker, P. Poole and F. Starr, (2006) [102]	ST2 water	$D \propto \left(\frac{\tau}{T}\right)^{-\xi}$	ξ in the range $0.7-0.8$. Cross-over to normal ($\xi = 1$) SER as T increases.
S. Chen *et al.*, (2006) [101]	Water	$D \propto \tau^{-\xi}$ (τ is translational relaxation time)	$\xi = 0.74$ in fragile phase and $\xi = 2/3$ in strong phase.
F. Fernandez-alonso *et al.*, (2007) [103]	Hydrogen Fluoride	$D \propto \left(\frac{\eta}{T}\right)^{\xi}$	$\xi = 0.71$. Cross-over to normal ($\xi = 1$) SER as T increases.
L. Xu *et al.*, (2009) [105]	Water	$D \propto \left(\frac{\tau}{T}\right)^{-\xi}$	$\xi = 0.62$. Cross-over to normal ($\xi = 1$) SER as T increases.

4.1.1 The SE breakdown as an indicator of heterogeneity

The predominant view in the literature is that some kind of heterogeneity which develops as liquids are supercooled, is responsible for the SE breakdown. It is natural to consider the dynamical heterogeneity which develops as liquids are supercooled to be the origin of the SE breakdown. However we note that the many different theories proposed to explain the SE breakdown, *e.g.* the dynamical facilitation model [110], the random first order transition theory [111], the shear transformation zone theory [112] and the obstruction model [109] mutually disagree about the nature and the origin of the heterogeneities. In the present thesis our aim is to understand the relation between the dynamical heterogeneity and the SE breakdown. Here we briefly discuss phenomenological arguments why the SE breakdown is considered to be an

indicator of heterogeneity.

In a *homogeneous* liquid the $G_s(r,t)$ is Gaussian which leads to $D\tau = constant$, (Eqn. 4.2), which may be considered as the normal, high temperature behaviour. Similarly, the *homogeneous* mode coupling theory, which is one of the most successful microscopic theories of supercooled liquids, predicts power law T dependence of D and τ with *the same exponent* and T_c: $D \propto (T - T_c)^{\gamma}, \tau \propto (T - T_c)^{-\gamma}$ leading to $D\tau = constant$.

One of the earliest theories of the SE breakdown is by Hodgdon and Stillinger [108] who imagined that the highly viscous supercooled liquid is composed of sparse "fluid-like" regions of low viscosity in a matrix of more viscous fluid. Thus both D and η are space-dependent. By calculating the viscous drag force on the diffusing particle in the "fluid-like" region they showed that the local drag force decreases from the Stokes' value, hence the local diffusion coefficient increases. Hence if one uses the bulk viscosity (which is dominated by the more viscous regions) in the SER, one expects a breakdown. In order to apply their model to realistic systems and to explain that the translational diffusion coefficient shows breakdown while the orientational diffusion coefficient does not, they had to impose certain special properties on their model. However, Tarjus and Kivelson [96] later gave a simple argument that *the mere existence of domains is a sufficient condition for the SE breakdown.* They considered that there are domains (of unspecified nature) of size L with a size distribution $\rho(L)$ such that $\rho(L)L^2dL$ is the probability of finding a molecule in a domain of size between L and $L + dL$. They assumed that the local relaxation time $\tau(L)$ in a domain is size dependent and the measured α relaxation time (τ_α) is the average of $\tau(L)$:

$$\begin{aligned} \tau_L &\propto \exp(E(L)/k_BT) \\ \tau_\alpha = \langle \tau_L \rangle &\propto \int_0^\infty \rho(L) \exp(E(L)/k_BT) L^2 dL \end{aligned} \tag{4.3}$$

In their picture, the SER is *valid inside a domain.* However, the translational diffusion involves passage through *many* domains. This is the reason that the *average* D is different from the SER prediction. Assuming that a diffusing particle performs a random walk across domains and the $D(L)$ changes

abruptly at interfaces, then neglecting a term involving gradient of D:

$$\begin{aligned} D(L) &\propto T/\eta(L), \eta(L) \propto \exp(E(L)/k_BT) \\ D = \langle D(L) \rangle &\propto \int_0^\infty \rho(L) D(L) L^2 dL \\ &\propto \int_0^\infty \rho(L) \exp(-E(L)/k_BT) L^2 dL \end{aligned} \tag{4.4}$$

Unless $\rho(L)$ is a δ function, Eqns. 4.3 and 4.4 lead to a violation of the normal behaviour $D\tau = constant$. Tarjus and Kivelson picture of the heterogeneity may also be interpreted in terms of the existence of a distribution of local relaxation times. Blackburn *et al.* [89] argued that the translational diffusion coefficient D and the rotational correlation time τ_c measure different moments of the distribution, thus causing the SE breakdown:

$$\begin{aligned} D &\propto \langle \frac{1}{\tau} \rangle, \tau_c = \langle \tau \rangle \\ D\tau_c &\propto \langle \tau \rangle \langle \frac{1}{\tau} \rangle \\ \langle \tau \rangle \langle \frac{1}{\tau} \rangle &= 1 \text{ for } \delta \text{ distribution, normal SE} \\ &> 1 \text{ SE breakdown} \end{aligned} \tag{4.5}$$

La Nave *et al.* showed [180] using the potential energy landscape framework, that in the 3D KA model the product $< D >< 1/D >$ indeed grows as the temperature decreases. Swallen *et al.* [91] argued that since $D\tau_c$ increases with decreasing temperature, Eqn. 4.5 implies that the distribution of relaxation time should be *broader at lower* T. The stretched exponent β_{KWW} provides a measure of the width of the distribution. Let $\rho(\tau)$ denote the distribution of relaxation times τ where each of the local relaxation function is exponential (with relaxation time τ). The overall correlation function $\phi(t)$ is empirically given by a stretched exponential:

$$\phi(t) = \int_0^\infty d\tau \rho(\tau) \exp(-t/\tau) = \exp\left(-(t/\tau_{KWW})^{\beta_{KWW}}\right) \tag{4.6}$$

Using the following two identities [21]:

$$\begin{aligned}\int_0^\infty dt t^{n-1}\phi(t) &= \int_0^\infty dt t^{n-1}\int_0^\infty d\tau\rho(\tau)\exp(-t/\tau) \\ &= \int_0^\infty d\tau\rho(\tau)\int_0^\infty dt t^{n-1}\exp(-t/\tau) \\ &= \int_0^\infty d\tau\rho(\tau)\tau^n\Gamma(n) \\ &= \langle\tau^n\rangle\Gamma(n) \end{aligned} \tag{4.7}$$

$$\begin{aligned}\int_0^\infty dt t^{n-1}\exp(\left(-(t/\tau_{KWW})^{\beta_{KWW}}\right) &= \tau_{KWW}^n\int_0^\infty y^{n-1}\exp\left(-y^{\beta_{KWW}}\right)dy \\ &= \frac{\tau_{KWW}^n}{\beta_{KWW}}\Gamma\left(\frac{n}{\beta_{KWW}}\right) \end{aligned} \tag{4.8}$$

we get,

$$\langle\tau^n\rangle = \frac{\tau_{KWW}^n}{\beta_{KWW}}\frac{\Gamma\left(\frac{n}{\beta_{KWW}}\right)}{\Gamma(n)} \tag{4.9}$$

Using the above formula, we can find the first moment $\langle\tau\rangle$ and the second moment $\langle\tau^2\rangle$. Hence the *relative* variance, which provides a measure of the width of the distribution, is given by:

$$\frac{\langle\tau^2\rangle - \langle\tau\rangle^2}{\langle\tau\rangle^2} = \frac{1}{\Gamma\left(\frac{1}{\beta_{KWW}}\right)}\left[\frac{\beta_{KWW}\Gamma\left(\frac{2}{\beta_{KWW}}\right)}{\Gamma\left(\frac{1}{\beta_{KWW}}\right)} - \Gamma\left(\frac{1}{\beta_{KWW}}\right)\right] \tag{4.10}$$

From the RHS, the *relative* variance depends *only* on β_{KWW} and Fig. 4.1 shows that it *increases monotonically as* β_{KWW} *decreases.*

The above analysis suggests the following interpretation: as the temperature decreases, heterogeneity (of unspecified nature) develops which leads to the existence of a *distribution* of local relaxation times, the width of which *increases* as T decreases which is manifested as (i) the lowering of β_{KWW} *and* (ii) the SE breakdown. In other words, *the SE breakdown is a manifestation of heterogeneity and so also is the lowering of* β_{KWW} *from 1, hence they should occur simultaneously.*

We note, however, the following two points: (i) the lowering of β_{KWW} does

not *prove* the existence of a distribution of relaxation times [21] *i.e.* liquids at low temperature can be dynamically homogeneous with a single relaxation time but inherently non-exponential decay of correlation function and (ii) some experiments on OTP seem to suggest that β_{KWW} remains in fact *constant* in the relevant low temperature range (See [91] and references therein). In that case the width of distribution does not change with temperature hence Eqn. 4.5 can not explain that the degree of the SE breakdown becomes progressively larger as temperature decreases.

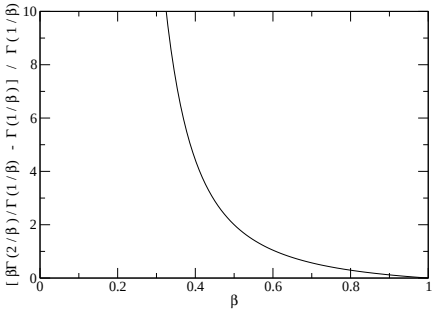

Figure 4.1: The quantity $\frac{\langle\tau^2\rangle-\langle\tau\rangle^2}{\langle\tau\rangle^2}$ *vs.* β. See Eqn. 4.10 and the accompanying text.

4.1.2 Other indicators of dynamical heterogeneity

The dynamical heterogeneity can be measured by more direct indicators. In the present thesis, we have used the following quantities in addition to the SE breakdown to characterize the dynamical heterogeneity.

Dynamical Susceptibility χ_4: The dynamical susceptibility $\chi_4(t)$ (see Chapter 1) measures the integral of the four-point correlation function $g_4(\vec{r},t)$ as well as the *fluctuation* in the two-point correlation function $q(t)$ (overlap function). Thus $\chi_4(t)$ is a direct measure of the dynamical heterogeneity. for supercooled liquids, $\chi_4(t)$ show a peak at a timescale proportional to the α relaxation time [67]. The peak of the dynamical susceptibility - χ_4^{peak} - is a *direct* measure of the volume of space correlated during structural relaxation [13]. Experiments and simulations, *typically in three dimensions*, show that $\chi_4^{\text{peak}}(T)$ grows monotonically as the temperature T is lowered, which indicates that bigger regions of space are dynamically correlated at

lower temperature i.e. *the dynamical heterogeneity is more prominent at lower temperature.*

Stretched Exponent β_{KWW}: The stretched exponent β_{KWW} is a measure of how non-exponential the decay of time correlation function (See Chapter 1). As discussed in the previous section, according to the heterogeneous interpretation of the non-exponential decay, *lower value of β_{KWW} implies stronger dynamical heterogeneity.*

Fragility: Fragility (see Chapter 1) is a material parameter that measures how rapidly the viscosity (or relaxation time) of supercooled liquids increases as the temperature decreases. Böhmer *et al.* [126] in their extensive compilation of available literature data found that the kinetic fragility m (defined from the slope of the Angell plot at T_g) has negative correlation with the stretched exponent β_{KWW}, *i.e.*, lower β_{KWW} implies more fragile liquids. This conclusion remains same for both isobaric and isochoric fragilities [118]. Based on the above-mentioned correlation between fragility and β_{KWW}, fragility can be considered an indicator of the dynamical heterogeneity - *more fragile systems are more heterogeneous.*

However, we note that there are evidences against this correlation as well : (i) In the experiment on supercooled water confined in nanopore, Chen *et al.* [101] observed fragile to strong transition and found fractional SE relations in both the regimes. However, the breakdown exponent is closer to 1 for fragile water (= 0.74) than that for strong water (= 0.67). (ii) Similarly, the breakdown exponent *computed* by Jung *et al.* [110] using dynamical facilitation theory was also closer to 1 for a fragile (= 0.73) glass-former model than for a strong glass-former (= 0.67) model. (iii) In [72] it was shown that the strong correlation found by Böhmer *et al.* [126] between the kinetic fragility and β_{KWW} becomes much weaker if subgroups *e.g. only* simple and complex molecular glass-formers are considered. (iv) Dyre also claimed [14] based on experiments on simple, organic glass-forming liquids that no clear correlation is present between these two quantities. (v) In the simulation of ST2 water, Becker *et al.* [102], observed the breakdown of SE relation at low T in both strong and fragile regime. However they found that the breakdown exponent is nearly same for both strong and fragile water.

4.1.3 Relations among heterogeneity, SE breakdown and fragility in 3D

Here we summarize the picture that emerges based on the above discussions. As the temperature decreases, the dynamics of a supercooled liquid becomes gradually more heterogeneous (bigger $\chi_4^{\rm peak}(T)$). This is manifested in the breakdown of SE relation as well as the value of the stretched exponent being less than 1 - stronger heterogeneity implies stronger breakdown as well as lower value of β_{KWW}. Besides, at the same (scaled) temperature, systems which are more fragile are more heterogeneous. Based on this picture, the trends expected for the SE breakdown are : (i) lower β_{KWW} implies stronger SE breakdown as found by Blackburn *et al.* [89] and (ii) more fragile liquids show stronger breakdown of SE relation [13].

We, however, emphasize that the above picture is based on experiments and simulations predominantly in *three dimensions* and does not tell *a priori* about behaviours in other spatial dimensions.

4.1.4 Previous works in other spatial dimensions

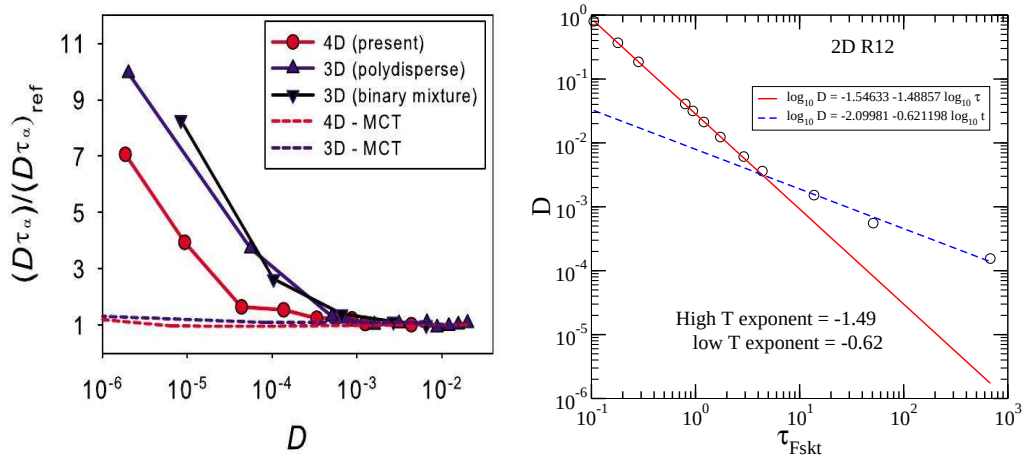

Figure 4.2: Fig. 4.2(a): The breakdown of SE relation in three and four dimensional hard sphere models show that the SE breakdown is weaker at higher dimensions. Fig. taken with permission from [116]. Fig. 4.2(b): A fractional SE relation dimensions. $D \propto \tau^{-\xi}$ is a good description of data in two dimensions at *both* low *and* high temperatures, implying the behaviour is more complicated in two dimensions. Data taken with permission from [117].

We briefly discuss previous works on the SE breakdown in other spatial dimensions. Eaves *et al.* [115] studied the SE breakdown in the Kob Andersen model in three and four spatial dimensions *at similar fragility* and found that in both 3 and 4D, a fractional SE relation $D \propto \tau^{-1+w}$ described data well with the breakdown exponent smaller in 4D ($w = 0.14$) than in 3D ($w = 0.16$) implying that *the SE breakdown is weaker in higher dimensions*. Charbonneau *et al.* [116] also found that the mono-dispersed hard sphere in 4D show weaker deviation from the MCT prediction (no SE breakdown) than bi- and poly-dispersed hard sphere models in 3D, see Fig. 4.2(a). In both the studies, the breakdown of SE relation was reported as the *only* indicator of the dynamical heterogeneity and it was concluded that *the heterogeneity decreases in higher dimensions*. In lower dimensions, Perera *et al.* have studied the SE breakdown in a binary mixture of repulsive soft spheres ($V(r) \sim r^{-12}$). Their data (see Fig. 4.2(b)) can be described by a fractional SE relation $D \propto \tau^{-\xi}$ at low temperatures ($\xi = -0.62$) *as well as* at high temperatures ($\xi = -1.49$) implying the normal SE relation is not obeyed at any temperatures. This indicates that the behaviour in two dimensions may be more complicated than in three and higher dimensions.

4.1.5 Our aim

In the present thesis, based on the observations in *three* dimensions about the relations among dynamical heterogeneity, the SE breakdown and the fragility, we aim to understand how such inter-relations may be generalized in other spatial dimensions by systematically studying model glass-forming liquids in 2,3 and 4 dimensions and by considering *both* the SE breakdown *and direct* measures (χ_4, β_{KWW} as well as fragility) as indicators of DH.

4.2 Simulation details

We perform NVT molecular dynamics simulations in the Kob-Andersen binary LJ mixture at the 80 : 20 composition in 4, 3 and 2 dimensions (denoted by 4DKA, 3DKA, 2DKA respectively) at number densities $\rho = 1.60$ (4D), $\rho = 1.20$ (3D and 2D). In addition, we have also studied the following models: (i) the modified Kob-Andersen model in 2 dimensions (denoted by 2DMKA) at the same number density $\rho = 1.20$ but a different composition 65 : 35 and (ii) the 50:50 binary mixture of purely repulsive soft sphere potential ($V(r) \sim r^{-10}$, denoted by 2DR10) at a number density $\rho = 0.85$. The details of the models are described in Appendix B.

4.3 Validation of the computation of the shear viscosity η:

The shear viscosity η is computed using the Green Kubo and the Einstein relations for 3D KA model. Since numerical accuracy is an important issue we discuss below the computational details and the checks used to validate the computation:

1. It is checked that both the stress (pressure) tensor and the Helfand moment tensor are symmetric tensor.

2. The average trace of the stress tensor matches with the average pressure obtained using virial equation.

3. Both the diagonal and the off-diagonal elements of the Helfand moments computed using two-point trapezoidal rule and five-point Boole's rule matches with each other.

4. It is checked that the Helfand moment tensor has a well-defined linear regime at long time and the cumulative sum of the stress autocorrelation function reaches a plateau value around the time when the stress autocorrelation first decays to zero (See Figs. 4.3, 4.4) .

5. The shear viscosity computed from Green-Kubo relation and from Einstein relation should agree with each other. (See Fig. 4.5).

6. We also compare the shear viscosity values with earlier computations [94, 106, 175] for the same system. (See Fig. 4.5).

4.3.1 Details of the statistics

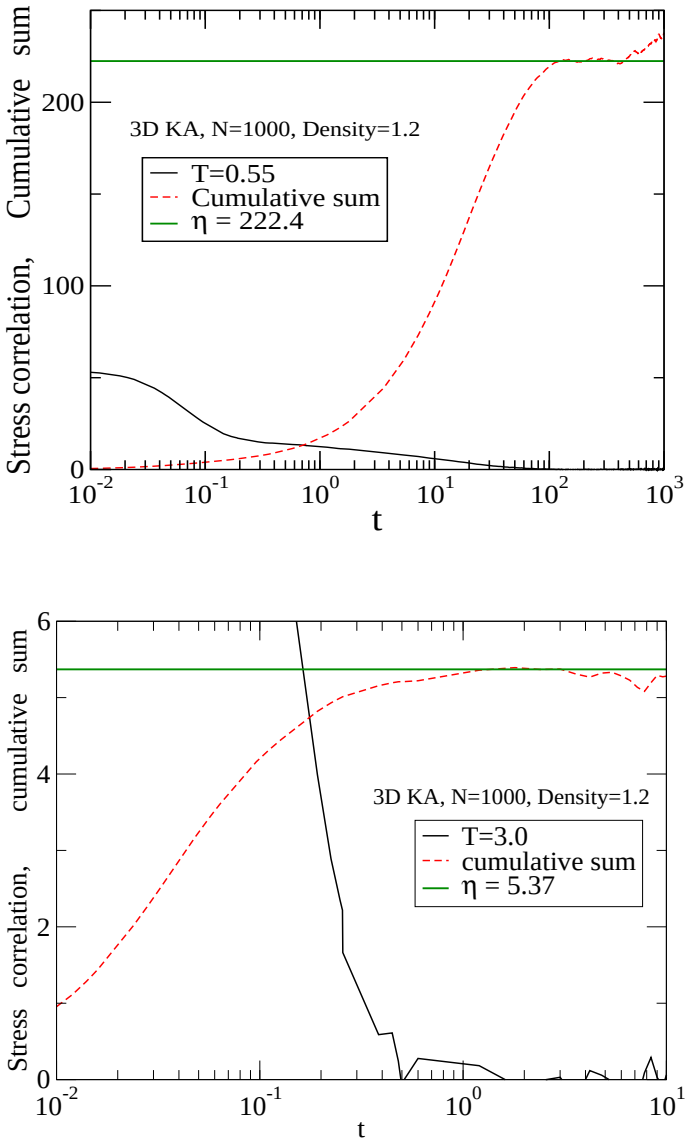

Figure 4.3: Stress correlation function and its cumulative sum at $T = 0.55$ and $T = 3.0$. There is an approximate plateau in the cumulative sum around the time when correlation function first decays to zero. The height of this plateau is considered to be the value of the shear viscosity.

Table 4.2: Simulation details for the computation of the shear viscosity for 3D KA model at density $\rho = 1.20$ and system size $N = 1000$ using NVT MD runs. In order to improve numerical accuracy for the integrations involved (Helfand moment and cumulative sum of stress-auto correlation function), the time step dt at low T (= 0.003) is taken lower than what has been used previously (typically $dt = 0.005$) for other analyses. The number of time origins in the columns refer to the number of time origins over which averaging is done at the time point when stress correlation function is less than zero *for the first time* (Green Kubo method) and in the linear region of Helfand moment used to measure slope (Einstein method). This is an indicator of the quality of statistics.

T	No. of independent MD runs	Runlength (MDsteps, m=million)	$\frac{\mathrm{dt}}{\sigma_{AA}\epsilon_{AA}^{1/2}m_{AA}^{-1/2}}$	No. of time origins (GK)	No. of time origins (Einstein)	Relaxation time from overlap function $\frac{\tau_{qt}}{\sigma_{AA}\epsilon_{AA}^{1/2}m_{AA}^{-1/2}}$
0.55	10	51 m(1 run), 60 m (1 run), 120 m (8 runs)	0.003	$>$ 85000(50m), $>$ 99900(60m), $>$ 199900(120m)	$>$ 94400	55.8
0.60	10	60 m	0.003	$>$ 99900	$>$ 94400	23.2
0.65	8	60 m	0.003	$>$ 99900	$>$ 94400	13.1
0.70	10	60 m	0.003	$>$ 99900	$>$ 94400	8.3
0.80	10	60 m	0.003	$>$ 99900	$>$ 98300	4.4
0.90	10	60 m	0.001	$>$ 99900	$>$ 98300	2.8
1.00	10	60 m	0.001	$>$ 99900	$>$ 99500	2.1
1.20	10	40 m (1 run), 60 m (9 runs)	0.001	$>$ 68300(40m), $>$ 99900(60m)	$>$ 98600	1.3
1.40	5	60 m	0.001	$>$ 99900	$>$ 99800	0.94
1.80	5	60 m	0.001	$>$ 99900	$>$ 99800	0.62
2.50	5	60 m	0.001	$>$ 99900	$>$ 99800	0.40
3.00	5	60 m	0.001	$>$ 99900	$>$ 99800	0.34

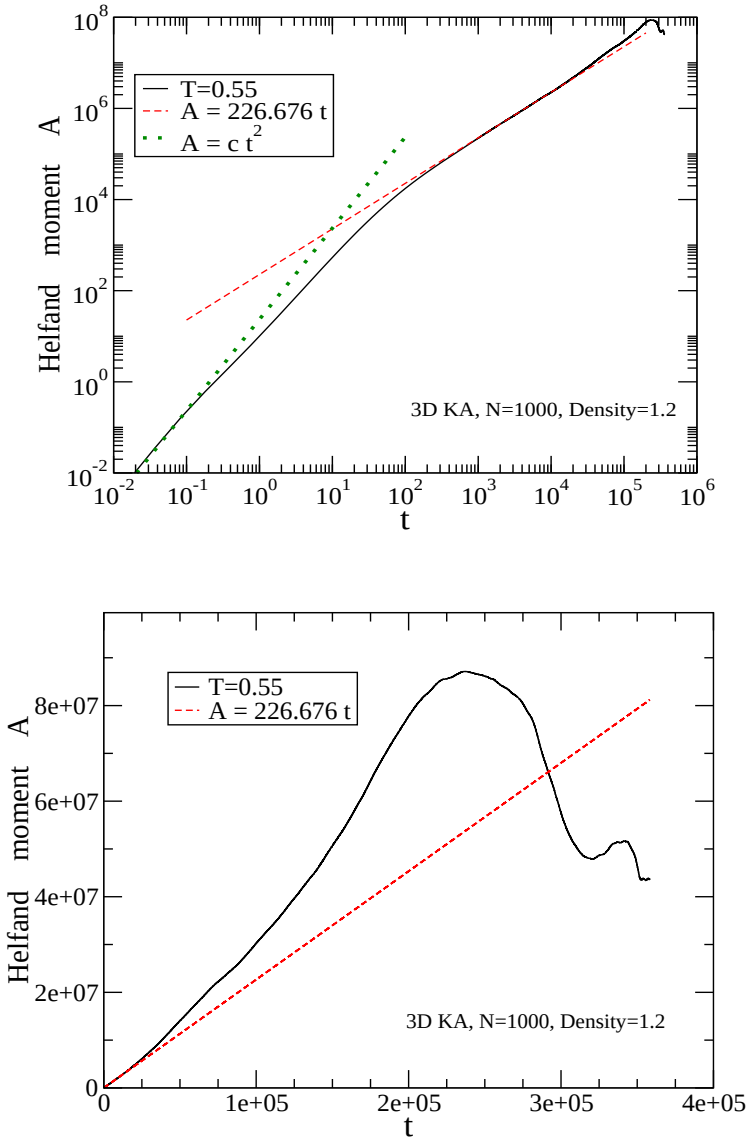

Figure 4.4: Helfand moment at $T = 0.55$ in log-log (top) and linear (bottom) plots . At short time, t dependence is close to quadratic (like ballistic regime in normal MSD) and at longer time scale crosses over to linear t dependence. The slope of dashed curve of the form $A = \eta t$ fitted in the linear region at long time gives the shear viscosity η.

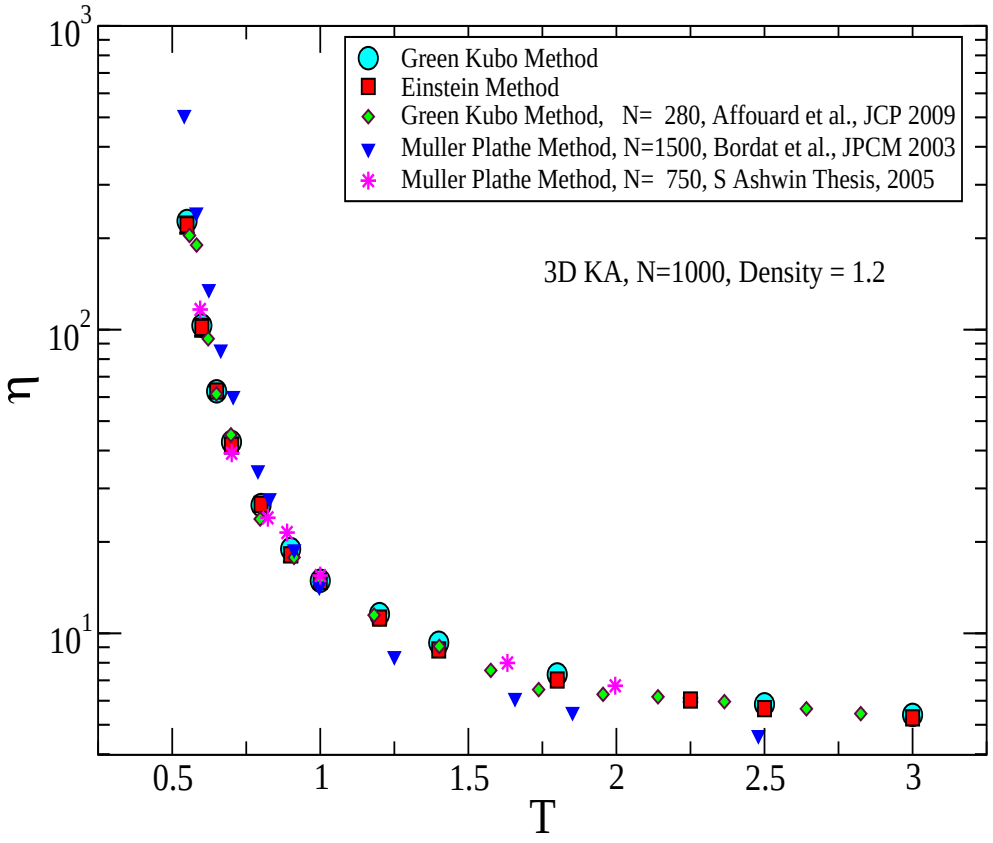

Figure 4.5: T dependence of the shear viscosity in 3D KA model at density=1.2 from various studies. The shear viscosity obtained from the Green Kubo (circle) and the Einstein (square) method in the present study are shown with error bars. The error bars denote standard deviation about the mean value. It is seen that they match with each other. Further, the values in the present study are comparable with earlier studies of Affouard *et al.* [106] using Green Kubo method (diamond) and S. Ashwin [94] using Müller-Plathe method (star). The T dependence obtained by Bordat *et al.* [175] using Müller-Plathe method (triangle) is somewhat different.

4.4 Results: Comparison of time scales

Many different timescales (see Chapter 1) are defined to characterize the slow dynamics and the dynamical heterogeneity in particular. A critical examination of the inter-relation between different time scales is important to understand the nature of the dynamical heterogeneity [181]. In studies of the SE breakdown, the shear viscosity (η) is often replaced by an appropriate relaxation time (τ). However, to justify such a replacement, one needs to find the relation between η and τ. By definition, the shear relaxation time ($\tau_{shear} = \frac{\eta}{G_\infty}$, G_∞ is the infinite frequency shear modulus) is related to η in a straightforward way *v*ia the Maxwell's relation, but the relation between the shear viscosity and the α relaxation time (τ_α) is not obvious. In literature, there is an *implicit* assumption that they are mutually proportional, but one finds an ambiguity whether $\eta \propto \tau_\alpha$ (*e.g.* [72, 102, 113]) or $\eta \propto \frac{\tau_\alpha}{T}$ (*e.g.* [114]). This point is important because (i) the factor of T makes a *qualitative* as well as a *quantitative* difference as we will show below. (ii) If $\eta \propto \tau_\alpha/T$ then the relations $D\eta/T = constant$ and $D\tau_\alpha = constant$ can be treated on equal footing. Although, we note that the derivations of $D\eta/T = constant$ and $D\tau_\alpha = constant$ are completely independent and hence no connection between these two relations is *a priori* expected. In the present section we present a systematic comparison of different characteristic time scales using 3D and 4D KA models.

List of the different timescales considered: In the present study, we consider the following time scales (see Chapter 1 for details):

1. The shear viscosity from the Einstein and the Green-Kubo relations .

2. α relaxation times estimated from (i) the time taken to decay to $1/e$ of the initial value of (a) the overlap function $q(t)$, (b) the intermediate scattering function $F(k,t)$, and (c) the self part of the intermediate scattering function $F_s(k,t)$.

3. The time scale of the dynamical heterogeneity estimated as the time at which the "dynamical susceptibility" $\chi_4(t)$ is maximum. This time scale is another measure of τ_α.

4. The translational diffusion coefficient D.

5. The time scale t^* at which the non-Gaussian parameter $\alpha_2(t)$ reaches a maximum. This time scale is a different measure of the time scale of heterogeneity.

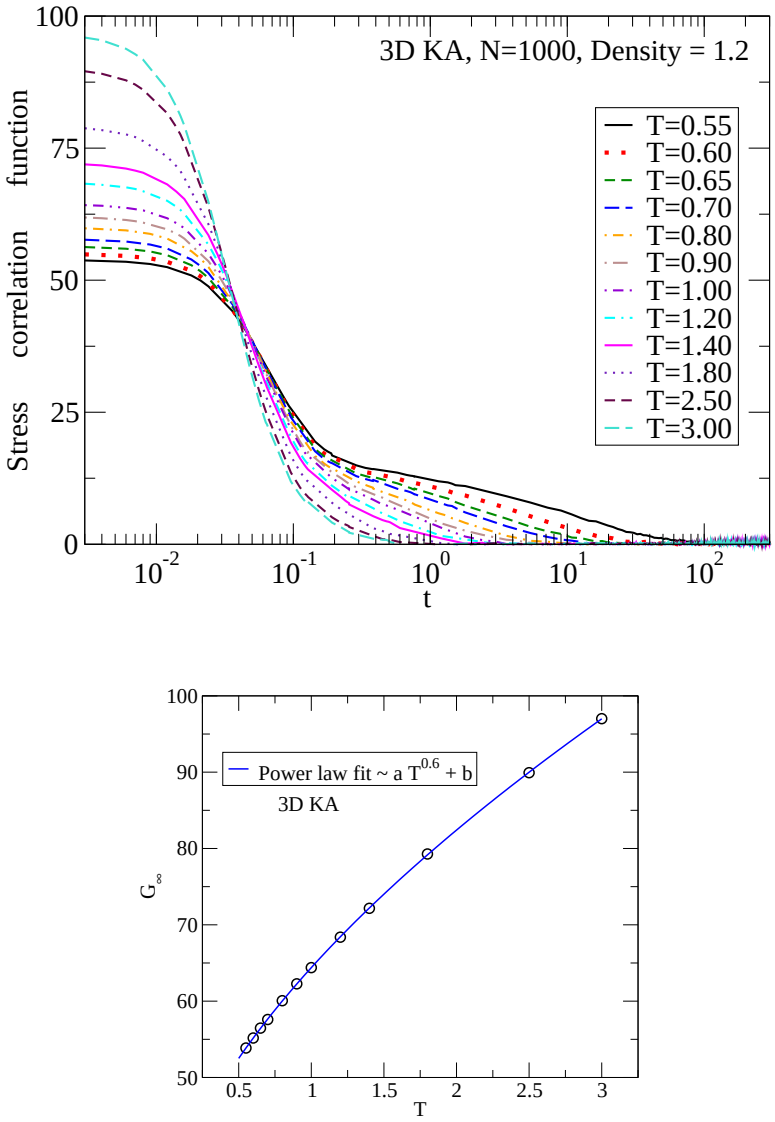

Figure 4.6: Top : The component-averaged stress correlation functions (Eqn. 2.21) at different T in 3D KA model. Bottom: The T dependence of the instantaneous shear modulus G_∞ computed as $t = 0$ value of the stress correlation function. The solid line is a power law fit of the form $G_\infty = aT^b + c$

$\eta \not\propto \tau_{\mathbf{shear}}$: First, we compare τ_{shear} with η. Fig. 4.6 shows the T dependence of the decay of the stress correlation functions ($C(t)$). The $t = 0$ values of the stress correlation functions $C(0)$ give the G_∞. Fig. 4.6 also

shows that G_∞ has a significant T dependence. Hence one should not expect that $\tau_{shear} \propto \eta$. Fig. 4.7 compares the T dependence of the shear relaxation time τ_{shear} with that of the shear viscosity η and clearly shows that *the shear viscosity and the shear relaxation time are not mutually proportional.*

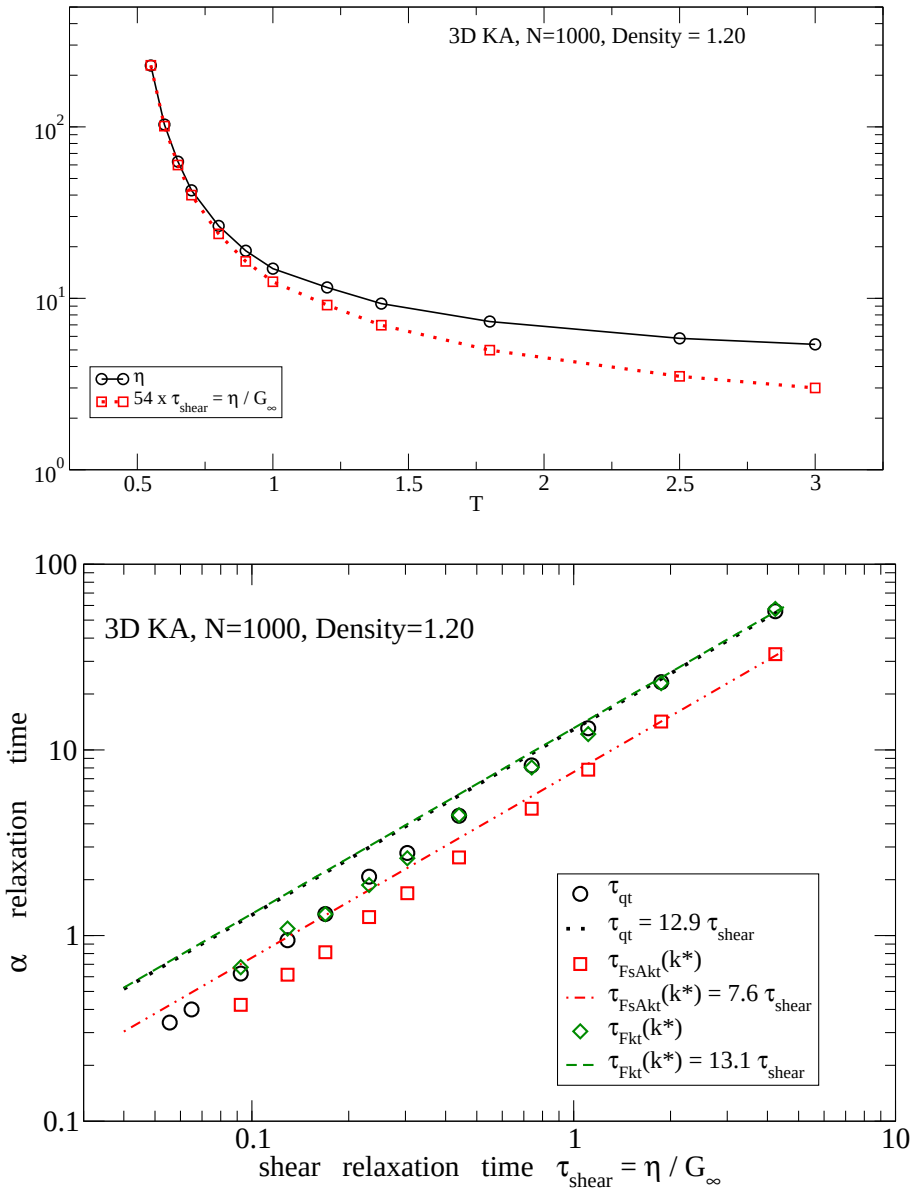

Figure 4.7: Top: T dependence of viscosity (η) and shear relaxation time $\tau_{shear} = \eta/G_\infty$ Lines are guide to eyes. All data sets are matched at $T = 0.55$. The shear relaxation time is *not* proportional to η because G_∞ changes with T. Bottom: α relaxation time is *not proportional* to the shear relaxation time. Lines are fit of the form $y = mx$. Three measures of τ_α are compared. k^* is the value corresponding to the first peak of the structure factor.

$\tau_{\mathbf{shear}} \not\propto \tau_\alpha$**:** Second, we compare in Fig. 4.7 the shear relaxation time ($= \frac{\eta}{G_\infty}$) with the α relaxation time measured from the decay of (a) the overlap function (τ_{qt}), (b) the self intermediate scattering function ($\tau_{Fskt}(k^*)$) and (c) the intermediate scattering function ($\tau_{Fkt}(k^*)$) (k^* is the first peak of the structure factor). We see that *the shear relaxation time is not proportional to the α relaxation time*. However, we highlight that Fig. 4.8 shows that the *three measures of the α relaxation time are mutually proportional*.

$\tau_\alpha \propto \eta/\mathbf{T}$**:** Third, we show in Fig. 4.8 that *empirically $\tau_\alpha \propto \eta/T$ is a good description of data* although some systematic deviations can be seen at high T.

$\mathbf{t}^* \propto (\mathbf{D}/\mathbf{T})^{-\mathbf{1}}$**:** Fourth, we consider the time scale (t^*) of the maximum of the non-Gaussian parameter $\alpha_2(t)$, which is expected to be related to the diffusion coefficient. In Fig. 4.9, which is for 4D KA model, by comparing different time scales and MSD, we show that (i) t^* can be considered as the onset time of the diffusive regime which is already noted in literature [31] and (ii) $t^* \propto (D_A/T)^{-1}$. (D_A is the diffusion coefficient of the A particles.)

Summary: Finally, in Fig. 4.10, we show the T dependence of the following different characteristic time scales in 3D KA model: (a) the self diffusion coefficients of the A particles D_A^{-1}; (b) the viscosity in the form $\frac{\eta}{T}$; (c) the α relaxation times (τ_{qt}, $\tau_{Fskt}(k^*)$, $\tau_{Fkt}(k^*)$; (d) the time scale τ_4 of the heterogeneity obtained from the maximum of the dynamic susceptibility $\chi_4(t)$ and (e) the time scale t^* of the heterogeneity obtained from maximum of the non-Gaussian parameter $\alpha_2(t)$. The different data sets are matched at a low T. It shows there are differences in high T and low T behaviour which indicates a breakdown of the SER.

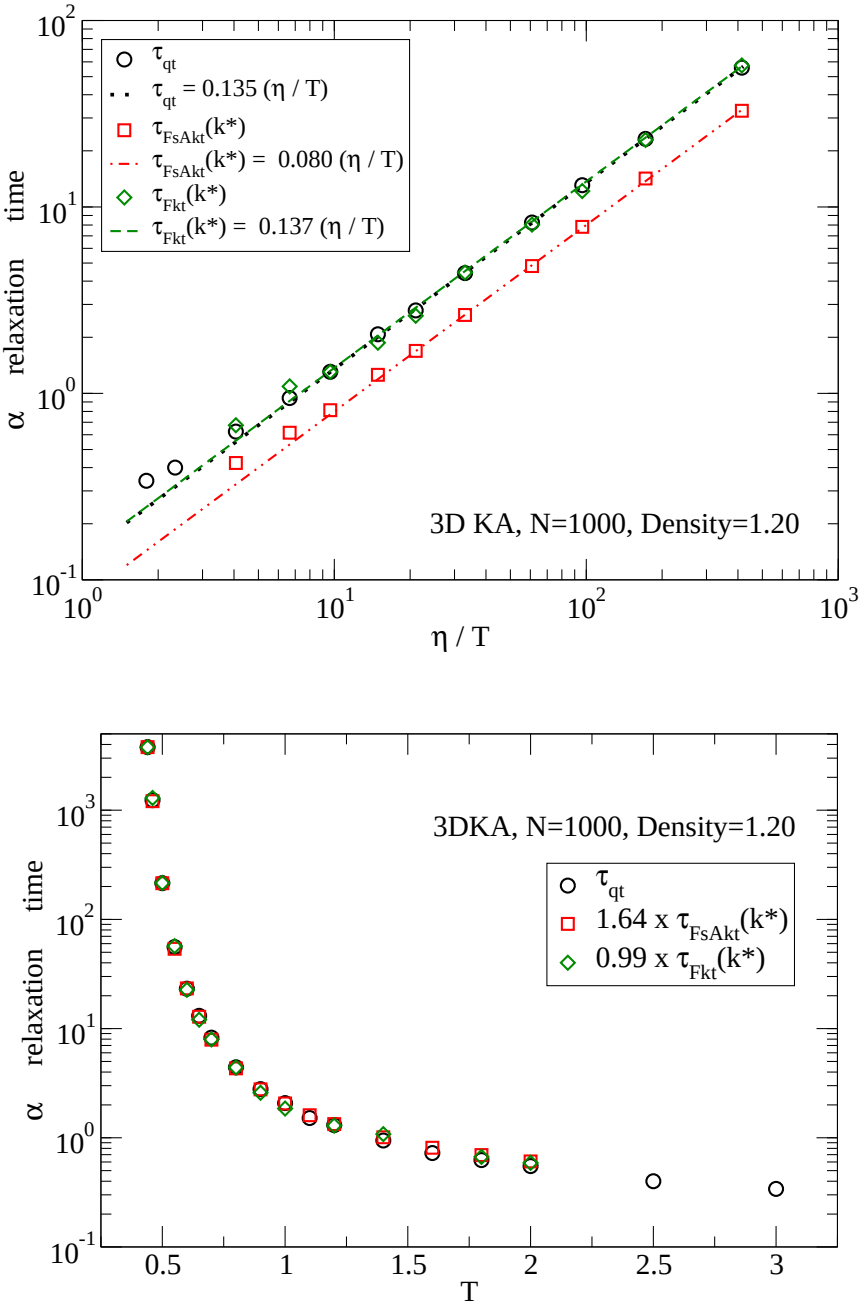

Figure 4.8: Top: $\tau_\alpha \propto \eta/T$ is a good description of data at low T in 3D KA model. Systematic deviations are seen at high T. Bottom: The three measures of τ_α are mutually proportional.

4.5 Results: The dimension dependence of the SE breakdown

4.5.1 Observed trends

The breakdown of the SER in three dimensions in 3D Kob-Andersen (KA) model has been reported before [94, 106, 175]. Our data agree reasonably

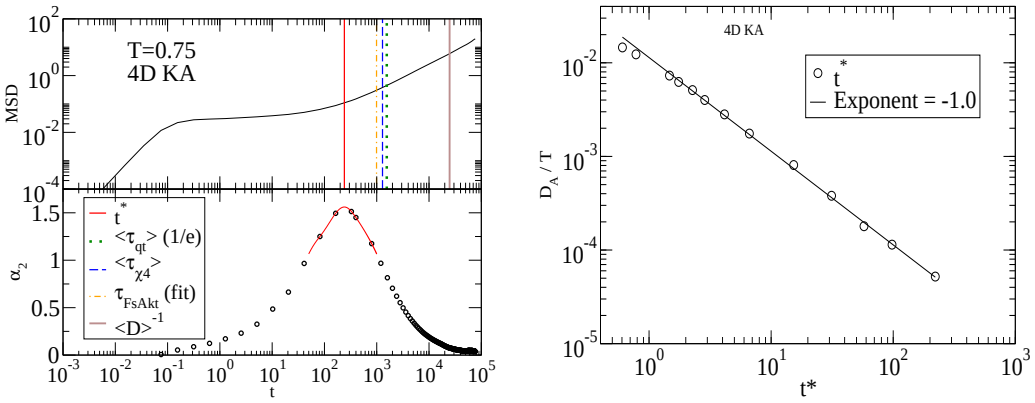

Figure 4.9: Left: Comparison of MSD and α_2 in 4D KA model at a low T. Different timescales are shown on the MSD curve. Right: $D_A/T \propto t^*$ in 4D KA model.

well with these previous works (See Fig. 4.5). Here we study the spatial dimension dependence of the SER by considering the following models : (i) 2DR10, (ii) 2DMKA (iii) 3DKA and (iv) 4DKA (See "simulation details" and Appendix B for details). The breakdown of the SE relation is shown in Figs. 4.11 (2DR10), 4.12 (2DMKA), 4.13(3DKA) and 4.14 (4DKA). We use the following two representations to plot data:

i) In a D_A *vs.* τ_α or $\frac{\eta}{T}$ plot, by fitting the data to a power law of the form $D_A \propto \tau_\alpha^{-\xi}$, or $D_A \propto \left(\frac{\eta}{T}\right)^{-\xi}$ we test if the effective exponent ξ is different from 1 (which is the SER prediction).

ii) From the T dependence of $D_A\tau_\alpha$ or $\frac{D_A\eta}{T}$ we test if these quantities are constant (SER) or becomes T dependent (breakdown).

From D_A *vs.* τ_α or $\frac{\eta}{T}$ plots, we see that in *all* spatial dimensions, the *low T data follow a fractional SE relation* indicating a breakdown of the SER. The breakdown exponent is closer to one at higher dimensions indicating that the *SE breakdown is weaker at higher dimensions.* In the same dimension ($D = 2$), the breakdown exponent is different for different models.

Further, as the temperature increases, there is a *clear change of the exponent value* in D_A *vs.* τ_α or $\frac{\eta}{T}$ plots indicating a *qualitative* difference between high T and low T behaviour. Surprisingly, in two dimensions, in both the models, the high T exponent from D_A *vs.* τ_α is *higher than 1.* However, in 3 dimensions, the SE relation $D_A \propto \frac{\eta}{T}$ is recovered at high T as expected. We

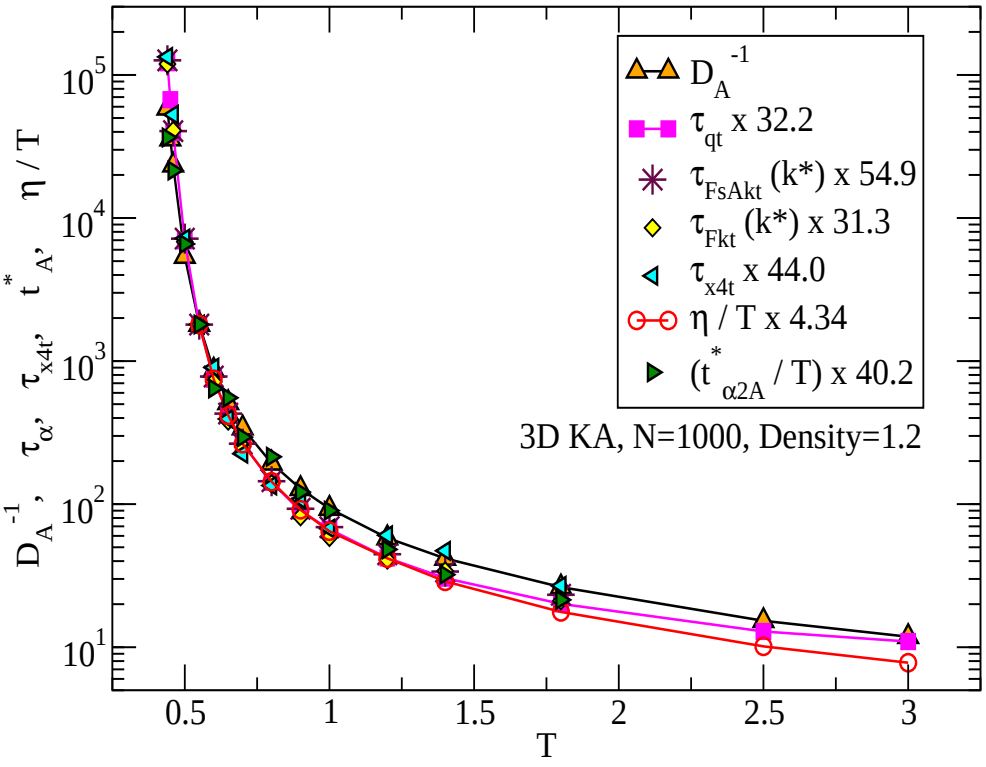

Figure 4.10: T dependence of different time scales in 3D KA model: (i) inverse of self diffusion coefficient of A particles (D_A^{-1}); α relaxation times measured from (ii) the overlap function τ_{qt}, (iii) the $F_s(k^*,t)$ of A particles $\tau_{FsAkt}(k^*)$; (iv) the $F(k^*,t)$ ($\tau_{Fkt}(k^*)$); (v) the heterogeneity time scale from χ_4 (τ_4) and (vi) from $\alpha_2(t)$ of A particles (t^*) scaled by temperature; (vii) shear viscosity scaled by temperature (η/T). k^* is the value corresponding to the first peak of the structure factor. The format of plotting is suggested by the SER (Eqn. 4.1) and testing the proportionality between different time scales.

note that η and τ_α are *not* proportional at high T, hence the exponent from D_A *vs.* τ_α at high T is somewhat *bigger* than 1. Finally, as we go to still higher dimension ($D = 4$), the D_A *vs.* τ_α plot shows the expected relation ($D_A \propto \tau_\alpha^{-1}$) at high T.

The above correlation between D_A and τ_α is also reflected in the T dependence of $D_A\tau_\alpha$. Since the diffusion coefficient *decreases* but the relaxation time *increases* as the temperature *decreases*, there is a competition between two opposing effects. The respective rates of increase and decrease with T will exactly cancel each other *only* if the exponent is 1. Since in 2D, the exponent is never 1, the quantity $D_A\tau_\alpha$ goes through an extremum and is never constant. Qualitatively same T dependence of $D_A\tau_\alpha$ is observed in 3D,

however the minimum is less pronounced, indicating that in 3D, the breakdown is weaker than in 2D. Finally, in 4D, $D_A\tau_\alpha$ = *constant* at high T as expected and *increases* as T decreases as low T.

As a comparison, we also show the behaviour of D_A/T *vs.* τ_α and the T dependence of $\frac{D_A\tau_\alpha}{T}$ in the bottom row of each of the Figs. 4.11 (2DR10), 4.12 (2DMKA), 4.13(3DKA) and 4.14(4DKA). The D_A/T *vs.* τ_α plots show a fractional SE relation at both low *and* high T in *all dimensions*. This is qualitatively a different behaviour than the D_A *vs.* τ_α plot which emphasizes the importance of the temperature factor. Also the value of the breakdown exponent from the D_A/T *vs.* τ_α plot is somewhat different from the D_A *vs.* τ_α plot. However, the magnitude of the exponents is closer to 1 at higher dimensions - thus we are led to the same conclusion that the SE breakdown is weaker at higher dimensions.

The estimates of the breakdown exponents are summarized in Table 4.3.

Figs. 4.11 - 4.14 also show that the temperature of SE breakdown (T_{SEB}), estimated as the point of interaction of the low T and the high T fit in D_A *vs.* τ_α or $\frac{\eta}{T}$ plots (and using VFT fits to convert relaxation time to temperature), is *close to the Arrhenius to non-Arrhenius cross-over temperature* T_{onset} *in all dimensions*. Thus - at least in NVT simulations - the *SE breakdown occur at a much higher temperature than the divergence temperature* T_c *of the MCT* (all data are above T_c estimated from the fit of the T dependence of relaxation time).

4.5.2 Rationalization of the low T exponents from the AG relation

The fractional SE behaviour at low T can be rationalized by considering the *different* dependence of the diffusion coefficient and α relaxation time on the configuration entropy (S_c). The Adam Gibbs (AG) relation $X = X_0 \exp(\frac{A_x}{TS_c})$, if it is valid, provides a way to test this hypothesis quantitatively (X represents the dynamics: $X = \tau_\alpha$, $(D_A)^{-1}$ or $(D_A/T)^{-1}$ in the present study). Fig. 4.15 shows that the AG relation is valid in KA model in 3 (top row) and 4 dimensions (bottom row). We see that the slope of $(D_A)^{-1}$ or $(D_A/T)^{-1}$ *vs.* $(TS_c)^{-1}$ is *different* from that of τ_α *vs.* $(TS_c)^{-1}$. Table 4.3 shows that the *observed fractional SE exponent at low* T *can be interpreted*

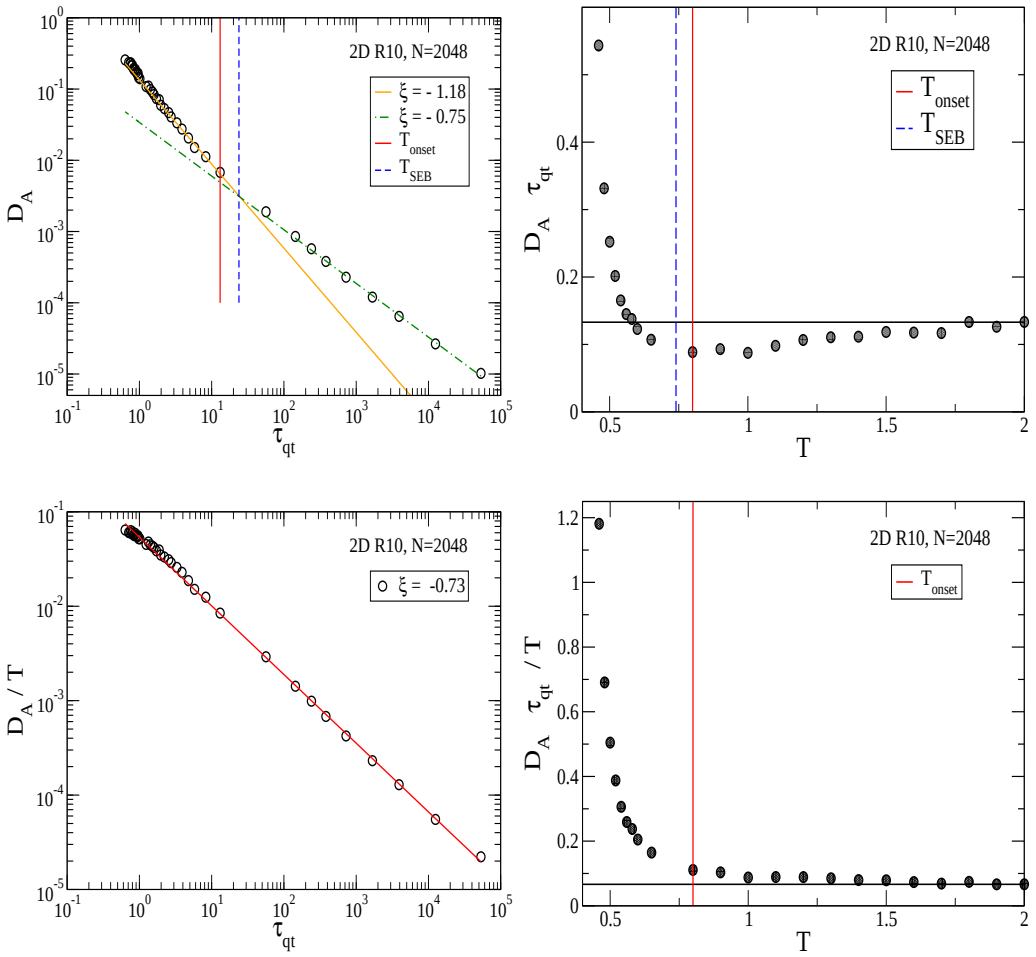

Figure 4.11: Plots showing the breakdown of SER in 2DR10 model. *Top left*: D_A *vs.* τ_α plot. *Top right:* T dependence of $D_A\tau_\alpha$. *Bottom left:* D_A/T *vs.* τ_α plot. *Bottom right:* T dependence of $\frac{D_A\tau_\alpha}{T}$. The low T data follow a fractional SE relation. A clear change of exponent occurs at high T in D_A *vs.* τ_α plot, although the high T exponent is *bigger* than 1. The SE breakdown occurs at a temperature T_{SEB} closer to the onset temperature T_{onset} than T_c. (T_{SEB} estimated as the point of intersection of high T and low T fits; T_{onset} is the Arrhenius to non-Arrhenius cross-over temperature; T_c is the MCT transition temperature. All data points shown here are at $T > T_c$.)

as the ratio of the slopes in the AG plots in Fig. 4.15.

4.5.3 Summary

To summarize, we show that (i) the SE breakdown in weaker in four dimensions than in three dimensions which is consistent with earlier works

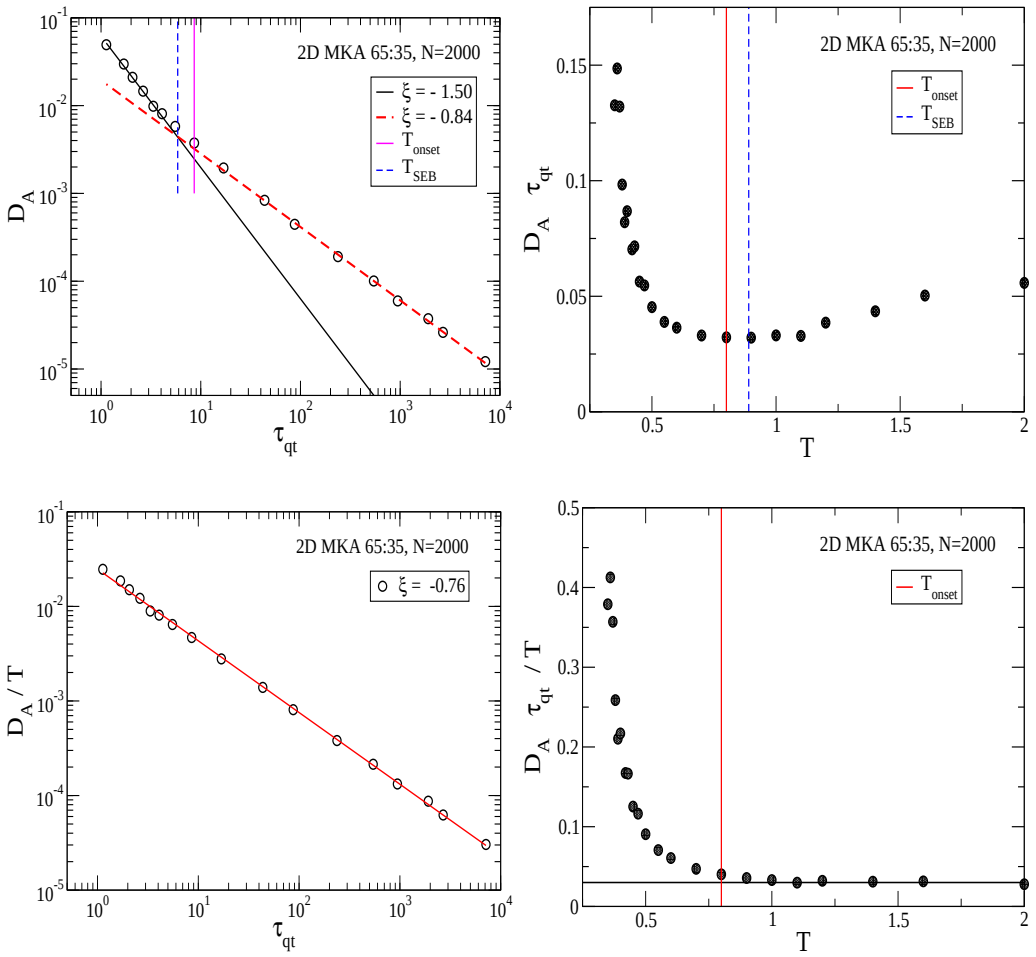

Figure 4.12: Plots showing the breakdown of SER in 2DMKA model. *Top left*: D_A *vs.* τ_α plot. *Top right:* T dependence of $D_A\tau_\alpha$. *Bottom left:* D_A/T *vs.* τ_α plot. *Bottom right:* T dependence of $\frac{D_A\tau_\alpha}{T}$. The low T data follow a fractional SE relation. A clear change of exponent occurs at high T in D_A *vs.* τ_α plot, although the high T exponent is *bigger* than 1. The SE breakdown occurs at a temperature T_{SEB} closer to the onset temperature T_{onset} than T_c. (T_{SEB} estimated as the point of intersection of high T and low T fits; T_{onset} is the Arrhenius to non-Arrhenius cross-over temperature; T_c is the MCT transition temperature. All data points shown here are at $T > T_c$.)

[115,116]. (i) The breakdown exponent can be rationalized from the different scaling of the diffusion coefficient and the relaxation time with the configurational entropy. (iii) The behaviour in two dimensions is more complicated but consistent with earlier work [117].

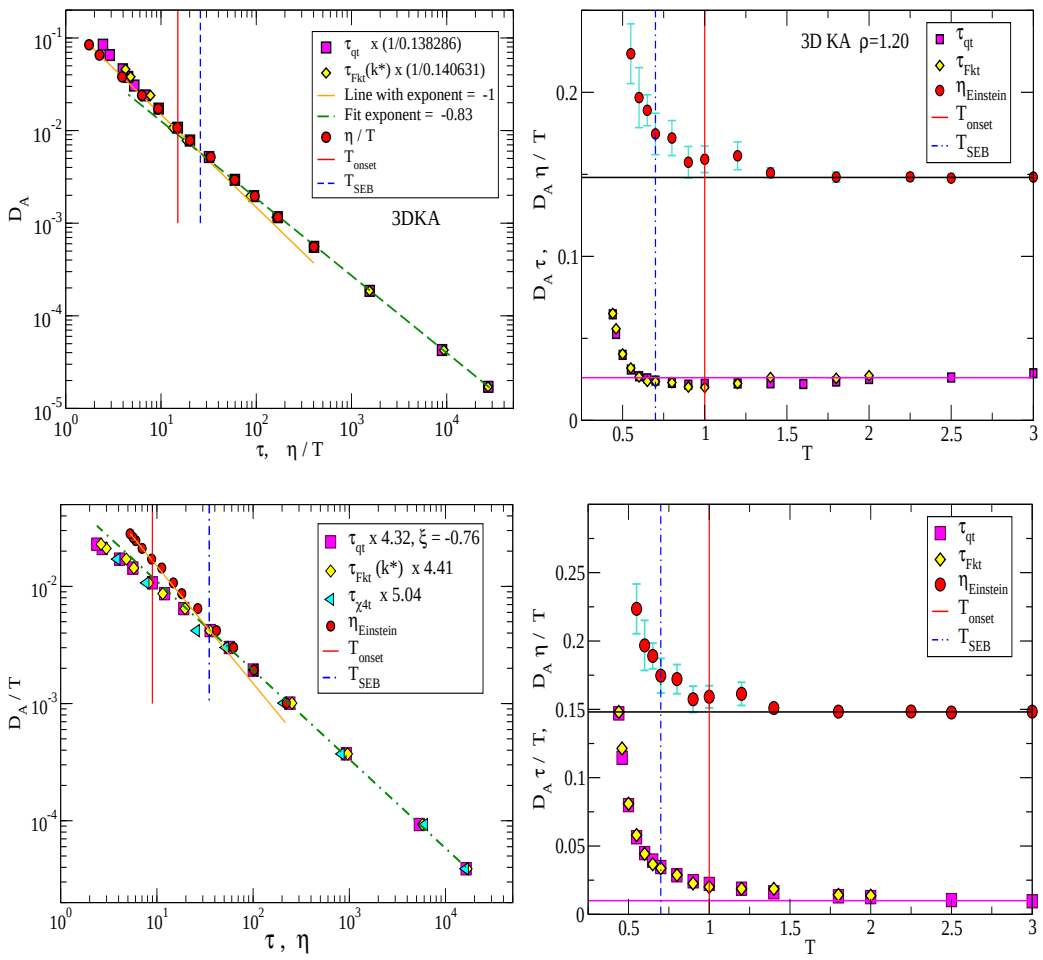

Figure 4.13: Plots showing the breakdown of SER in 3DKA model. *Top left*: D_A *vs.* τ_α and $\frac{\eta}{T}$ plot. *Top right:* T dependence of $D_A\tau_\alpha$ and $\frac{D_A\eta}{T}$. *Bottom left:* D_A/T *vs.* τ_α and η plot. *Bottom right:* T dependence of $\frac{D_A\tau_\alpha}{T}$ and $\frac{D_A\eta}{T}$. The low T data follow a fractional SE relation. A clear change of exponent occurs at high T in D_A *vs.* τ_α plot. The high T exponent (=-1) expected from the SER is obtained from D_A *vs.* $\frac{\eta}{T}$ plot. The SE breakdown occurs at a temperature T_{SEB} closer to the onset temperature T_{onset} than T_c. (T_{SEB} estimated as the point of intersection of high T and low T fits; T_{onset} is the Arrhenius to non-Arrhenius cross-over temperature; T_c is the MCT transition temperature. All data points shown here are at $T > T_c$.)

4.6 Results: Dependence of the fragility on spatial dimensions

In this section we characterize the spatial dimension dependence of the fragility. We estimate the kinetic fragility from the VFT fit to the T dependence of the α relaxation times:

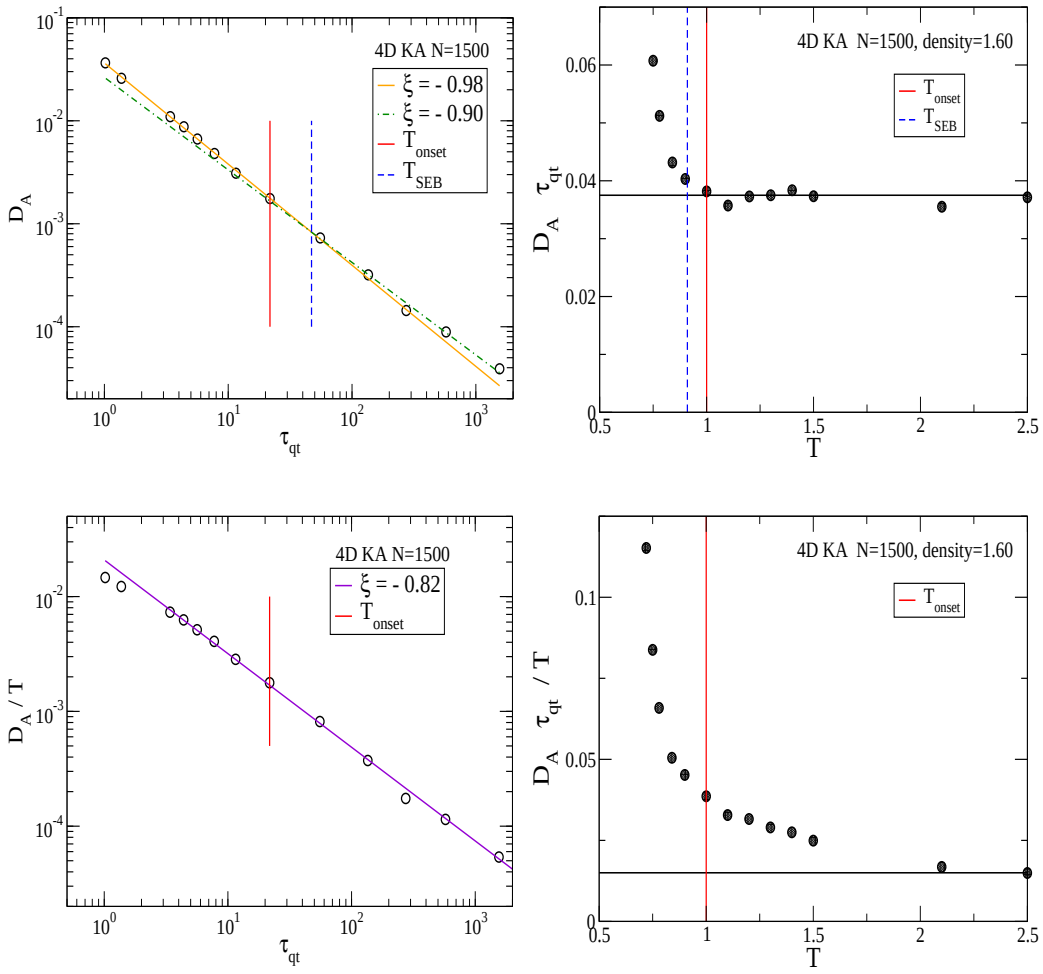

Figure 4.14: Plots showing the breakdown of SER in 4DKA model. *Top left*: D_A *vs.* τ_α plot. *Top right:* T dependence of $D_A\tau_\alpha$. *Bottom left:* D_A/T *vs.* τ_α plot. *Bottom right:* T dependence of $\frac{D_A\tau_\alpha}{T}$. The low T data follow a fractional SE relation. A clear change of exponent occurs at high T in D_A *vs.* τ_α plot. The high T exponent (=-1) expected for a homogeneous (Gaussian distribution of particle displacements) system is obtained from D_A *vs.* τ_α plot. The SE breakdown occurs at a temperature T_{SEB} closer to the onset temperature T_{onset} than T_c. (T_{SEB} estimated as the point of intersection of high T and low T fits; T_{onset} is the Arrhenius to non-Arrhenius cross-over temperature; T_c is the MCT transition temperature. All data points are at $T > T_c$.)

$$\tau(T) = \tau_0 \exp\left[\frac{1}{K_{VFT}(\frac{T}{T_{VFT}} - 1)}\right] \tag{4.11}$$

Fig. 4.16 shows the T dependence of the α relaxation times in five different

Table 4.3: Estimates of the magnitude of the SE breakdown exponents in different spatial dimensions D. *Notations:* (a) ξ_1^{SE} = SE breakdown exponent obtained from D_A *vs.* τ_α or $\frac{\eta}{T}$ plots; (b) ξ_1^{AG} = ratio of slopes from AG plots using D_A and τ_α; (c) ξ_2^{SE} = SE breakdown exponent obtained from D_A/T *vs.* τ_α plots; (d) ξ_2^{AG} = ratio of slopes from AG plots using D_A/T and τ_α. High T exponents are obtained from D_A *vs.* τ_α plots.

D	Model	Low T Exponents				High T exponents
		ξ_1^{SE}	ξ_1^{AG}	ξ_2^{SE}	ξ_2^{AG}	
2	2DR10	0.75	-	0.73	-	1.18
2	2DMKA	0.84	-	0.76	-	1.50
3	3DKA	0.83	0.85	0.76	0.75	≈ 1
4	4DKA	0.90	0.90	0.82	0.84	$0.98 \approx 1$

models: (a) the KA model in 2,3,4 dimensions; (b) the modified KA model in 2 dimensions and (c) the repulsive 2D R10 model. It is clearly seen that for the same model (KA) the *kinetic fragility is higher at higher dimensions.* This is also shown in the "fragility plot" in the bottom panel of Fig. 4.16 using a "simulation glass transition temperature" defined from $\tau(T_g) = 10^5$ (reduced unit). The above trend indicates that the *systems studied here are more fragile at higher dimensions.* Given the observed trends in *3 dimensions*, this suggests that systems at higher dimension are *more heterogeneous.* which is counter-intuitive.

We present the following argument to partially explain this trend. Intuitively, fragility should be related to the mechanical stability of the packing of configurations - a system is more fragile if the packing of microscopic configurations are less stable. Stability of packing reduces if the energy barrier for rearrangement is less. A less stable packing also implies more number of configurations sampled by the system *i.e.* higher configurational entropy. Thus there are two contributions to fragility: (i) configurational entropy and (ii) energy barrier for rearrangement. A more precise analysis [128] using the potential energy landscape formalism showed that for Gaussian distribution of inherent structures and harmonic approximation for basin entropy, the T dependence of TS_c is linear:

$$TS_c = K_T \left(\frac{T}{T_K} - 1 \right), \tag{4.12}$$

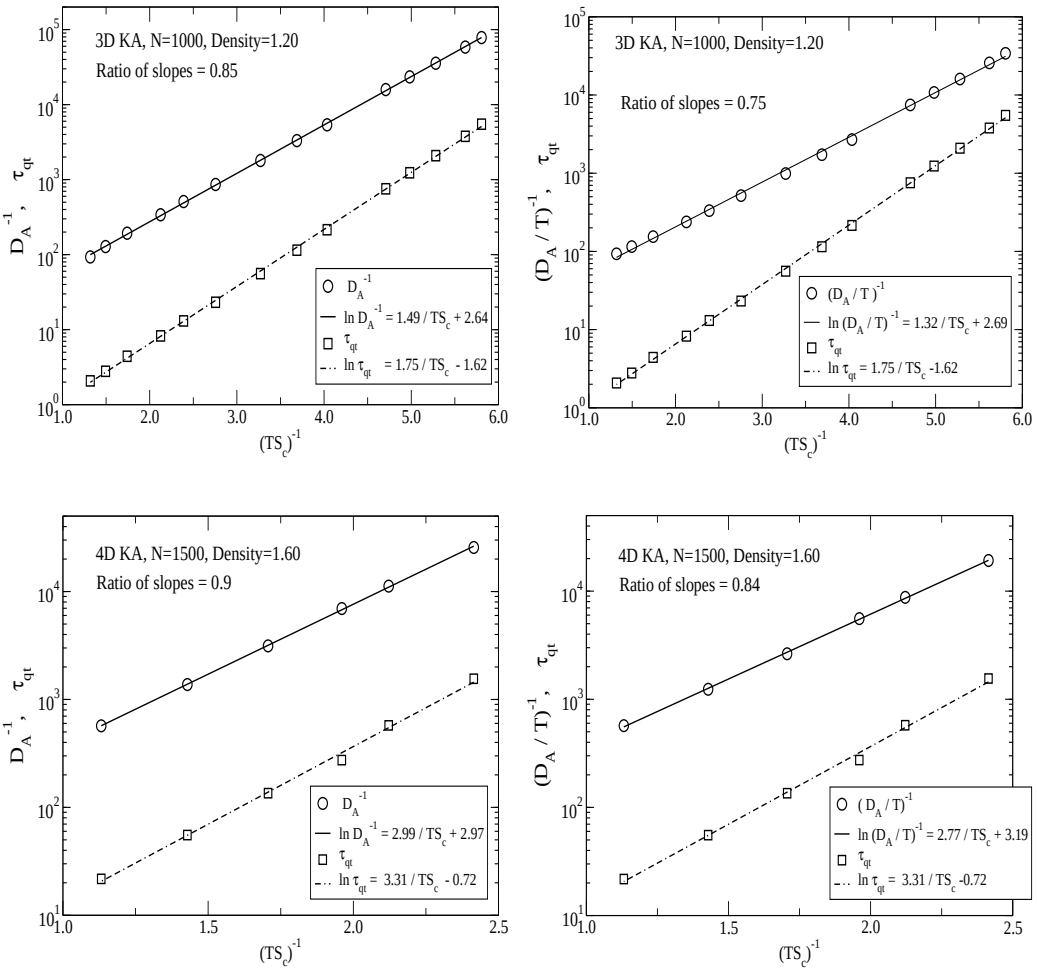

Figure 4.15: *Top row*: The Adam Gibbs (AG) relation in 3DKA model using as the dynamical quantities D_A, τ_α (*top left*) and D_A/T, τ_α (*top right*). *Bottom row*: The AG relation in 4DKA model using as the dynamical quantities D_A, τ_α (*bottom left*) and D_A/T, τ_α (*bottom right*). The slopes are different for D_A, D_A/T and τ_α indicating that the diffusion coefficient has a *different* dependence on the configuration entropy than the α relaxation time. Besides the fractional SE exponent at low T can be interpreted as the ration of the slopes (Table 4.3).

Eqn. 5.3 defines the thermodynamic fragility K_T which represents the contribution of the configuration entropy to the kinetic fragility. The origin of K_T can be understood from the properties (statistics and curvatures of the potential energy hypersurface at minima) of the *minima* of the PEL [128]:

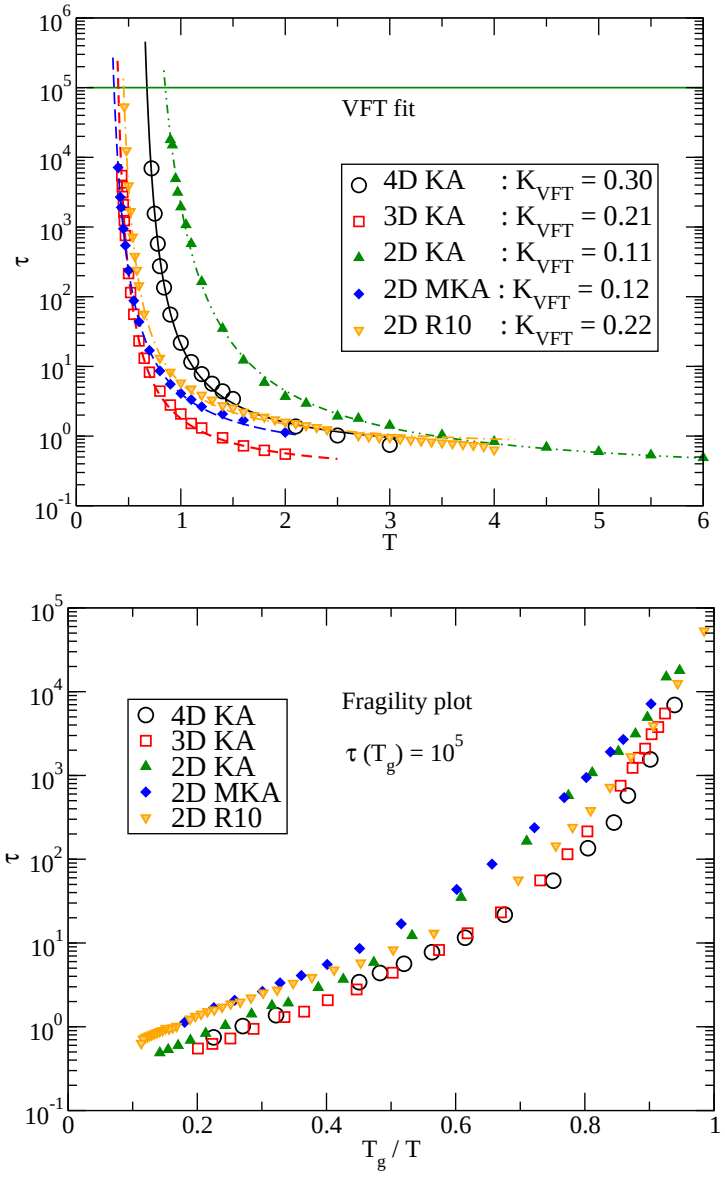

Figure 4.16: *Top:* VFT fit to relaxation times of five models in 2,3,4 spatial dimensions to obtain the kinetic fragility K_{VFT}. The top panel is also used to estimate the simulation glass transition temperature T_g defined as $\tau(T_g) = 10^5$ (reduced unit). The K_{VFT} values are listed in Table 4.4. *Bottom:* Fragility plot for five models in 2,3,4 spatial dimensions. *The plots show that systems at higher dimensions are more fragile.*

$$\begin{aligned} K_T &= \left(\frac{\sigma\sqrt{\alpha}}{2} - \frac{\sigma^2\delta S}{2Nk_B}\right) + \left(\frac{\sigma\sqrt{\alpha}}{2} + \frac{\sigma^2\delta S}{4Nk_B}\right)\frac{T_K}{T} \\ &\approx \left(\frac{\sigma\sqrt{\alpha}}{2} - \frac{\sigma^2\delta S}{2Nk_B}\right) \quad T \gg T_K \end{aligned} \tag{4.13}$$

Specifically, for $T \gg T_K$, K_T is approximately constant and is determined by (i) the spread of the density of states $\sigma\sqrt{\alpha}$ and (ii) the variation of basin free energy with inherent structure energy δS.

Fig. 4.17 shows the T dependence of the configurational entropy in all five models. We see that the *thermodynamic fragility increases significantly as the spatial dimension increases*. Further, in Fig. 4.18 we show that the quantity $\sigma\sqrt{\alpha}$ estimating the width of the configurational entropy density increases with spatial dimension, which partially explains the increase of the thermodynamic fragility with increasing spatial dimensions.

The thermodynamic fragility K_T can be related to the kinetic fragility K_{VFT} by combining the AG relation $\tau = \tau_0 \exp(\frac{A}{TS_c})$, the linear T dependence of TS_c (Eqn. 5.3) and the VFT law Eqn. 6.3 to obtain,

$$K_{VFT} = K_T/A \quad \text{if AG relation is valid and } T_{VFT} = T_K \quad \text{see Table 4.4} \tag{4.14}$$

Eqn. 4.14 formally resolves the contributions of configurational entropy (K_T) and the energy barrier (A) to the kinetic fragility. Figs. 4.17 and 4.18 shows that the configurational entropy contribution increases with increasing dimension thus partially explaining the increase in the kinetic fragility at higher dimensions.

Table 4.4: Characteristic parameters for the models in different dimensions. T_K is the Kauzmann temperature obtained from extrapolating TSc to zero. K_{VFT} is the kinetic fragility obtained from VFT fit to relaxation times. K_T is the thermodynamic fragility obtained from T-dependence of TSc. A is the Adam Gibbs coefficient. $K_{AG} = K_T/A$ is the estimated kinetic fragility estimate using AG relation.

Model	Density	T_K	T_{VFT}	T_g	K_{VFT}	K_T	A	$K_{AG} = K_T/A$
4D KA	1.60	0.525	0.530	0.676	0.30	0.972	3.382	0.29
3D KA	1.20	0.28	0.295	0.402	0.21	0.314	1.79	0.17
2D KA	1.20	0.477	0.501	0.852	0.11	0.260	-	-
2D MKA	1.20	0.251	0.214	0.361	0.12	0.166	-	-
2D R10	0.85	0.181	0.326	0.453	0.22	0.177	-	-

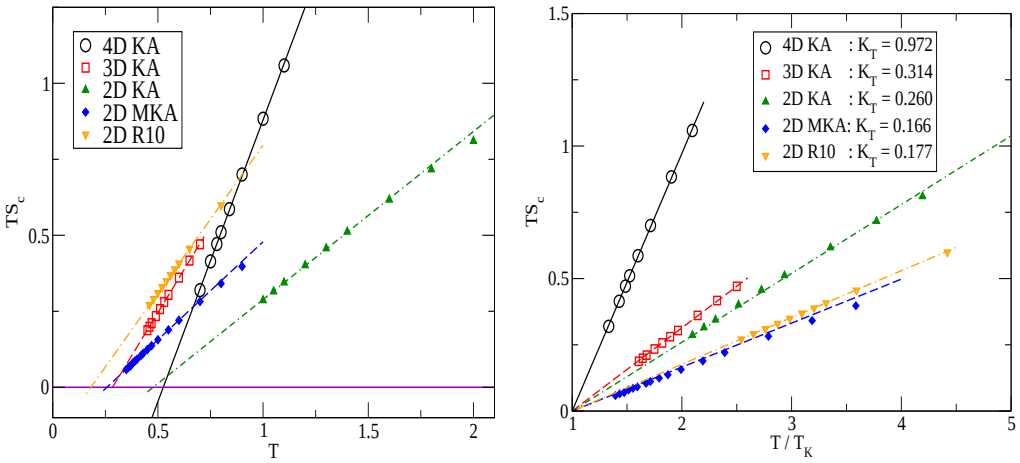

Figure 4.17: *Left:* T dependence of TS_c of five models in 2,3,4 spatial dimensions. *Right*: Same data plotted as TS_c *vs.* T/T_K so that the slope is an estimate of thermodynamic fragility K_T (listed in Table 4.4). *The plots shows that the thermodynamic fragility increases with increasing spatial dimension.*

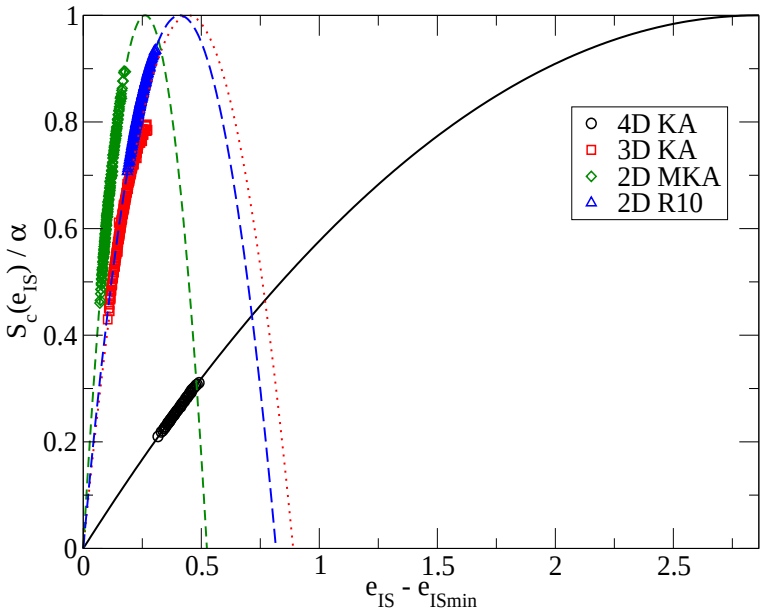

Figure 4.18: The configurational entropy density $S_c(e_{IS})$ of the inherent structure (IS) energy minima plotted *vs.* IS energy minima shifted by the minimum possible value e_{ISmin}. The lines are fits to the parabolic form: $\frac{S_c(e_{IS})}{\alpha} = 1 - \frac{(e_{IS}-e^0_{IS})^2}{(\sigma\sqrt{\alpha})^2}$ (with appropriate change of variable). The distribution is broader at higher dimension which partially explains the increase of the thermodynamic fragility with increasing spatial dimensions.

4.7 Results: Direct estimate of heterogeneity in different spatial dimensions

4.7.1 Estimate of DH from χ_4^{peak} and α_2^{peak}

Temperature dependence: Here we report the temperature dependence of the peak of the dynamical susceptibility χ_4^{peak} and that of the non-Gaussian parameter α_2^{peak} in different models in Figs. 4.19, 4.20, 4.21 and 4.22. Clearly, in *all dimensions*, the peak heights χ_4^{peak} and α_2^{peak} grows as the temperature decreases. This provides *direct evidence that the dynamics is heterogeneous in all dimensions* at least in the range of the present study.

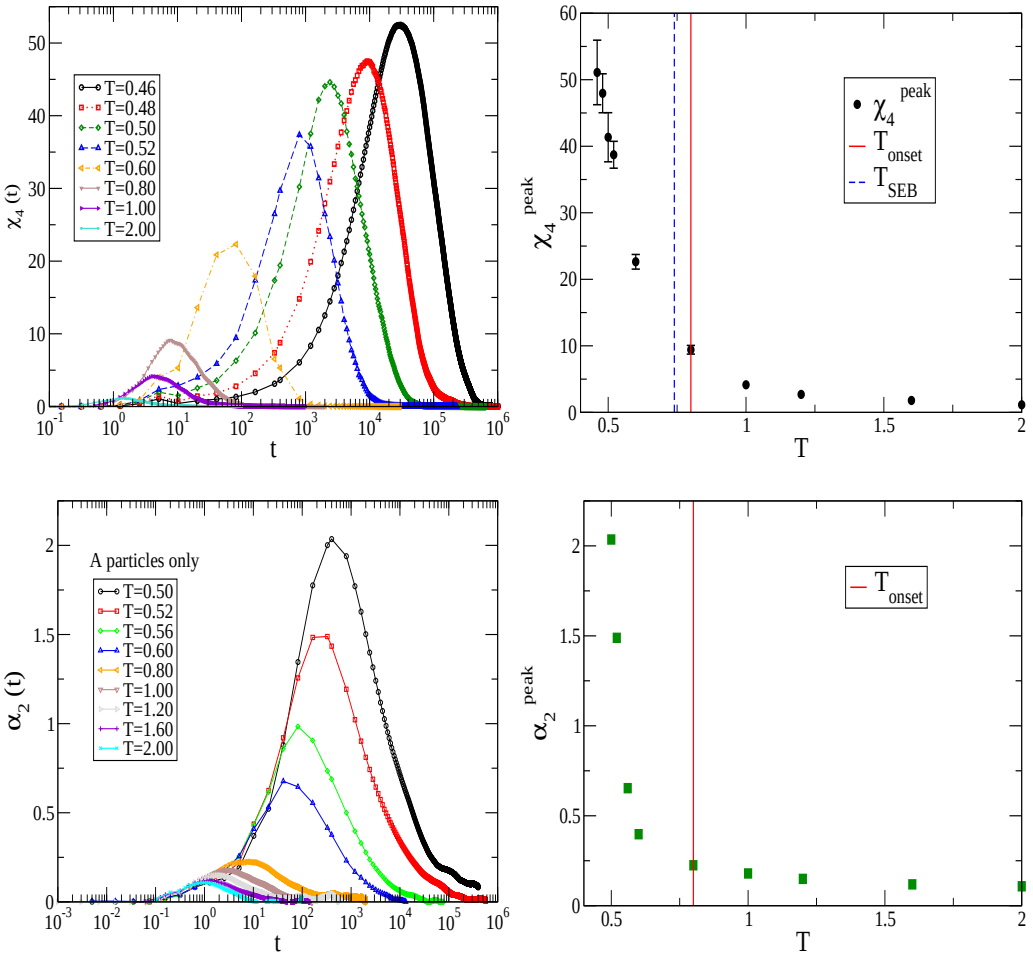

Figure 4.19: Top row: T dependence of $\chi_4(t)$ and the peak height χ_4^{peak} in 2D R10 model. Bottom row: T dependence of the non-Gaussian parameter $\alpha_2(t)$ and the peak height α_2^{peak} in 2D R10 model.

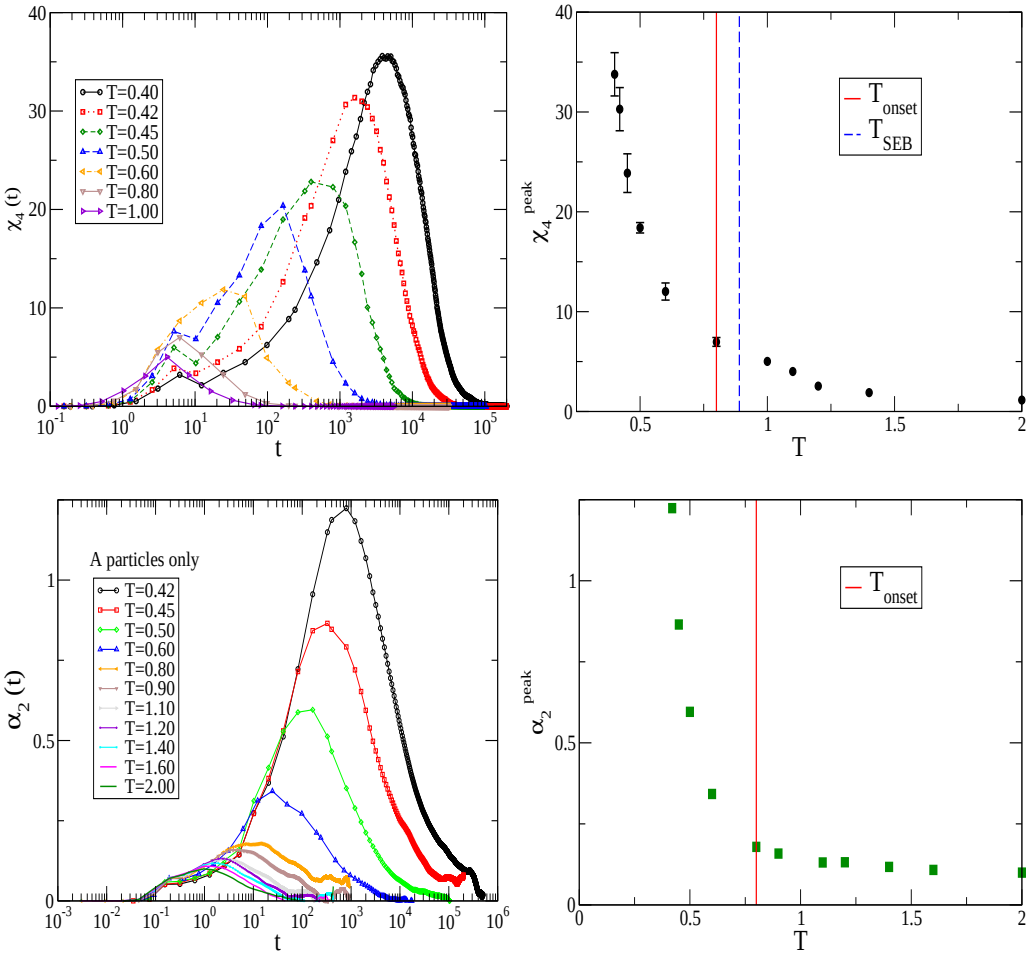

Figure 4.20: Top row: T dependence of $\chi_4(t)$ and the peak height χ_4^{peak} in 2DMKA model. Bottom row: T dependence of the non-Gaussian parameter $\alpha_2(t)$ and the peak height α_2^{peak} in 2DMKA model.

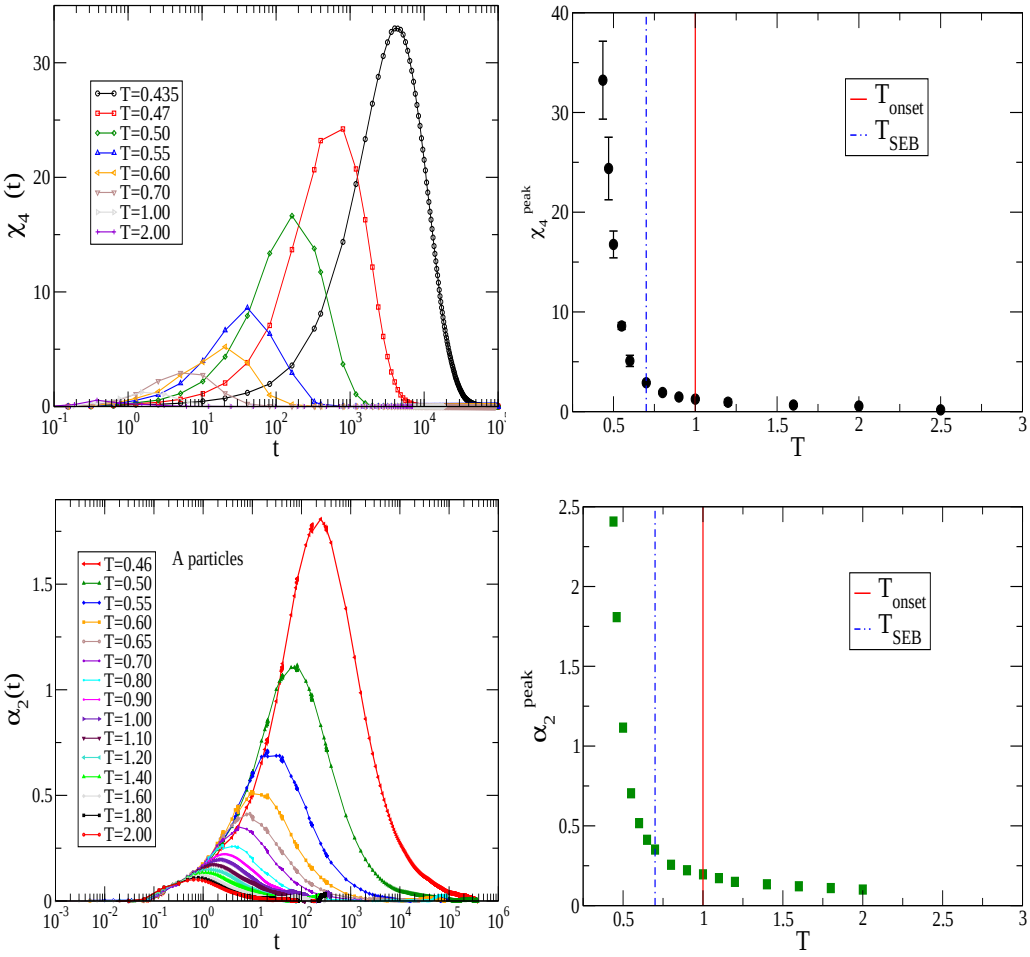

Figure 4.21: Top row: T dependence of $\chi_4(t)$ and the peak height χ_4^{peak} in 3DKA model. Bottom row: T dependence of the non-Gaussian parameter $\alpha_2(t)$ and the peak height α_2^{peak} in 3DKA model.

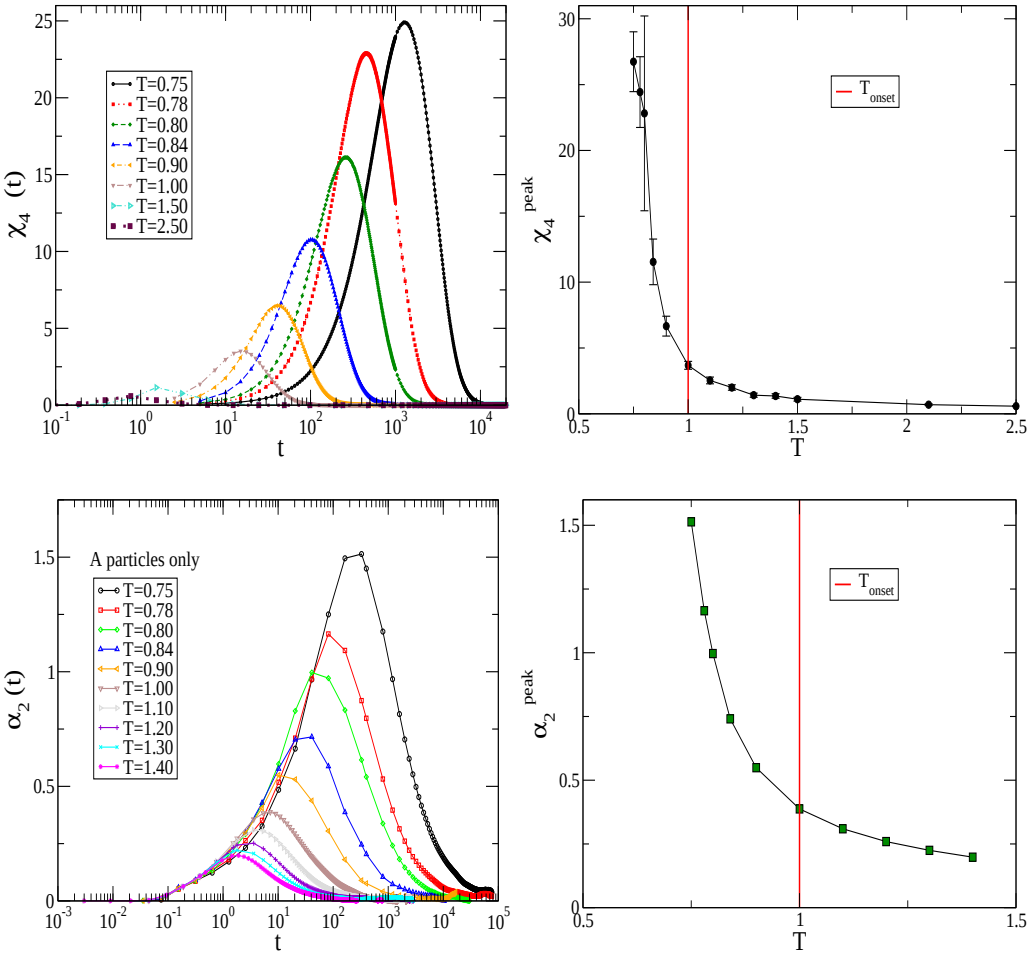

Figure 4.22: Top row: T dependence of $\chi_4(t)$ and the peak height χ_4^{peak} in 4DKA model. Bottom row: T dependence of the non-Gaussian parameter $\alpha_2(t)$ and the peak height α_2^{peak} in 4DKA model.

Comparison of different models: As the temperature scales are different in different models, one needs a dimensionless temperature to compare the behaviour heterogeneity in different models. Here we use, somewhat arbitrarily, the onset temperature to scale the temperature axis. We estimate the degree of heterogeneity from the ratio $\chi_4^{peak}(T)/\chi_4^{peak}(T_{onset})$. The comparison of this degree of heterogeneity for different models are shown in Fig. 4.23. We see that the degree of heterogeneity grows more steeply in 4D than in 3D for the KA model. This is another evidence that the 4D KA model is more heterogeneous than the 3D KA model. However, Fig. 4.23 also shows that this trend does not continue to two dimensions.

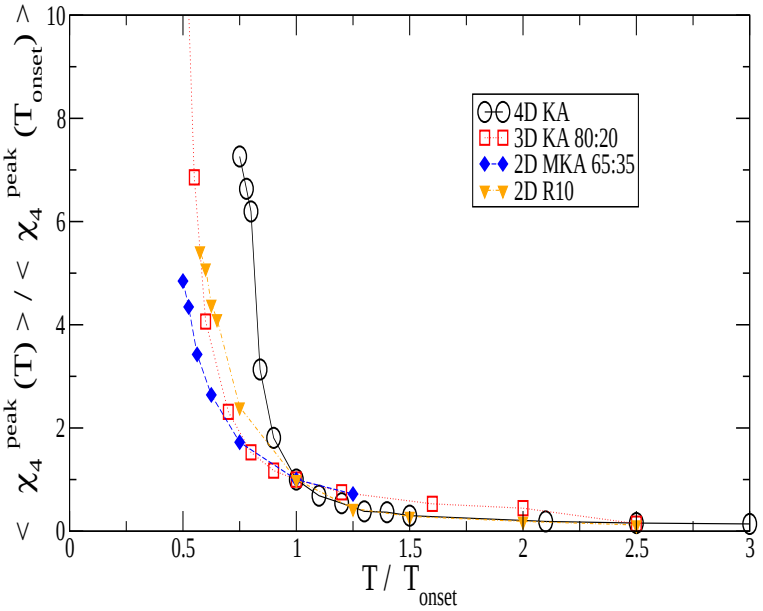

Figure 4.23: Comparison of the *degree of heterogeneity in different dimensions* using the χ_4^{peak} as a measure. χ_4^{peak} scaled by the value at the T_{onset} is plotted against temperature scaled by the onset temperature T_{onset}.

4.7.2 Estimate of DH from β_{KWW}

As a third direct measure of the degree of dynamical heterogeneity, we estimate the stretched exponent β_{KWW}. We have computed β_{KWW} from the self intermediate scattering function $F_{sA}(k,t)$ for k at the peak of the structure factor. Fig. 4.24 shows the temperature dependence of $F_{sA}(k,t)$ for different models. The values of β_{KWW} for different models are compared in Fig. 4.25

with respect to the dimensionless temperature T/T_{onset}. We see that (i) for all models β_{KWW} decreases monotonically with lowering temperature. On increasing temperature, β_{KWW} approaches 1, albeit at a temperature much higher than the onset temperature. (ii) At the same dimensionless *temperature*, the value of β_{KWW} is lower in 4D KA model than in 3D KA model. This is another indication that dynamics is more heterogeneous in 4D KA model than in 3D KA model. (iii) This trend does not continue in two dimensions.

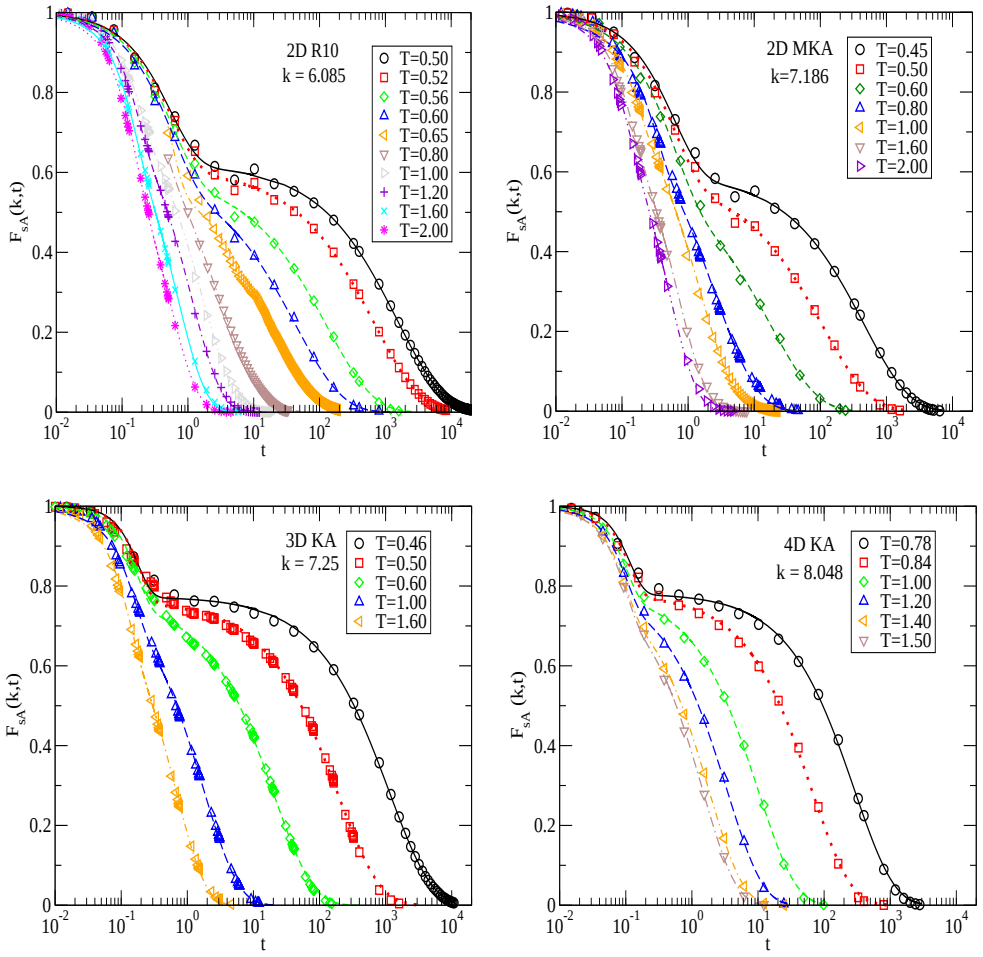

Figure 4.24: T dependence of F_{sAkt} in 2D KA 80:20, 2D MKA, 3DKA and 4DKA models. $F_s(k,t)$ is fitted to the 4-parameter form $F_s(k,t) = (1 - f_c)\exp(-(t/\tau_s)^n) + f_c \exp(-(t/\tau_\alpha)^{\beta_{KWW}})$ with $0 \leq \beta_{KWW} \leq 1$. $n = 2$ in 4D and 3D and $n = 1$ at low temperatures in 2D.

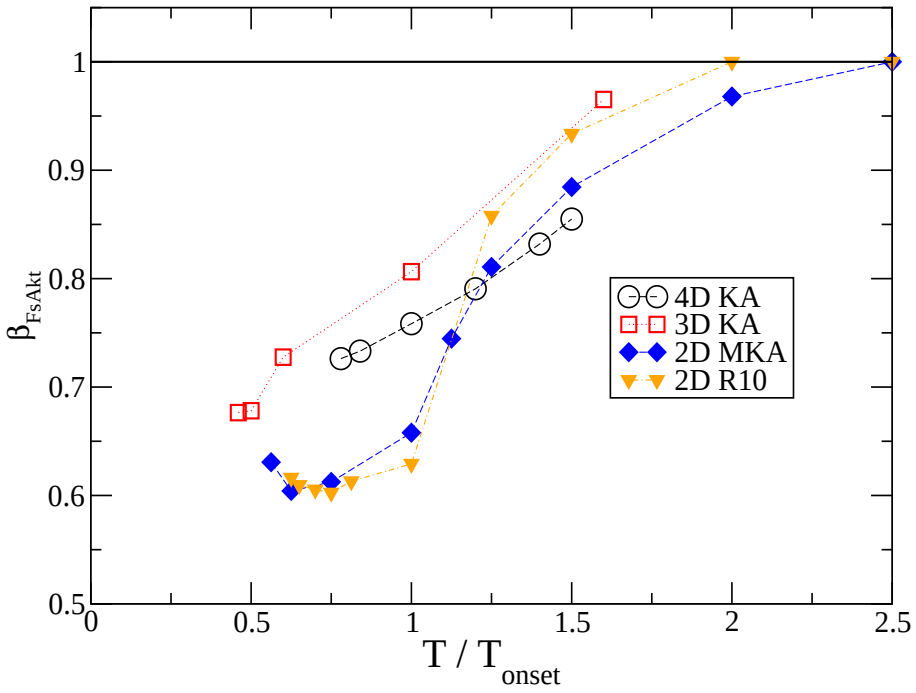

Figure 4.25: Comparison of the *degree of heterogeneity in different dimensions* using the β_{KWW} as a measure.

4.8 Attempts to reconcile the opposite trends

In the present study, the observed trend in the SE breakdown suggests that the systems in higher dimensions are *less* heterogeneous. However, the observed trends in the direct indicators of heterogeneity ($\beta_{KWW}, \chi_4^{peak}$) as a function of (dimensionless) *temperature* suggest that the systems in higher dimensions are *more* heterogeneous which is not only contradictory but also counter-intuitive. In an attempt to resolve this opposing trends, we compare the degree of SE breakdown and the degree of heterogeneity in different models in Fig. 4.26. We estimate the degree of SE breakdown as the ratio $\frac{D\tau/T}{(D\tau/T)_{T_{onset}}}$. We see that for each model, the degree of SE breakdown is well correlated with and varies monotonically with the degree of heterogeneity.

The main difficulty of comparing different models is to find the appropriate dimensionless control variable as a function of which a given indicator of heterogeneity can be plotted for different models. We argue that it is perhaps more natural to compare the heterogeneity for different models at the same *time* rather than at the same (dimensionless) *temperature*. Additionally, one may use the absolute value of the relaxation time thus eliminating

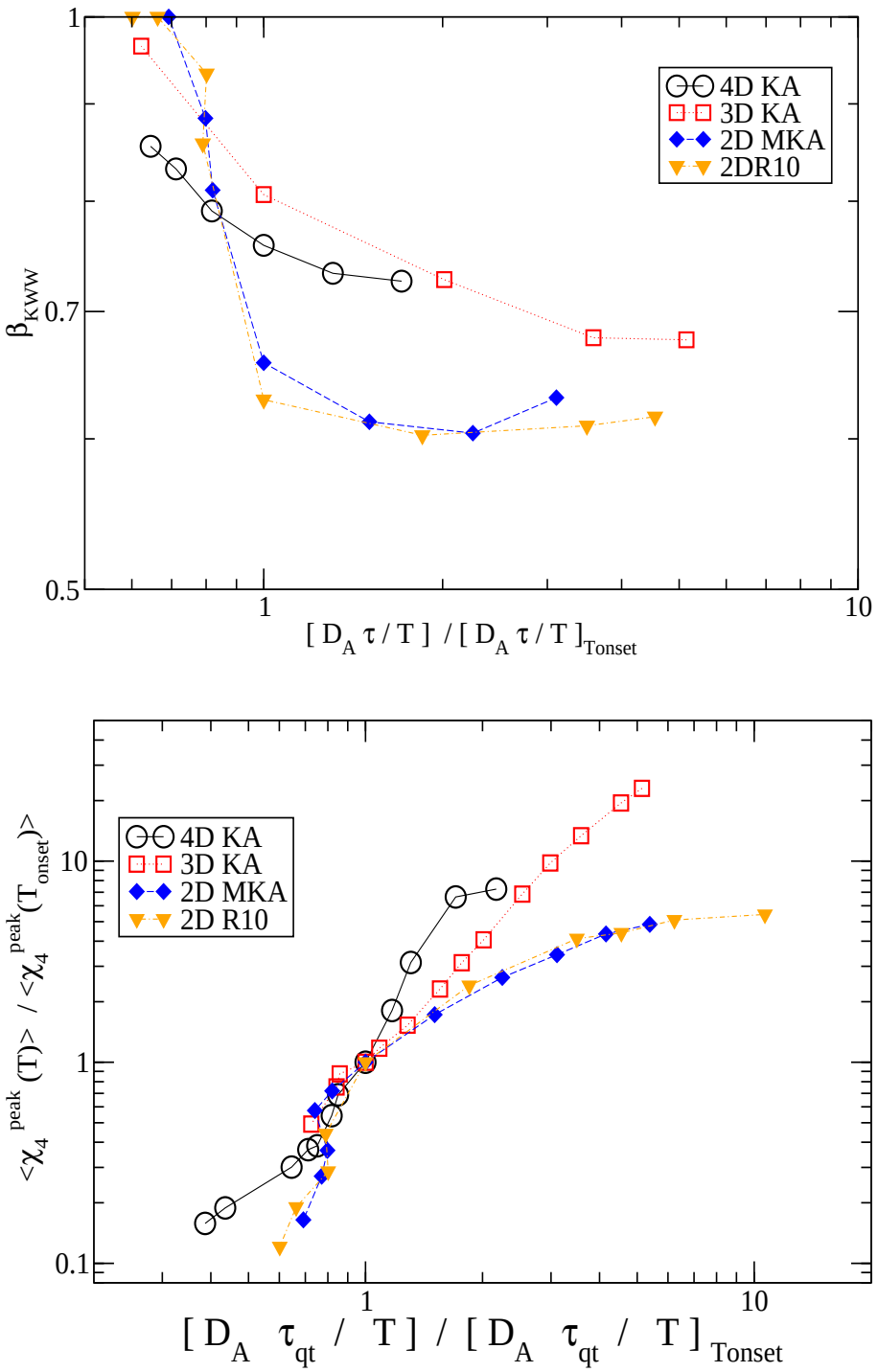

Figure 4.26: Parametric plots of the degree of SE breakdown $D\tau/T$ *vs.* and the other direct indicators of DH - (i) β_{KWW} and (ii) χ_4^{peak} scaled with the value at the onset temperature.

the ambiguity about choosing appropriate reference temperature to make temperature dimensionless. In Fig. 4.27 we show the comparison of β_{KWW}

and χ_4^{peak} *vs.* τ for different models. We see that when compared at the same characteristic *time*, the systems in higher dimensions are *less* heterogeneous at low temperatures. We, however note in Fig. 4.28 when $\alpha_{2,A}^{peak}$ is used as a measure of heterogeneity, 2D systems break this trend.

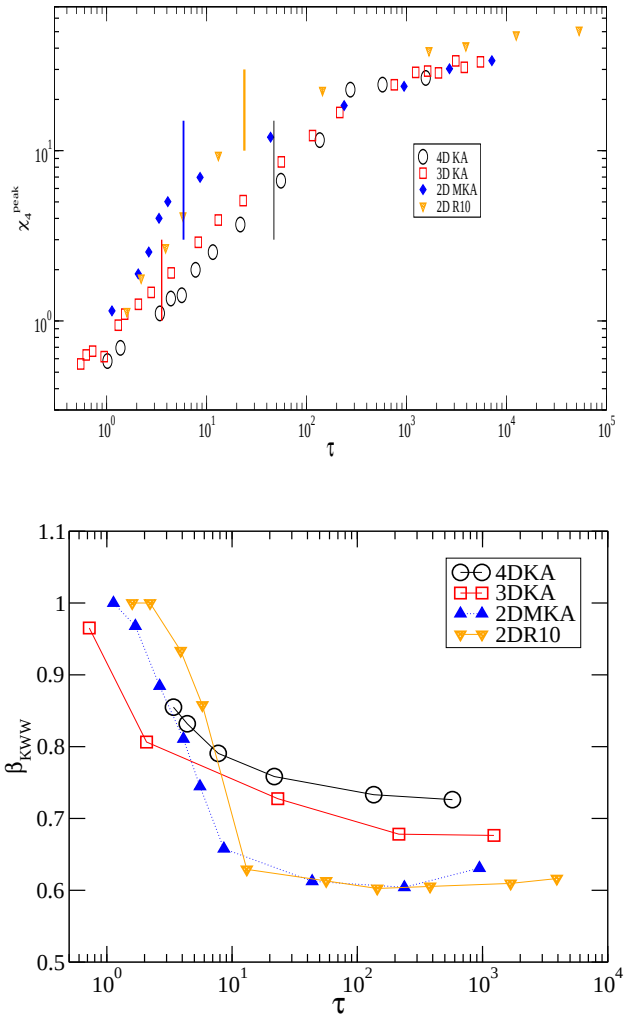

Figure 4.27: Comparison of the degree of heterogeneity in different dimensions at the same characteristic time using χ_4^{peak} and β_{KWW} as direct indicators of heterogeneity. Vertical lines denote the SE breakdown temperatures T_{SEB}.

4.9 Summary and conclusions

The present study is an attempt to generalize in other spatial dimensions, the inter-relations among the dynamical heterogeneity, the SE breakdown

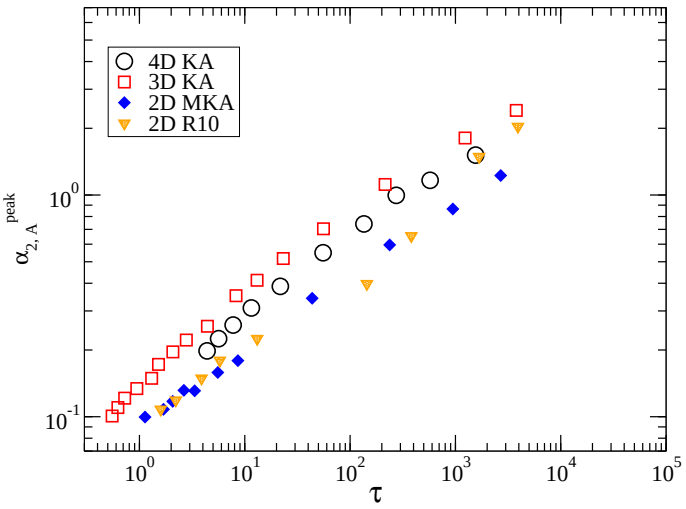

Figure 4.28: Comparison of the degree of heterogeneity in different dimensions at the same characteristic time using $\alpha_{2,A}^{peak}$ (taking A type particles only) as a direct indicator of heterogeneity.

and the fragility which is mainly based on observations in three dimensions. We have considered five models in 2,3,4 spatial dimensions and have characterized the dynamical heterogeneity using both direct ($\chi_4^{\text{peak}}, \alpha_2^{\text{peak}}, \beta_{KWW}$) and indirect (the degree of SE breakdown, fragility) indicators. The conclusions are :

1. The data clearly show that the SE breakdown at low temperatures, which can be represented by a fractional SE relation in all models studied here, becomes weaker at higher dimensions which can be rationalized in three and four dimensions in terms of different dependence of the diffusion coefficient and the relaxation time on the configuration entropy. This trend is expected based on earlier works [115, 116]. However, we note that the description of SE breakdown is somewhat complicated by the fact that the method of representation of data is important. We also note that based on the observed trends in 3D, the dimension dependence of the SE breakdown indicated that systems in 4D are *less* heterogeneous than in 3D.

2. We have also conclusively shown that the systems at higher dimensions are more fragile. Similarly, by direct estimates of the dynamical heterogeneity from $\chi_4^{\text{peak}}, \alpha_2^{\text{peak}}, \beta_{KWW}$ suggest that systems in 4D are *more* heterogeneous than in 3D at the same (dimensionless) *temperature*.

3. The contradictory trend with dimensions is resolved by comparing the degree of heterogeneity in different dimensions at constant relaxation *time* rather than at constant *temperature*. At the same relaxation time, and at low temperatures, all three direct measures of heterogeneity *i.e.* $\chi_4^{\text{peak}}, \alpha_2^{\text{peak}}, \beta_{KWW}$ clearly show that 4D is *less* heterogeneous than 3D.

4.10 Future works

- It is interesting to study the k-dependence of the SE breakdown and calculate the Fickian lengthscale for different models.
- In order to pinpoint the relation between the SE breakdown and heterogeneity, it is interesting to devise a test by which one can suppress the heterogeneity in a controlled way and study the effect on the SE relation. Such test has been discussed in literature [102].
- In order to completely understand the dimension dependence of the kinetic fragility, one needs to compare the effective energy barriers in different dimensions, which may be estimated from the relaxation time.

Chapter 5

Dependence of the fragility of a glass former on the softness of interparticle interactions

5.1 Introduction

The relaxation times of supercooled liquids rise rapidly as the liquids are cooled towards their laboratory glass transition temperatures (T_g). The concept of *fragility* [27, 126], introduced and analyzed extensively by Angell, quantifies how rapidly relaxation times increase in different materials as temperature decreases. It is a material property and has been proved to be useful in organizing and understanding the diverse behaviour seen in glass formers. Fragility can be defined in various ways (see Chapter 1). In the present study, a kinetic index of fragility (K_{VFT}) is defined from a VFT fit of the relaxation times (or the diffusion coefficients),

$$\tau(T) = \tau_0 \exp\left[\frac{1}{K_{VFT}(\frac{T}{T_{VFT}} - 1)}\right] \tag{5.1}$$

Despite considerable research efforts [126–142], and the observation of many empirical correlations between fragility and other material properties [133], a fully satisfactory understanding of fragility has not been reached yet. Such understanding has been sought, broadly, along two lines. The first is a conceptual understanding of fundamental quantities that may govern fragility.

An example of this kind is the use of the potential energy landscape approach in combination with the Adam Gibbs (AG) relation [37] between the relaxation time and the configuration entropy [Eqn. 6.4] to relate features of the energy landscape of a glass former to the fragility. The Adam-Gibbs relation

$$\tau(T) = \tau_0 \exp(\frac{\delta\mu S^* k_B^{-1}}{TS_c}) \tag{5.2}$$

relates the temperature dependence of the relaxation times to the temperature change in the configuration entropy S_c, where $\delta\mu$ is an activation free energy for particle rearrangements, and S^* is the configurational entropy of cooperatively rearranging regions invoked in Adam-Gibbs theory (see Chapter 1).

If $A \equiv \delta\mu S^* k_B^{-1}$ has no significant role to play in determining the fragility of a substance, it is the temperature variation of TS_c that dictates the fragility. If the T-dependence of S_c is given by

$$TS_c = K_T \left(\frac{T}{T_K} - 1 \right), \tag{5.3}$$

the Adam-Gibbs relation yields the VFT relation, with the identification $K_{VFT} = K_T/A$, $T_{VFT} = T_K$. Thus, K_T is a *thermodynamic index of fragility.*

In the potential energy landscape approach [71, 72] configuration entropy is associated with the number of local potential energy minima or *inherent structures* (IS) [76], and can be computed in terms of parameters describing the energy landscape [128]. Hence thermodynamic fragility can be understood in terms of parameters of the potential energy landscape, namely the distribution of inherent structures and the dependence of the vibrational or basin entropy corresponding to inherent structures on theie energies. Although the exact temperature dependence of the configuration entropy depends on detailed properties of the distribution of inherent structures, and K_T is not a constant even in the simplest case, such analysis does yield insight into the relationship between the energy landscape features and fragility. To a first approximation, the broader the distribution of energies of inherent structures, the larger the fragility of a glass former [128]. Going beyond such analysis, one needs to also understand the behavior of the prefactor A, which is related to the high temperature activation energy [130, 131, 137, 146]. To

the extent that the Adam-Gibbs relation quantitatively describes the temperature dependence of the relaxation times, such analysis provides a route to a fundamental understanding of fragility in terms of the phase space properties of a substance.

However, such a conceptual understanding does not directly address the dependence of fragility on specific, controllable material properties, an understanding that is desirable from the perspective, *e.g.*, of materials design. The investigation of the dependence of fragility on the nature of molecular architecture and intermolecular interactions defines therefore a second distinct line of investigation, which has been pursued by various groups. For example, Dudowicz, Freed and Douglas [135, 136] have investigated the role of backbone and side group stiffness in determining the fragility of polymer glass formers. In another recent example, from an experimental investigation on deformable colloidal suspensions, Mattsson *et al.* [141,142] suggested that increasing the softness of the colloidal particles should decrease the fragility of the colloidal suspensions, and that such a principle should be more generally applicable. Indeed, this conclusion is consistent with that of Douglas and co-workers [135] that the ability to better pack molecules leads to lower fragilities. In energy landscape terms, one may understand this conclusion as implying that molecules that pack well together will have narrower distributions of inherent structure energies.

The influence of the softness of interaction on the fragility was also investigated some time ago *via* computer simulations of model glass formers by Bordat *et al* [133,134]. They considered a binary mixture of particles interacting *via* generalized Lennard Jones potentials, of the form

$$V(r) = \frac{\epsilon}{(q-p)} \left(p(\frac{\sigma}{r})^q - q(\frac{\sigma}{r})^p \right) \tag{5.4}$$

for combinations of the exponents (q, p) of repulsive and attractive parts of the potential (12,11), (12,6) and (8,5). These combinations, corresponding to models labeled I, II and III, have decreasing curvatures at the minimum of the potential, and thus increasing softness. In other words, Model I $(12, 11) <$ Model II $(12, 6) <$ Model III $(8, 5)$ in *increasing order of softness,* that is, Model III $(8, 5)$ is the softest potential [See Figs. 5.1 and 5.2]. By evaluating the *kinetic* fragility of these models (the steepness index defined above), Bordat *et al.* found that *increasing* softness of the interaction potential

increases the kinetic fragility [133, 134].

The trend found by Bordat *et al.* therefore is apparently not consistent with expectations arising from the other studies mentioned, although the nature of the changes in the interactions considered are not strictly the same. In order to understand better the relationship between the nature of the intermolecular interactions and fragility, in the present work we calculate the kinetic fragility K_{VFT} using computer simulation data of the diffusion coefficient, and relaxation times obtained by a number of different means. We also calculate, using the procedure in [69, 70, 128], the configuration entropy, from which we calculate a thermodynamic fragility (K_T). We find that these two fragilities show opposite trends, with the kinetic fragility increasing with softness, and the thermodynamic fragility decreasing with softness. In order to understand this apparent disagreement, we must consider the full form of the Adam-Gibbs relation, including terms that relate to the high temperature activation energy. We present our analysis along these lines below.

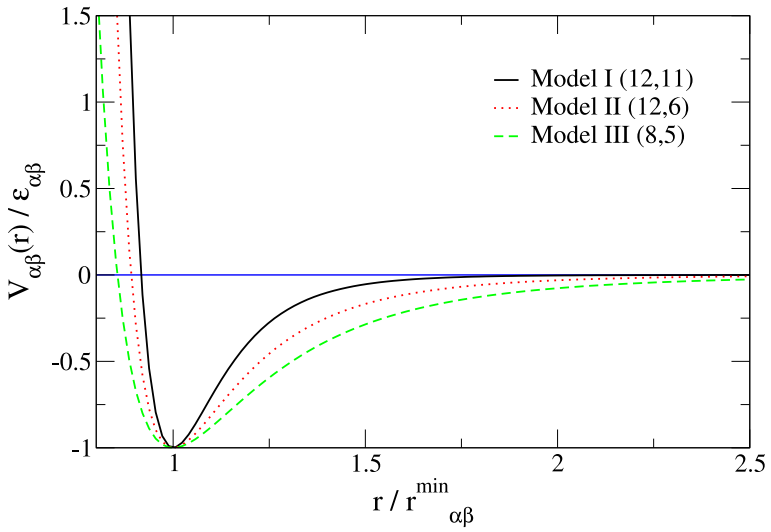

Figure 5.1: Comparison of pair interaction potential $V_{\alpha\beta}$ without truncation for the three different potentials used in the present study. $r_{\alpha\beta}^{min}$ are the positions of the minima of the interaction potentials.

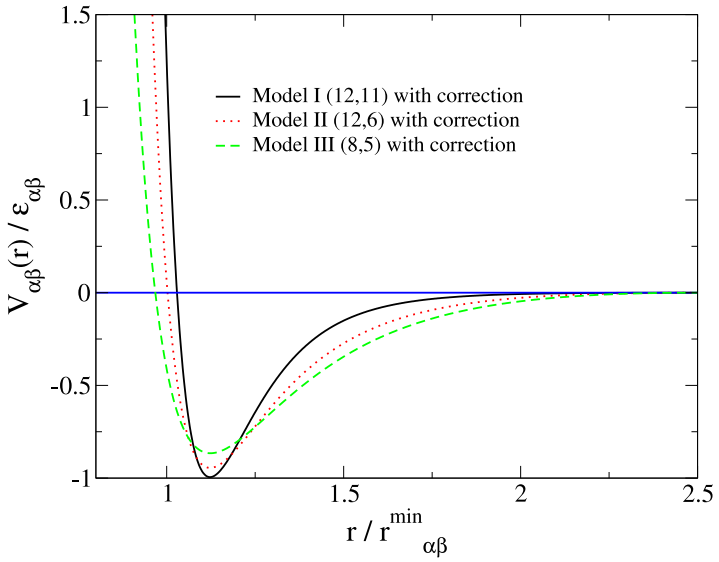

Figure 5.2: Comparison of pair interaction potential $V_{\alpha\beta}$ with truncation for the three different potentials. $r_{\alpha\beta}^{min}$ are the positions of the minima of the interaction potentials.

5.2 Simulation Details

We have studied a 80:20 binary mixture of modified Lennard Jones particles in three dimensions. The interaction potential is of the form given above in Eq. 5.4 with a truncation that makes both the potential and force go to zero smoothly at a cutoff distance r_c. The potential and the other simulation details are described in Chapter 2. The three different models without and with cutoff are shown in Figs. 5.1 and 5.2 respectively.

5.3 Methods

In this section, we describe the various quantities that have been calculated and the methods employed for such calculations.

5.3.1 The α relaxation time

The following measures have been used to extract the α relaxation times (see Chapter 2).

1. Diffusion coefficient (D_A) from the mean squared displacement (MSD) of the A type particles.

2. Relaxation times obtained from (i) the decay of overlap function $q(t)$ using the definition $q(t = \tau_\alpha, T)/N = 1/e$. (ii) The characteristic time $\tau_4(T)$ at which the dynamical suscetibility $\chi_4(t)$ is maximum. (iii) The decay of the self intermediate scattering function $F_s(k, t)$ using the definition $F_s(k, t = \tau_\alpha, T) = 1/e$ at $k \simeq \frac{2\pi}{r_{min}}$.

Since the relaxation times from $q(t)$, $\chi_4(t)$ and $F_s(k, t)$ are mutually proportional as shown in Fig. 4.8 in Chapter 4, we discuss further only the time scale obatined from $q(t)$.

5.3.2 The configurational entropy

The configurational entropy (S_c) per particle, is calculated [69] by subtracting from the total entropy of the system the vibrational component (see Chapter

1):

$$S_c(T) = S_{total}(T) - S_{vib}(T) \tag{5.5}$$

The total entropy of the liquid is obtained *via* thermodynamic integration from the ideal gas limit (see Chapter 2). The vibrational entropy (also called the basin entropy) is calculated by making a harmonic approximation to the potential energy about a given local minimum [69–72]. The procedure (see Chapter 2) used for generating local energy minima, and calculating the vibrational entropy is as outlined in [69, 70].

We have also computed the configurational entropy density $S_c(e_{IS}) = k_B \ln \Omega(e_{IS})$ where $\Omega(e_{IS})$ is the number density of inherent structures with energy e_{IS} and to a good approximation may be described by a Gaussian. Equivalently, $S_c(e_{IS})$ can be described by a parabola,

$$S_c(e_{IS}) = \alpha - \frac{(e_{IS} - e_{IS}^0)^2}{\sigma^2} \tag{5.6}$$

The parameter α denotes the peak value of $S_c(e_{IS})$ which occurs at energy e_{IS}^0. $S_c(e_{IS})$ is zero at $e_{IS} = e_{IS}^0 \pm \sigma\sqrt{\alpha}$. Thus $\sigma\sqrt{\alpha}$ is a measure of the spread of $S_c(e_{IS})$. We denote the lower root $e_{IS}^0 - \sigma\sqrt{\alpha}$ by e_{IS}^{min}.

In the harmonic approximation to the vibrational entropy, the average value of IS energy sampled by a system at a given temperature $< e_{IS} > (T)$ is predicted to be linear in inverse temperature $\beta = 1/T$:

$$\langle e_{IS} \rangle (T) = \langle e_{IS} \rangle (\infty) - \frac{\sigma^2}{2T} \tag{5.7}$$

where $\langle e_{IS} \rangle (\infty)$ is the extrapolated limiting value of $\langle e_{IS} \rangle$ at high temperatures. These parameters which characterizes the potential energy landscape are tabulated in Table 5.2 for different potentials.

5.3.3 Characteristic temperature scales

We mention briefly how the different characteristic temperatures (see Chapter 1) are determined in the present study.

1. T_{onset} : The onset temperatures are estimated from the temperature dependence of the inherent structure energies.

2. T_{MCT} : The apparent divergence temperature of the mode coupling theory

Table 5.1: Characteristic Temperatures

Quantity	(12,11)	(12,6)	(8,5)
T_{onset}	1.27	0.9	0.42
T_c from $(\frac{D_A}{T})^{-1}$	0.77	0.42	0.22
T_c from $q(t)$	0.77	0.42	0.23
T_{VFT} from $(\frac{D_A}{T})^{-1}$	0.59	0.32	0.17
T_{VFT} from $q(t)$	0.55	0.29	0.16
T_K	0.54	0.28	0.16

is estimated from the MCT fit : $\ln \tau = a_0 - \delta \ln(T - T_{MCT})$ to the temperature dependence of both relaxation times and diffusion coefficients.

3. T_{VFT} : The divergence temperature of the Vogel-Fulcher-Tamman (VFT) law is also estimated from both both relaxation times and diffusion coefficients using $\ln \tau = a_0 + \frac{A}{T - T_{VFT}}$.

4. T_K : The Kauzmann temperature at which the configurational entropy becomes zero on extrapolation is determined from the temperature dependence of the average configurational entropy (Eqn. 5.3) using the condition $S_c(T_K) = 0$.

The different characteristic temperature scales for different potentials are tabulated in Table 5.1.

5.3.4 Choice of density

In supercooled liquids, at low temperature, a pressure *vs.* density isotherm go through a minimum [69] called the spinodal density. A spinodal is defined by the condition $\frac{\partial P}{\partial V}|_T = 0$. At a given temperature, below the spinodal density the liquid state is unstable (system has negative compressibility). The pressure calculated from inherent structure (IS) trajectories as a function of density also show this minimum and corresponds to the zero temperature limit of the spinodal density. Any simulation of system in the (metastable) homogeneous liquid state must be performed above the spinodal density. In Fig. 5.3 the IS pressure *vs.* density isotherms are shown for all models. The present simulation is done at density $\rho = 1.2$ which is well above the spinodal densities for all models.

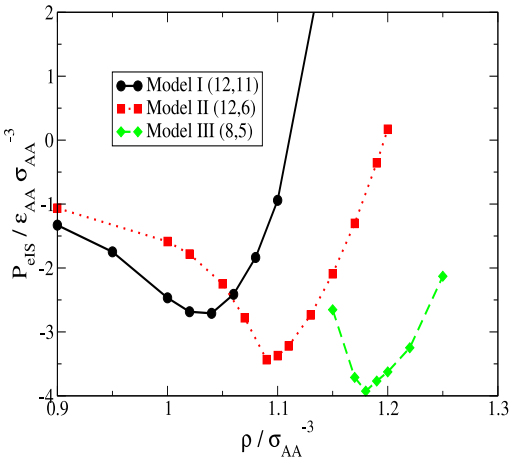

Figure 5.3: Inherent structure pressure *vs.* density isotherms for all models. The density minimum for IS pressure occurs at $\rho = 1.04, 1.09, 1.18$ respectively for models I $(12, 11)$, II $(12, 6)$, and III $(8, 5)$. This density defines the lower bound for simulations of the system in the homogeneous liquid state.

5.4 Results: the thermodynamic fragility

5.4.1 Inherent Structure energy

The inherent structure energy of a fragile glass forming liquid is approximately constant above a characteristic cross-over temperature T_{onset} and show significant decrease with decreasing temperature below T_{onset}. This reflects the qualitative change in phase space sampling as temperature decreases. The system samples all of the potential energy lanscape (PEL) at high temperature (above T_{onset}) hence the average inherent structure energy is independent of temeprature. However, phase space sampling becomes "landscape influenced" at low temperature (below T_{onset}) hence average IS energy becomes temperature dependant. This behaviour is seen for all the models in Fig. 5.4. We note that the cross-over temperature T_{onset} *decreases* as the softness *increases* from models $I(12, 11)$ to $III(8, 5)$. The average IS energy depends linearly on inverse temperature ($\beta = 1/T$) if (i) the number density of inherent structures with energy e_{IS} is a Gaussian and (ii) the basin free energy can be approximated by a harmonic approximation to the potential energy about a given local minimum. We show in Fig. 5.5 that average IS energy is indeed linear with $1/T$ at low temperatures for all models. Fig. 5.5 also provides a more precise estimate of the location of T_{onset}.

We also compute the distribution of distribution $P(e_{IS}, T)$ of IS energies sampled at different temperature and show in Fig. 5.6 that they are well descibed by a Gaussian for all softnesses.

5.4.2 The configuration entropy

The total entropy

The total (or bulk) entropy ($S_{total}(\rho, T)$) of the system is calculated from the total (bulk) free energy of the system by thermodynamic integration (see Chapter 2). Typical pressure *vs.* density isotherms at T_{ref} and temperature dependence of potential energies are shown in Figs. 5.7 and 5.8 respectively. Temperature dependence of the total free energy and the total entropy are shown in Figs. 5.9 and 5.10. We see that at a given temperature, total entropy *increases* as softness *increases*. The calculation is validated by checking

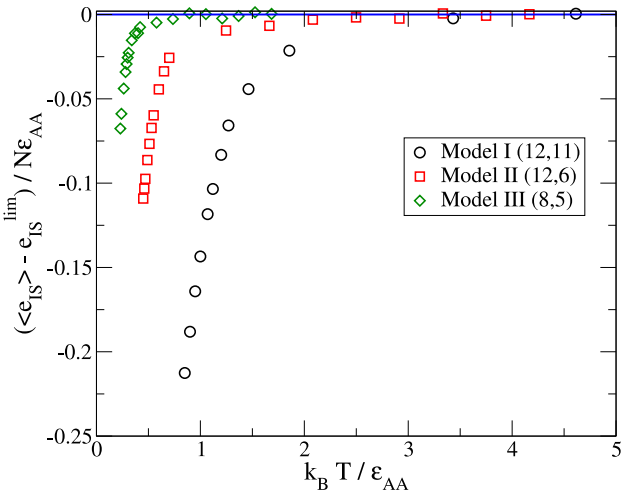

Figure 5.4: Temperature dependence of the inherent structure energy e_{IS} for the studied models shifted by the corresponding high temperature limiting values e_{IS}^{lim} for clarity. The values of e_{IS}^{lim} are $-6.003, -6.886, -7.191$ for models I $(12, 11)$, II $(12, 6)$ and III $(8, 5)$ respectively.

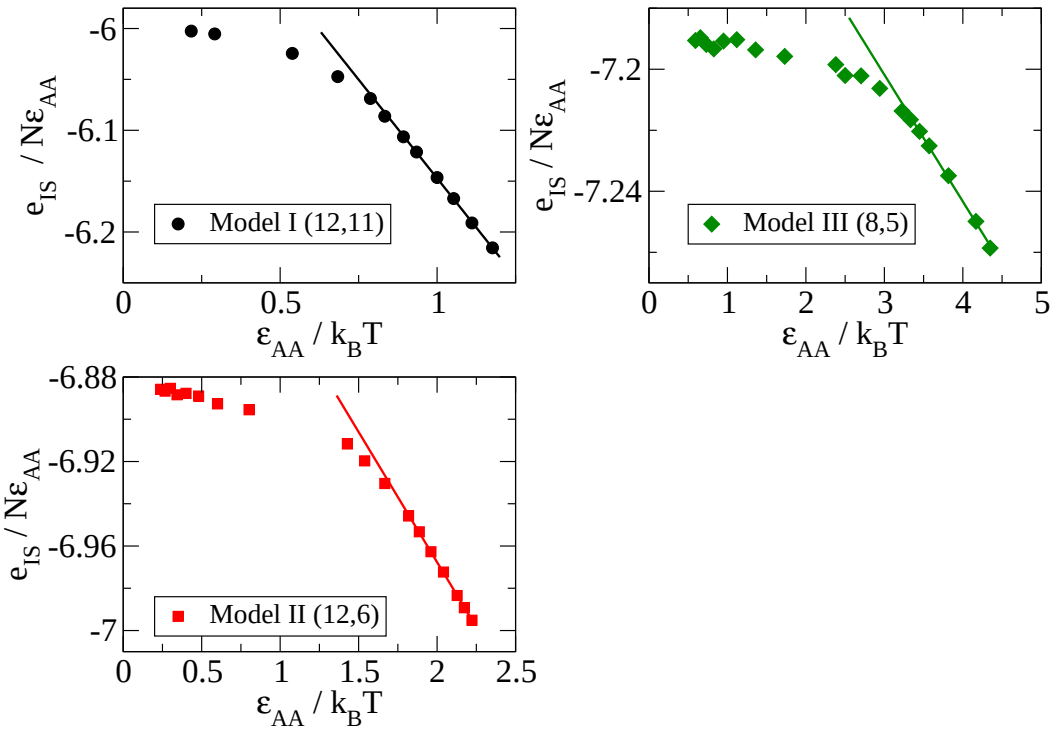

Figure 5.5: Inverse temperature dependence of IS energy shows linear dependence at low T for all softnesses.

that the total free energy and entropy computed using two different reference high temperatures match at all temperatures to an excellent degree of

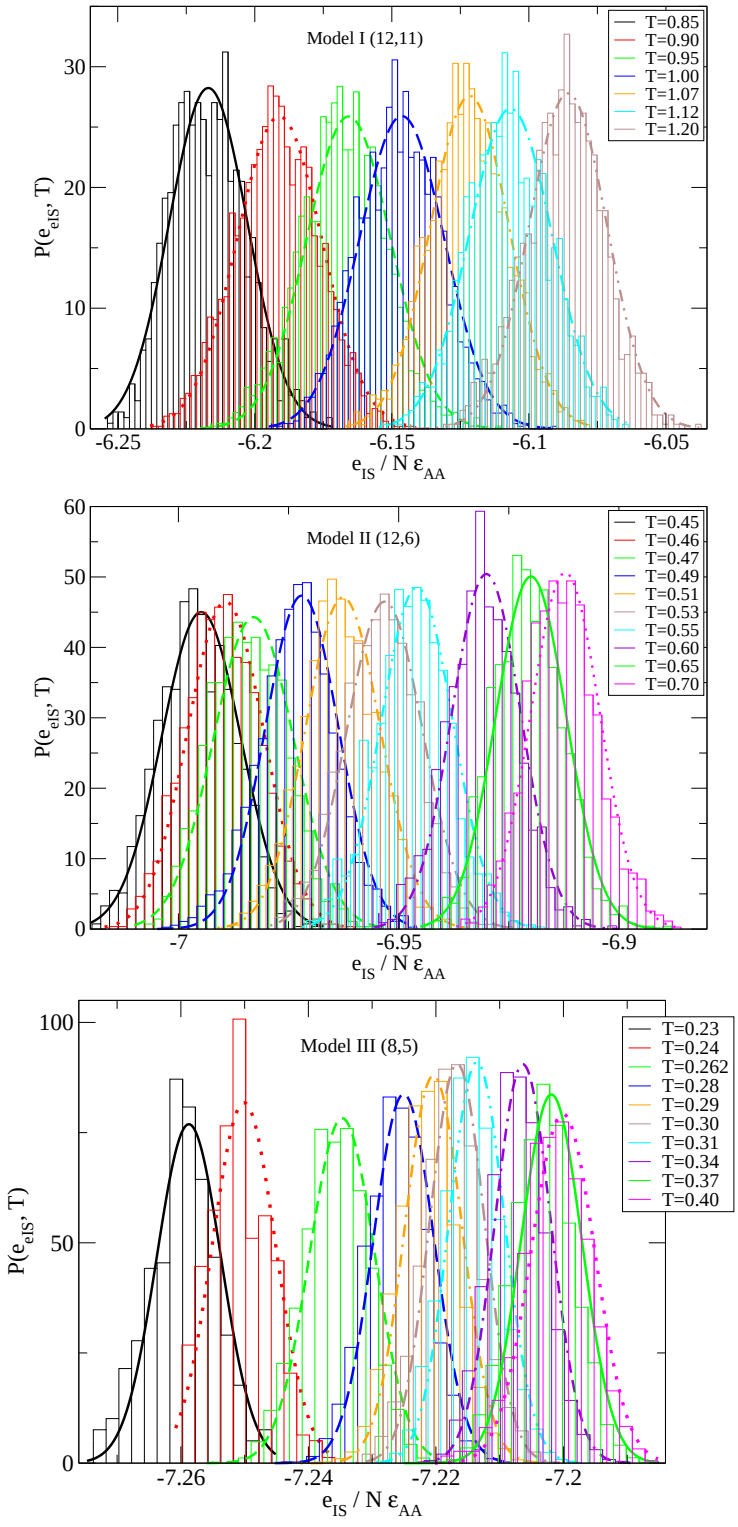

Figure 5.6: Normalized probability distribution ($P(e_{IS}, T)$) of sampling inherent structures at different temperatures for models I,II and III. Inherent structures are taken from three to five independent samples with runlengths $\sim$ 100 times longer than α relaxation times. It is seen that distribution is Gaussian for all state points considered here.

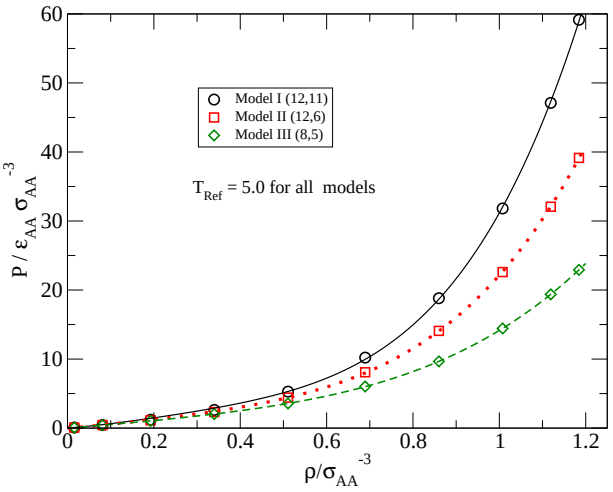

Figure 5.7: Typical pressure *vs.* density isotherms for all three models at the same reference temperature $T_{ref} = 5.0$. Lines are guide to eyes.

accuracy.

The basin and the configuration entropy

The basin free energy and the basin entropy are computed in harmonic approximation using the inherent structure approach (see Chapter 1). Fig. 5.10 shows the temperature dependence of the basin entropy for different softnesses. It is seen that at a given temperature, the basin entropy *increases* as softness *increases*.

The configuration entropy $S_c(T)$ is computed as the difference of the total and the basin entropy. It is seen from Fig. 5.11 that at a given temperature, the configuration entropy *increases* as softness *increases*. The configuration entropy density $S_c(e_{IS})$ is by definition independent of temperature. Hence $S_c(e_{IS})$ calculated using the IS formalism at different temperatures (equivalent to sampling different regions of configuration space) should fall on the same master curve. Further for all models, this master curve is found to be well approximated by a parabola: $S_C(e_{IS}) = \alpha - \frac{(e_{IS}-e^0_{IS})^2}{\sigma^2}$. This is shown in Fig. 5.12 and used to validate the calculation. Here α is the peak value of $S_C(e_{IS})$ occuring at e^0_{IS}. Various parameters related to the distribution of inherent structure energies are listed in Table 5.2.

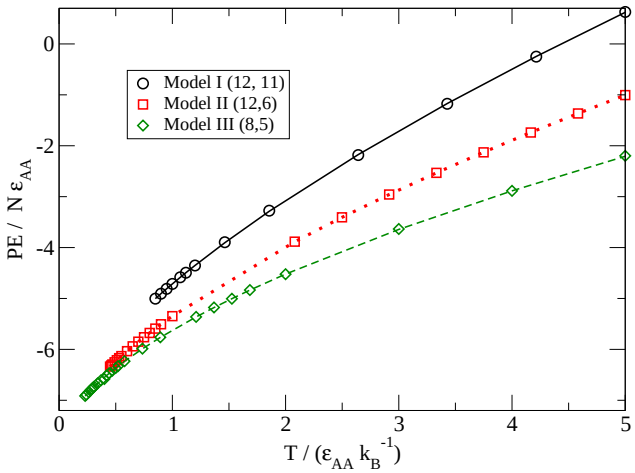

Figure 5.8: T dependence of potential energy ($< PE >$) vs. T for all models. The lines are fit to the form $PE = a + bT^c$. For model II (12,6), the exponent $c = 0.618$ which agrees reasonably well with $c = 0.612$ reported in ([69]).

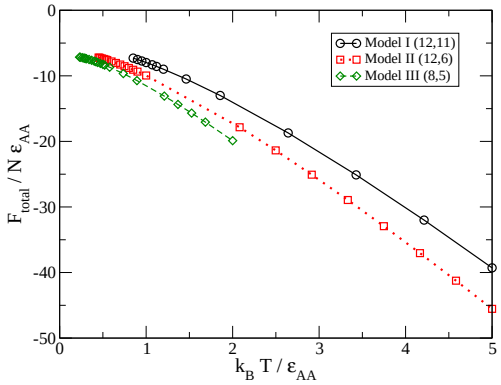

Figure 5.9: Temperature dependence of total (bulk) free energy for all models from low T to T_{ref}. Lines are guide to eyes.

5.4.3 Thermodynamic fragility *vs.* softness

The harmonic approximation of basin entropy predicts that at low temperatures well below T_{onset}, The product $TS_c(T)$ has linear T dependence. Fig. 5.13 shows that indeed, $TS_c(T)$ varies linearly with temperature, which allows us to define T_K. The T_K values for the different potentials are listed in Table 5.1. Thermodynamic fragility K_T as defined in eqn. 5.3 is computed from the slope of TS_c *vs.* T/T_K. It is found to *decrease* as the softness of the interaction potential *increases*, as shown in Fig. 5.14. Such behavior is in line with expectations, *e. g.* from [135, 141].

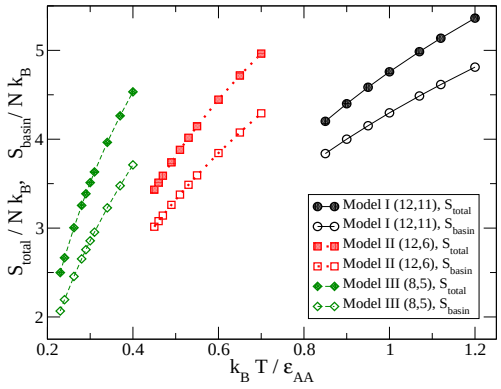

Figure 5.10: Temperature dependence of total (bulk) entropy (filled symbols) and basin entropy (open symbols) for all models below the onset temperature. Both total and basin entropy decreases as softness increases. Lines are guide to eyes.

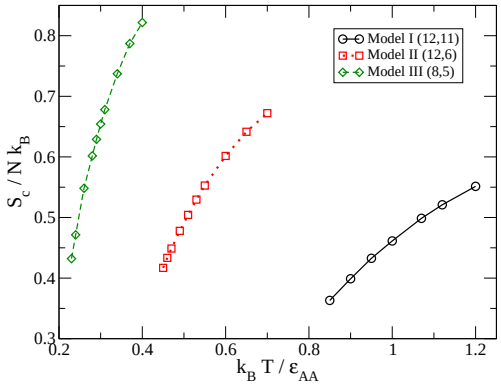

Figure 5.11: Temperature dependence of configuration entropy $S_c(T)$ for all models below the onset temperature. Lines are guide to eyes.

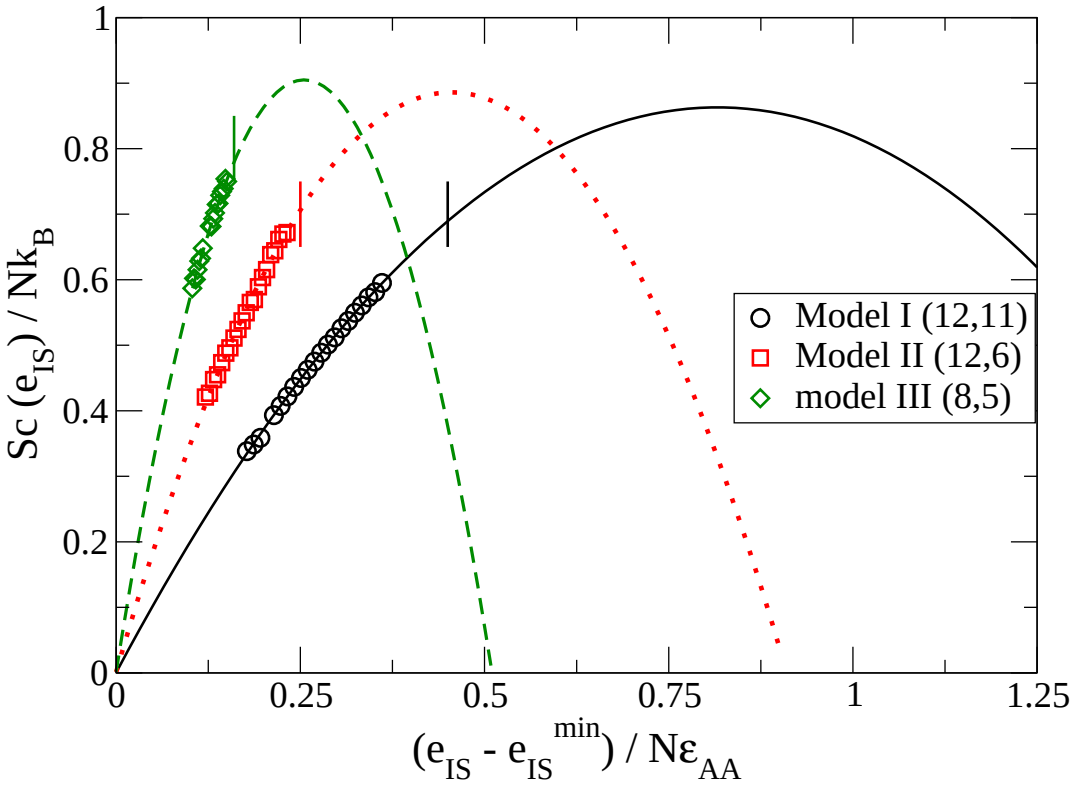

Figure 5.12: Configuration entropy density $S_c(e_{IS})$ *vs.* inherent structure energy (e_{IS}) for models I, II and III. Configuration entropy densities are computed at all low T fall on the same master curve because configuration entropy density is a geometric property of potential energy landscape and hence independentof temperature. Here this is used to validate the computational method. Besides, the master curve is expected to be a parabola which is demonstrated by the fit lines to the form $S_C(e_{IS}) = \alpha - \frac{(e_{IS}-e^0_{IS})^2}{\sigma^2}$. Here α is the peak value of $S_C(e_{IS})$ occuring at e^0_{IS}. For clarity, the X axis is shited by subtracting $e^{min}_{IS} = e^0_{IS} - \sigma\sqrt{\alpha}$, the IS energy where $S_C(e_{IS}) = 0$. The vertical tics on the fitting curves denote the positions of the limitting value at high T, $S_c(e^{lim}_{IS})$. The numerical values of different parameters are summarized in Table 5.2.

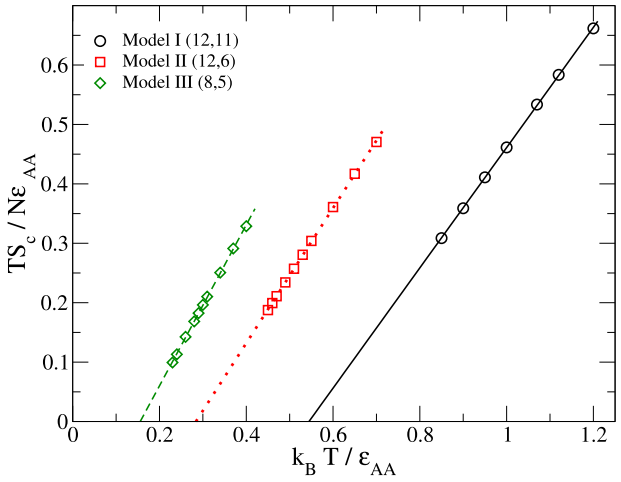

Figure 5.13: Temperature dependence of TS_c for the studied models to determine the Kauzmann temperature. $T_K = 0.54, 0.28, 0.16$ respectively for models I $(12, 11)$, II $(12, 6)$, and III $(8, 5)$. The value of T_K from the extrapolated crossing of bulk and basin entropies *vs.* temperature reported in [70] is $T_K = 0.2976$ and in [51] is $T_K \sim 0.29$. The T_K values obtained from this plot is used to determine the thermodynamic fragility in Fig. 5.14.

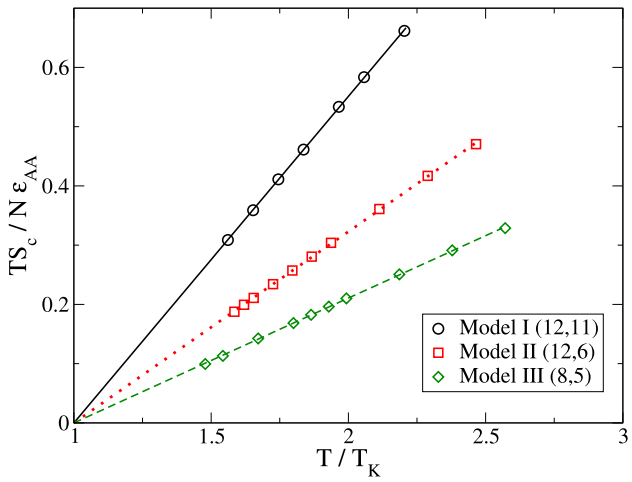

Figure 5.14: Determination of the thermodynamic fragility from the relation $TS_c = K_T(\frac{T}{T_K} - 1)$ for the studied models. K_T is the slope of the linear fit shown. T_K is the temperature at which $S_c = 0$, obtained from the linear fit shown in Fig. 5.13. Thermodynamic fragility (K_T) values are $0.551, 0.323, 0.211$ for models I $(12, 11)$, II $(12, 6)$, and III $(8, 5)$ respectively

5.5 Results : the kinetic fragility

5.5.1 The mean squared displacement and the time correlation functions

We first show in Figs. 5.15 - 5.20 the time dependence of (i) the mean squared displacement (MSD) of A particles (ii) the overlap function $q(t)$ (iii) the dynamical susceptibility ($\chi_4(t)$ and (iv) the self-intermediate scattering function ($F_s(k,t)$) computed for representative trajectories at different temperatures in increasing order of softness. These plots are used to check that each trajectory is long enough such that the overlap function decays to zero and the MSD is well into the diffusive regime.

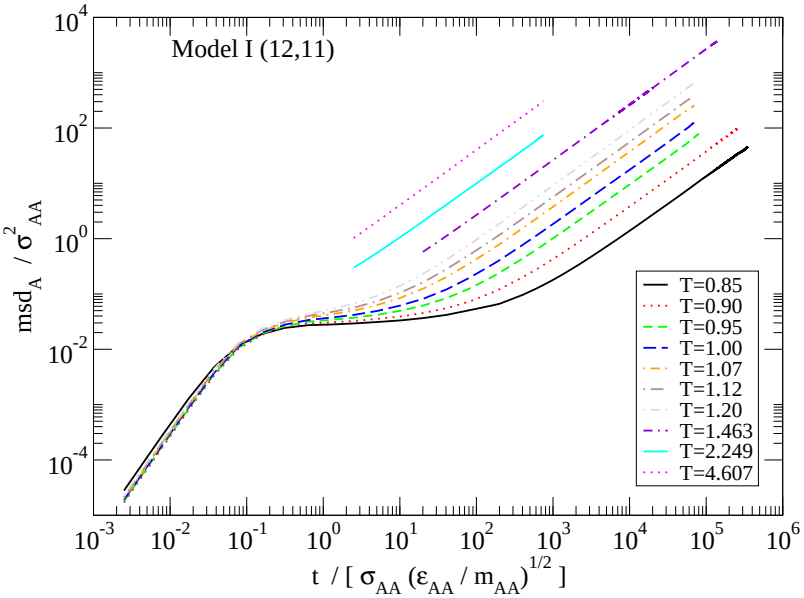

(a)

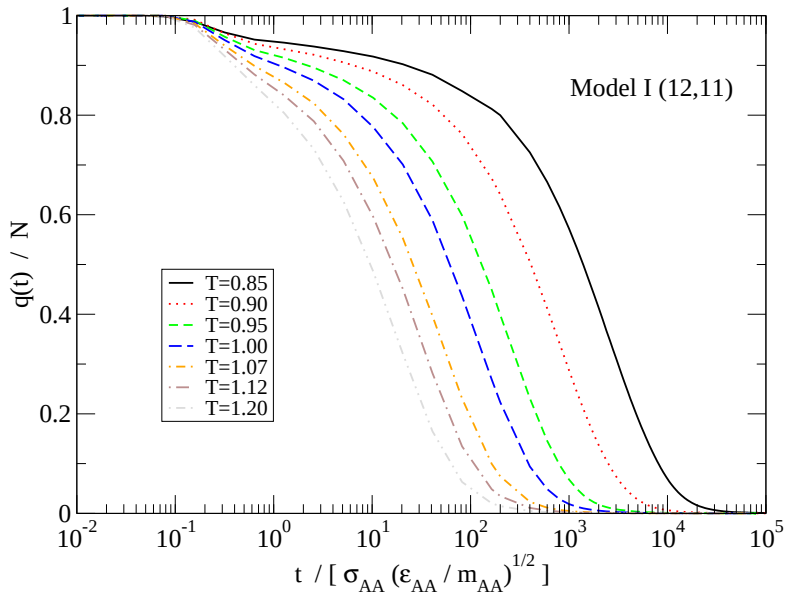

(b)

Figure 5.15: Representative MSD of A (bigger) particles and the overlap function for model I(12,11).

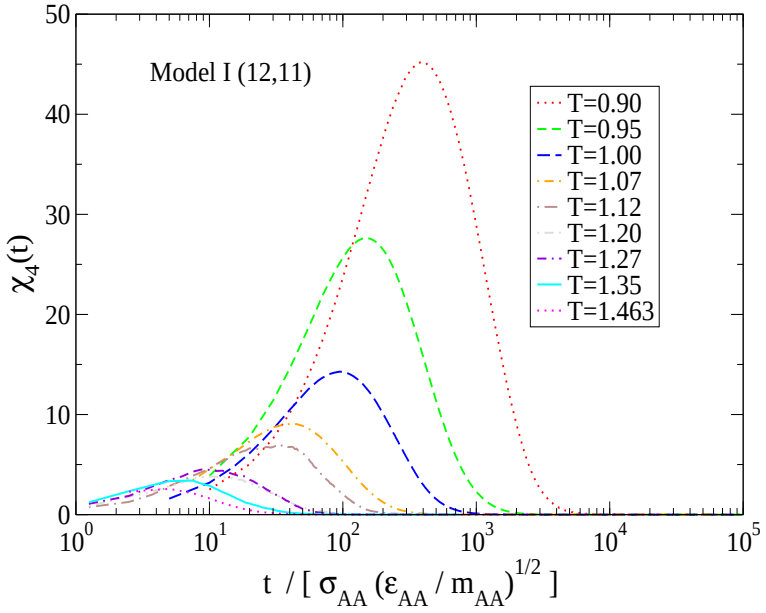

(a)

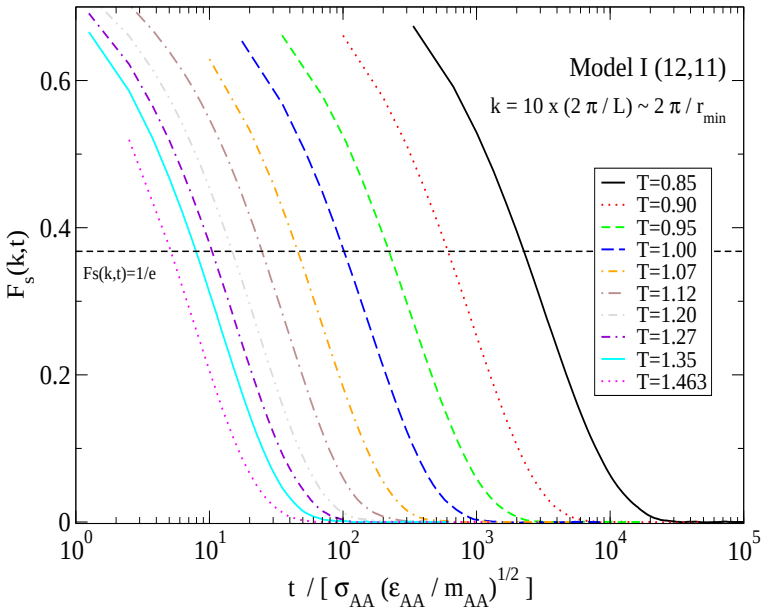

(b)

Figure 5.16: Time dependence of $\chi_4(t)$ and $F_s(k,t)$ for model I (12,11).

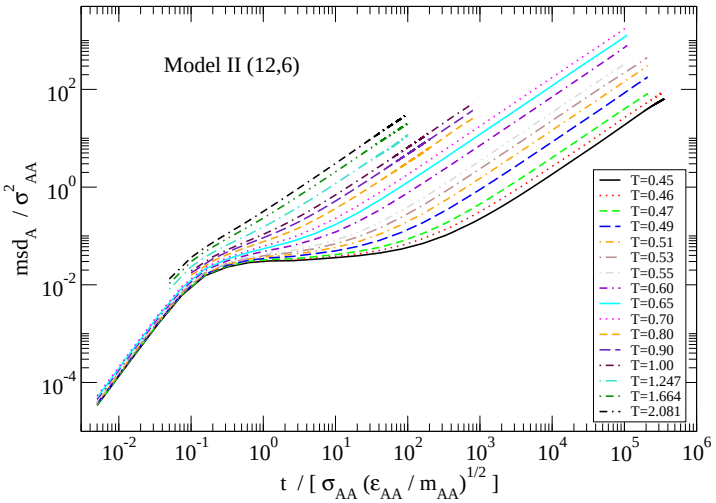

(a)

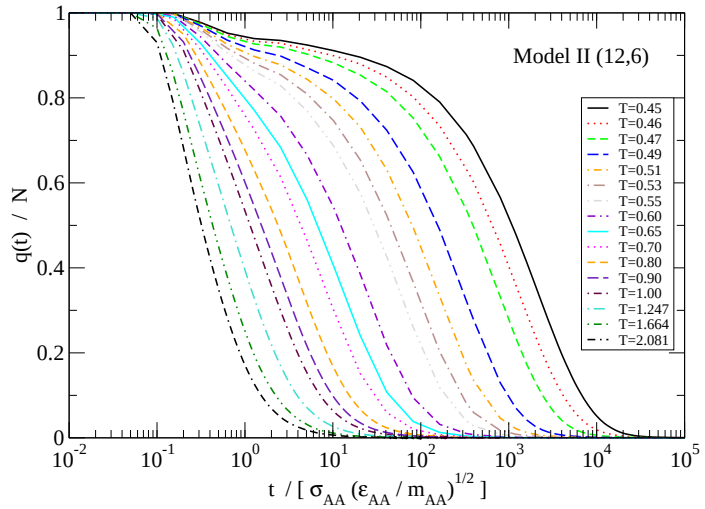

(b)

Figure 5.17: Representative MSD of A (bigger) particles and the overlap function for model II(12,6).

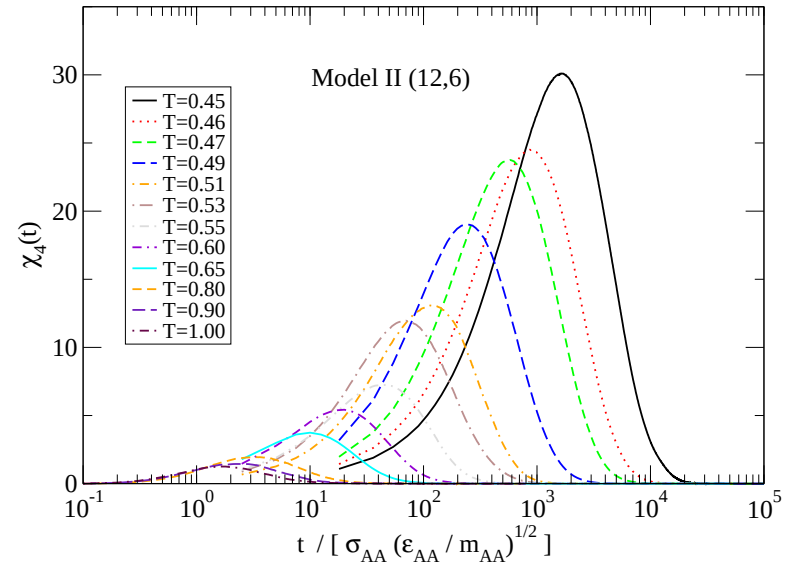

(a)

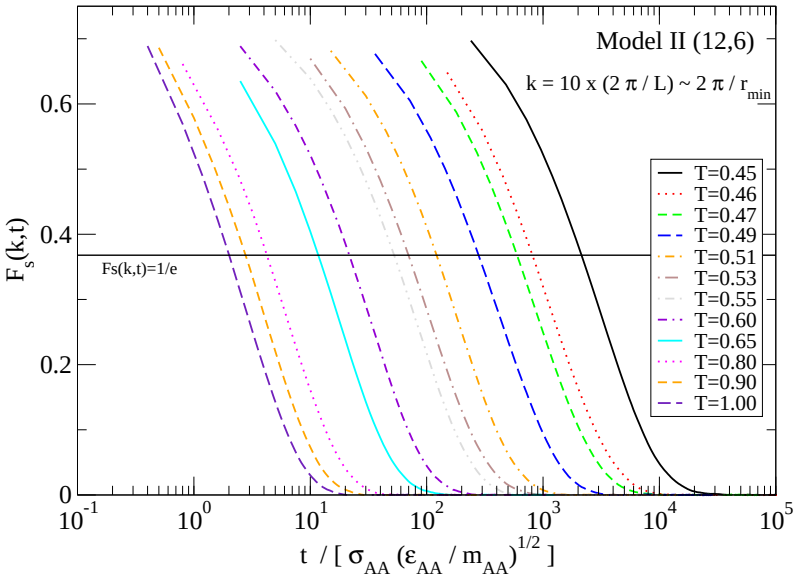

(b)

Figure 5.18: Time dependence of $\chi_4(t)$ and $F_s(k,t)$ for model II (12,6).

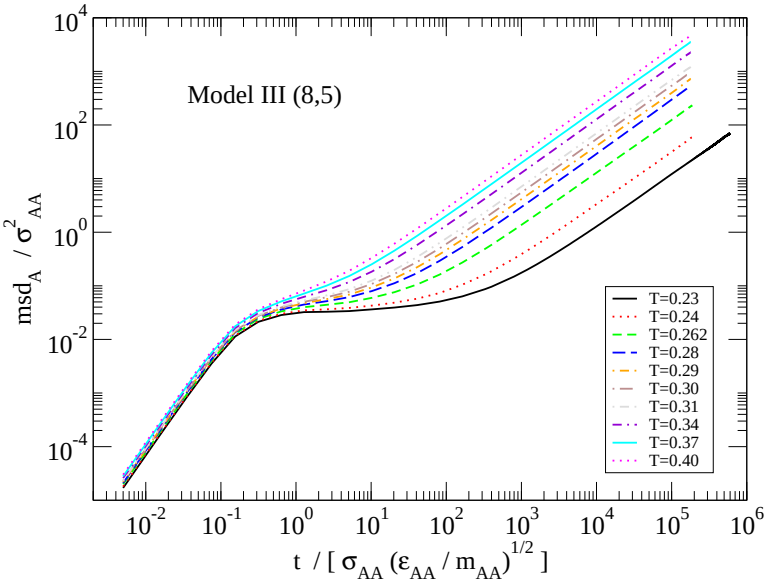

(a)

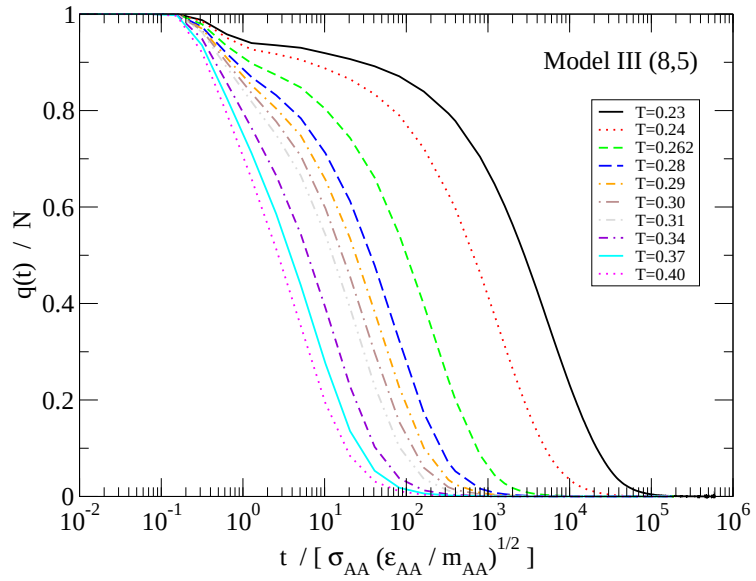

(b)

Figure 5.19: Representative MSD of A (bigger) particles and the overlap function for model III(8,5).

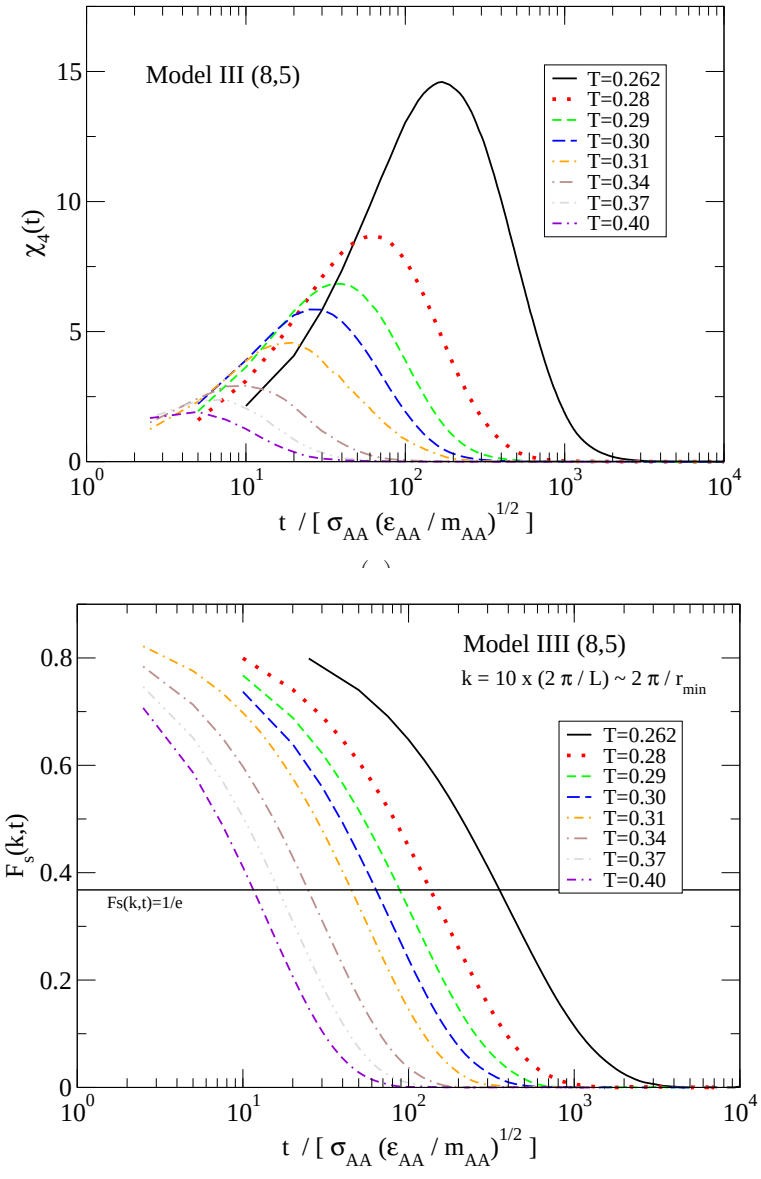

(b)

Figure 5.20: Time dependence of $\chi_4(t)$ and $F_s(k,t)$ for model III (8,5).

5.5.2 Kinetic fragility *vs.* softness

Kinetic fragility (K_{VFT}) is estimated by fitting to the VFT form Eq. 6.3 the diffusion coefficients and the relaxation times.

In Figs. 5.21 and 5.22 (top panels), we show the Arrhenius plot of the diffusion coefficients and the relaxation times from the $q(t)$, plotted against T_K/T. The VFT divergence temperatures T_{VFT}, obtained from VFT fits to the data for temperatures below the onset temperature, are found to be close to T_K and are listed in Table 5.1. The middle panels of Figs. 5.21 and 5.22 show Arrhenius fits to high temperature data (above the onset temperature), from which activation energies E_0 (such that $\tau(T) = \tau_0 \exp(E_0/k_B T)$ are obtained. These are listed in Table 5.3, and will be discussed later. In the bottom panels of Fig. 5.21 and 5.22, we show the effective activation energy defined as $E(T) \equiv k_B T \ln(\tau(T)/\tau_0)$ scaled by E_0 (similarly for D_A/T), plotted against $k_B T/E_0$. The usual three-parameter-VFT fits (without assuming $T_{VFT} = T_K$) to diffusion coefficients and relaxation times from $q(t)$ are shown in Fig. 5.23. We also show in Figs. 5.24 and 5.25 the VFT fits to relaxation times obtained from the $\chi_4^{\rm peak}$ and the $F_s(k,t)$ for the sake of completeness. However, we do not use the relaxation times from the $\chi_4^{\rm peak}$ and the $F_s(k,t)$ for further analyses.

We note in the passing that for model $(12, 6)$ the proportionality $E_0 \sim 6T_c$ [135] is reasonably well satisfied. However, the ratio E_0/T_c decreases from ~ 7 to ~ 5 as softness increases.

Next, we calculate the kinetic fragilities K_{VFT}, from diffusion coefficients and relaxation times, using the divergence temperature T_{VFT} obtained with T_{VFT} as a fit parameter, as well as using T_K estimates from the configuration entropy as the divergence temperatures. The corresponding kinetic fragilities, labeled K^I_{VFT} and K^{II}_{VFT}, are listed in Table 5.4, along with the thermodynamic fragilities K_T. We find that *the kinetic fragilities increase as the softness of the interaction potential increases, thus showing a trend that is opposite to that of the thermodynamic fragility.*

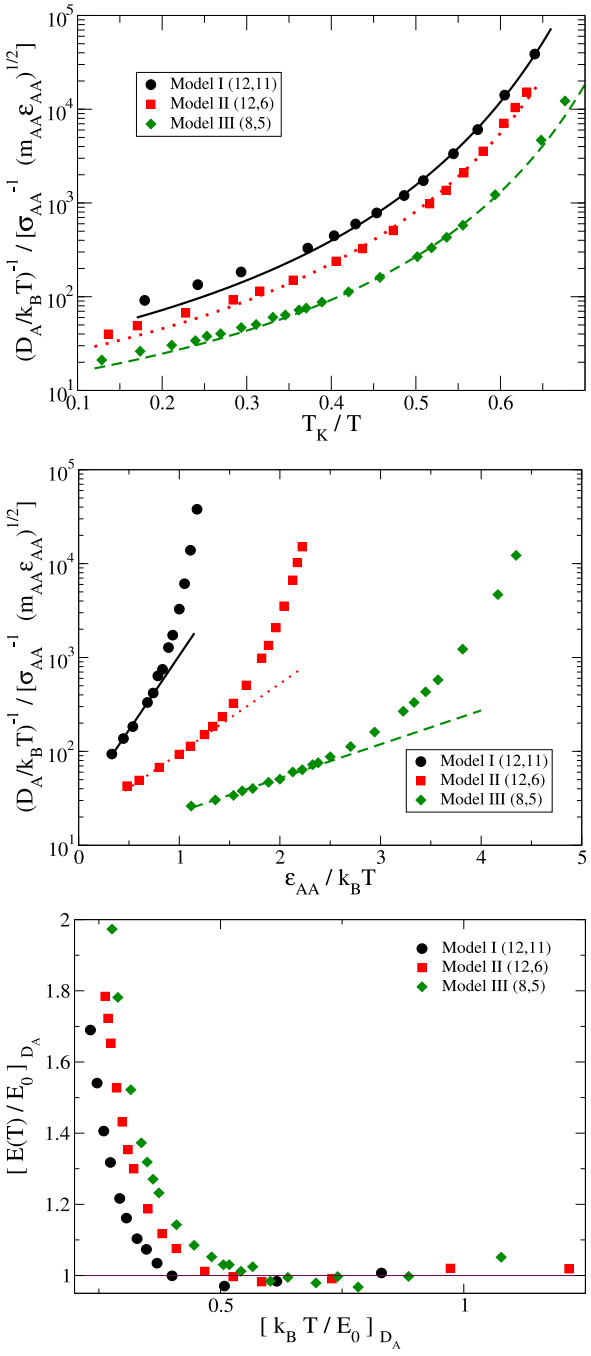

Figure 5.21: Top row: Inverse diffusion coefficient *vs.* scaled inverse temperature $\frac{T_K}{T}$. Lines through the data show VFT fits to the data below the onset temperature. T_K estimated from Fig. 5.13 are used as the divergence temperatures in the VFT fits. Middle row: Arrhenius fits to high temperature data of inverse diffusion coefficient to determine high temperature activation energies E_0. Bottom row: effective activation energy $E(T)$ (see text) scaled by E_0, plotted against k_BT/E_0.

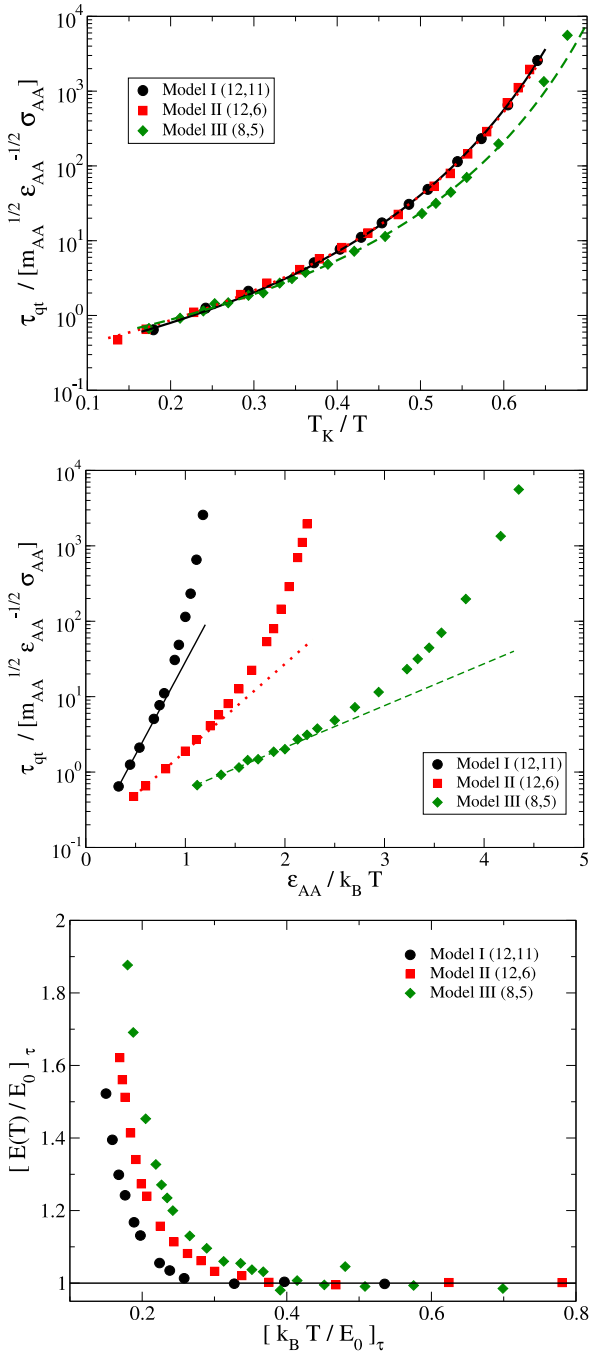

Figure 5.22: Top row: Relaxation time from overlap function *vs.* scaled inverse temperature $\frac{T_K}{T}$. Lines through the data show VFT fits to the data below the onset temperature. T_K estimated from Fig. 5.13 are used as the divergence temperatures in the VFT fits. Middle row: Arrhenius fits to high temperature data of relaxation time from overlap function to determine high temperature activation energies E_0. Bottom row: effective activation energy $E(T)$ (see text) scaled by E_0, plotted against k_BT/E_0.

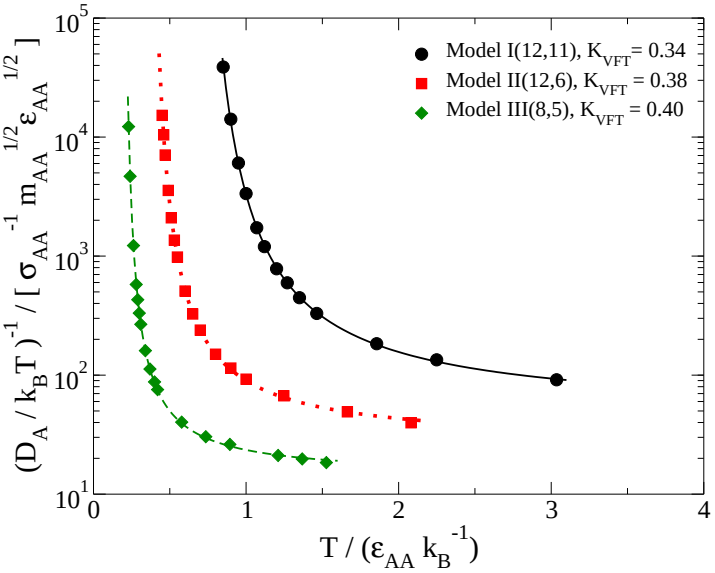

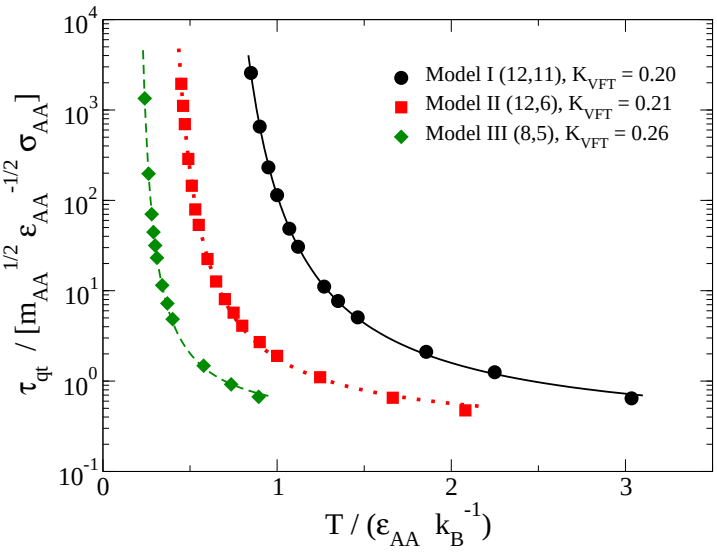

(b)

Figure 5.23: Three-parameter, usual VFT fit to diffusion coefficients and relaxation time from $q(t)$ for all models.

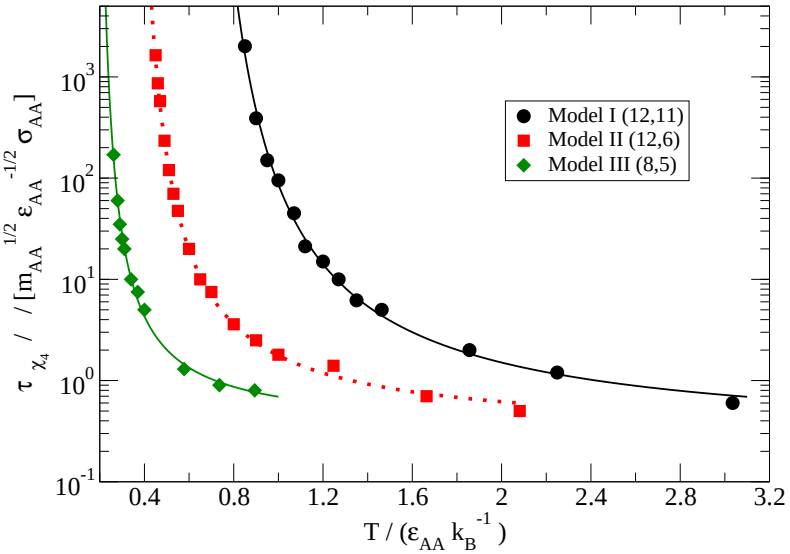

Figure 5.24: VFT fit to relaxation times from the $\chi_4^{peak}(t)$ *vs.* temperature for all models.

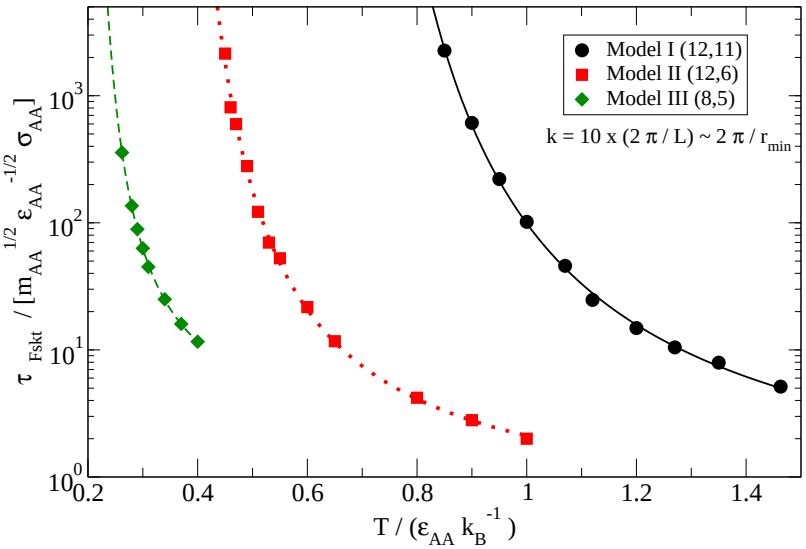

Figure 5.25: VFT fit to relaxation times from the $F_s(k,t)$ *vs.* temperature for all models.

5.6 Adam Gibbs relation and fragility

In order to understand this discrepancy, we consider again the Adam-Gibbs relation, which relates the kinetic and thermodynamic fragilities. Comparing Eq. 6.3, Eq. 6.4 and Eq. 5.3, we note that the relationship between the kinetic and thermodynamic fragilities that we may deduce assuming the validity of the VFT and the AG relations is

$$K_{VFT} = K_T/A \tag{5.8}$$

and we expect at least the same trend in the two fragilities under the assumption that the term A does not substantially alter the proportionality between kinetic and thermodynamic fragilities. To assess the degree to which this is true in our models, we show in Figs. 5.26, 5.27 and 5.28 the Adam-Gibbs plots of the diffusion coefficient and relaxation times. These plots show that the coefficient A, obtained from the slopes (and listed in Table 5.3), indeed varies from one model to the other, *decreasing* as the softness increases. Thus, the ratio K_T/A shows the opposite trend, *increasing* as the softness increases.

We next attempt to understand the dependence of the Adam-Gibbs coefficient A on the softness of the interaction. First we consider the high temperature Arrhenius behavior of relaxation times, in terms of the Adam-Gibbs relation. Such Arrhenius behavior can be expected if the configuration entropy effectively becomes a constant, in which case, the high temperature activation energy will be given by

$$E_0 = Ak_B/Sc_\infty \tag{5.9}$$

However, the asymptotic high temperature configuration entropy is difficult to assess directly, as the various available approaches to computing the basin entropy do not work well in this regime(see *e. g.* [68]). We thus use the following procedure: First, we determine directly from simulations the high temperature limit of the inherent structure energies, e_{IS}^{lim} (see Fig. 5.4). Then, we use the extrapolation of the dependence of the configuration entropy S_c on the inherent structure energy e_{IS} obtained below the onset temperature to obtain the high temperature limit of the configuration entropy (see Fig. 5.12), $S_c(e_{IS}^{lim})$, which do not vary appreciably with softness of interaction,

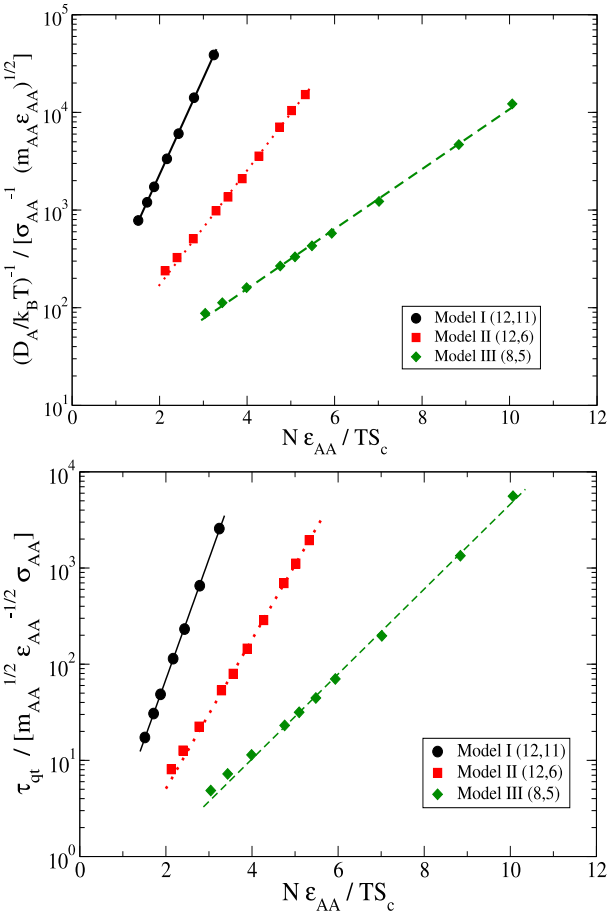

Figure 5.26: Adam Gibbs plots for the inverse diffusion coefficient of A particles and relaxation time from overlap function, for the three models studied. The activation energy parameter A in Eq. 6.4, obtained from the slopes of the data shown, are tabulated in table 5.3.

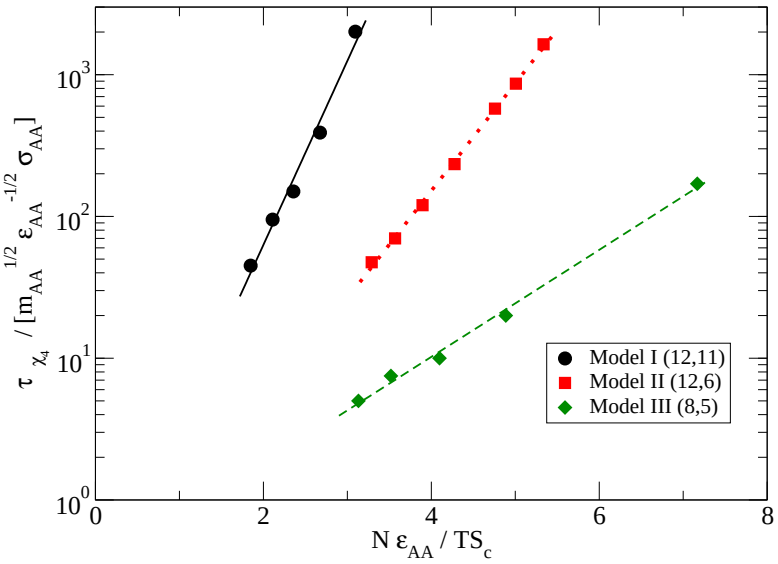

Figure 5.27: Adam Gibbs relation for different softnesses where the relaxation time is measured from χ_4^{peak} time.

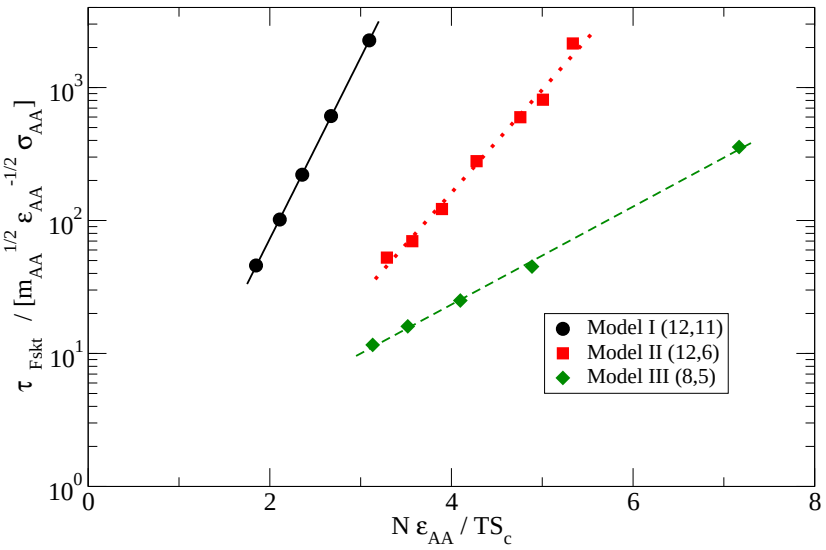

Figure 5.28: Adam Gibbs relation for different softnesses where the relaxation time is measured from $F_s(k,t)$.

and are listed in Table 5.2 . Table 5.2 also lists $S_c(\infty)$, the infinite temperature value of S_c obtained by extrapolating Eq. 5.3 to infinite temperature, a procedure that is not justified at temperatures above the onset temperature. Using these $S_c(e_{IS}^{lim})$ values, and the activation energies E_0 shown in Table

5.3, we obtain estimates for the AG coefficient

$$A_{est} = E_0 S_c(e_{IS}^{lim})/k_B \tag{5.10}$$

which are shown in Table 5.3. We note in Table 5.3 that E_0 values decrease strongly as the softness of the interactions increases, and with a corresponding moderate increase of $S_c(e_{IS}^{lim})$, our estimates of A_{est} agree rather well with the values obtained directly from the Adam-Gibbs plots. We now designate the thermodynamic fragility estimates obtained by considering the full form of the Adam-Gibbs relation as

$$K_{AG} = K_T/A \tag{5.11}$$

and list them along side the thermodynamic and kinetic fragility estimates in Table 5.4 . As expected from the above discussion, the "Adam-Gibbs" fragility estimates (K_{AG}^I in Table 5.4) agree rather well with the kinetic fragilities.

Although the above picture provides a consistent description of the fragilities from kinetic and thermodynamic data, a question remains regarding the variation of the high temperature activation energy E_0 with the softness of the interaction potential. To seek some insight into this question, we consider works in recent years concerning the scaling of the temperature dependence of dynamic and thermodynamic quantities at different densities [130, 146, 147]. It has been shown by many groups that a scaled variable ρ^γ/T, where ρ is the density, captures the density variation of properties in many liquids. The exponent γ can easily be shown to be $n/3$ for inverse power law potentials, where n is the power of the inverse power law, but even for other liquids, an effective γ has been shown to be derivable by considering the correlated fluctuations of potential energy and the virial [146]. The exponent γ is obtainable as the ratio of fluctuations. We discuss this density-temperature scaling in more detail in Chapter 6. Although such a ratio is state point dependent, a "best fit" value, typically obtained from high temperature state points, has been shown to effectively describe the scaling of properties at different densities. Since we do not perform a full analysis of the density dependence here, we do not estimate the best value of γ but instead use the value at twice the onset temperature as an indicative value. Fig. 5.29 shows the fluctuation data from which the γ value is obtained,

Table 5.2: Potential energy landscape parameters and density temperature scaling exponents for the studied models. Fit forms used: $\langle e_{IS}\rangle(T) = \langle e_{IS}\rangle(\infty) - \frac{\sigma^2}{2T}$; $S_C(e_{IS}) = \alpha - \frac{(e_{IS}-e^0_{IS})^2}{\sigma^2}$.

Quantity	(12,11)	(12,6)	(8,5)
Density minimum for IS pressure	1.04	1.09	1.18
Height of $S_C(e_{IS})$ distribution α	0.863	0.886	0.905
Spread of $S_C(e_{IS})$ distribution $\alpha^{1/2}\sigma$	0.816	0.455	0.255
IS Energy where $S_C(e_{IS}) = 0$, $e^{min}_{IS} = e^0_{IS} - \sigma\sqrt{\alpha}$	-6.457	-7.132	-7.346
$\langle e_{IS}\rangle(\infty)$	-5.761	-6.734	-7.098
Limiting value of IS energy e^{lim}_{IS}	-6.003	-6.886	-7.191
$S_c(e^{lim}_{IS})$	0.69	0.7	0.78
$S_c(\infty) = \frac{K_T}{T_K}$	1.01	1.14	1.35
Density temperature scaling exponent at $2 \times T_{onset}$			
γ_1	6.09	4.99	3.71
γ_2	6.18	5.07	3.89
γ_3	6.27	5.15	4.09
$\rho^{\gamma_1} = 1.2^{\gamma_1}$	3.04	2.48	1.97
$\rho^{\gamma_2} = 1.2^{\gamma_2}$	3.09	2.52	2.03
$\rho^{\gamma_3} = 1.2^{\gamma_3}$	3.14	2.56	2.11

and the temperature variation of the exponents. The values of γ we use are shown in Table 5.2.

Based on the above considerations, we should expect the high temperature activation energies to be proportional to ρ^γ. Accordingly, we obtain estimates of the activation energy in the form $E_0 = E_{00}\rho^\gamma$. These values, shown in Table 5.3, have a weaker temperature dependence than the directly evaluated E_0, and correspondingly, the fragility estimates obtained (shown in Table 5.4), while showing a smaller decrease with softness, nevertheless decrease with increasing softness of interaction. A further analysis is needed, therefore, to elucidate the relevance of these considerations to evaluating the variation of the high temperature activation energy.

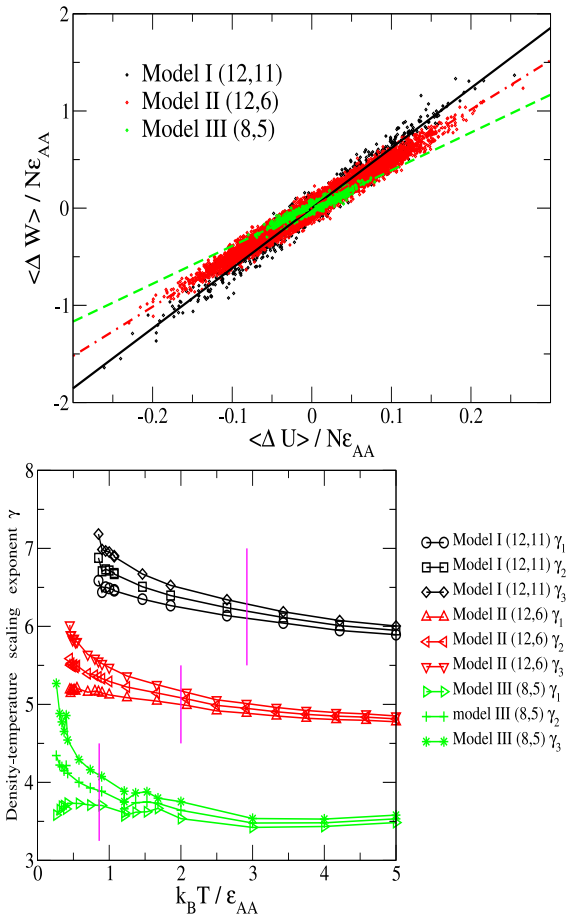

Figure 5.29: Determination of the density-temperature scaling exponent γ from the correlation between instantaneous potential energy (U) and virial (W). $\gamma_1 = \frac{\langle \Delta W \Delta U \rangle}{\langle (\Delta U)^2 \rangle}$, $\gamma_2 = \frac{\sqrt{\langle (\Delta W)^2 \rangle}}{\sqrt{\langle (\Delta U)^2 \rangle}}$, $\gamma_3 = \frac{\langle (\Delta W)^2 \rangle}{\langle \Delta W \Delta U \rangle}$ where $\Delta U = U - \langle U \rangle$ and $\Delta W = W - \langle W \rangle$ represent fluctuations about mean of potential energy and virial respectively. The left panel shows the correlation between energy and virial at temperatures $\approx 2T_{onset}$, with straight line fits $\langle \Delta W \rangle = \gamma_2(2T_{onset})\langle \Delta U \rangle$. The right panel shows the temperature dependent values of γ for the studied models.

Table 5.3: Comparison of activation energy parameters. A is the activation parameter in the Adam Gibbs (AG) relation. E_0 is the high temperature activation energy in Arrhenius fit. $S_c(e_{IS}^{lim})$ is the values of configuration entropy density at the limiting value of inherent structure energies at high temperatures. $A_{est}^{I} = E_0 S_c(e_{IS}^{lim})/k_B$ is the expected value of parameter A obtained from E_0. $E_0^{est} = E_{00}\rho^{\gamma}$ is the estimate of E_0 from density - temperature scaling of relaxation time where γ_2 are the values of the scaling exponent at twice the onset temperature. $A_{est}^{II} = E_0^{est} S_c(e_{IS}^{lim})$ is the expected value of energy barrier A obtained from E_0^{est}.

	From $q(t)$						From $(\frac{D_A}{T})^{-1}$					
Model	A	E_0	A_{est}^{I}	E_{00}	E_0^{est}	A_{est}^{II}	A	E_0	A_{est}^{I}	E_{00}	E_0^{est}	A_{est}^{II}
(12,11)	2.88	5.67	3.91		4.13	2.85	2.27	3.65	2.52		2.63	1.81
(12,6)	1.79	2.67	1.87	1.34	3.38	2.40	1.35	1.71	1.20	0.85	2.14	1.52
(8,5)	1.02	1.28	1.00		2.72	2.12	0.71	0.83	0.65		1.73	1.35

Table 5.4: Comparison of fragility parameters. K_T is thermodynamic fragility obtained from temperature dependence of $TS_c(T)$. K_{VFT}^{I} is kinetic fragility from VFT fit and K_{VFT}^{II} is kinetic fragility obtained from VFT fit assuming $T_{VFT} = T_K$. $K_{AG}^{I} = \frac{K_T}{A_{est}^{I}}$ is the fragility expected from high temperature activation energy E_0 obtained from an Arrhenius fit. $K_{AG}^{II} = \frac{K_T}{A_{est}^{II}}$ where the high temperature activation energy is estimated from density-temperature scaling.

		From $q(t)$				From $(\frac{D_A}{T})^{-1}$			
Model	K_T	K_{VFT}^{I}	K_{VFT}^{II}	K_{AG}^{I}	K_{AG}^{II}	K_{VFT}^{I}	K_{VFT}^{II}	K_{AG}^{I}	K_{AG}^{II}
(12,11)	0.551	0.20	0.19	0.14	0.19	0.34	0.24	0.22	0.30
(12,6)	0.323	0.21	0.20	0.17	0.13	0.38	0.26	0.27	0.21
(8,5)	0.211	0.26	0.23	0.21	0.10	0.40	0.32	0.32	0.16

5.7 Conclusions

To summarize, we have studied the effect of the softness of the interaction potential on fragility in three model glass formers. We find on the one hand that the kinetic fragility obtained from diffusion coefficients and relaxation times *increases* with increasing softness of the interaction potential, contrary to expectations based on earlier studies [135, 141]. On the other hand, a thermodynamic fragility obtained from the temperature variation of the configuration entropy *decreases* with increasing softness of the interaction potential. By taking into consideration the model dependence of the high temperature activation energy, in addition to the temperature dependence of the configuration entropy, we define an "Adam-Gibbs" fragility whose model dependence accurately captures the variation of the kinetic fragilities that we find. An attempt to rationalize the model dependence of the high temperature in terms of the scaling of properties with respect to density is encouraging but fails to fully explain the observed decrease of the fragility with increasing softness of the interaction potential.

Chapter 6

Density-temperature scaling in the Kob-Andersen model and its implication for the fragility

6.1 Introduction

Glass forming liquids show a wide variety of dynamical behaviours (see Chapter 1), typically at low temperatures and high densities (pressures), which are yet to be satisfactorily described in full detail by any microscopic theory. However, recent analyses of many liquids over a wide range of temperatures and densities (pressures) have shown two interesting properties which considerably simplifies the description of dynamics.

Firstly, it has been found empirically that relaxation times of many liquids, *when expressed in appropriate units*, depend on density (ρ) and temperature (T) through a specific combination only. This implies the interesting possibility of a "hidden" density -temperature scaling law in liquids. Roland and co-workers [147–149] found this combination to be $\frac{\rho^\gamma}{T}$, *i.e.* $\tau = f(\frac{\rho^\gamma}{T})$ where the function f is in general unknown and depends on the material. The exponent γ can be found empirically by demanding collapse of relaxation times (or diffusion coefficients) at different densities (or pressures) and temperatures on a single master curve. For a certain class of liquids, γ may also be computed from thermodynamic quantities as will be explained later. Alba-Simionesco and co-workers [150] also found similar empirical data collapse for relaxation times with the above mentioned functional form. However,

they also show that data collapse can be obtained with a different form $\tau = f(\frac{\rho-\rho^*}{T})$ as well. In a separate line of reasoning, Alba-Simionesco and co-workers [151] propose the hypothesis that for many liquids the density dependence of relaxation times can be described by a *single* density-dependent parameter (occurring as a temperature or energy scale, say $E_0(\rho)$). According to their hypothesis, when the temperature dependent activation energy ($E(T)$, obtained by inverting the relaxation time using Arrhenius law) scaled by $E_0(\rho)$ is plotted against temperature scaled by $E_0(\rho)$, relaxation times for different densities should fall on the same master curve.

Secondly, recent works [152–156] have shown that many liquids show strong correlation (defined as the correlation coefficient > 0.9) between instantaneous values of the potential energy (U) and the virial (W). This correlation is exact for a class of hypothetical liquids denoted by IPL liquids in which the interparticle interactions are described by purely repulsive inverse power law (IPL) potentials: $v(r) \sim r^{-n}$. Since $v(r)$ is a homogeneous function of r, it follows that the instantaneous potential energy is proportional to the instantaneous virial with the proportionality constant $\gamma = n/D, D =$ the spatial dimension. In other words, this is a consequence of the power law nature of the potential [159, 160]. The density-temperature scaling can also be straight forwardly shown to be valid for IPL liquids. The observations of (i) the strong correlation between instantaneous values of the potential energy and the virial, and (ii) the density-temperature scaling in a non-IPL liquid is rationalized by approximating the interaction potential of an non-IPL liquid by an effective inverse power law (IPL) potential where the power is *different* from the repulsive part of the original potential. This is further generalized by introducing the concept of *isomorphs* [155]. Schrøder, Dyre and co-workers have shown that the exponent γ in density-temperature scaling of relaxation time can be computed from the virial-potential energy correlation [152–156].

However, two things complicate this picture. First, the values of γ computed from virial-potential energy correlation depend on state points. Second, Tarjus and coworkers have come up with a counter example (WCA version of the KA liquid) which show strong correlation but not density-temperature scaling [157, 158].

Here, we study the standard Kob-Andersen (KA) model in three dimensions in the context of the above findings. The key aims of the present study are:

1. To verify the strong correlation between the instantaneous potential energy and the instantaneous virial in the 3D KA model.

2. To verify the density-temperature scaling of dynamics. Available literature results show that in the KA model, the dynamical quantities $(F_s(k^*, t^*)vs.t^*, \chi_4 vs.t^*)$ obey density temperature scaling for the *entire time range*. Also, relaxation times and diffusion coefficients (τ^*, D^*) in appropriate units show density temperature scaling.

3. If the 3D KA model shows both the strong pressure-energy correlation and the density-temperature scaling, as shown earlier by Schrøder and coworkers, the main question is then to understand how the thermodynamic (K_{AG}) and the kinetic fragility (K_{VFT}) (defined later) vary with density.

6.2 Simulation details

We have studied the Kob-Andersen model [173] which is a 80:20 binary mixture of Lennard Jones particles (see Chapter 2). Molecular dynamics (MD) simulations were done in a cubic box with periodic boundary conditions in the constant number, volume and temperature (NVT) ensemble at five densities $(\rho = 1.1, 1.15, 1.2, 1.25, 1.35)$. The integration time step was in the range $dt = 0.001 - 0.005$. Temperatures were kept constant using an algorithm due to Brown and Clarke [177]. System size were $N = 1000, N_A = 800$ (N = total number of particles, N_A = number of particles of type A). The temperature range for different densities are shown in Table 6.1. For all state points, three to five independent samples was used with run lengths $> 100\tau_\alpha$ (τ_α is the relaxation time, see Chapter 1). We also tabulate for comparison in Table 6.2 the density and temperature range of the 3D KA model studied in earlier works [69, 128].

6.3 Definitions of the relevant quantities

6.3.1 The diffusion coefficient and the α relaxation time

The following measures have been used to extract α relaxation times (see Chapter 2). (i) The self diffusion coefficient (D_A) from the mean squared

Table 6.1: The range of the density and the temperature of the 3D KA model simulated in the present study.

N	Density / σ^{-3})	Temperature range / ϵ_{AA}/k_B)
1000	1.10	0.28 - 2.00
	1.15	0.34 - 2.00
	1.20	0.435 - 2.00
	1.25	0.52 - 2.00
	1.35	0.78 - 2.00

Table 6.2: The range of the density and the temperature of the 3D KA model taken from Sastry [69] to compare diffusion coefficients and the kinetic fragilities.

Source	N	Density / σ^{-3})	Temperature range / ϵ_{AA}/k_B)
Sastry, PRL 2000 [69]	256	1.10	$\sim 0.28 - 0.8$
		1.15	$\sim 0.39 - 0.9$
		1.20	$\sim 0.5 - 0.9$
		1.25	$\sim 0.57 - 1.0$
		1.35	$\sim 0.85 - 1.15$

displacement (MSD) of the A type particles. (ii) The relaxation times obtained from the decay of the overlap function $q(t)$ using the definition $q(t = \tau_\alpha, T)/N = 1/e$.

6.3.2 The configurational entropy

The configurational entropy (S_c) per particle (see Chapter 1), is calculated [69] by subtracting from the total entropy of the system the vibrational component:

$$S_c(T) = S_{total}(T) - S_{vib}(T) \tag{6.1}$$

The total entropy of the liquid is obtained via thermodynamic integration from the ideal gas limit and the vibrational entropy is calculated by making a harmonic approximation to the potential energy about a given local minimum [69–72]. The procedure used for generating local energy minima, and calculating the vibrational entropy is as outlined in [69, 70].

We have also computed the configuration entropy density $S_c(e_{IS}) = k_B \ln \Omega(e_{IS})$ where $\Omega(e_{IS})$ is the number density of inherent structures with energy e_{IS} and to a good approximation may be described by a Gaussian. Equivalently, $S_c(e_{IS})$ can be described by a parabola

$$S_c(e_{IS}) = \alpha - \frac{(e_{IS} - e^0_{IS})^2}{\sigma^2} \tag{6.2}$$

The parameter α denotes the peak value of $S_c(e_{IS})$ which occurs at energy e^0_{IS}. $S_c(e_{IS})$ is zero at $e_{IS} = e^0_{IS} \pm \sigma\sqrt{\alpha}$. Thus $\sigma\sqrt{\alpha}$ is a measure of the spread of $S_c(e_{IS})$.

6.3.3 Fragility

Fragility, is a material parameter which quantifies how rapidly the shear viscosity, relaxation times and diffusion coefficients rises with temperature as glass forming liquids approach their (laboratory) glass transition temperatures (see Chapters 1 and 5). In the present study the kinetic fragility is defined from the Vogel-Fulcher-Tammann (VFT) fits to relaxation times

(and diffusion coefficients):

$$\tau(T) = \tau_0 \exp\left[\frac{1}{K_{VFT}(\frac{T}{T_{VFT}} - 1)}\right] \tag{6.3}$$

which defines the kinetic fragility K_{VFT} and the divergence temperature T_{VFT}. We refer to K_{VFT}, which is measured from relaxation times (and diffusion coefficients), as the *kinetic* fragility to distinguish from the *thermodynamic* fragility defined later. However, we note that since we have performed NVT simulations, we have measured the *isochoric fragility*.

Although easy to define, a fully satisfactory understanding of the fundamental quantities that determine fragility has not been reached yet. One approach along which considerable progress has been made is to connect fragility to thermodynamic quantities *via* the Adam Gibbs (AG) relation [37] between the relaxation time and the configuration entropy (S_c):

$$\tau(T) = \tau_0 \exp(\frac{A}{TS_c}) \tag{6.4}$$

and to use the potential energy landscape approach to relate features of the energy landscape of a glass former to the configuration entropy and thus to fragility [128]. If the T-dependence of S_c is given by

$$TS_c = K_T\left(\frac{T}{T_K} - 1\right) \tag{6.5}$$

the Adam-Gibbs relation [Eqn. 6.4] yields the VFT relation, with the identification $K_{VFT} = K_T/A$, $T_{VFT} = T_K$. Thus, we denote K_T as the thermodynamic fragility.

6.3.4 Reduced units appropriate for density-temperature scaling

The reduced unit system appropriate for the density-temperature scaling is defined by choosing $l = (V/N)^{1/3} = \rho^{-1/3}$ as the unit of length, the mass of one atom m as the unit of mass and $t_0 = \rho^{-1/3}(k_BT/m)^{-1/2}$ as the unit of time [144,145]. Here N, V, ρ and T are the number of particles, the volume, the density and the temperature of the system respectively. The conversion of dynamical quantities from the conventional reduced unit system to this

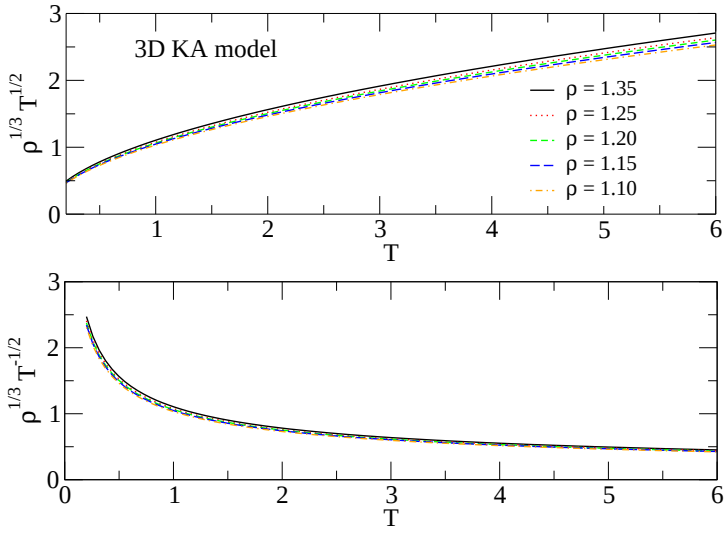

Figure 6.1: Conversion factors from the conventional reduced unit system to the reduced unit system appropriate for the density-temperature scaling, $\rho^{1/3}(k_BT/m)^{1/2}$ and $\rho^{1/3}(k_BT/m)^{-1/2}$ for τ and D respectively, are $\mathcal{O}(1)$ (with $k_B = 1, m = 1$).

reduced unit system (denoted by *) is given by:

$$\begin{aligned} \tau^* &= \tau/t_0 = \rho^{1/3}(k_BT/m)^{1/2}\tau \\ D^* &= D/(l^2t_0^{-1}) = \rho^{1/3}(k_BT/m)^{-1/2}D \end{aligned} \tag{6.6}$$

As shown in Fig. 6.1, the conversion factors are $\mathcal{O}(1)$. Hence bare relaxation time (τ) and diffusion coefficients (D) also show reasonably good data collapse.

6.3.5 The scaling exponent γ

Recent analyses [147, 150, 155, 156] of liquid state properties show that relaxation times at different densities (ρ) and temperatures (T) are function of the single combined variable ρ^γ/T. One way to rationalize this empirical observation is through the concept of *isomorphs* and the strong correlation between the instantaneous potential energy (U) and the instantaneous virial W [155, 156]. The correlation is measured in terms of the coefficient

$$R = \frac{\langle \Delta W \rangle \langle \Delta U \rangle}{\sqrt{\langle (\Delta W)^2 \rangle \langle (\Delta U)^2 \rangle}} \tag{6.7}$$

where $\Delta U = U - \langle U \rangle, \Delta W = W - \langle W \rangle$ represent instantaneous fluctuations about the mean values of the potential energy and the virial respectively. A liquid is said to be strongly correlating at a given state point (ρ, T) if $R \geq 0.9$.

The exponent $\gamma(\rho, T)$ can be computed from the fluctuations in the instantaneous potential energy and instantaneous virial using three possible definitions [155]:

$$\begin{aligned} \gamma_1 &= \frac{\langle \Delta W \Delta U \rangle}{\langle (\Delta U)^2 \rangle} \\ \gamma_2 &= \frac{\sqrt{\langle (\Delta W)^2}}{\sqrt{\langle (\Delta U)^2 \rangle}} \\ \gamma_3 &= \frac{\langle (\Delta W)^2 \rangle}{\langle \Delta W \Delta U \rangle} \end{aligned}$$

They are related to each other as $\gamma_1 = R\gamma_2 = R^2\gamma_3$. For perfect correlation $R = 1$, as in the case of an IPL liquid, all definitions are equal to each other. In general, for $0 \leq R \leq 1$, $\gamma_1 \leq \gamma_2 \leq \gamma_3$. Representative values of $\gamma_1, \gamma_2, \gamma_3, R$ are shown in Fig. 6.2 which shows that the exponent values depend on state points.

If the density-temperature scaling of the form $\tau(\rho, T) = f(\rho^\gamma/T)$ holds, the density dependent activation energy parameters $A(\rho)$ in Adam Gibbs relation [Eqn. 6.4] and $E_0(\rho)$ in the Arrhenius law $\tau(\rho, T) = \tau(\rho, \infty) \exp(E_0(\rho)/T)$ are expected to have the density dependence of the form:

$$\begin{aligned} A(\rho) &\sim \rho^\gamma \\ E_0(\rho) &\sim \rho^\gamma \end{aligned}$$

which provides another way to compute γ.

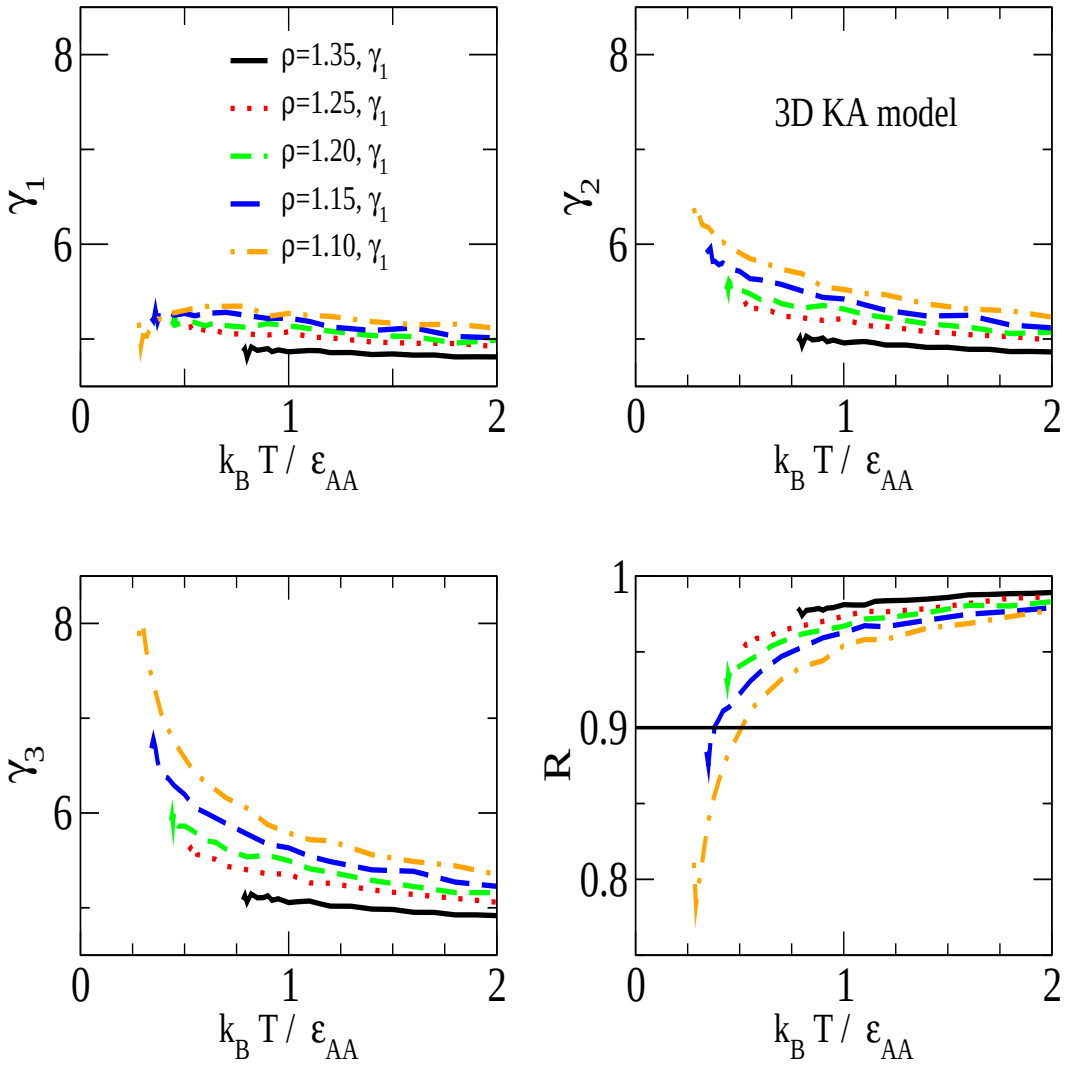

Figure 6.2: Determination of the density-temperature scaling exponent γ from the correlation between instantaneous potential energy (U) and virial (W). $\gamma_1 = \frac{\langle \Delta W \Delta U \rangle}{\langle (\Delta U)^2 \rangle}$, $\gamma_2 = \frac{\sqrt{\langle (\Delta W)^2 \rangle}}{\sqrt{\langle (\Delta U)^2 \rangle}}$, $\gamma_3 = \frac{\langle (\Delta W)^2 \rangle}{\langle \Delta W \Delta U \rangle}$ where $\Delta U = U - \langle U \rangle$ and $\Delta W = W - \langle W \rangle$ represent fluctuations about mean of potential energy and virial respectively. $R = \frac{\langle \Delta W \rangle \langle \Delta U \rangle}{\sqrt{\langle (\Delta W)^2 \rangle \langle (\Delta U)^2 \rangle}}$ is a measure of correlation between potential energy and virial. The liquid is said to be strongly correlating if $R \geq 0.9$.

6.4 The density-temperature scaling in the 3D KA model

6.4.1 The Arrhenius plots

Here, we show the Arrhenius fits to relaxation times and diffusion coefficients to obtain the high temperature activation energy parameters $E_0(\rho)$. At very high temperatures, the data deviates from the Arrhenius law. This trend is most prominent at the lowest density $\rho = 1.10$. For the estimation of the parameters E_0 such very high temperatures are excluded.

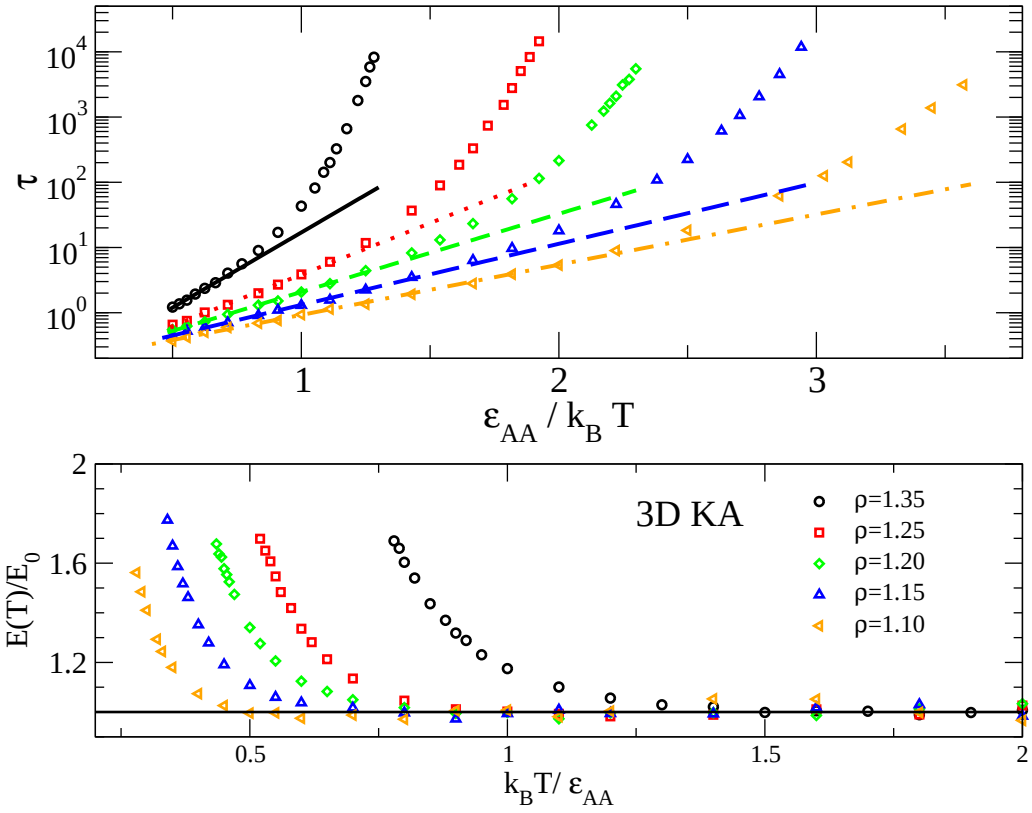

Figure 6.3: The Arrhenius fit to relaxation times to estimate high temperature activation energies $E_0(\rho)$.

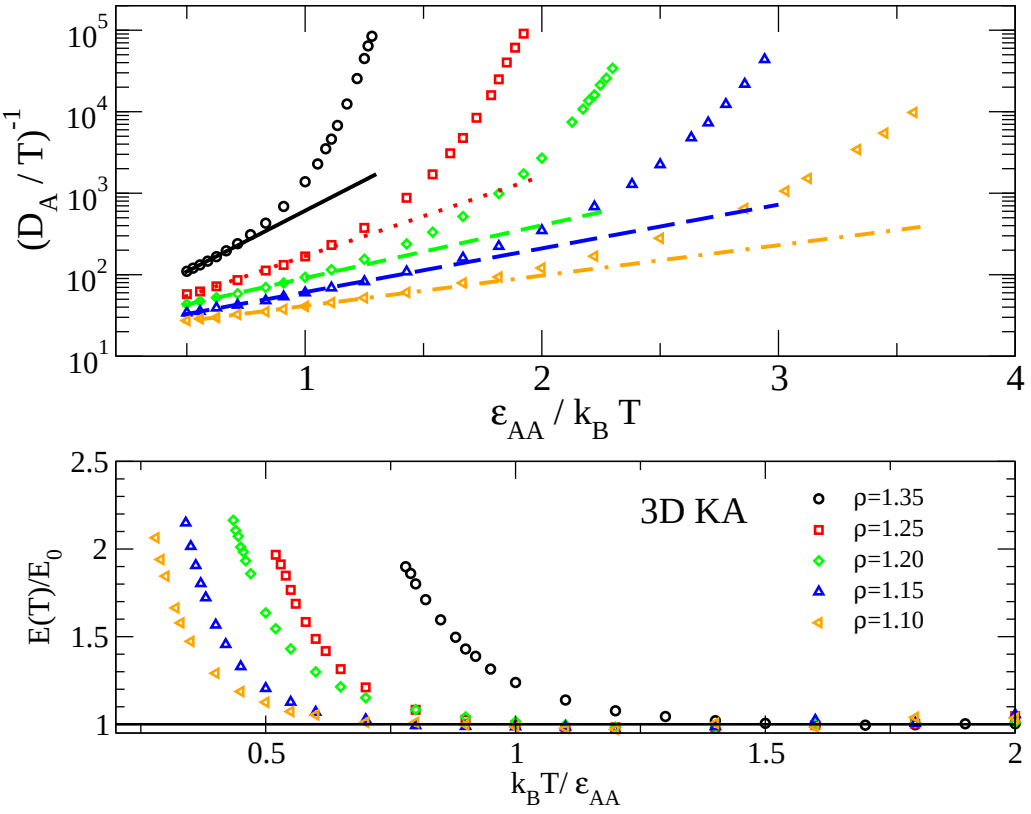

Figure 6.4: The Arrhenius fit to the self diffusion coefficients of A particles to estimate the high temperature activation energies $E_0(\rho)$.

6.4.2 Testing the scaling relations

The density-temperature scaling of dynamical quantities in the $3D$ KA model has been reported earlier for relaxation times [148] where it was found that τ^* *vs.* ρ^γ/T for all temperatures in the density range $1.15-1.35$ follow the same master curve with $\gamma = 5.1$. Similar data collapse for diffusion coefficient is also reported in an equimolar mixture of $LJ(12,6)$ model (different from the KA model) [149]. In Figs. 6.5(a) and 6.5(b) we verify for *both* the relaxation time *and* the diffusion coefficient the density-temperature scaling in the KA model : $\tau^* = f(\rho^\gamma/T), D_A^* = g(\rho^\gamma/T)$ with the same $\gamma = 5.1$ for both the relaxation time and the diffusion coefficient and find that the data collapse is comparable to [148] for the relaxation time. However, we note that some data points at lower densities does not fall on the master curve. We discuss this issue later.

We also test in Figs. 6.7 and 6.8, if the scaling suggested by Alba-Simionesco *et al.* in [151] holds in the present model. Surprisingly, we find that relaxation times but not diffusion coefficient obey this scaling. This implies that the T-dependence of relaxation time but not of diffusion coefficient can be described by a *single* $\rho-$ dependent parameter. Of course, an empirical data collapse for the diffusion coefficient can be obtained by introducing a second $\rho-$ dependent parameter ξ. We have tentatively computed ξ from a fractional Stokes Einstein relation $D/T \propto \tau^{-\xi}$ where $0 \leq \xi \leq 1$. However, this analysis is inconclusive.

6.4.3 Negative virial states

In Fig. 6.9 we show the state points where the pressure and virial are negative in which case the effective repulsive inverse power law potential may not be a good approximation to KA model. We find that most of the simulated state points have positive virial and pressure. Negative virial states are most abundant at the lowest density but becomes rare as the density increases. Figs. 6.6(a) and 6.6(b) show that the degree of data collapse improves if the negative virial states are removed.

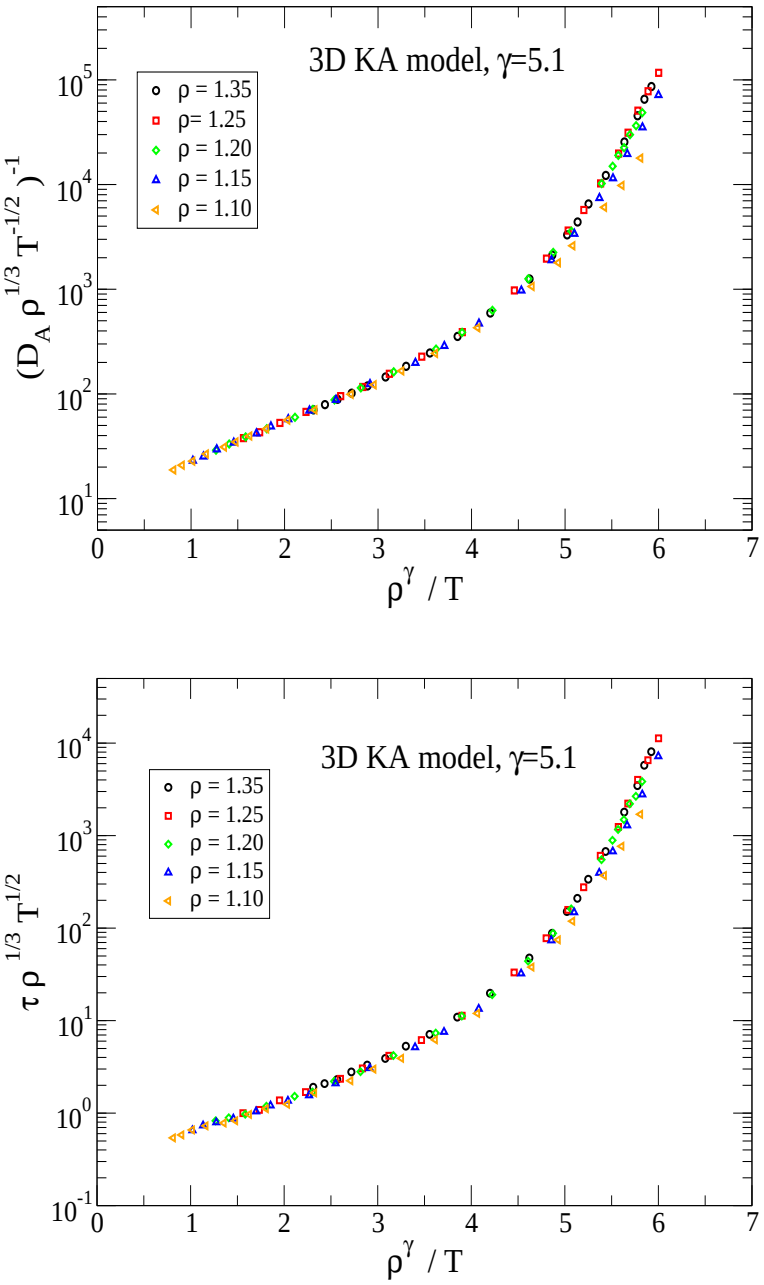

Figure 6.5: The density-temperature scaling of the reduced diffusion coefficient of A particles $D_A^* = \rho^{1/3}(k_BT/m)^{-1/2}$ and the reduced relaxation time $\tau^* = \rho^{1/3}(k_BT/m)^{1/2}\tau$ in the $3D$ KA model.

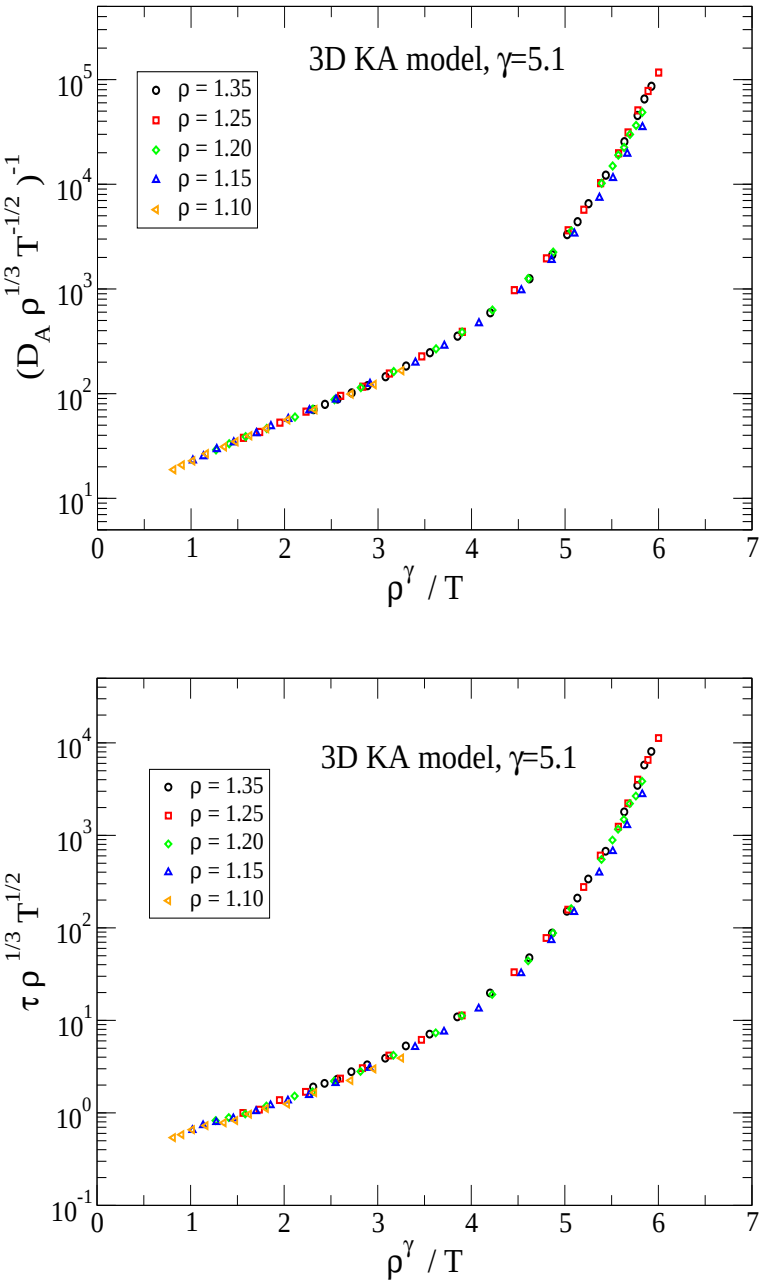

Figure 6.6: The density temperature scaling of the reduced diffusion coefficient of A particles $D_A^* = \rho^{1/3}(k_BT/m)^{-1/2}D_A$ and the reduced relaxation time $\tau^* = \rho^{1/3}(k_BT/m)^{1/2}\tau$ in the $3D$ KA model improves if state points with negative virial (Fig. 6.9) states are removed.

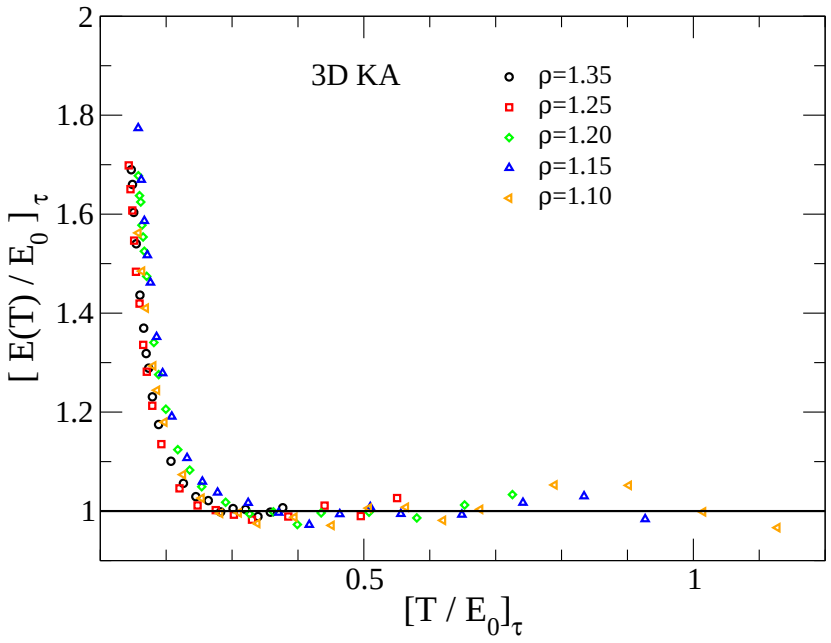

Figure 6.7: Relaxation times obey the density scaling suggested by Alba-Simionesco *et al.* in [151].

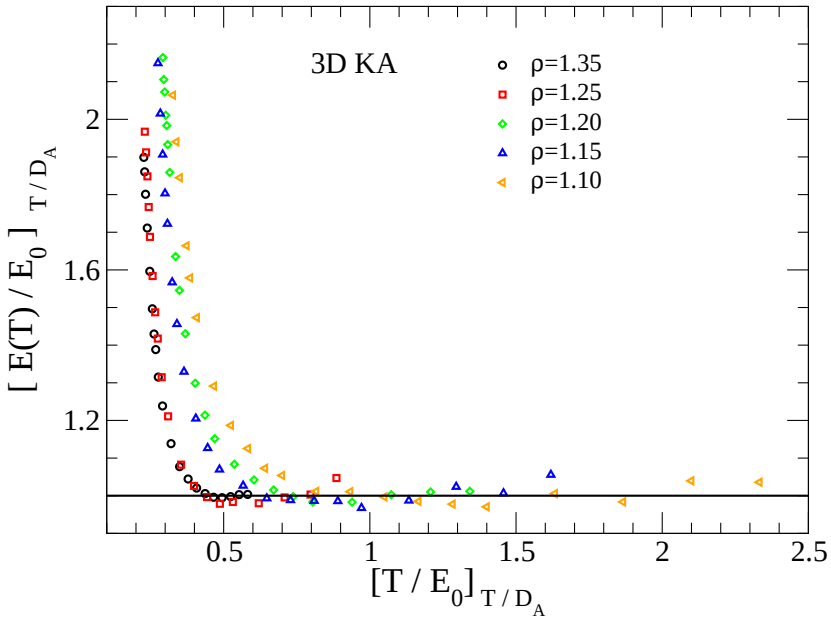

Figure 6.8: Diffusion coefficients does not obey the density scaling suggested by Alba-Simionesco *et al.* in [151].

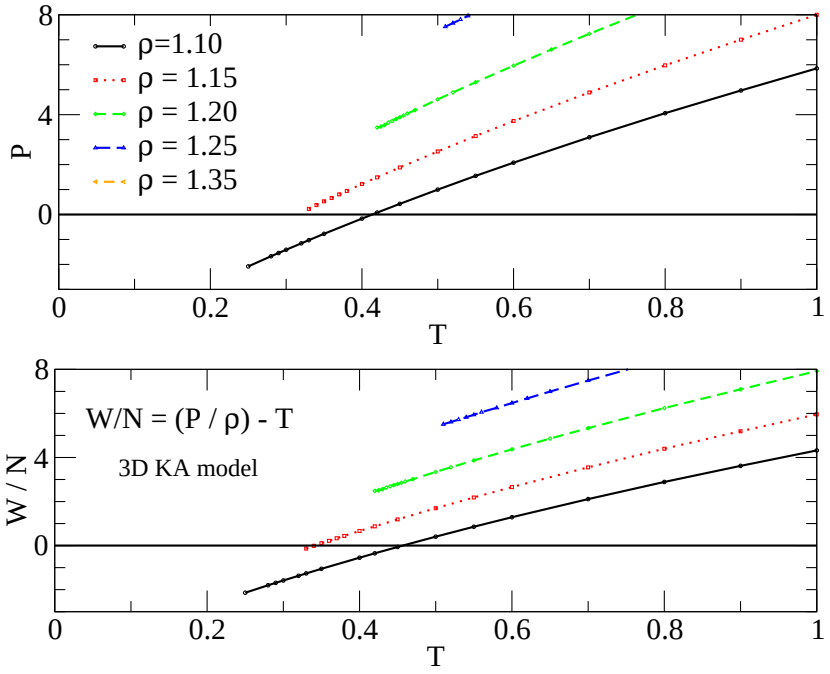

Figure 6.9: Negative pressure states occur only at the density $\rho = 1.10$ for temperature $T < 0.42$. Negative virial states occur only at densities $\rho = 1.10$ for temperature $T < 0.45$ and at $\rho = 1.15$ for $T < 0.35$.

6.4.4 The density-temperature scaling holds for the entire time range

In Fig. 6.10 we verify the interesting observation [148] that not only the α relaxation time but also the entire correlation function and the MSD obey the density-temperature scaling.

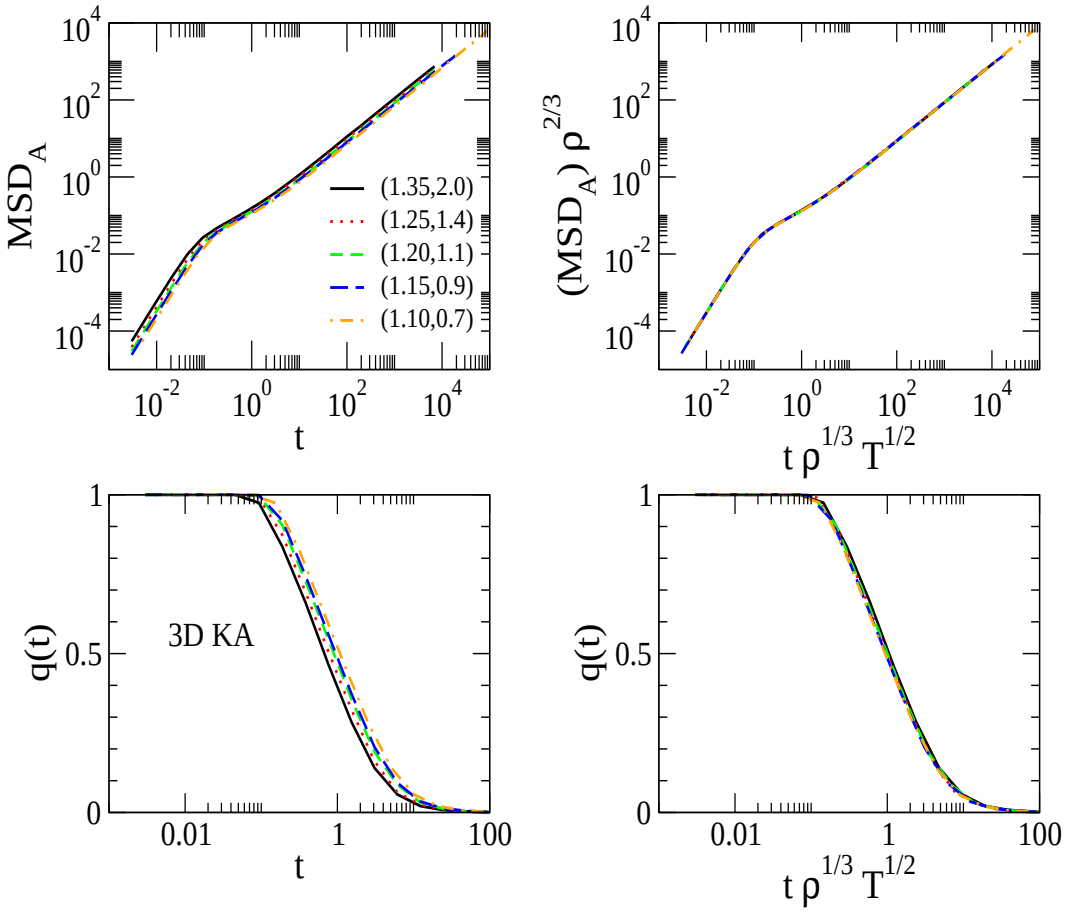

Figure 6.10: The MSD (of A particles) and the overlap function for five state points are shown in the conventional reduced unit and the reduced unit appropriate for density-temperature scaling. The state points are chosen from Fig. 6.5(a) and have approximately same values of coordinates $(\rho^{5.1}/T, D_A^*)$. The coordinates are $(\rho^{5.1}/T, D_A^*) \equiv$ (2.31,70.4),(2.23, 67.4), (2.30, 71.2), (2.27,69.5), (2.32,70.3) at densities $\rho = 1.35, 1.25, 1.20, 1.15, 1.10$ respectively. The same state points in (ρ, T) coordinates are $(\rho, T) \equiv (1.35, 2.0), (1.25, 1.4), (1.20, 1.1), (1.15, 0.9), (1.10, 0.7)$ respectively. The figures show that density-temperature scaling holds for *entire* time range [148].

6.5 How does the fragility depend on density?

If the density-temperature scaling holds the kinetic fragility should be independent of density. In our case, given that the density-temperature scaling holds approximately, we expect that the kinetic fragility should at best be weakly dependent on density. This expectation apparently contradicts the findings in an earlier work [128] where it was noted that the kinetic fragility is bigger at higher densities for the 3D KA model. However, it was noted by comparing the kinetic and the thermodynamic fragilities that the density dependence of the kinetic fragility is *weaker* than that of the thermodynamic fragility for the 3D KA model. Here we compute the kinetic and the thermodynamic fragility for the 3D KA model taking a bigger temperature range and system size (N=1000 in the present work compared to N=256 in the earlier works) than in [128] to see if the density dependence of the kinetic and the thermodynamic fragilities are consistent with the expectation from the observed (approximate) density-temperature scaling. Below we describe the details of the comparison.

6.5.1 Comparison of diffusion coefficients with earlier works

We have compared the diffusion coefficient data in the present study with the earlier work [69] in Figs. 6.11 - 6.15 and have found that they agree well.

6.5.2 Comparison of the density dependence of the fragility

The kinetic fragility values are estimated from the diffusion coefficient data in Figs. 6.11 - 6.15 using the definition in Eqn. 6.3. The diffusion coefficient data of the earlier work are taken from Ref. [69]. The thermodynamic fragility values in the present study are estimated using Eqn. 6.5 from the temperature dependence of TS_c and are shown in Fig. 6.16. Fig. 6.17 shows the comparison of the density dependence of the kinetic and the thermodynamic fragility for the 3D KA model in the present study and the earlier

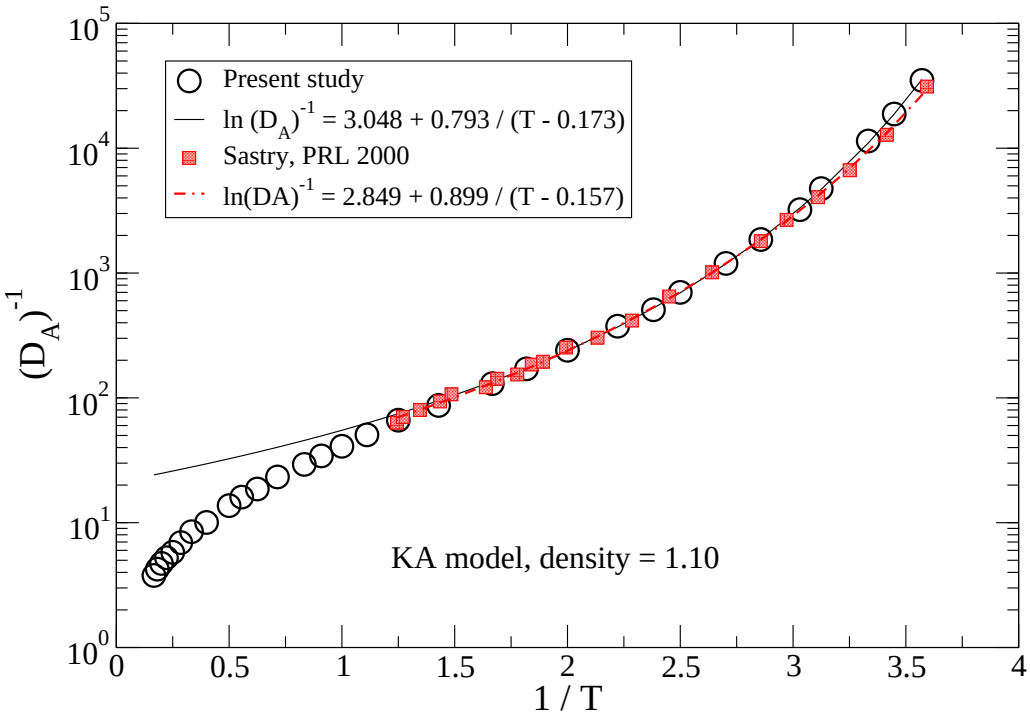

Figure 6.11: Comparison of D_A^{-1} for the 3D KA model at the density = 1.10.

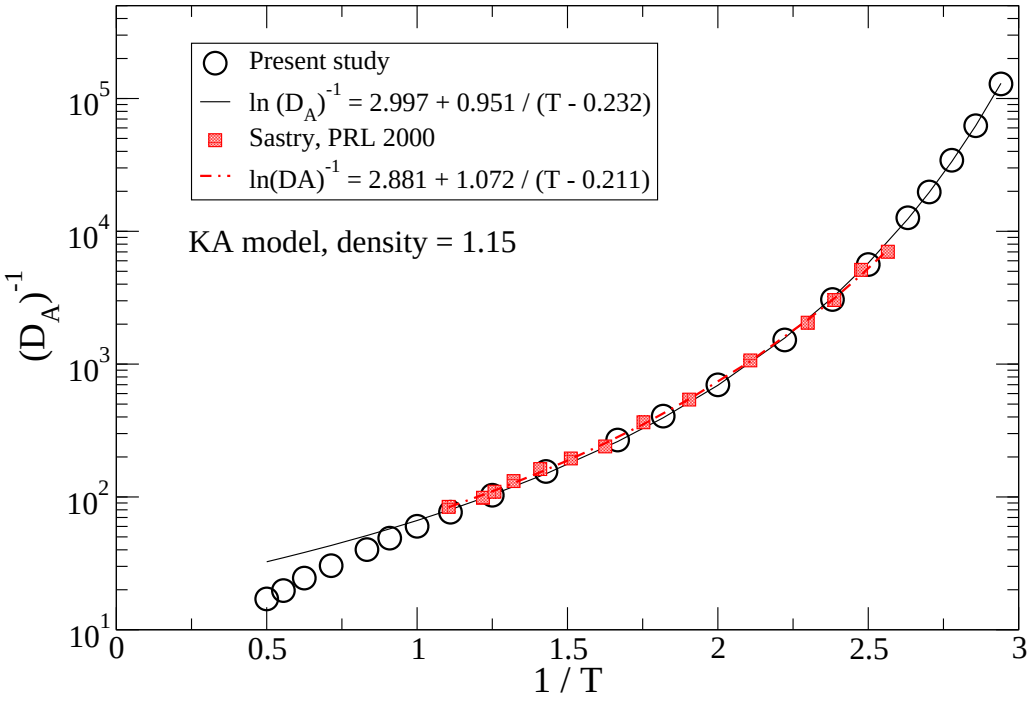

Figure 6.12: Comparison of D_A^{-1} for the 3D KA model at the density = 1.15.

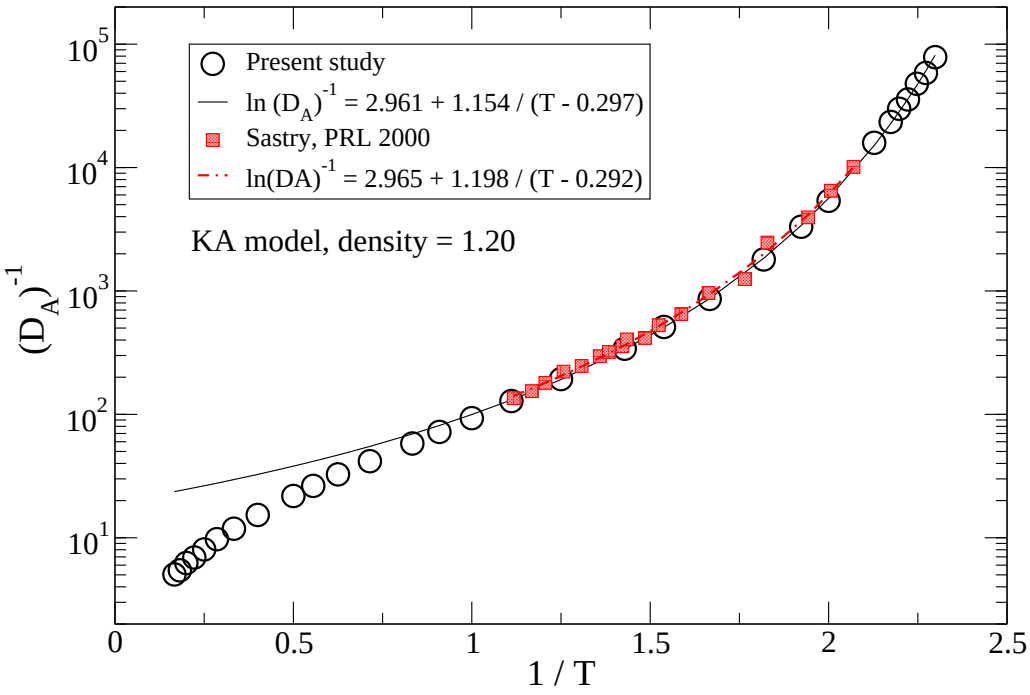

Figure 6.13: Comparison of D_A^{-1} for the 3D KA model at the density = 1.20.

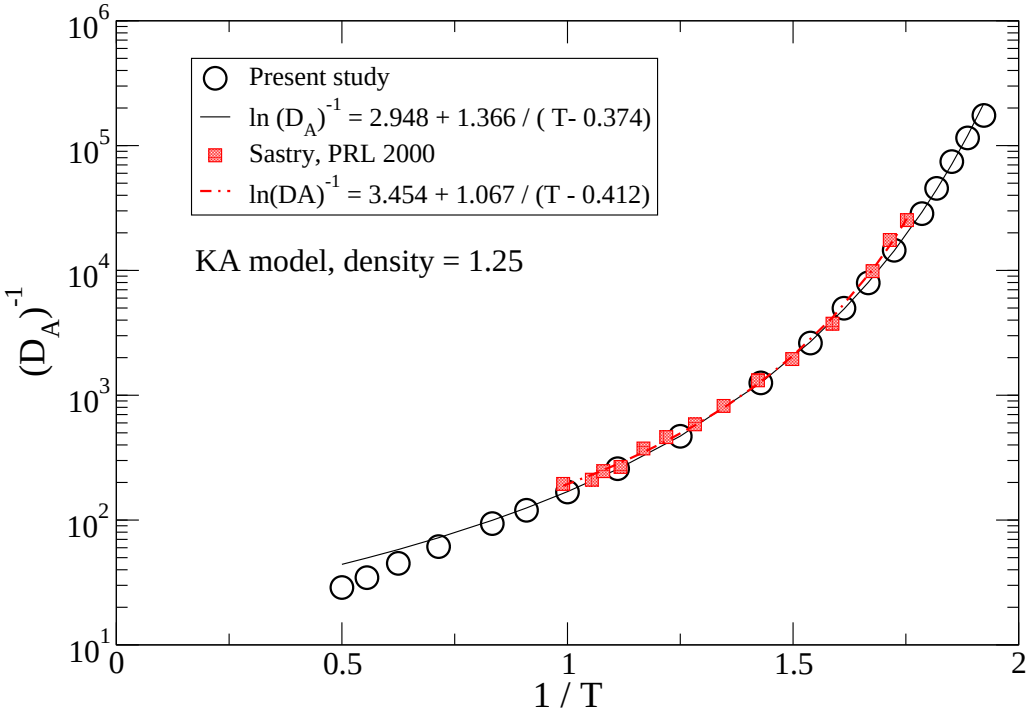

Figure 6.14: Comparison of D_A^{-1} for the 3D KA model at the density = 1.25.

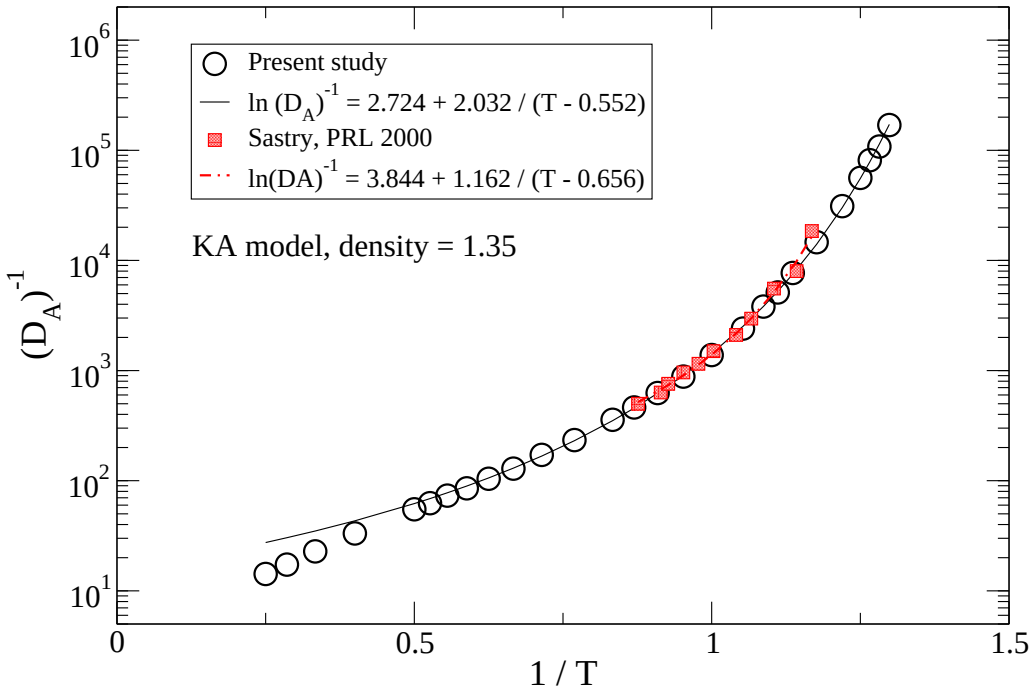

Figure 6.15: Comparison of D_A^{-1} for the 3D KA model at the density = 1.35.

work [128] and shows that (i) the density dependence of the kinetic fragility is much weaker in the present study which can be understood from the approximate density-temperature scaling we observe. (ii) The density dependence of the thermodynamic fragility in the present study agrees well with the earlier work.

To understand the difference between the present study and the earlier work in the K_{VFT} values despite good agreement in the D_A^{-1} data, we estimate in Fig. 6.18 the sensitivity of the estimated K_{VFT} values on the temperature range by fitting data from the lowest available temperature to a variable highest temperature. The choice of the highest temperature at each density varies from the onset temperature obtained from the T-dependence of the average inherent structure energy to the highest available temperature. We see that the estimation of K_{VFT} from the VFT fit is sensitive to some extent on the selection of the temperature range. Thus the relatively high values of K_{VFT} at higher densities in the earlier work may be attributed to taking relatively shorter range of temperature for study.

We also study the density dependence of the coefficient A in the Adam Gibbs relation (Eqn. 6.4). In Figs. 6.20(a) and 6.20(b) we show the Adam Gibbs

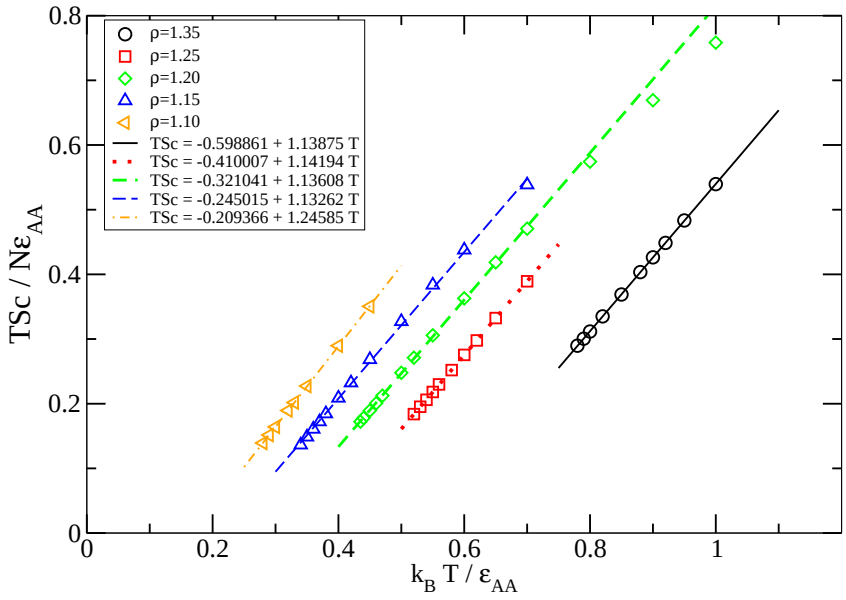

Figure 6.16: The linear temperature dependence of TS_c obtained in the present study at different densities for the 3D KA model. The thermodynamic fragility K_T at different densities are obtained from this plot.

plots at different densities obtained in the present study. The values of A are estimated from these data.

The density dependence of (i) the Adam Gibbs coefficient A, (ii) the thermodynamic fragility K_T, (iii) the kinetic fragility K_{VFT} and (iv) the ratio K_T/A for the 3D KA model obtained in the present study are summarized in Fig. 6.19 which shows that (i) the power law density dependence of $A \sim \rho^{\gamma_A}, K_T, \sim \rho^{\gamma_{KT}}$ describes data well at higher densities. (ii) The density dependence of the ratio K_T/A (which is an estimate of the kinetic fragility if the Adam Gibbs relation is valid) is weak which can be understood from the approximate density-temperature scaling we observe.

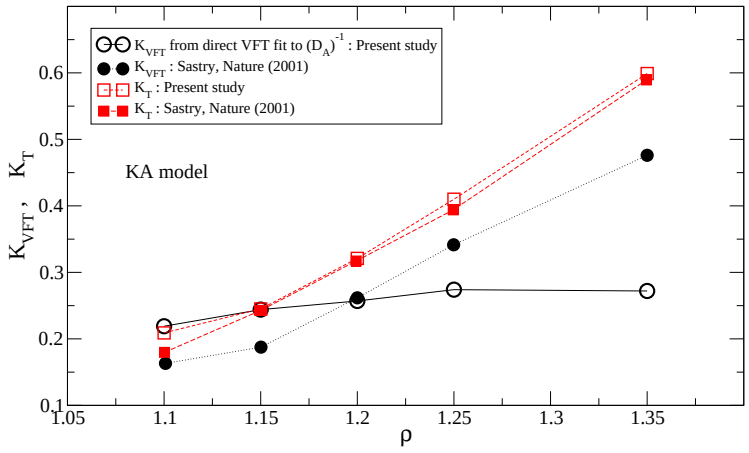

Figure 6.17: The density dependence of K_{VFT} is much weaker in the present study compared to the earlier work [128]. The density dependence of the thermodynamic fragility K_T is comparable to the earlier study.

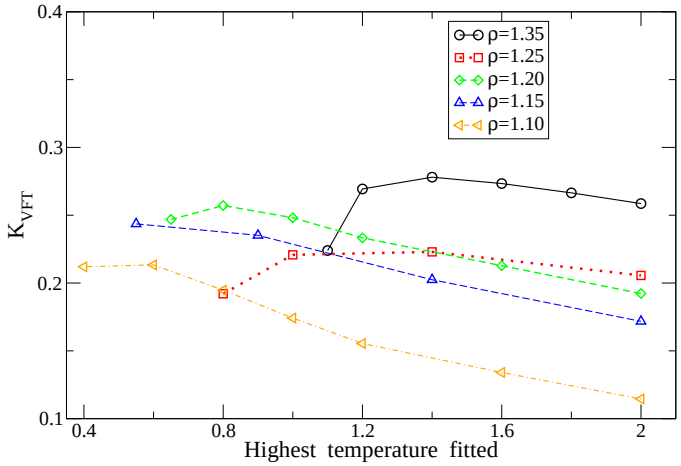

Figure 6.18: We show estimates of K_{VFT} from the data of the present study by performing VFT fits from the lowest available temperature to different choice of the highest temperature. The choice of the highest temperature for fit at each density varies from the onset temperature obtained from the T-dependence of the average inherent structure energy to the highest available temperature. The lines are guides to eyes.

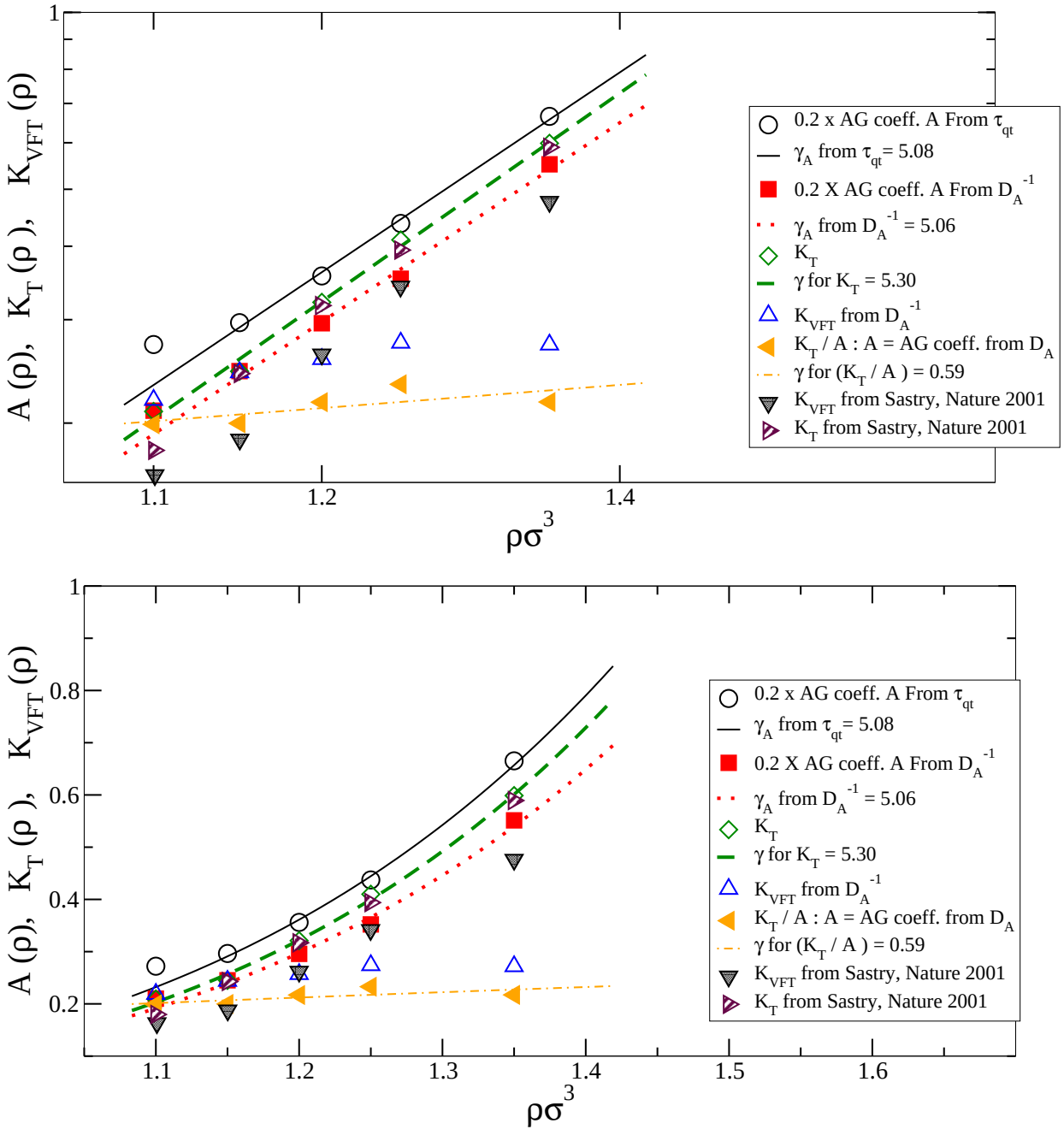

Figure 6.19: Comparison in log-log and in linear scale of the density dependence of (i) the Adam Gibbs coefficient A (shifted by a constant factor), (ii) the thermodynamic fragility K_T, (iii) the kinetic fragility K_{VFT} and (iv) the ratio K_T/A for the 3D KA model obtained in the present study. Also shown for comparison are the fragility values from the earlier work.

6.5.3 Density-temperature scaling of the Adam Gibbs relation

Given the observed density dependence of $A : A \sim \rho^{\gamma_A}$, the quantity A/TS_c is approximately a function of the form $h(\rho^{\gamma_A}/T)$ if the configuration entropy S_c is an isomorphic invariant [155] and hence a function of the form $S_c(\rho^{\gamma_A}/T)$. We test this expectation in Fig. 6.21 using the scaling exponent $\gamma_A = 5.06$ obtained from the density dependence of A. We see that at higher densities one gets reasonably good data collapse in a plot of S_c *vs.* ρ^{γ_A}/T. Based on this observation one expects that the Adam Gibbs plots at different densities can be collapsed on a master curve - at least at higher densities where S_c shows density-temperature scaling. This is shown in Fig. 6.22.

6.5.4 Comparison of the PEL properties with earlier work

In this section, the potential energy landscape parameters for the 3D KA model are evaluated and compared against earlier works [68, 69, 128]. The notations used here are same as in the previous works. We note that there are systematic differences in the values of the configuration energy density $S_c(e_{IS})$ between the present and the earlier work. However, this difference is numerically insignificant on the scale of the variation with density of the thermodynamic fragility. Hence the thermodynamic fragility values in the present and the earlier study agrees well with each other in Fig. 6.19.

Table 6.3: Comparison of PEL parameters with Ref. [68]. See also Figs. 6.24,6.26, 6.27 and 6.28.

Density	α^{ref}	$\alpha^{present}$	ϕ_0^{ref}	$\phi_0^{present}$	σ^{ref}	$\sigma^{present}$	δf^{ref}	$\delta f^{present}$
1.10	1.020	0.916	-6.579	-6.58	0.312	0.332	0.616	0.633
1.15	0.963	0.838	-6.680	-6.69	0.379	0.395	0.603	0.572
1.20	0.921	0.817	-6.700	-6.70	0.470	0.492	0.455	0.412
1.25	0.875	0.786	-6.642	-6.61	0.550	0.615	0.350	0.256
1.35	0.860	0.772	-6.080	-6.07	0.870	0.901	0.159	0.157

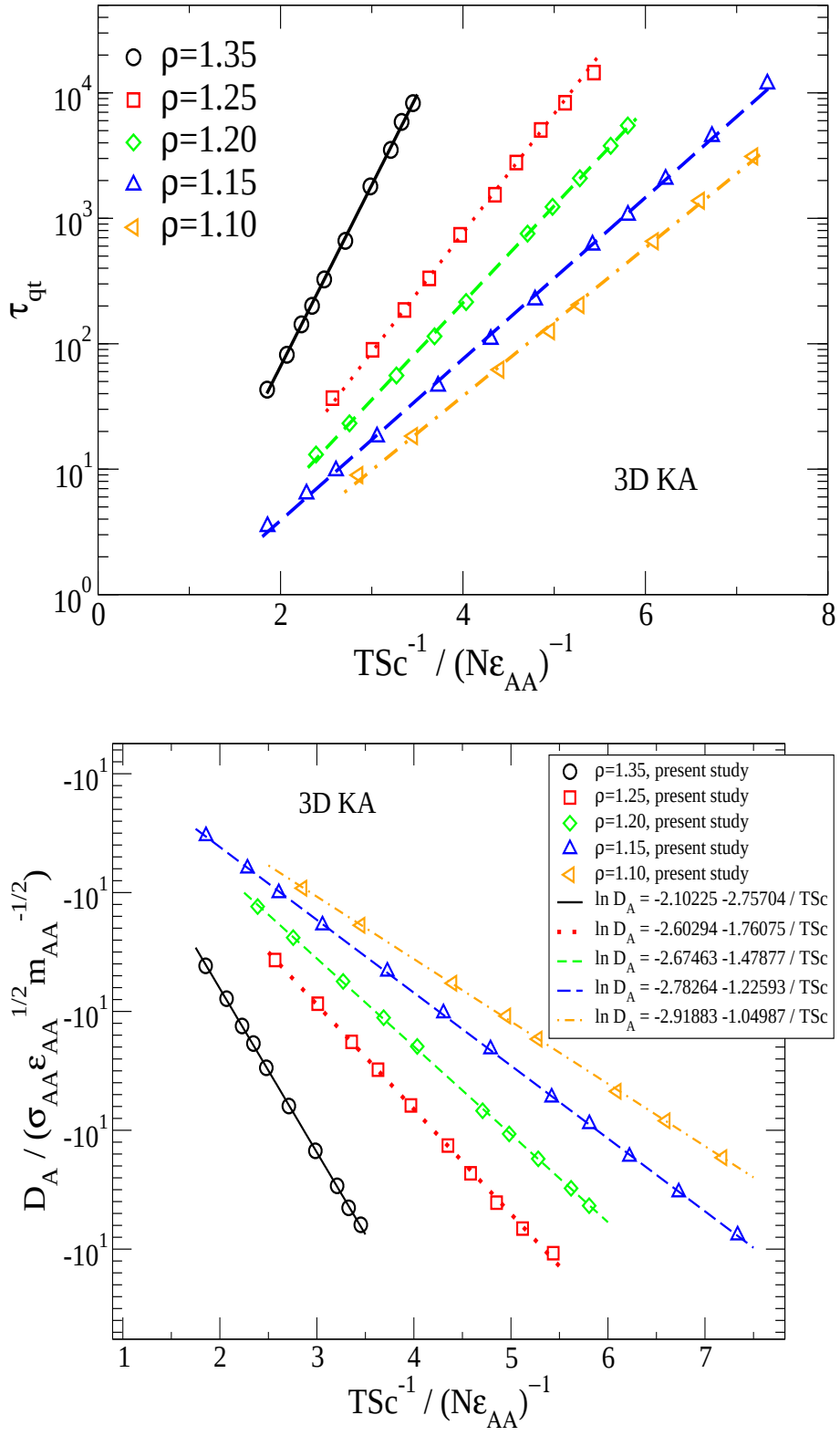

Figure 6.20: The Adam Gibbs plots for the 3D KA model in terms of the relaxation times and the diffusion coefficients at different densities obtained in the present study.

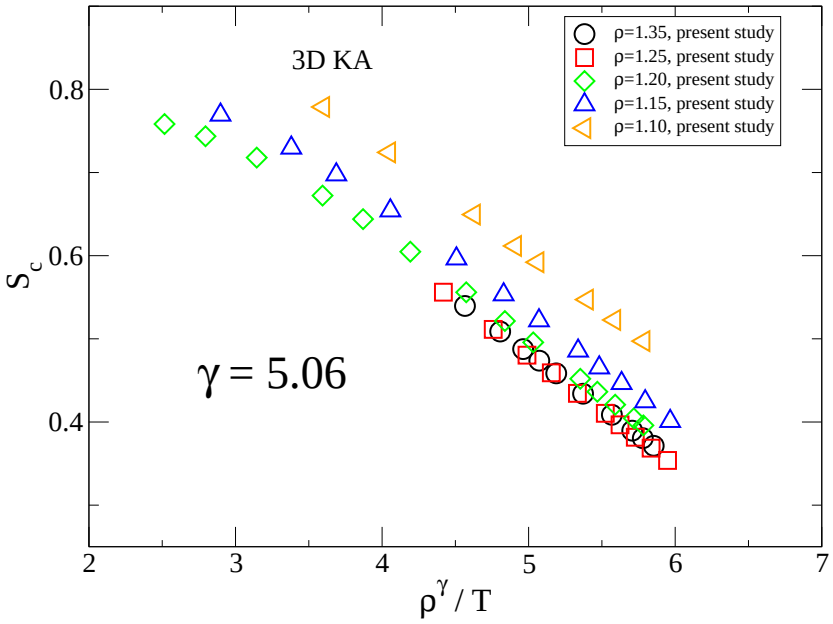

Figure 6.21: Testing if S_c is an invariant under the density - temperature scaling with the scaling exponent $\gamma = 5.06$ obtained from the density dependence of the Adam Gibbs coefficient from Fig. 6.19. We find reasonably good data collapse at high densities.

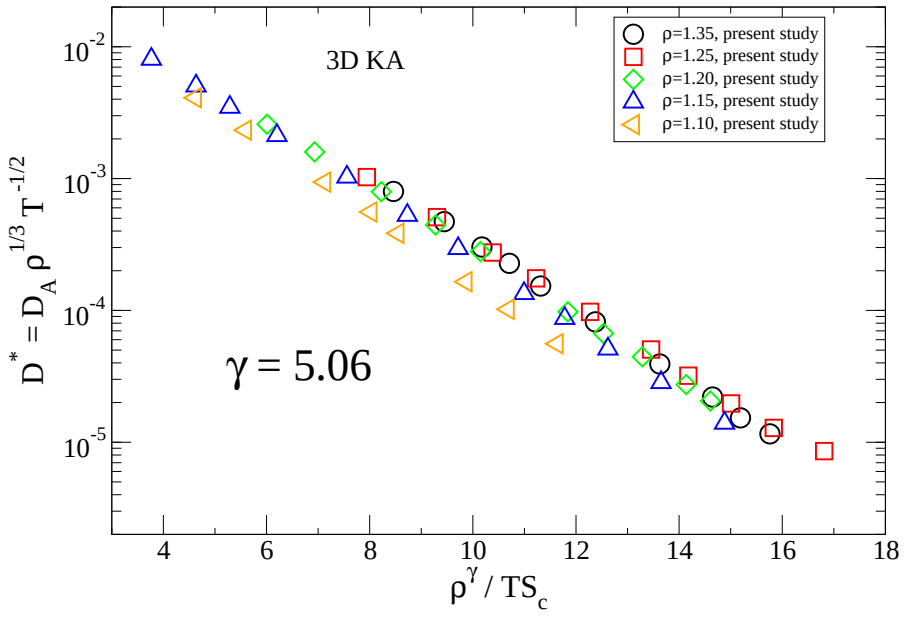

Figure 6.22: Density - temperature scaling of the Adam Gibbs relation between the diffusion coefficient and the configuration entropy. The scaling exponent $\gamma = 5.06$ obtained from the density dependence of the Adam Gibbs coefficient from Fig. 6.19.

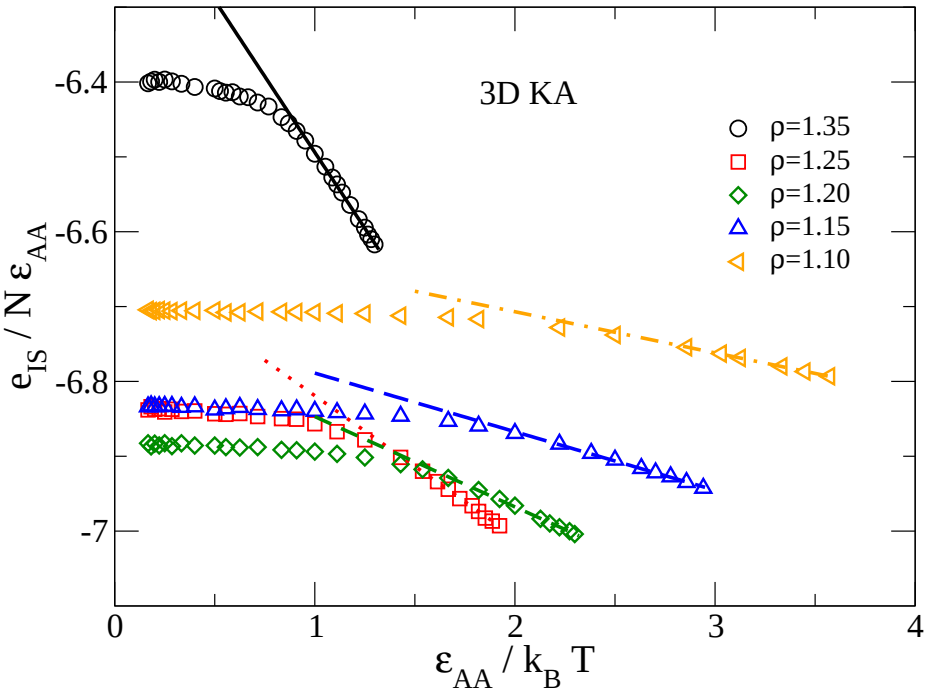

Figure 6.23: Temperature dependence of the average IS energy at different densities. At low T, the dependence is expected to be linear. The slope is denoted by $\frac{\sigma^2}{2}$.

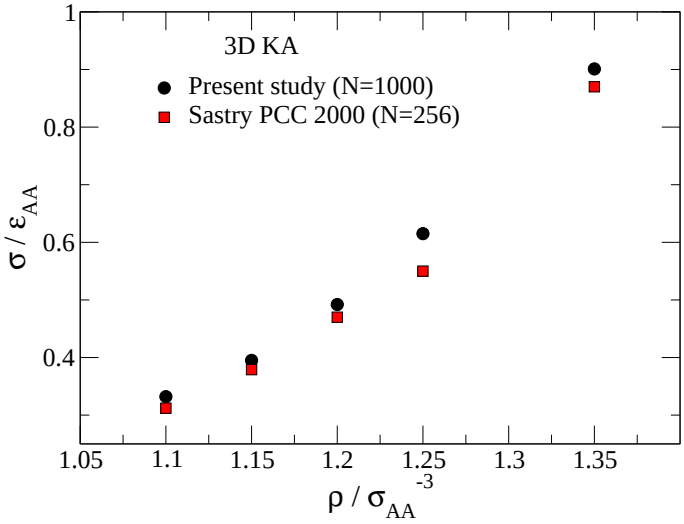

Figure 6.24: Comparison of the fitting parameter σ (measured from slope $=\frac{\sigma^2}{2}$ in Fig. 6.23) with ref. [68].

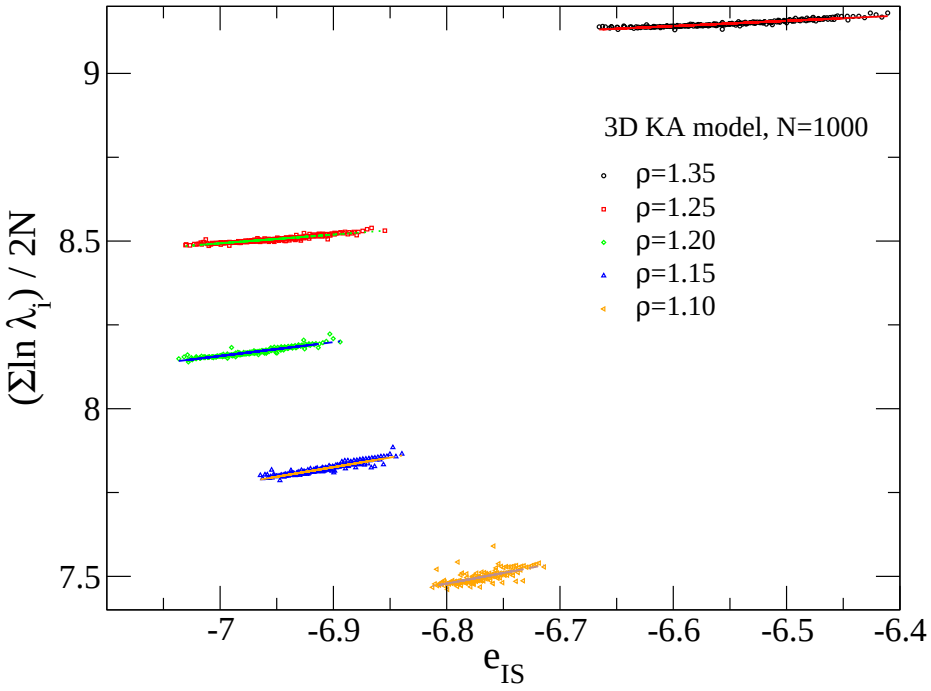

Figure 6.25: IS energy dependence of the eigenvalues (λ_i) of the Hessian of potential at inherent structures. The dependence is considered to be linear and quantified by the slope of the best linear fit δf.

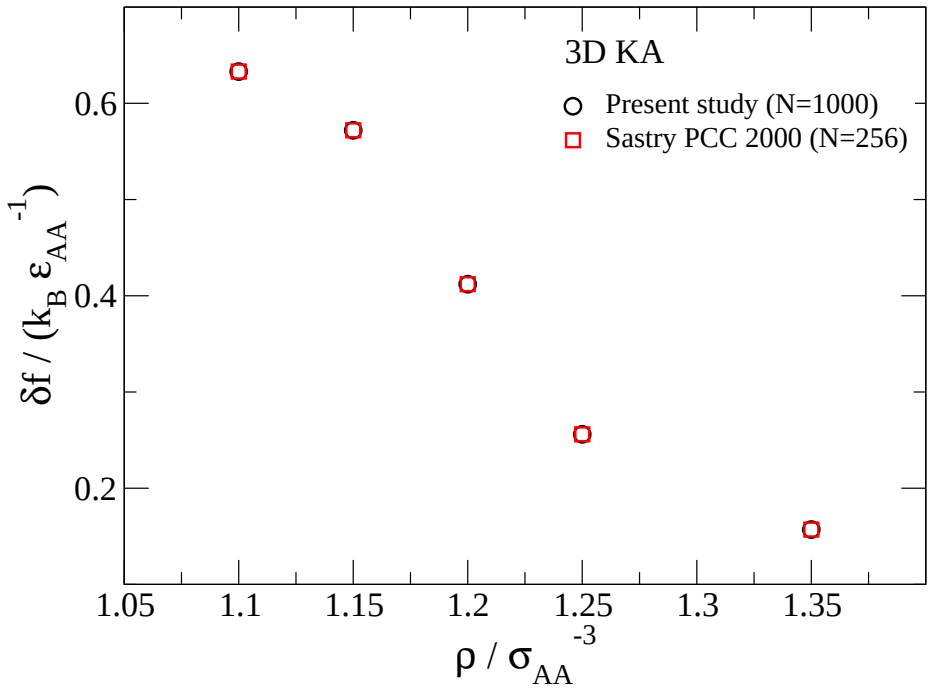

Figure 6.26: Comparison of the parameter δf (measured from slope in fig. 6.25) with ref. [68].

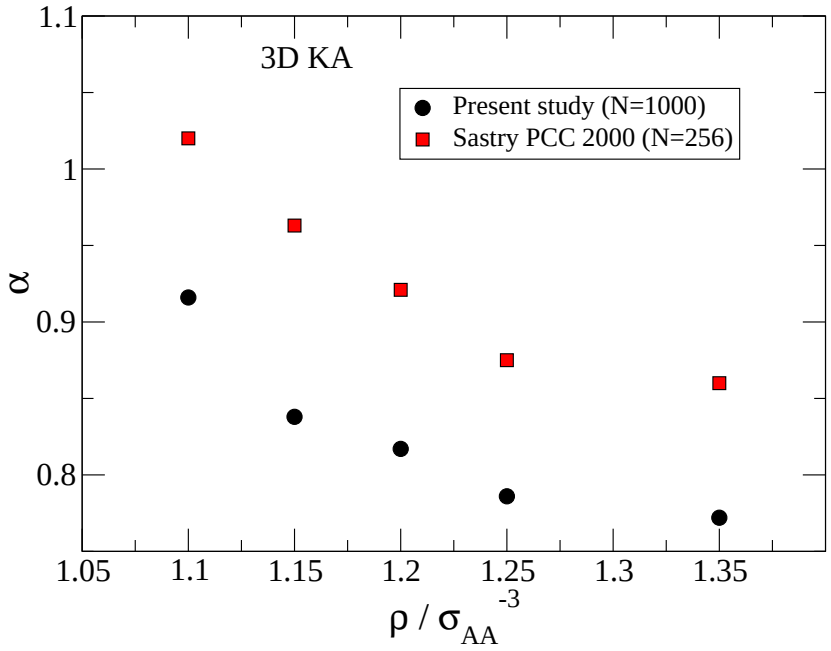

Figure 6.27: Comparison of the parameter α (measured from parabolic fit of $S_c(e_{IS}) = \alpha - \frac{(e_{IS}-\phi_0)^2}{\sigma^2}$) with ref. [68].

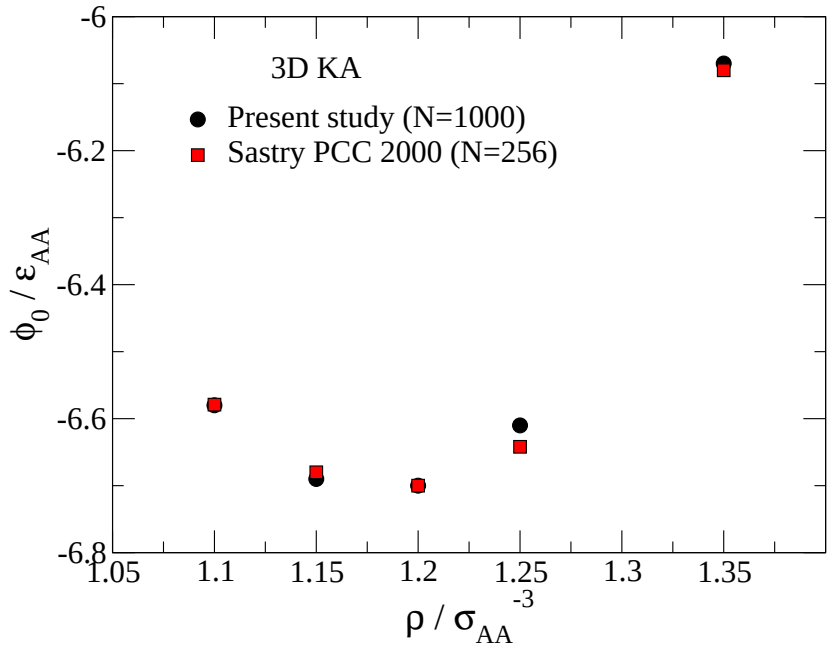

Figure 6.28: Comparison of the parameter ϕ_0 (measured from parabolic fit of $S_c(e_{IS}) = \alpha - \frac{(e_{IS}-\phi_0)^2}{\sigma^2}$ and from intercept of $e_{IS}(T)$. The average of these two values are reported here.) with ref. [68].

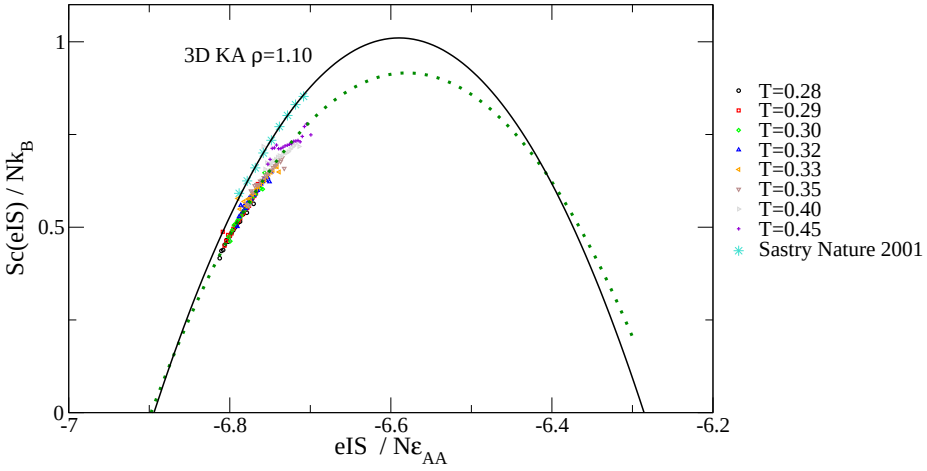

Figure 6.29: The configuration entropy density $S_c(e_{IS})$ for the 3D KA model at $\rho = 1.1$ are plotted against the inherent structure energy (per particle) e_{IS}. Symbols represent data points and lines represent parabolas of the form $S_c = \alpha - \frac{(e_{IS}-\phi_0)^2}{\sigma^2}$. Also shown are data and fits from the earlier work.

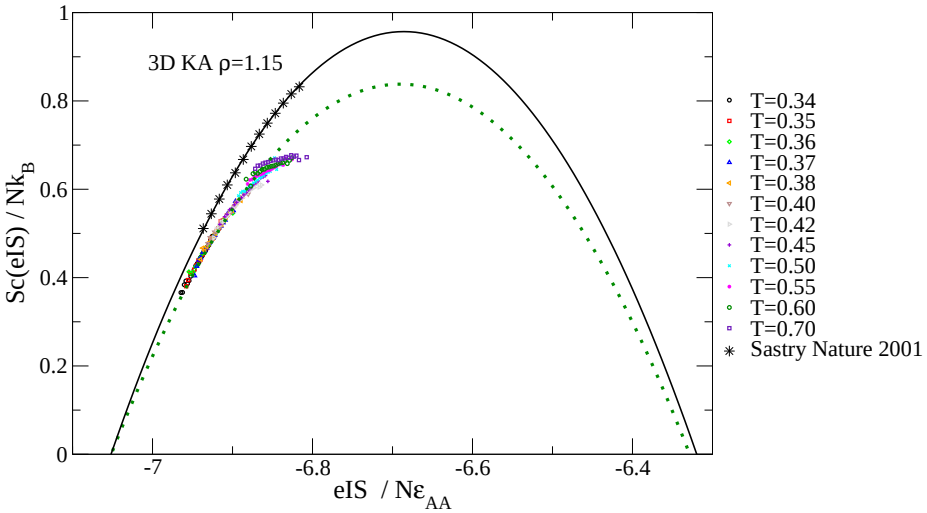

Figure 6.30: The configuration entropy density $S_c(e_{IS})$ for the 3D KA model at $\rho = 1.15$ are plotted against the inherent structure energy (per particle) e_{IS}. Symbols represent data points and lines represent parabolas of the form $S_c = \alpha - \frac{(e_{IS}-\phi_0)^2}{\sigma^2}$. Also shown are data and fits from the earlier work.

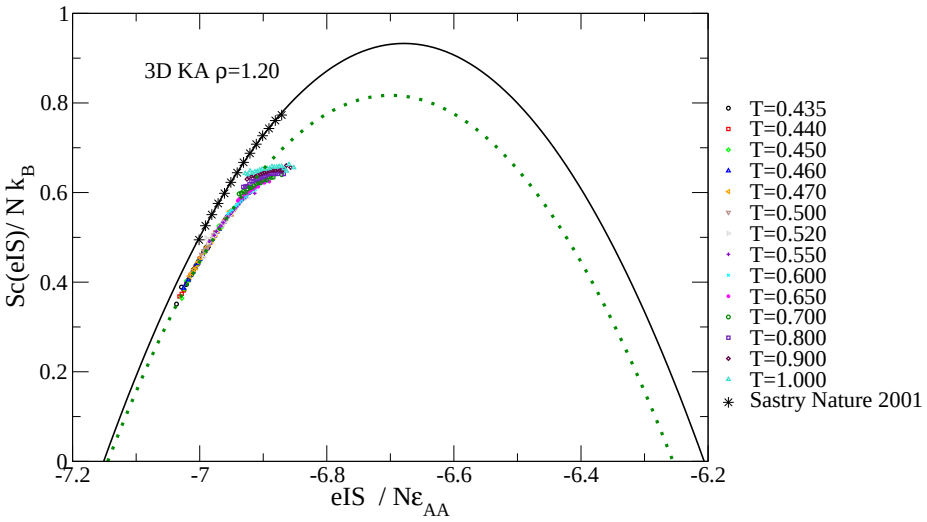

Figure 6.31: The configuration entropy density $S_c(e_{IS})$ for the 3D KA model at $\rho = 1.2$ are plotted against the inherent structure energy (per particle) e_{IS}. Symbols represent data points and lines represent parabolas of the form $S_c = \alpha - \frac{(e_{IS}-\phi_0)^2}{\sigma^2}$. Also shown are data and fits from the earlier work.

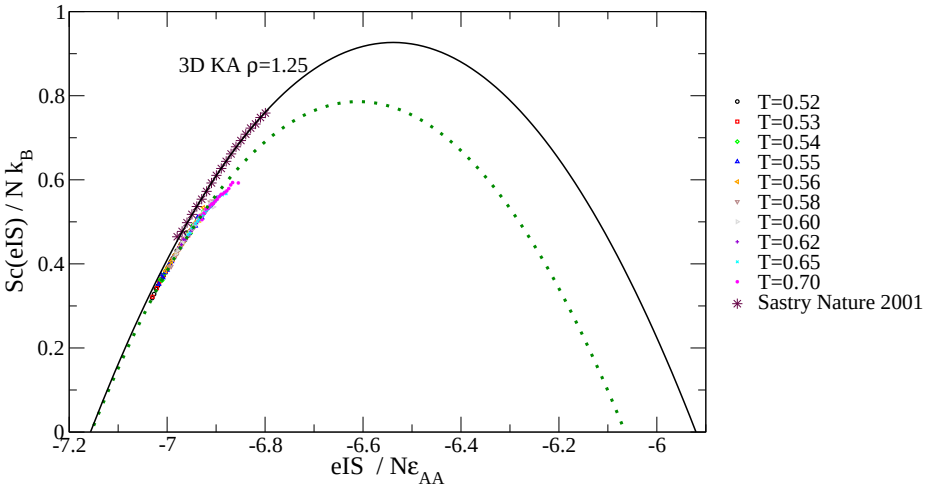

Figure 6.32: The configuration entropy density $S_c(e_{IS})$ for the 3D KA model at $\rho = 1.25$ are plotted against the inherent structure energy (per particle) e_{IS}. Symbols represent data points and lines represent parabolas of the form $S_c = \alpha - \frac{(e_{IS}-\phi_0)^2}{\sigma^2}$. Also shown are data and fits from the earlier work.

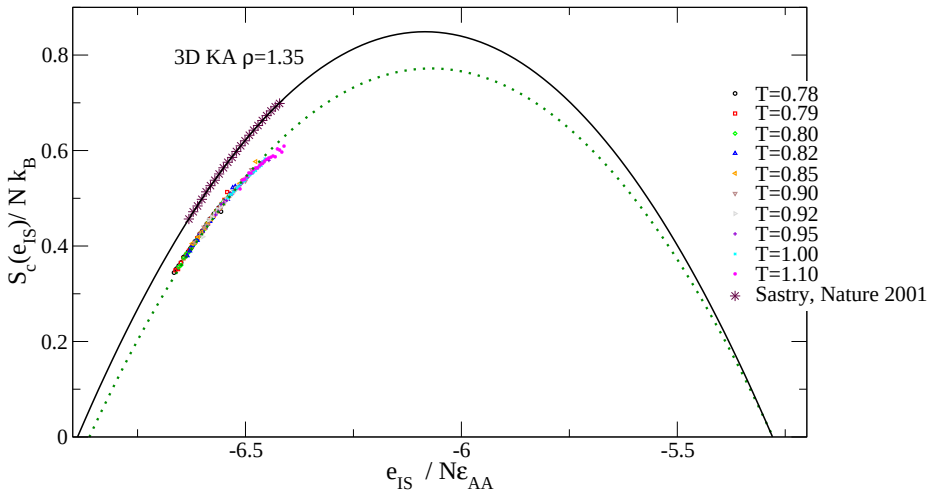

Figure 6.33: The configuration entropy density $S_c(e_{IS})$ for the 3D KA model at $\rho = 1.25$ are plotted against the inherent structure energy (per particle) e_{IS}. Symbols represent data points and lines represent parabolas of the form $S_c = \alpha - \frac{(e_{IS}-\phi_0)^2}{\sigma^2}$. Also shown are data and fits from the earlier work.

6.6 Conclusions

Here we summarize the present study and present the conclusions.

1. We have verified that (i) the dynamical quantities (the MSD, the overlap function, the diffusion coefficient and the relaxation time) show impressive density-temperature scaling where the scaling exponent γ is obtained empirically. (ii) There is strong correlation between instantaneous values of the potential energy and the virial in the 3D KA model. However, the values of the scaling exponent γ computed from such correlation depend on the choice of state point.

2. If the density-temperature scaling were perfect then the kinetic fragility would be independent of density. In an earlier work [128] it was found that the kinetic fragility has a weak dependence on density and the density dependence of the kinetic fragility is weaker than that of the thermodynamic fragility. We show that the difference may be understood from the density-temperature scaling. However, a weak density dependence of the kinetic fragility may be expected owing to the presence of imperfect density-temperature scaling arising from the sampling of states with negative virial coefficients *etc.*

3. In the 3D KA model, the diffusivity is well described by Adam Gibbs relation (Eqn. 6.4) as shown in Fig. 6.20(b). The density dependence of the coefficient A in the Adam-Gibbs relation is well characterized by the density-temperature scaling. At higher densities, reasonably good data collapse can be obtained in a scaled Adam Gibbs plot as well as for the configuration entropy with a scaling exponent computed from the density dependence of the Adam Gibbs coefficient A in Eqn. 6.4. It may be possible to improve the quality of data collapse by fine tuning the γ values.

Chapter 7

Maxima of diffusion coefficients in the modified SW model

7.1 Introduction

The phenomenology of dynamical, structural and thermodynamic behaviours of supercooled liquids is quite complex. Some of the diverse behaviours that are observed in a (dense) liquid on cooling are discussed in Chapter 1. In addition, some liquids show "anomalous" behaviours in dynamics, structure and thermodynamics. Perhaps the most well-known of such anomalies is the increase in the density of water between 0^oC and 4^oC under normal pressure. Water and Silicon - both of which are network-forming liquids - are in fact two well-known examples of anomalous liquids. In view of the complex behaviours in both "normal" and "anomalous" liquids, scaling relations are extremely useful to organize and rationalize data because they provide (i) connections between dynamics, structure and thermodynamics thus offer insights to understand the complex behaviours and (ii) simplified and unified description of data. The Adam-Gibbs (AG) relation [37] which explains the rapid rise of relaxation time - a dynamical quantity - in terms of decrease in configurational entropy - a thermodynamical quantity - is a prominent example. The Adam Gibbs relation was applied to water to show that the anomalous behaviour in the diffusion coefficient of water can be related to the anomalous behaviour of the configuration entropy [45, 167]. Similarly, Errington *et al.* observed [164] that the region of water phase diagram which

shows anomalous behaviour in diffusion coefficient and thermal expansion coefficient also show structural anomalies. Thus there are connections between structural, thermodynamic and dynamic anomalies. In the present chapter, we study a specific anomaly of the diffusion coefficient in a range of model tetrahedral liquids. Our aim is to find out to what extent the anomalous behaviour in dynamics can be related to the anomalous behaviour in structure and thermodynamics by applying a scaling relation, namely, the Rosenfeld scaling relation.

Observation of the anomaly of the diffusion coefficient in previous work: Stillinger-Weber potential (SW) is a well-known model [166] of liquid Silicon. The SW model can be written as a sum of two-body (isotropic) and three-body (anisotropic) interactions:

$$U_{SW} = \sum_{i<j} u_2(r_{ij}/\sigma) + \lambda \sum_{i<j<k} u_3(\mathbf{r}_i/\sigma, \mathbf{r}_j/\sigma, \mathbf{r}_k/\sigma), \tag{7.1}$$

Here u_2 is the two-body term and u_3 is the three-body term with λ representing the strength of the three-body interaction. In the original SW model for Silicon, $\lambda = 21$. Molinero *et al.* have showed [165] that by tuning λ, the glass-forming ability of the resulting systems can be tuned. In the course of this study they have noticed that at fixed pressure and temperature, the diffusion coefficient (D) as a function of λ always undergoes a maximum. The present study aims to rationalize this anomalous behaviour using the Rosenfeld scaling relation.

The Rosenfeld scaling relation: Rosenfeld proposed [168,169], based on studies in purely repulsive inverse power law and Lennard-Jones potentials, that the diffusion coefficient expressed in certain units can be related by simple empirical formula to the excess entropy S_E (excess over the ideal gas value):

$$D^* = D\rho^{1/3}(k_BT/M)^{-1/2} \approx A\exp(-bS_E) \tag{7.2}$$

We note that different systems may have different values of A and b [168,169].

The pair-correlation entropy: The excess entropy S_E (computationally costlier) can be approximated by the pair-correlation entropy S_2 (computationally cheaper) which depends only on the 2-particle distribution function. The pair-correlation entropy is defined as [170] :

$$\frac{S_2}{Nk_B} = -2\pi\rho \int \left[g(r)\ln g(r) - g(r) + 1\right] r^2 dr \tag{7.3}$$

In the present study we have used the pair-correlation entropy S_2 as a proxy for the excess entropy S_E in the Rosenfeld scaling relation.

7.2 Simulation details:

NPT MD simulations were done for the modified SW model (with varying λ) using an in-house code optimized for the energy and force calculations at zero pressure for several λ values in the range $\lambda = 16 - 21.5$. At each λ, simulations were done over a range of densities and temperatures both above and below the melting points. The range of state points are shown in Fig. 7.1 in $\rho - T$ plane and in Fig. 7.2 in $T - \lambda$ plane. Note that we report data in the present study in the reduced units. The units of mass, energy and length are defined in [166].

1

7.3 Results

Density anomaly: Fig. 7.1 shows that the density anomaly (at zero pressure) in the modified SW model can be tuned by tuning the strength of the anisotopric part of the SW potential. The density shows monotonic temperature dependence for lower value of λ and shows maxima (no minimum was found in the temperature range studied) for higher value of $\lambda > 19.5$. This is consistent with earlier work [170].

Anomalous behaviour of the isothermal D: Fig. 7.3 verifies that the isothermal diffusion coefficient (at zero pressure) indeed shows a non-monotonic dependence on λ. We have shown the variation of D with λ for four representative temperatures selected from Fig. 7.2 (solid horizontal

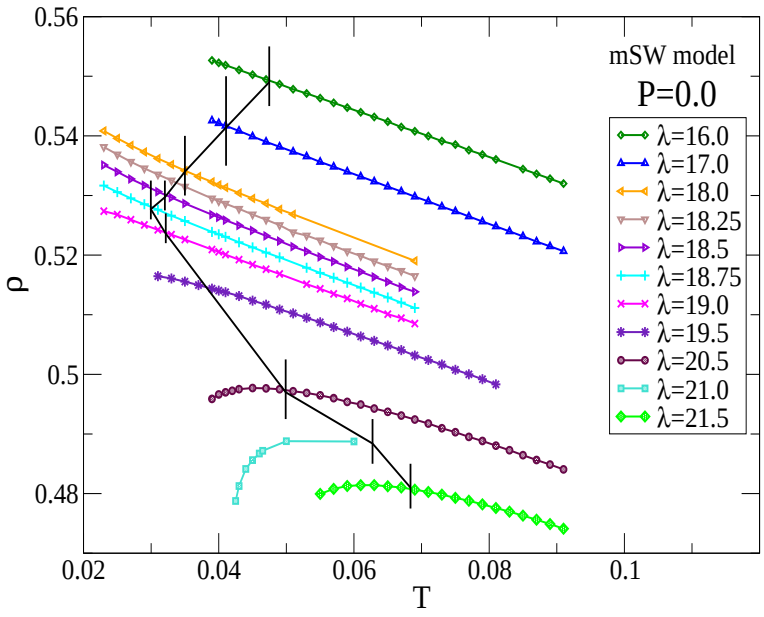

Figure 7.1: ρ *vs.* T phase diagram at zero pressure ($P = 0$) for the mSW model showing the range of the state points explored in the present study. The lines connecting the data are guide to eyes. The vertical lines are the melting temperatures reported in [165] joined by the black line representing the locus of the melting temperatures at different λ's demarcating the high T and the supercooled liquids.

lines). We find maxima in all cases in the range $\lambda \approx 17.6 - 17.8$ indicating that the positions of maxima vary weakly with temperature.

Pair correlation functions $g(r)$: In Fig. 7.4, the pair correlation functions ($g(r)$) at zero pressure are shown for different λ at a representative high ($T = 0.069$) and a low temperature ($T = 0.039$). The $g(r)$ shows more features at higher λ and lower temperature.

Correlation between D and S_2: Figs. 7.5 (bare D) and 7.6 (scaled D^*) test to what extent the diffusion coefficient may be related to the pair correlation entropy *via* the Rosenfeld scaling relation. Fig. 7.5 shows that (i) there is a well defined correlation between D and S_2 at all values of λ with data points being more scattered at higher λ. (ii) However, the functional form depends on the value of λ. *The Rosenfeld scaling relation (linear in the log-linear scale of Fig. 7.5) describes data better at lower* λ, although the deviations are small at higher λ.

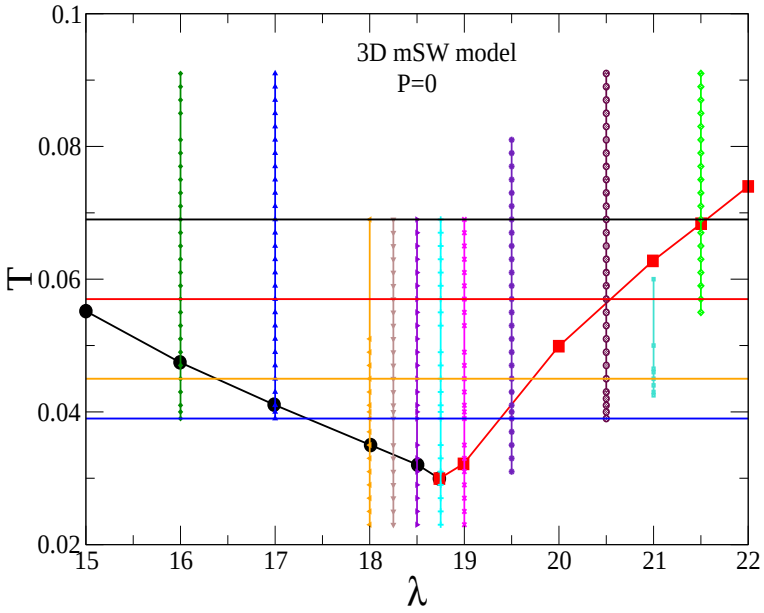

Figure 7.2: T *vs.* λ phase diagram at zero pressure ($P = 0$) for the mSW model showing the range of the state points explored in the present study. The black circles and the red squares represent the melting temperatures reported in [165]. The horizontal lines indicate a number of representative temperatures chosen to calculate isothermal diffusion coefficients.

Anomalous behaviour of S_2: The correlation in Figs. 7.5 and 7.6 suggests that the pair-correlation entropy S_2 should also show anomalous variation with λ which is verified in Fig. 7.7 for four representative temperatures. At each temperature, a maximum is found in the range $\lambda \approx 19.9 - 20.9$. We note however that (i) at the same temperature, the maximum of S_2 occur at a bigger value of λ than that of D and (ii) the temperature dependence of the maximum of S_2 is stronger than that of D.

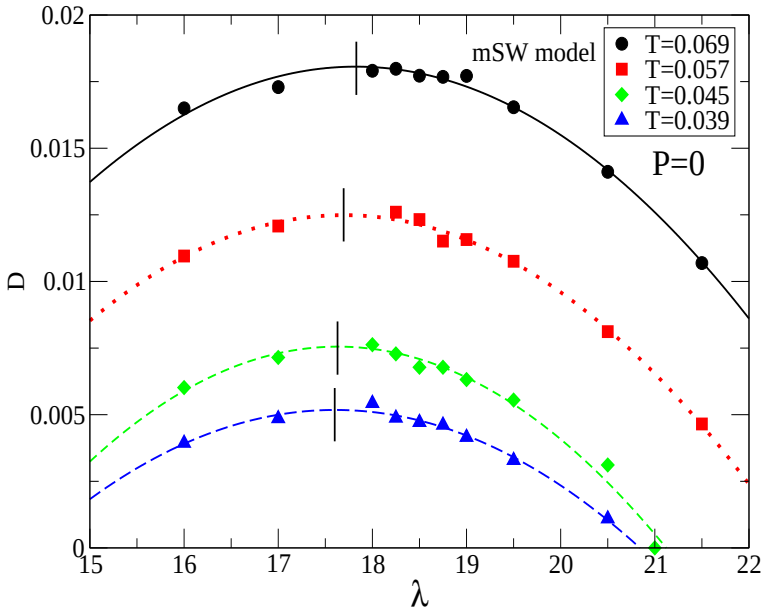

Figure 7.3: The λ dependence of the isothermal diffusion coefficient at zero pressure ($P = 0$) shows that this quantity goes through a maximum both at high and at low temperatures. The lines through data points are fit to quadratic polynomials. The black vertical lines indicate the position of the maxima of the fit curves. The maxima of the isothermal diffusion coefficients occur in the range $\lambda \approx 17.6 - 17.8$ and varies only very weakly with temperature.

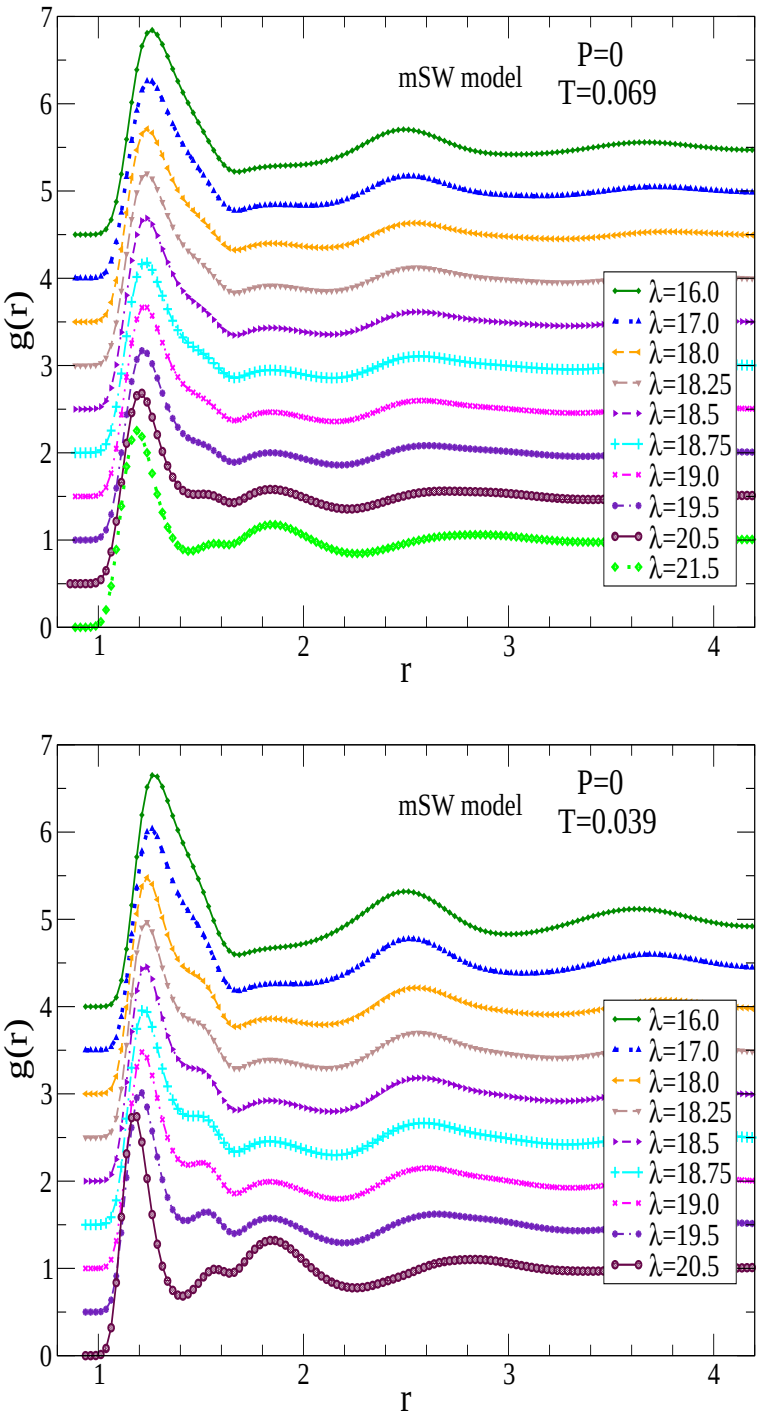

Figure 7.4: At zero pressure, the λ dependence of the $g(r)$ at two representative temperatures.

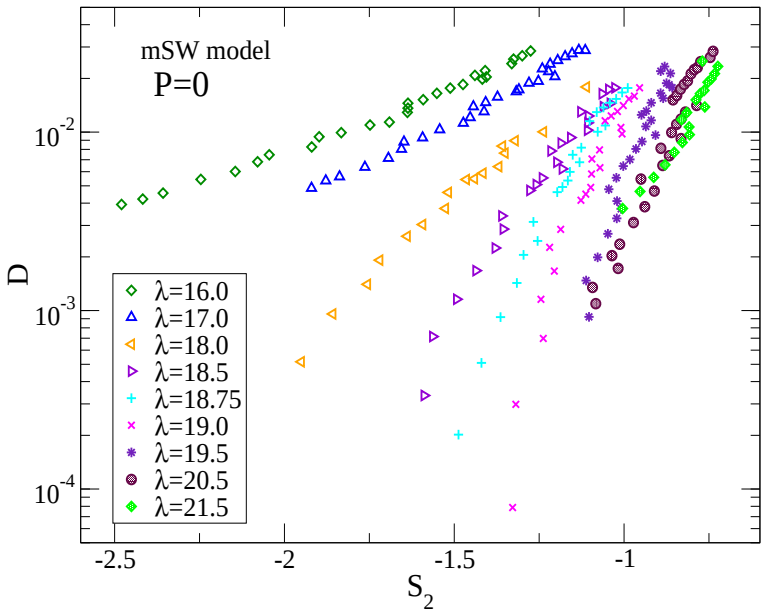

Figure 7.5: At zero pressure, the plot of the isobaric diffusion coefficient *vs.* the pair correlation entropy S_2 for different λ. The diffusion coefficient $\ln D$ is linearly correlated with S_2 for the lowest two $\lambda = 16.0, 17.0$. As λ increases, the correlation persists but the scatter of data points increases significantly.

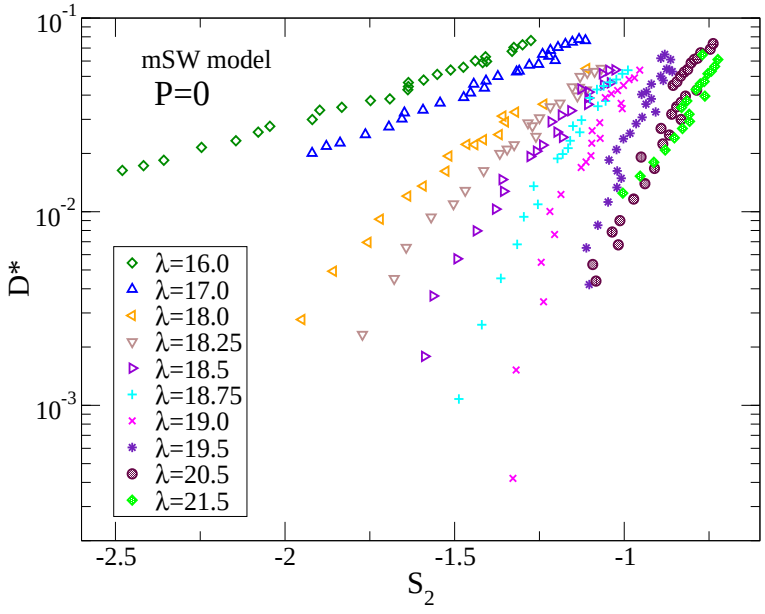

Figure 7.6: At zero pressure, the plot of the *reduced* isobaric diffusion coefficient $D^* = \frac{\rho^{1/3}}{(k_B T/m)^{-1/2}} D$ *vs.* the pair correlation entropy S_2 for different λ. Since the conversion factors are $\mathcal{O}(1)$, D^* and D behaves qualitatively similarly.

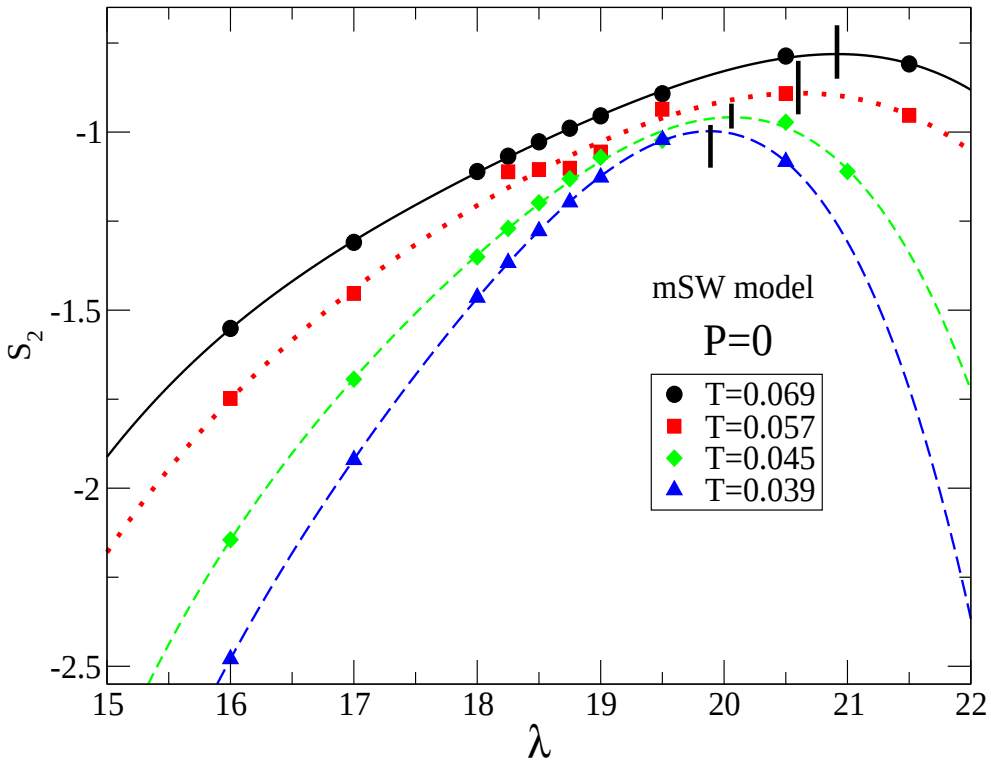

Figure 7.7: At zero pressure, the λ dependence of the isothermal pair correlation entropy S_2. This quantity also goes through a maximum both at high and at low temperatures. The lines through data points are fit to 4th order polynomials. The black vertical lines indicate the position of the maxima of the fit curves. The maxima of the isothermal diffusion coefficients occur in the range $\lambda \approx 19.9 - 20.9$ which is somewhat higher than the maxima of isothermal diffusion coefficient in the same temperature range.

7.4 Summary and conclusion

We have studied the anomalous behaviour in dynamics and thermodynamics at zero pressure over a range of densities and temperatures both above and below melting temperatures, in a range of model tetrahedral liquids (modified SW potential) by tuning the interaction potential. The conclusions are :

1. The isothermal diffusion coefficient goes though a maximum as a function of the potential parameter λ as noted in a previous work [165].

2. The diffusion coefficient at different λ are well correlated with the pair correlation entropy S_2 which is expected from the Rosenfeld scaling relation. The Rosenfeld scaling relation describe data better at lower values of λ. At higher values of λ although correlation is poorer.

3. The pair correlation entropy S_2 also show an anomalous behaviour as a function of λ. Thus we may relate the anomalous behaviour in D *i.e.* to the anomalous behaviour in S_2 *i.e.* thermodynamics.

Open questions and future works: The following issues are still open and require further analyses.

1. Whether the scaling relation between the *excess* entropy and diffusion coefficient as in the original Rosenfeld scaling relation, can describe data better. In other words, one should check to what extent the pair correlation entropy S_2 can approximate the excess entropy S_E.

2. Whether one sees better data collapse for different λ values with the excess entropy S_E.

3. Whether the scaling relation between the diffusion coefficient and the *configurational* entropy yield a better organization of data.

Chapter 8

Conclusions

In the present chapter, we summarize the work done in this thesis, describe the main conclusions and point to the open questions and future directions. A major theme of the thesis is to understand to what extent the dynamical behaviours of supercooled liquids can be described by thermodynamics when various controlling factors are *tuned* to change dynamical properties, specifically the α relaxation time of the system. In addition to the more familiar control parameters like temperature and density, we have explored the effects of "tuning" higher level parameters like the spatial dimension and the nature of the inter-particle interactions.

In chapter 3, we examine the validity of the Adam Gibbs (AG) relation in different spatial dimensions. The AG relation connects dynamics (the relaxation time) with thermodynamics (the configurational entropy) and is a central relation to understand the dynamical behaviour of glass forming liquids. We find that the AG relation is valid in four and three dimensions, but is not obeyed in two dimensions and the nature of the deviation from the AG relation depends on the details of the inter-particle interactions.

In chapter 4, we study the inter-relations among the direct measures (dynamical susceptibility, KWW exponent) and the indirect indicators (the breakdown of the Stokes Einstein relation, fragility) of the dynamical heterogeneity in different spatial dimensions. We find that as spatial dimensionality increases, on the one hand the degree of the breakdown of the SE relation becomes weaker but on the other hand the systems are more fragile. This

contradicts the observation - based on experiments and simulations predominantly in three dimensions - that more fragile systems show stronger breakdown. These correlations have however been questioned. Our results lend support to such skepticism and suggest that one should exercise caution in generalizing such trends in different spatial dimensions.

We also point out that our results in chapter 3 and 4 indicates that the behaviour in two dimensions can be qualitatively different from three dimensions. Given the importance of two (and lower) dimensional systems as model systems of study, one requires further analyses to characterize and understand the behaviours of two dimensional systems.

In chapter 5 we analyze the effect of the softness of the interaction potential on fragility in three model glass formers in three dimensions. We find on the one hand that the kinetic fragility obtained from diffusion coefficients and relaxation times *increases* with increasing softness of the interaction potential, contrary to expectations based on earlier studies [135, 141]. On the other hand, a thermodynamic fragility obtained from the temperature variation of the configuration entropy *decreases* with increasing softness of the interaction potential. We resolve this apparent contradictory trends by taking into consideration the softness dependence of the high temperature activation energy.

In chapter 6 we explore the consequences of the density-temperature scaling and strong pressure-energy correlation properties of the Kob-Andersen model in three dimensions. We provide evidence that a consequence of the scaling property which we observe to be valid approximately is that the kinetic fragility has much weaker density dependence than the thermodynamic fragility. Besides, the Adam Gibbs relation at different densities can be scaled to collapse on a master curve, albeit approximately.

In chapter 7 we analyze the unusual behaviour of the diffusion coefficient in the modified Stillinger-Weber (mSW) model. We show that the behaviour of the diffusion coefficient can be correlated with that of the pair-correlation entropy which is expected from the Rosenfeld scaling relation between diffusion coefficient and the excess entropy. However, we point out that one needs to test in the mSW model, the observation found in other systems that the pair-correlation entropy is a good approximation for the excess entropy. Besides one needs to explore whether the AG relation or the Rosenfeld relation

yields better organization of data. These are open questions and need to be pursued in the future.

Bibliography

[1] C. Angell, *Science*, **267**, 1924 (1995).

[2] Stealing the Gold: a Celebration of the Pioneering Physics of Sam Edwards, Eds. P. Goldbart, N. Goldenfeld and D. Sherrington, Chap 15 by M. Mézard, Clarendon Press, Oxford (2005).

[3] G. Tarjus, Chapter of "Dynamical heterogeneities in glasses, colloids, and granular media", Eds.: L. Berthier, G. Biroli, J-P Bouchaud, L. Cipelletti and W. van Saarloos (Oxford Univ. Press, 2011); *arXiv:1010.2938v1 [cond-mat.stat-mech]*, (2010).

[4] J. C. Dyre, *Rev. Mod. Phys.*, **78**, 953 (2006).

[5] A. Cavagna, *Phys. Rep.*, **476**, 51, (2009).

[6] M. D. Ediger, *Annu. Rev. Phys. Chem.*, **51**, 99, (2000).

[7] C. A. Angell *et al.*, *J. App. Phys.*, **88**, 3113 (2000).

[8] P G. Debenedetti and F. H. Stillinger, *Nature*, **410**, 259 (2001).

[9] J. Horbach, W. Kob and K. Binder, *Phil. Mag. B*, **77**, 297, (1998).

[10] C. Dasgupta, *Pramana*, **64**, 679, (2005).

[11] W. Kob, Lecture notes for Les Houches 2002 Summer School - Session LXXVII on Slow Relaxations and Nonequilibrium Dynamics in Condensed Matter; Les Houches: July 1-26, 2002, Springer-Verlag, (2003).

[12] L. Berthier and G. Biroli, Encyclopedia of Complexity and Systems Science, Springer, (2009).

[13] L. Berthier, G. Biroli, J-P. Bouchaud and R. L. Jack, Chapter of "Dynamical heterogeneities in glasses, colloids, and granular media", Eds.: L. Berthier, G. Biroli, J-P Bouchaud, L. Cipelletti and W. van Saarloos (Oxford Univ. Press, 2011); *arXiv:1009.4765v2 [cond-mat.stat-mech]*, (2010).

[14] J. C. Dyre, *J. Phys. Condens. Matt.*, **19**, 205105 (2007).

[15] D. S. corti, P. G. Debenedetti, S. Sastry and F. H. Stillinger, *Phys. Rev. E*, **55**, 5522 (1997).

[16] D. Kivelson and H. Reiss, *J. Phys. Chem. B*, **103**, 8337 (1999).

[17] W. Kauzmann, *Chem. Rev.*, **43**, 219 (1948).

[18] F. H. Stillinger, *J. Chem. Phys.*, **88**, 7818 (1988).

[19] Introduction to Phase Transitions and Critical Phenomena, H. E. Stanley, Oxford Univ. Press, (1971).

[20] The Feynman Lectures on Physics, vol II, R.P. Feynman, R. Leighton and M. Sands, Addison-Wesley, (1964).

[21] F. Alvarez, A. Alegria and J. Colmenero, *Phys. Rev. B*, **44**, 7306 (1991).

[22] F. Stickel, E. W. Fischer and R. Richert, *J. Chem. Phys.*, **102**, 6251 (1995).

[23] D. Kivelson, G. Tarjus, X. Zhao, and S. A. Kivelson, *Phys. Rev. E*, **53**, 751 (1996).

[24] H. Z. Cummins, *Phys. Rev. E*, **54**, 5870 (1996).

[25] H.Z. Cummins, Gen Li, Y.H. Hwang, G.Q. Shen, W.M. Du, J. Hernandez and N.J. Tao, *Z. Phys. B*, **103**, 501 (1997).

[26] M. L. Williams, R. F. Landel, and J. D. Ferry, J. Am. Chem. Soc. **77**, 3701 (1955); Viscoelastic Properties of Polymers, 3rd ed., J. D. Ferry, Wiley, New York, (1980).

[27] W. T. Laughlin and D. R. Uhlmann, *J. Phys. Chem.*, **76**, 2317 (1972).

[28] K. Schmidt-Rohr and H. W. Spiess, *Phys. Rev. Lett.* **66**, 3020 (1991).

[29] M. T. Cicerone and M. D. Ediger, *J. Chem. Phys.*, **103**, 5684 (1995).

[30] E. V. Russell and N. E. Israeloff, *Nature*, **408**, 695 (2000).

[31] W. Kob, C. Donati, S.J. Plimpton, P.H. Poole, and S.C. Glotzer *Phys. Rev. Lett.*, **79**, 2827 (1997).

[32] C. Donati, S. C. Glotzer, P. H. Poole, W. Kob and S. J. Plimpton, *Phys. Rev. E*, **60**, 3107 (1999).

[33] W. K. Kegel and A. van Blaaderen, *Science*, **287**, 290 (2000).

[34] E. R. Weeks, J.C. Crocker, A. C. Levitt, A. Schoeld and D.A. Weitz, *Science*, **287**, 627 (2000).

[35] A. Widmer-Cooper, H. Perry, P. Harrowell and D. R. Reichman, *Nat. Phys.*, **4**, 711, (2008).

[36] J. H. Gibbs and E. A. DiMarzio, *J. Chem. Phys.* **28**, 373 (1958).

[37] G. Adam and J. H. Gibbs, *J. Chem. Phys.* **43**, 139 (1965).

[38] Metastable Liquids: Concepts and Principles, P G. Debenedetti, Princeton Univ. Press, (1996).

[39] T. R. Kirkpatrick, D. Thirumalai, and P. G. Wolynes, *Phys. Rev. A* **40**, 1045 (1989); V. Lubchenko and P. G. Wolynes, *Annu. Rev. Phys. Chem.*, **58**, 235 (2007).

[40] J-P. Bouchaud and G. Biroli, *J. Chem. Phys.*, **121**, 7347 (2004).

[41] R. J. Greet and D. Turnbull, *J. Chem. Phys.* **47**, 2185 (1967).

[42] R. Richert and C. A. Angell, J. Chem. Phys., **108**, 9016 (1998).

[43] R. J. Speedy, Mol.Phys. **95**, 169 (1998).

[44] G. P. Johari, J. Chem. Phys., **112**, 8958 (2000).

[45] A. Scala, F. W. Starr, E. La Nave, F. Sciortino and H. E. Stanley, Nature (London) **406**, 166 (2000).

[46] S. Sastry, *Nature* **409**, 164 (2001).

[47] S. Sastry, P.G. Debenedetti and F. H. Stillinger, Nature, **393**, 554 (1998).

[48] S. Mossa *et al.*, Phys. Rev. E **65**, 041205 (2002).

[49] C. M. Roland *et al.*, J. Chem. Phys., **120**, 10640 (2004).

[50] S. Karmakar, Unpublished results.

[51] S. Karmakar, Ph D. Thesis (2008).

[52] W. Kob and H.C. Anderson, *Phys. Rev. Lett.*, **73**, 1376 (1994).

[53] Y. Gebremichael, M. Vogel,M. N. J. Bergroth, F. W. Starr and S. C. Glotzer, *J. Phys. Chem. B*, **109**, 15068, (2005).

[54] C. De Michele, F. Sciortino and A. Coniglio, *J. Phys.: Condens. Matter*, **16**, L489 (2004).

[55] S. Sengupta, S. Karmakar, C. Dasgupta and S. Sastry, *Phys. Rev. Lett.*, **109**, 095705 (2012).

[56] T. R. Kirkpatrick and P. G. Wolynes, *Phys. Rev. A*, **35**, 3072 (1987); *Phys. Rev. B*, **36**, 8552 (1987).

[57] T. R. Kirkpatrick and D. Thirumalai, *Phys. Rev. B*, **36**, 5388 (1987); *Phys. Rev. A*, **37**, 4439 (1998); *Phys. Rev. B*, **37**, 5342 (1988); *J. Phys. A*, **22**, L149 (1989).

[58] D. Thirumalai and T. R. Kirkpatrick, *Phys. Rev. B*, **38**, 4881 (1988).

[59] S. Capaccioli *et al.*, *J. Phys. Chem. B*, **112**, 10652 (2008).

[60] C. Cammarota *et al.*, *J. Chem. Phys.*, **131**, 194901 (2009).

[61] A. Cavagna *et al.*, arXiv:1006.3746v2 (2010).

[62] S. Franz, *J. Stat. Mech.*, (2005) P04001.

[63] C. Dasgupta, A. V. Indrani, S. Ramaswamy and M. K. Phani, *Europhys. Lett.* **15**, 307 (1991).

[64] S. C. Glotzer, V. N. Novikov and T. B. Schrøder, *J. Chem. Phys.* **112**, 509 (2000).

[65] C. Donati *et al.*, *J Non-Cryst Solids*, **307**, 215224 (2002).

[66] N. Lačević, F. W. Starr, T. B. Schrøder, and S. C. Glotzer, *J. Chem. Phys.* **119**, 7372 (2003).

[67] S. Karmakar, C. Dasgupta, S. Sastry, *Proc. Natl. Acad. Sci. (US)* **106**, 3675, (2009).

[68] S. Sastry, *PhysChemComm*, **3**, 79, (2000).

[69] S. Sastry, *Phys. Rev. Lett.*, **85**, 590 (2000).

[70] S. Sastry, *J. Phys.: Condens. Matter*, **12**, 6515 (2000).

[71] F. Sciortino, *J. Stat. Mech.*, P05015 (2005).

[72] A. Heuer, *J. Phys.: Condens. Matter*, **20**, 373101 (2008).

[73] A. Crisanti, F. Ritort, A. Rocco and M. Sellitto, *J. Phys.: Condens. Matter*, **14**, 1523 (2002).

[74] M. Goldstein, *J. Chem. Phys.*, **51**, 3728 (1969).

[75] F. H. Stillinger and T. A. Weber, *Phys. Rev. A* **25**, 978 (1982).

[76] F. H. Stillinger and T. A. Weber, *Science* **225**,983 (1984); F. H. Stillinger, *Science* **267**, 1935 (1995).

[77] T. B. Schrøder, S. Sastry, J. C. Dyre and S. C. Glotzer, *J. Chem. Phys.*, **112**, 9834 (2000).

[78] Y. Roseneld and P. Tarazona, *Mol. Phys.* **95**, 141 (1998)

[79] D. Frenkel and B. Smit, Understanding Molecular Simulation, 2nd ed. Academic Press (2002)

[80] W. Press, S. Teulolsky, W. Vetterling and B. Flannery, Numerical Recipes in Fortran, 2nd Ed., Cambridge University Press (1992).

[81] S. Karmakar, E. Lerner and I. Procaccia, *Physica A*, **391**, 1001 (2012).

[82] H. Tanaka, T. Kawasaki, H. Shintani and K. Watanabe, *Nat. Mater.*, **9**, 324 (2010).

[83] J. Hansen and I. R. McDonald, Theory of Simple Liquids (3rd Ed.), Elsevier (2008).

[84] G. L. Pollack, *Phys. Rev. A*, **23**, 2660 (1981).

[85] F. Fujara, B. Geil, H. Sillescu and G. Fleischer, *Z. Phys. B*, **88**, 195 (1992); I. Chang, F. Fujara, B. Geil, G. Heuberger, T. Mangel and H. Silescu, *J. Non-Cryst. Solids*, **172-174**, 248 (1994).

[86] I. Chang and H. Silescu, *J. Phys. Chem. B*, **101**, 8794 (1997).

[87] G. Heuberger and H. Sillescu, *J. Phys. Chem.*, **100**, 15255 (1996).

[88] M. T. Cicerone and M. D. Ediger, *J. Chem. Phys.*, **104**, 7210 (1996); M. T. Cicerone, F. R. Blackburn, and M. D. Ediger, *ibid.*, **102**, 471 (1995).

[89] F. R. Blackburn, C. Yang and M. D. Ediger, *J. Phys. Chem.*, **100**, 18249 (1996).

[90] M. K. Mapes, S. F. Swallen, K. L. Kearns and M. D. Ediger, *J. Chem. Phys.*, **124**, 054710 (2006).

[91] S. F. Swallen, K. Traynor, R. J. McMahon, M. D. Ediger and T. E. Mates, *J. Phys. Chem. B*, **113**, 4600 (2009).

[92] S. F. Swallen, P. A. Bonvallet, R. J. McMahon and M. D. Ediger, *Phys. Rev. Lett.*, **90**, 015901 (2003).

[93] E. Rössler, Phys. Rev. Lett., **65**, 1595, (1990); E. Rössler and P Eiermann, J. Chem. Phys., **100**, 5237 (1994).

[94] S. S. Ashwin, Ph D. Thesis (2005).

[95] W. Kob and H. C. Andersen, Phys. Rev. Lett., **73**, 1376 (1994).

[96] G. Tarjus and D. Kivelson, J. Chem. Phys., **103**, 3071 (1995).

[97] G. Monaco, D. Fioretto, L. Comez and G. Ruocco, Phys. Rev. E, **63**, 061502, (2001).

[98] K. Ngai, J. Magill and D. Plazek, *J. Chem. Phys.*, **112**, 1887 (1999).

[99] C. Hansen, F. Stickel, T. Berger, R. Richert, and E. W. Fischer, *J. Chem. Phys.*, **107**, 1086 (1997).

[100] L. Liu *et al.*, *Phys. Rev. Lett.*, **95**, 117802 (2005).

[101] S. Chen *et al.*, *Proc. Natl. Acad. Sci. (US)*, **103**, 12974 (2006).

[102] S. Becker, P. Poole, F. Starr, *Phys. Rev. Lett.*, **97**, 055901, (2006).

[103] F. Fernandez-Alonso, F. J. Bermejo, S. E. McLain, J. F. C. Turner, J. J. Molaison, and K. W. Herwig, *Phys. Rev. Lett.*, **98**, 077801 (2007).

[104] F. Mallamace *et al.*, *J. Phys. Chem. B*, **114**, 1870, (2010).

[105] L. Xu *et al.*, *Nature Physics*, **5**, 565, (2009).

[106] F. Affouard, M. Descamps, L.-C. Valdes, J. Habasaki, P. Bordat, and K. L. Ngai, *J. Chem. Phys.*, **131**, 104510 (2009).

[107] X. J. Han and H. R. Schober, *Phys. Rev. B*, **83**, 224201 (2011).

[108] J. A. Hodgdon and F. H. Stillinger, *Phys. Rev. E*, **48**, 207 (1993); F. H. Stillinger and J. A. Hodgdon, *Phys. Rev. E*, **50**, 2064 (1994).

[109] J.F. Douglas and D. Leporini, *J. Non-Cryst. Solids*, **235**, 137 (1998).

[110] Y. Jung,1 J. P. Garrahan and D. Chandler, *Phys. Rev. E*, **69**, 061205 (2004).

[111] X. Xia and P. G. Wolynes, *J. Phys. Chem. B* **105**, 6570 (2001).

[112] J. S. Langer, arXiv:1108.2738v2 [cond-mat.stat-mech] (2011).

[113] L. Berthier, *Phys. Rev. E*, **69**, 020201 (2004).

[114] S. Chong and W. Kob, *Phys. Rev. Lett.*, **102**, 025702 (2009).

[115] J. D. Eaves and D. R. Reichmann, *Proc. Natl. Acad. Sci. (US)* **106**, 15171, (2009).

[116] P. Charbonneau, A. Ikeda, J. A. van Meel, and K. Miyazaki, *Phys. Rev. E*, **81**, 040501 (R), (2010).

[117] D. N. Perera and P. Harrowell, *Phys. Rev. Lett.*, **81**, 120, (1998).

[118] K. Niss, C. Dalle-Ferrier, G. Tarjus, C. Alba-Simionesco, *arXiv:cond-mat/0611253v1 [cond-mat.soft]*, (2006).

[119] L. D. Landau and E. M. Lifshitz, Fluid Mechanics, 2nd. Ed., Pergamon Press (1987).

[120] P. Langevin, C. R. Acad. Sci. (Paris) **146**, 530 (1908); English translation: D. S. Lemons and A. Gythiel, Am. J. Phys. **65**, 1079 (1997).

[121] W. Sutherland, Phil. Mag., **9**, 781 (1905).

[122] A. Einstein, Ann. Phys. **17**, 549 (1905); English translation: A. Einstein, Investigations on the theory of the Brownian movement, Dover, NY (1956).

[123] A. Tolle, *Rep. Prog. Phys.*, **64**, 1473 (2001).

[124] A. Rahman, *Phys. Rev.*, **136**, A 405 (1964).

[125] C. De Michele and D. Leporini, *Phys. Rev. E*, **63**, 036701 (2001).

[126] C. A. Angell, *J. Non-Cryst. Solids* **131-133**, 13 (1991); R. Böhmer, K. L. Ngai, C. A. Angell and D. J. Plazek, *J. Chem. Phys.* **99**, 4201 (1993);

[127] R. J. Speedy, *J. Phys. Chem. B*, **103**, 4060 (1999).

[128] S. Sastry, *Nature*, **409**, 164 (2001).

[129] D. J. Wales and J. P. K. Doye *Phys. Rev. B*, **63**, 214204 (2001); **64**, 024205 (2001).

[130] C. Alba-Simionesco, D. Kivelson, and G. Tarjus, *J. Chem. Phys.* **116**, 5033 (2002); G. Tarjus, D. Kivelson, S. Mossa and C. Alba-Simionesco, *J. Chem. Phys.* **120**, 6135 (2004); C. Alba-Simionesco, A. Cailliaux, A. Alegr´ia and G. Tarjus, *Europhys. Lett.*, **68**, 58, (2004).

[131] G. Ruocco *et al.*, *J. Chem. Phys.*, **120**, 10666 (2004).

[132] V. N. Novikov and A. P. Sokolov, *Nature*, **431**, 961 (2004).

[133] P. Bordat, F. Affouard, M. Descamps, *Phys. Rev. Lett.*, **93**, 105502 (2004).

[134] P. Bordat, F. Affouard, M. Descamps, *J. Non Cryst. Solids*, **353**, 3924 (2007).

[135] J. Dudowicz, K. F. Freed and J. F. Douglas, *J. Phys. Chem. B*, **109**, 21350 (2005).

[136] J. Dudowicz, K. F. Freed and J. F. Douglas, *J. Chem. Phys.*, **123**, 111102 (2005).

[137] J. F. Douglas, J. Dudowicz and K. F. Freed, *J. Chem. Phys.* **125**, 144907 (2006); R. A. Riggleman, J. F. Douglas and J. J. de Pablo, *J. Chem. Phys.* **126**, 234903 (2007).

[138] F. W. Starr and J. F. Douglas, *Phys. Rev. Lett.* **106** 115702 (2011).

[139] S. E. Abraham, S. M. Bhattacharrya, and B. Bagchi, *Phys. Rev. Lett.* **100**, 167801 (2008).

[140] H. Shintani and H. Tanaka, *Nat. Mater.* **7**, 870 (2008).

[141] J. Mattsson *et al*, *Nature* **462**, 83, (2009).

[142] C. A. Angell and K. Ueno, *Nature* **462**, 45, (2009).

[143] S. Sengupta, *et al.* J. Chem. Phys. **135**, 194503 (2011).

[144] T. B. Schrøder *et al.*, *Phys. Rev. E*, **80**, 041502 (2009).

[145] D. Fragiadakis and C. M. Roland, *J. Chem. Phys.*, **134**, 044504 (2011).

[146] N. Gnan *et al*, *J. Chem. Phys.* **131**, 234504 (2009); T. B. Schrøder, *J. Chem. Phys.* **134** 164505 (2011), and other papers in the series.

[147] C. M. Roland, S. Hensel-Bielowka, M. Paluch and R. Casalini, *Rep. Prog. Phys.* **68**, 1405 (2005); C. M. Roland, *Macromolecules* **43**, 7875 (2010).

[148] D. Coslovich and C. M. Roland, *J. Chem. Phys.*, **131**, 151103 (2009).

[149] D. Coslovich and C. M. Roland, *J. Phys. Chem. B*, **112**, 1329 (2008).

[150] C. Alba-Simionesco, A. Cailliaux, A. Alegr´ia and G. Tarjus, *Europhys. Lett.*, **68**, 58 (2004).

[151] C. Alba-Simionesco, D. Kivelson, G. Tarjus, *J. Chem. Phys.*, **116**, 5033 (2002).

[152] N. Bailey *et al.*, *J. Chem. Phys.*, **129**, 184507 (2008).

[153] N. Bailey *et al.*, *J. Chem. Phys.*, **129**, 184508 (2008).

[154] T. B. Schrøder *et. al.*, *J. Chem. Phys.*, **131**, 234503 (2009).

[155] N. Gnan *et al.*, *J. Chem. Phys.*, **131**, 234504 (2009).

[156] T. B. Schrøder *et al.*, arxiv1004.5142v2 (2010).

[157] L. Berthier and G. Tarjus, *Phys. Rev. Lett.*, **103**, 170601 (2009).

[158] L. Berthier and G. Tarjus, arXiv:1103.0432v1 (2011).

[159] J. Broughton, G. Gilmer and J. Weeks, *Phys. Rev. B*, **25**, 4651 (1982).

[160] Y. Hiwatari *et al.*,*Prog. Theor. Phys.*, **52**, 1105 (1974).

[161] J. D. Weeks, D. Chandler and H. C. Andersen, *J. Chem. Phys.* **54**, 5237 (1971).

[162] L. Berthier and G. Tarjus, *J. Chem. Phys.* **134**, 214503 (2011).

[163] S. Toxvaerd and J. C. Dyre, *J. Chem. Phys.* **135**, 134501 (2011).

[164] J. R. Errington and P. G. Debenedetti, Nature, **409**, 318 (2001).

[165] V. Molinero, S. Sastry and A. A. Angell, *Phys. Rev. Lett.*, **97**, 075701 (2006).

[166] F. H. Stillinger and T. A. Weber, *Phys. Rev. B* **31**, 5262 (1985).

[167] F. W. Starr, S. Sastry, E. La Nave, A. Scala, H. E. Stanley, and Francesco Sciortino, *Phys. Rev. E*, **63**, 041201 (2001).

[168] Y. Rosenfeld, *Phys. Rev. A*, **15**, 2545 (1977).

[169] Y. Rosenfeld, *J. Phys. Condens. Matt.*, **11**, 5415 (1999).

[170] W. Hujo, B. S. Jabes, V. K. Rana, C. Chakravarty and V. Molinero, *J. Stat. Phys.*, **145**, 293 (2011).

[171] Karmakar et. al., Phys. Rev. Lett., **104**, 215502 (2010).

[172] D. Perera, P. Harrowell, Phys. Rev. E, **59**, 5721 (1999). D. Perera, P. Harrowell, *J. Chem. Phys.*, **111**, 5441 (1999).

[173] W. Kob, H. C. Andersen, *Phys. Rev. E*, **51**, 4626 (1995).

[174] R. Bruning *et al.*, J. Phys.: Condens. Matter , **21**, 035117 (2009).

[175] Bordat *et al.*, J. Phys.: Condens. Matter, **15**, 5397 (2003).

[176] F. Affouard, unpublished results.

[177] D. Brown and J. H. R. Clarke, *Mol. Phys.*, **51**, 5, 1243 (1984).

[178] W. G. Hoover, Computational Statistical Mechanics , Elsevier (Oxford) (1991)

[179] M. P. Allen and D. J. Tildesley, Computer Simulation of Liquids, Oxford University Press, 1991.

[180] E. La Nave, S. Sastry and F. Sciortino, *Phys. Rev. E*, **74**, 050501(R) (2006).

[181] F. W. Starr, J. F. Douglas and S. Sastry, to be submitted to *J. Chem. Phys.*, (2012).